Top-quark pair production in association with a Z boson in the final state with four charged leptons

Dissertation
zur
Erlangung des Doktorgrades (Dr. rer. nat.)
der
Mathematisch-Naturwissenschaftlichen Fakultät
der
Rheinischen Friedrich-Wilhelms-Universität Bonn

von
Sebastian Heer
aus
Troisdorf

Bonn, February 2019

Dieser Forschungsbericht wurde als Dissertation angefertigt mit Genehmigung der
Mathematisch-Naturwissenschaftlichen Fakultät der Rheinischen Friedrich-Wilhelms-Universität Bonn.

1. Gutachter:	Priv.-Doz. Dr. Markus Cristinziani
2. Gutachter:	Prof. Dr. Jochen Dingfelder
Tag der Promotion:	09.09.2019
Erscheinungsjahr:	2019

"*It's still magic even if you know how it's done*"
- Terry Pratchett

Written in vim

Acknowledgements

First and foremost, I would like to thank Priv. Doz. Dr. Markus Cristinziani for the supervision of this thesis. He is one of the nicest persons I have met and with his knowledge, support and patience I couldn't imagine having a better supervisor. During my years in his group since 2014, which includes both the master and PhD, he supported me by sending me to various schools and conferences and was always available to give his advice. In addition, I express my gratitude towards Prof. Dr. Jochen Dingfelder, Prof. Dr. Herbert Dreiner and Prof. Dr. Julia Verne, who agreed to be referees of this thesis. I would like to thank Prof. Dr. Norbert Wermes for providing the working environment on the third floor of the institute. Even though he is responsible for many students throughout different fields of research, he was always interested and supportive.

I thoroughly enjoyed being part of the reasearch group and would like to express my gratitude towards each member (listed in chronological order of meeting them): Dr. Liza Mijović was responsible to guide me through my master thesis and provided technical support on various occasions. During that time Dr. Kaven Yau Wong and Dr. Nello Bruscino shared an office with me and were always available to provide help or for a fun chat. Especially Kaven provided lots of invaluable advice, helping me advance during the master thesis and the first year of my PhD studies. With his vast experience, Dr. Vadim Kostyukhin, who visited Bonn once per month and shared an office with me during my stay at CERN in 2018, offered help and suggestions on the general structure of the analysis. I would like to thank Dr. Mazuza Ghneimat for continuing my work in the dilepton channel of $t\bar{t}\gamma$ during her PhD and helping me understand the unfolding procedure. I would like to thank Andrea Sciandra for providing his support, given that he was also working on a 4ℓ final state during his PhD, and the various fun discussions. I'm expressing my gratitude towards Carlo Alberto Gottardo, who taught me many things, both on the technical side and on italian culture, shared an office with me during my stay at CERN and was providing his support especially during the final year of the PhD. Dr. Julien Caudron, who was part of the group for two years, preceeding Liza, is one of the most patient persons I know and was always happy to give his help for any kind of problem. I thorougly thank Ö. Oğul Öncel, whom I had the pleasure to teach during his time of the master thesis, similar to how Kaven taught me and who held the help he received in very high regards. Finally I want to thank Arshia Ruina, Keshava Prasad and Matei Climescu, all master students of the group, that were always available for cheerful discussions. I want to wish all members of the group past and present, the best for their future careers.

Many thanks go to the members of the $t\bar{t}V$ multilepton analysis team of the ATLAS collaboration for their efforts and dedication they provided towards publishing the analysis.

Furthermore, I want to thank my family, especially my parents, Hannelore and Reinhard Heer, for their everlasting moral and financial support throughout my whole life and especially in recent years, to make it possible for me to graduate as a PhD. Finally, I express my deepest gratitude towards my girlfriend, Ronja Lauterbach, who provided the highest possible moral and emotional support and was always interested in my field of research, asking questions which always lead to very fun discussions.

Contents

CHAPTER 1

Introduction

The effort to understand the smallest constituents of matter started early in history, with the postulation of the four elements in ancient Greece, continuing with the formulation of early models of the atom and reaching its preliminary conclusion by developing the Standard Model, the fundamental theory describing the interactions of elementary particles, more than 60 years ago. Having discovered the Higgs boson [1, 2], the last missing elementary particle predicted by the Standard Model, experimental high-energy physics is in a stage of performing precision measurements, to further validate the Standard Model or be able to probe new physics. Even though the Standard Model delivers precise predictions, which are mostly confirmed by experiments, several questions remain open, such as observations of excess mass of unknown kind at cosmological scales or large quantum loop corrections to the Higgs mass, that cancel out due to unknown reasons.

The heaviest elementary particle known in the Standard Model is the top quark, with a mass of 173.34 ± 0.76 GeV [3], discovered in 1995 by the CDF and DØ collaborations [4, 5] at the Tevatron collider. Due to its large mass, it has the highest coupling to the Higgs boson among the particles in the Standard Model. This indicates that the effects of new physics causing the loop cancellations, which keep the Higgs mass small, could be found by studying the top-quark couplings.

Energies required to produce and detect the top quark or the Higgs boson are achievable by colliding particle beams using a particle accelerator. The accelerator facility best suited for these experiments nowadays is the Large Hadron Collider (LHC) at CERN (fr.: *"Conseil européen pour la recherche nucléaire"*), which started operating in 2008. The ATLAS and CMS experiments [1, 2], located at the LHC accelerator ring, were built to discover the Higgs boson, physics beyond the Standard Model prediction and to investigate the properties of Standard Model particles at the highest energies achievable by the LHC, colliding protons at four interaction points. With the amount of protons collided at sufficiently high energies at the LHC, several properties of the top quark, including it's coupling to gauge bosons, can be studied for the first time.

In this thesis, events of proton–proton collisions with a centre-of-mass energy of 13 TeV, collected by the ATLAS detector in the years 2015-2016, are analysed, with the aim of measuring the $t\bar{t}Z$ and $t\bar{t}W$ cross sections. Precise knowledge of the couplings of the top quark to the electroweak bosons is of interest because various models beyond the Standard Model, that modify these couplings, can be constrained.

The main focus of the thesis lies on the $t\bar{t}Z$ channel with four leptons in the final state (4ℓ). The measurement of the $t\bar{t}Z$ production cross section is performed using the profile-likelihood fit approach, combining several analysis channels. The presented analysis is the second $t\bar{t}V$ cross section measurement at 13 TeV with the ATLAS experiment, having access to rougly 11 times more data. The statistical

uncertainty of the extracted cross sections is expected to be of the same order as the systematic uncertainty, after combining all analysis channels, which motivates the effort to understand and study certain systematic uncertainties in the analysis. An unfolding procedure is performed in the 4ℓ channel and the effect of effective field theory (EFT) operators [6–8] on the $t\bar{t}Z$ cross section is studied.

The thesis is organised in the following way: Chapter 2 introduces the Standard Model, focuses on recent results of top-quark physics, motivates the measurement of the $t\bar{t}Z$ process, reviews previous measurements of the $t\bar{t}Z$ process and introduces the concepts of EFT in top-quark physics. Chapter 3 introduces the LHC, describes the ATLAS detector with its components and shows how physics processes are simulated. The main work of this thesis is documented in the Chapters 4-6, where the analysis to measure the $t\bar{t}Z$ cross section is presented, with the focus on the 4ℓ channel. Chapter 4 describes the object reconstruction in the analysis and introduces the data and simulated samples used. Chapter 5 covers the $t\bar{t}V$ multilepton analysis [9], but focuses on the $t\bar{t}Z$ 4ℓ channel. Finally, Chapter 6 documents the unfolding of data for the $t\bar{t}Z$ process, in addition to computing the differential cross section, for observables which are sensitive to EFT effects. The final chapter summarizes the obtained results and gives an outlook to possible future measurements of the $t\bar{t}Z$ process.

In addition, three appendices describe how secondary vertices are reconstructed, to improve the tagging of b-jets, how data and simulation are processed at the ATLAS experiment and how the $t\bar{t}Z$ channel with four reconstructed leptons can be improved by using multivariate methods.

CHAPTER 2

Top-Quark physics in the Standard Model

2.1 Introduction to the Standard Model

The Standard Model (SM) of particle physics is the commonly accepted, fundamental theory describing the elementary particles and their interactions. It is a gauge theory, that is based on quantum field theory (QFT) which relies on the interactions being mediated via the exchange of force carriers or mediators. These are particles themselves and are considered elementary. The theory categorizes elementary particles according to their spin.

- Bosons: These particles have integer values of spin and obey to Bose-Einstein statistics. This group consists of the gauge bosons, which are the force carriers and all have spin 1 and the recently discovered Higgs boson which has spin 0 [1, 2].
- Fermions: These particles have spin 1/2, obeying the Fermi-Dirac statistics and together with some of the bosons act as particles sensitive to the interactions carried by the gauge bosons. All the elementary fermions in the SM are the quarks and leptons which are sensitive to a different set of interactions.

A graphical overview of the elementary bosons and fermions in the Standard Model can be seen in Figure 2.1. The colours in the figure indicate which fermions are receptive to which force carrier and thus are sensitive to the corresponding interaction. The interactions described by the Standard Model and the corresponding gauge bosons can be seen in Table 2.1.

interaction	relative strength (TeV scale)	gauge boson	mass of the gauge boson [GeV]
strong	1	gluon (g)	$1.3 \cdot 10^{-3}$ eV
electromagnetic	$\sim 10^{-2}$	photon (γ)	$< 1 \cdot 10^{-18}$ eV
weak	$\sim 10^{-6}$	boson ($W^{+/-}$)	80.379 ± 0.012
		boson (Z^0)	91.1876 ± 0.0021

Table 2.1: Overview of the interactions described by the Standard Model and the corresponding gauge boson properties [10].

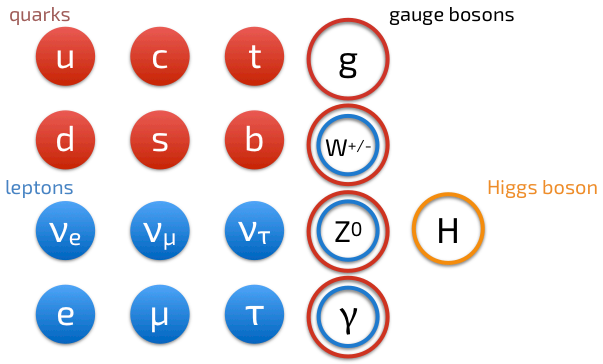

Figure 2.1: Sketch of the elementary particles in the Standard Model.

2.1.1 The electromagnetic interaction

The electromagnetic interaction describes the interaction between charged particles, as well as macroscopic charged objects. It is not limited to any range, although its potential decreases with the distance of two charged mediums: $V(r) \sim 1/r$. The corresponding theory to this interaction is Quantum Electrodynamics (QED). Since this interaction is not limited to particles, but can be observed macroscopically, a classical interpretation of the theory (quantum mechanical effects become negligible) was possible in the 19th century already [11]. In addition QED was the first among the relativistic quantum field theories to be established. The Lagrangian density of any quantum field theory introduces a wave function ψ, which is the fermion field in QED. The corresponding Lagrangian density $\mathcal{L}$ is gauge invariant under any transformation following the U(1) abelian group. Abelian denotes that the elements of the group commute, which means that the force carrier of the corresponding interaction is not able to interact with itself. The wave function transforms under the U(1) group like this:

$$\psi \rightarrow U\psi = e^{i\alpha(x)}\psi. \tag{2.1}$$

The function $\alpha(x)$ can be chosen arbitrarily, as long as it belongs to the U(1) group. The Lagrangian is:

$$\begin{aligned} \mathcal{L}_{\text{QED}} &= -\frac{1}{4}F^{\mu\nu}F_{\mu\nu} + \bar{\psi}(i\gamma_\mu D^\mu - m)\psi \text{ , with} \\ F_{\mu\nu} &= \partial_\mu A_\nu - \partial_\nu A_\mu. \end{aligned} \tag{2.2}$$

Here, $F^{\mu\nu}$ is the electromagnetic field tensor, D is the covariant derivative and A_μ is the electromagnetic field. Applied to particle physics, the fermion field can be any charged fermion, i.e. quarks or charged leptons.

2.1.2 The weak interaction

The weak interaction is responsible for radioactive decays, as it is able to change the flavour of quarks by radiating a W boson. In addition it is the only interaction which is able to affect the neutrinos in the Standard Model. Although this interaction can be described by a theory on its own, which follows the SU(2) gauge invariance, it is combined with QED as a unified theory called electroweak in the Standard Model [12–14]. It expands the idea of the fermion fields ψ, by categorizing them into left- and right-handed fields:

$$\begin{aligned} \psi_L &= \frac{1}{2}(1-\gamma^5)\psi, \\ \psi_R &= \frac{1}{2}(1+\gamma^5)\psi. \end{aligned} \tag{2.3}$$

The property of a particle to be left- or right-handed is also called chirality. Thus the operators $\frac{1}{2}(1(+/-)\gamma^5)$ are called chirality operators. In the Standard model the left-handed fields ψ_L correspond to doublets with isospin $I = \frac{1}{2}$, while the right-handed fields are described as singlets with isospins $I = 0$. The weak isospin is a quantum number of the weak interaction. It's third component I_3 is conserved in all interactions in the Standard Model. The U(1) transformation is similar to Equation 2.1 and functions for both ψ_L and ψ_R. The transformation for the left-handed doublet follows the SU(2) group. This is shown in Equation 2.4.

$$\begin{aligned} \psi_{L/R} &\xrightarrow{\mathrm{U}(1)} e^{i\alpha(x)\frac{Y}{2}}\psi_{L/R}, \\ \psi_L &\xrightarrow{\mathrm{SU}(2)_L} e^{i\beta^i(x)\frac{\sigma^i}{2}}\psi_L. \end{aligned} \tag{2.4}$$

where Y denotes the hypercharge and σ^i, $i = 1, 2, 3$ are the Pauli matrices. Combining the two groups via $G = \mathrm{SU}(2)_L \otimes \mathrm{U}(1)_Y$, and applying the product gauge invariance, four gauge fields emerge: A triplet W^i_μ that is associated to $\mathrm{SU}(2)_L$ which only interacts with left-handed fermion fields and a singlet B_μ that is associated to $\mathrm{U}(1)_Y$, which interacts with any chirality state. The Lagrangian thus becomes:

$$\begin{aligned} \mathcal{L}_{\mathrm{EW}} &= \bar{\psi}(i\gamma_\mu D^\mu - m)\psi - \frac{1}{4}W_i^{\mu\nu}W^i_{\mu\nu} - \frac{1}{4}B^{\mu\nu}B_{\mu\nu}, \\ W^i_{\mu\nu} &= \partial_\mu W^i_\nu - \partial_\nu W^i_\mu - g_W \epsilon^{ijk} W^j_\mu W^k_\nu, \\ B_{\mu\nu} &= \partial_\mu B_\nu - \partial_\nu B_\mu. \end{aligned} \tag{2.5}$$

Equation 2.5 shows the Lagrangian density for the electroweak interaction $\mathcal{L}_{\mathrm{EW}}$ as well as the definitions of the electroweak field tensors $W^i_{\mu\nu}$ and $B_{\mu\nu}$. Here, g_W is the coupling constant for the weak interaction. Since the SU(2) group is non-Abelian, the electroweak field tensor $W^i_{\mu\nu}$ contains a self-interaction term.

The W boson was discovered in 1983 at the SPS collider at Cern [15, 16]. A few months later in the same year the same experiments UA1 and UA2 found evidence for the Z boson as well [17, 18]. In 1992 and 1993 the CMS and ATLAS collaborations were founded [1, 2], continuing to explore at the high-energy frontier with pp collisions.

2.1.3 The electroweak symmetry breaking

Within the electroweak theory, the bosons, responsible for mediating the interactions, are predicted to be massless. Introducing a mass term for either the fermions or bosons in the Lagrangian density would violate the gauge invariance. However, massive electroweak bosons are observed. In addition, also fermions in the Standard Model are massive.

Even before the discovery of the heavy electroweak bosons, the "*Higgs Mechanism*" was formulated. The "Higgs field" is postulated, which is a field that permeates the universe, interacting with the elementary particles of the Standard Model. The masses of the bosons and fermions are obtained by interaction of the particles with the Higgs field, breaking the electroweak symmetry. The corresponding Lagrangian density for this interaction is:

$$\begin{aligned} \mathcal{L}_{\text{Higgs}} &= (D_\mu \phi^\dagger)\,(D^\mu \phi) - V(\phi), \\ \text{with } \phi &= \begin{pmatrix} \phi^+ \\ \phi^0 \end{pmatrix} \text{ and} \\ V(\phi) &= \mu^2 \phi^\dagger \phi + \lambda \left(\phi^\dagger \phi\right) = \mu^2 \phi^2 + \lambda \phi^4. \end{aligned} \tag{2.6}$$

Here, ϕ is a SU(2) doublet and ϕ^+ and ϕ^0 are complex scalar fields, while λ and μ are parameters of the potential term $V(\phi)$, with the assumption that $\lambda > 0$. Determining the ground state ϕ^0 depends on the sign of μ^2:

- $\mu^2 > 0$: The potential has a unique minimum at $\phi_0 = 0$, such that $\mathcal{L}_{\text{Higgs}}$ is symmetric under SU(2).
- $\mu^2 < 0$: As μ becomes a complex number, the potential has a minimum at $\phi_0^2 = -\frac{\mu^2}{2\lambda} = \frac{v^2}{2}$. The vacuum expectation value v of ϕ, which corresponds to the absolute value of the field at the minimum of the potential, becomes different from zero. A circle in the complex plane with radius $\frac{v}{\sqrt{2}}$ can be drawn for the potential, creating a set of available minima. Choosing any of these minima breaks the electroweak symmetry. This is illustrated in Figure 2.2.

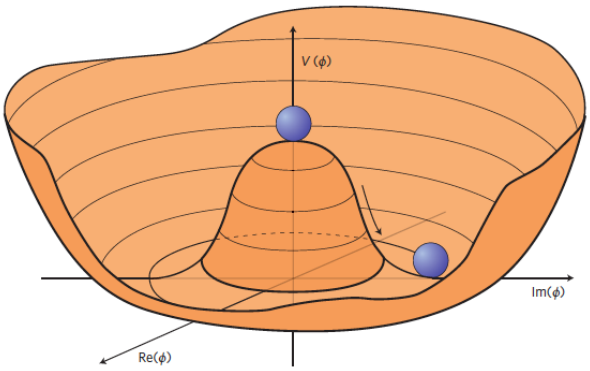

Figure 2.2: [19].

.

Further assuming $\mu^2 < 0$, in the vicinity of the minima of the potential, ϕ can be parameterised as:

$$\phi = \frac{1}{\sqrt{2}} \begin{pmatrix} 0 \\ v + h(x) \end{pmatrix}, \tag{2.7}$$

such that the vacuum expectation value of the physical Higgs field $< h >= 0$.

$$D_\mu \phi = \partial_\mu \phi - i g_W W_\mu \phi - i g_B Y \phi B_\mu \phi, \tag{2.8}$$

the first term of $\mathcal{L}_{\text{Higgs}}$ becomes:

$$\mathcal{L}^{\text{kinetic}}_{\text{Higgs}} = \frac{1}{2}\partial_\mu h \partial^\mu h + \frac{1}{2}(v+h)^2(2g_W^2|W_\mu^+|^2 + (g_B B_\mu - g_W W_\mu^3)^2). \tag{2.9}$$

The charged field $W_\mu^\pm$, introduced in Equation 2.5, is defined as: $W_\mu^\pm = \frac{1}{\sqrt{2}}(W_\mu^1 \mp i W_\mu^2)$. On the other hand, the neutral fields, B_μ and W_μ^3 are not mass eigenstates. Instead, they mix with the fields corresponding to the photon and the Z boson, A_μ and Z_μ, which are defined as:

$$\begin{pmatrix} Z_\mu \\ A_\mu \end{pmatrix} = \begin{pmatrix} \cos\theta_W & -\sin\theta_W \\ \sin\theta_W & \cos\theta_W \end{pmatrix} \begin{pmatrix} W_\mu^3 \\ A_\mu \end{pmatrix}, \tag{2.10}$$

with the weak mixing angle, also called Weinberg angle, θ_W. Taking a look at the second term proportional to v of Equation 2.9, the terms responsible for the masses of the electroweak boson can be identified:

- $\frac{1}{2}g^2 v^2 |W_\mu^+|^2 \equiv \frac{1}{2}m_W^2 |W_\mu^+|^2 \rightarrow m_W = \frac{1}{2}gv$
- $\frac{1}{2}(g_B B_\mu - g_W W_\mu^3)^2$: mixed mass term

Inserting the fields of the photon and the Z boson into the mixed mass term, the photon is found to be massless, while the mass of the Z boson can be expressed with the weak mixing angle: $m_Z = \frac{m_W}{\cos\theta_W}$.

In addition, the mass of the Higgs boson can be obtained from the potential term $V(\phi)$ of the Lagrangian (using $v = \frac{\mu}{\sqrt{\lambda}}$):

$$\begin{aligned} V(\phi) &= \lambda\left(\frac{(v+h)^2}{2} + \frac{v^2}{2}\right)^2 = \lambda v^2 h^2 + O(h^3), \\ \rightarrow m_H &= \sqrt{2\lambda}v. \end{aligned} \tag{2.11}$$

Since the value of the parameter λ is unknown, the mass of the Higgs boson is a free parameter of the Standard Model and needs to be determined through a measurement.

The masses of fermions are obtained by the Yukawa interaction after the electroweak symmetry breaking. Assuming a single generation of quarks and leptons the Lagrangian density for the Yukawa interaction is:

$$\begin{aligned} &\mathcal{L}_{\text{Yukawa}} = -Y_L \bar{L}_L \phi \ell_R - Y_d \bar{Q}_L \phi d_R - Y_u \bar{Q}_L \tilde{\phi} u_r + \text{ h.c.}, \\ &\text{with } L_L = \begin{pmatrix} \nu_L \\ \ell_L \end{pmatrix} \text{ and } Q_L = \begin{pmatrix} u_L \\ d_L \end{pmatrix}. \end{aligned} \tag{2.12}$$

Here, L_L and Q_L are the left-handed lepton and quark SU(2) doublets, while L_R, u_R and d_R are right-handed singlets. The Yukawa coupling constants between the Higgs boson and the respective fermions are part of the matrices Y_ℓ, Y_u and Y_d (for a single generation of quarks and leptons the matrices are scalar, instead). Finally, $\tilde{\phi}$ is the charge conjugate of the Higgs doublet ϕ.

After the symmetry breaking, illustrated in Figure 2.2, Equation 2.12 becomes:

$$\mathcal{L}_{\text{Yukawa}} = -\frac{v+h}{\sqrt{2}}\left(\bar{\ell}_L Y_L \ell_R + \bar{u}_L Y_u u_R + \bar{d}_L Y_d d_R\right) + \text{ h.c.}, \tag{2.13}$$

where the masses can be extracted to $m_{u,d} = vY_{u,d}/\sqrt{2}$ and $m_\ell = vY_L/\sqrt{2}$. Hence, the masses of the fermions are determined by the coupling to the Higgs boson.

Extending the problem to three quark generations introduces mixing between the quark mass and weak eigenstates, which is described by the Cabibbo-Kobayashi-Maskawa (CKM) matrix [20]. The CKM matrix is discussed further in Section 2.2.2. Introducing three lepton generations, provides mass to the charged leptons, while introducing right-handed neutrinos would create a mismatch between the neutrino flavour and mass eigenstates and lead to neutrino oscillations, which are described by the Pontecorvo–Maki–Nakagawa–Sakata (PMNS) matrix [21, 22], but are not part of the Standard Model.

The Higgs boson was discovered in 2012 at the LHC by the ATLAS and CMS collaborations [1, 2].

2.1.4 The strong interaction

The strong interaction is responsible for the confinement of quarks inside hadrons, by introducing the concept of colours and the creation of quark-antiquark pairs if enough energy is provided. Its force carrier, the gluon is the driving force in the creation of initial states via gluon-fusion for pp collisons at the LHC.

The corresponding theory to the strong interaction is Quantum Chromodynamics (QCD). It is a theory that follows the $\text{SU}(3)_C$ gauge symmetry. The QCD Lagragian is defined as:

$$\begin{aligned} \mathcal{L}_{\text{QCD}} &= \bar{\psi}(i\gamma_\mu D^\mu - m)\psi - \frac{1}{4} G^A_{\mu\nu} G^{\mu\nu}_A \\ G^{\mu\nu}_A &= \partial_\mu G^\nu_A - \partial_\nu G^\mu_A - g_s \epsilon^{ijk} G^\mu_j G^\nu_k \end{aligned} \tag{2.14}$$

Equation 2.14 shows the Lagrangian density for the strong interaction $\mathcal{L}_{\text{QCD}}$ as well as the definition of the gluon field tensor $G^{\mu\nu}_A$. Here, g_s is the coupling constant of the strong interaction. Similarly to SU(2), the SU(3) group is non-Abelian as well, which means that the gluon carries colour and is able to self-interact. This is reflected in the last term of the gluon field tensor. The gluon was discovered in 1979 at DESY with the PETRA collider [23, 24] .

With the three interactions of the Standard Model described by the electroweak theory and QCD the full gauge symmetry of the Standard Model is defined like this:

$$G_{\text{SM}} = \text{SU}(3)_C \otimes \text{SU}(2)_L \otimes \text{U}(1)_Y \tag{2.15}$$

2.1.5 Open questions in the Standard Model

The Standard Model proved to be very successful in predictions since it was first described. However, there are various open questions in particle physics today which cannot be answered by the Standard Model. A few examples are:

- gravity:
  This interaction is not included in the Standard Model, a potential graviton as the force carrier of gravity has not been discovered. Even though gravity is the force most noticeable on macroscopic scales, it's relative strength, acting on elementary particles is predicted to be $<10^{-40}$. compared

to the electromagnetic interaction and it is not included in the theory, since no common quantum gravity theory has been established.

- hierarchy problem:
  The Higgs boson with a mass of 126 GeV compared to gravitational Planck scale $M_{\text{Planck}} \sim 10^{19}$ GeV gives a ratio of $\sim 10^{-17}$. The interactions in the Standard model are believed to be unified at the Planck scale. In order for a fundamental theory based on QFT to function, quantum corrections need to be introduced that are on the order of the Planck scale. How can this hierarchy be stable with such large quantum corrections?

- neutrino masses:
  Neutrinos are predicted to be massless by the Standard Model. However, neutrino oscillations, first observed for solar neutrinos that travel to the earth (and later by neutrinos produced in reactors or in the atmosphere) cannot be explained without a mass among the three neutrino flavours [25].

- dark matter and dark energy:
  A number of observations in astronomy, such as the radial velocity of galaxies, led to the postulation of dark matter. In addition, the expansion of the universe is not understood and the driving force was labeled as dark energy of the universe is not understood and the driving force was labeled as dark energy. Recent experiments, like the Planck experiment, proved that the composition of matter in the universe is dominated by dark energy (68%), followed by dark matter (27%) and ordinary matter (5%) [26]. Dark matter could consist of particles, that could be discovered in the pp collisions at the LHC. The Standard Model gives no prediction to a potential dark matter candidate, nor any explanation what dark energy might be.

Theorists have proposed multiple BSM (beyond Standard Model) theories to answer these questions. The most prominent example is the theory of supersymmetry (SUSY), which introduces supersymmetric partners to fermions and bosons in the Standard Model and provides a dark matter candidate [27]. It was anticipated to find evidence for the existence of SUSY with early data taking of the LHC at 8 and 13 TeV, however only exclusion limits of potential SUSY particles could be adjusted, which makes it harder for SUSY to sustain its potential in answering most of the open questions in the Standard Model.

2.2 The top quark

The top quark was discovered in 1995 by the CDF and DØ collaborations [4, 5]. Recent reviews on results on top-quark physics can be found in References [28, 29]. With a mass of 173.34 ± 0.76 GeV [3], the top quark is the heaviest elementary particle known today. In addition, it is part of the third generation of quarks together with the bottom quark. A third generation was predicted already in 1973 to allow the gauge invariance to be preserved with CP-violating decays that have been observed in the weak interaction [20]. On top of its large mass, the top quark has a large decay width and therefore a short lifetime ($\sim 5 \times 10^{-25}$ s). This preceeds the time needed for the quark to hadronize (on the $\text{GeV} - \text{TeV}$ scale), making the top quark unique among all other quarks. So the top quark is detected via its decay products. Figure 2.3 shows a summary of direct top-mass measurements done by ATLAS and CMS [30].

2.2.1 Production

At the LHC, top quarks are most often produced in $t\bar{t}$ pairs via the strong interaction. At leading order there are two possible production processes to create a $t\bar{t}$ pair: $q\bar{q}$ annihilation and gluon fusion, as shown

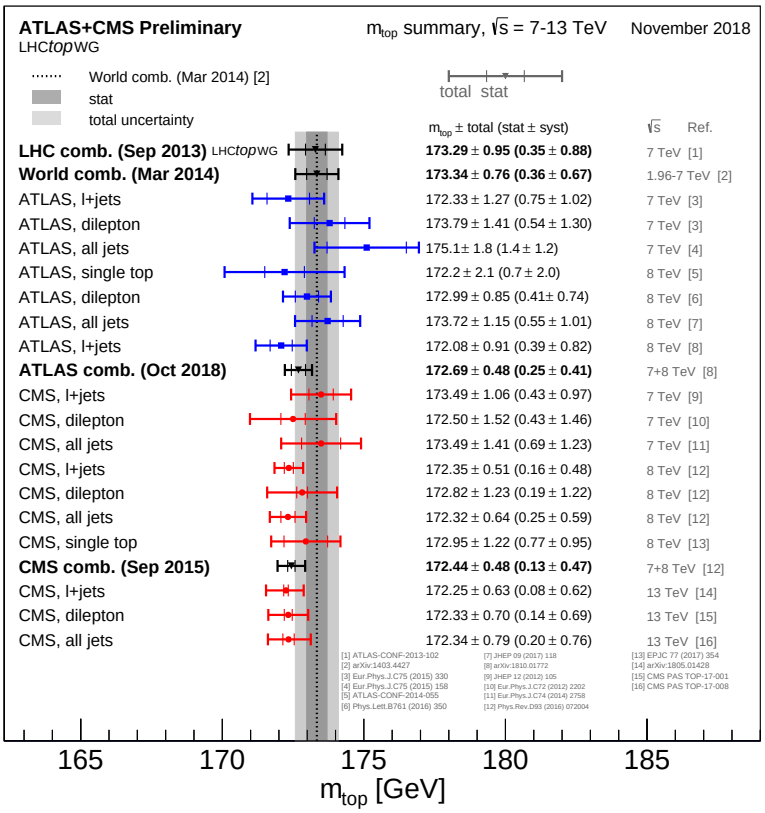

Figure 2.3: Summary of the ATLAS and CMS direct m_{top} measurements. The results are compared with the LHC and Tevatron+LHC m_{top} combinations. [30].

.

in Figure 2.4.

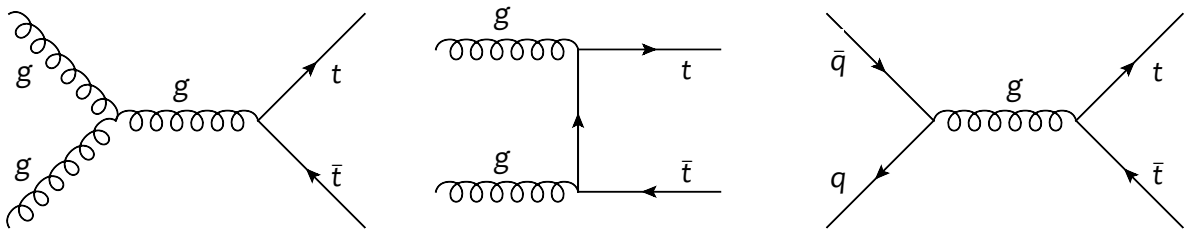

Figure 2.4: $t\bar{t}$ production diagrams. The diagrams on the left and in the centre show gluon fusion and the diagram on the right shows $q\bar{q}$ annihilation.

At the LHC 80-90% of all $t\bar{t}$ pairs are created via gluon fusion, increasing with the centre-of-mass energy $\sqrt{s}$. In contrast, at the Tevatron [31], where the top quark was discovered, the main production process was $q\bar{q}$ annihilation (85% of all $t\bar{t}$ pairs), since there protons collided with antiprotons and the centre-of-mass energy of 1.96 TeV was lower than at the LHC. The predicted $t\bar{t}$ cross section compared to the observed ones at the Tevatron and the LHC as a function of the centre-of-mass energy for both pp and $p\bar{p}$ collisions can be seen in Figure 2.5. The predicted cross section was calculated at next-to-next-to-leading order (NNLO) in α_S [32] and complemented with a next-to-next-to-leading-log order (NNLL)

soft-gluon resummation [33].

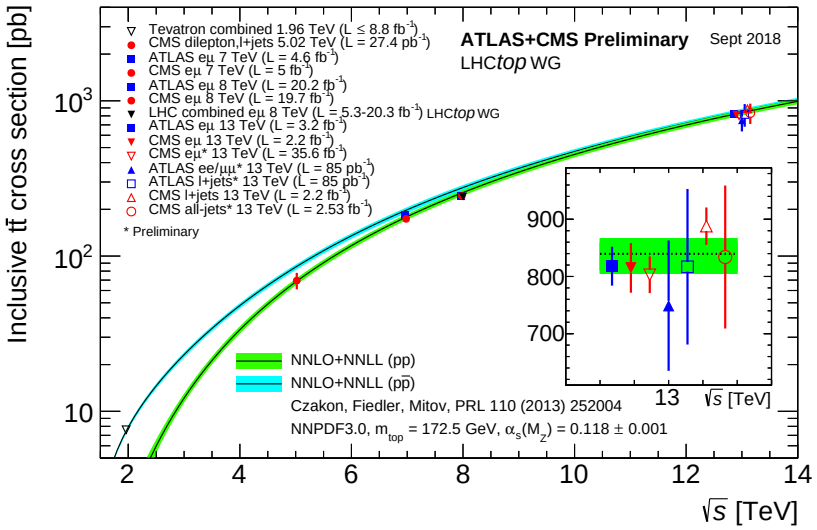

Figure 2.5: Summary of LHC and Tevatron measurements of the top-pair production cross section as a function of the centre-of-mass energy compared to the NNLO QCD calculation, complemented with NNLL resummation [30].

.

In addition to the production of a top-quark pair via the strong interaction, a single top quark can be produced via the electroweak interaction. There are three possible single top production diagrams in the Standard Model: the s-channel ($q\bar{q}'$ annihilation), the t-channel (exchange of a W boson between a light and a bottom quark) and the Wt-channel (associated production of a W boson with a single top quark) [34]. The corresponding diagrams for the single top-quark production can be seen in Figure 2.6, including a diagram for tWZ, which is a single top process where an extra Z boson is in the final state, that is a major background to $t\bar{t}Z$ in the tetralepton channel.

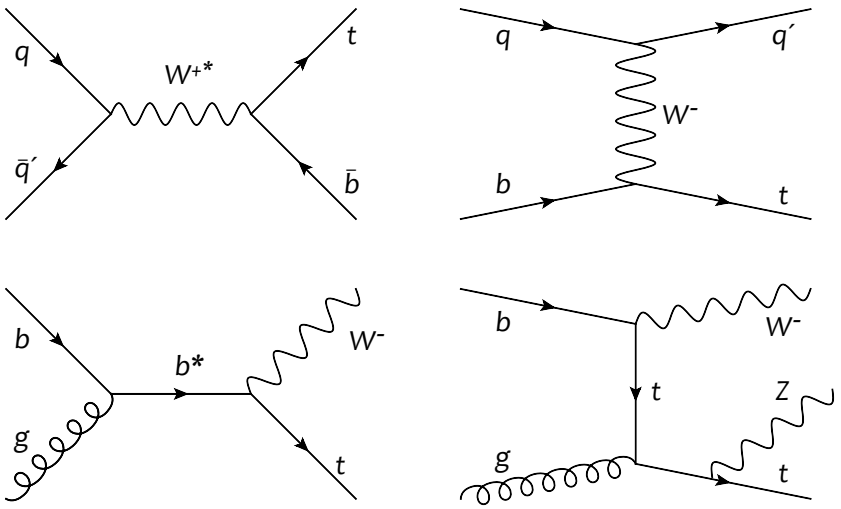

Figure 2.6: Single top production diagrams. From top left to bottom right, the diagrams show examples of single top production in the s-channel, t-channel, Wt-channel and tWZ-channel.

A summary of recent single-top quark production cross section measurements by the ATLAS and CMS experiments can be found in Figure 2.7. Here the predicted cross sections have been calculated at next-to-leading order (NLO) in α_s and the Wt cross section calculation has been complemented with a NNLL soft-gluon resummation, similar to the predicted $t\bar{t}$ cross section (at NNLO).

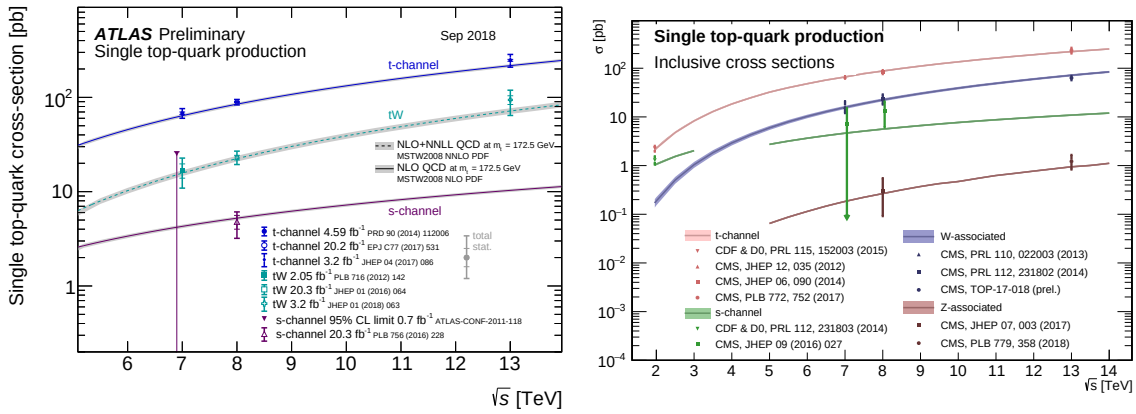

Figure 2.7: Summary of ATLAS (left) and CMS (right) measurements of the single top production cross sections in various channels as a function of the centre of mass energy compared to theoretical calculations based on NLO QCD and on NLO QCD complemented with NNLL resummation [35, 36].

2.2.2 Decay

The decay of the top quark happens before it is able to hadronize. It decays via the weak interaction to another quark flavour, with a probability dependent on the CKM matrix elements [20].

$$V_{\mathrm{CKM}} = \begin{pmatrix} V_{ud} & V_{us} & V_{ub} \\ V_{cd} & V_{cs} & V_{cb} \\ V_{td} & V_{ts} & V_{tb} \end{pmatrix} = \begin{pmatrix} c_{12}c_{13} & s_{12}c_{13} & s_{13}e^{-i\delta} \\ -s_{12}c_{23} - c_{12}s_{23}s_{13}e^{i\delta} & c_{12}c_{23} - s_{12}s_{23}s_{13}e^{i\delta} & s_{23}c_{13} \\ s_{12}s_{23} - c_{12}c_{23}s_{13}e^{i\delta} & -c_{12}s_{23} - s_{12}c_{23}s_{13}e^{i\delta} & c_{23}c_{13} \end{pmatrix} \tag{2.16}$$

Equation 2.16 shows the definition of the CKM matrix, with the CP-violating phase δ and sine and cosine of the three Euler angles $\theta_{12}, \theta_{23}, \theta_{13}$ denoted as s_{ij} and c_{ij} respectively. As such, all matrix elements can be determined from the three angle and the phase alone. The current best values for each matrix element are given in Table 2.2.

matrix element	experimental value / average
$\lvert V_{ud}\rvert$	0.97425 ± 0.00022 [37]
$\lvert V_{us}\rvert$	0.2253 ± 0.0008 [38]
$\lvert V_{cd}\rvert$	0.225 ± 0.008 [10, 39]
$\lvert V_{cs}\rvert$	0.986 ± 0.016 [40, 41]
$\lvert V_{cb}\rvert$	0.0411 ± 0.0013 [10]
$\lvert V_{ub}\rvert$	0.00413 ± 0.00049 [42, 43]
$\lvert V_{td}\rvert$	0.0084 ± 0.0006 [44]
$\lvert V_{ts}\rvert$	0.0400 ± 0.0027 [44]
$\lvert V_{tb}\rvert$	1.021 ± 0.032 [45–48]

Table 2.2: Measured values of all CKM matrix elements [10]. If multiple references are given the average value is quoted.

Since the $|V_{tb}|$ element is very close to one the top quark almost exclusively decays to a bottom quark and a W boson, while the other possible decays to a strange or an up quark are highly suppressed.

Assuming $t \to Wb$, the decay of a $t\bar{t}$ pair depends on the decay of the W boson only. It has two decay modes: $W \to q\bar{q}'$, with $q = u, d, s, c, b$ and $W \to \ell\nu_\ell$, with $\ell = e, \mu, \tau$ and branching fractions of $\sim 67\%$ and $\sim 33\%$ respectively [10]. However, the τ lepton decays before a direct detection in the ATLAS detector is possible, see Section 3. Therefore only decays of τ leptons to electrons or muons (with a branching fraction of $\sim 35\%$) are considered as leptonic decays for the W boson. The $t\bar{t}$ decay channels can be separated into three categories: all hadronic, lepton + jets and dilepton. If among the charged leptons only the τ leptons decaying to electrons and muons are counted, the branching ratios are $\sim 56\%$, 38% and 6%. respectively. A more precise example of calculating the branching ratios can be seen in Section 2.3, where the branching ratio of the $t\bar{t}Z$ 4ℓ channel is calculated.

2.3 Top-quark production in associating with electroweak bosons

Top quark pairs are produced in large quantities at the LHC, making it the best environment to study properties of the top-quark like the associated production of a top quark pair with one of the electroweak bosons ($t\bar{t}V$). Representative leading-order diagrams for the associated production of a top quark pair with a W or Z boson are shown in Figure 2.8.

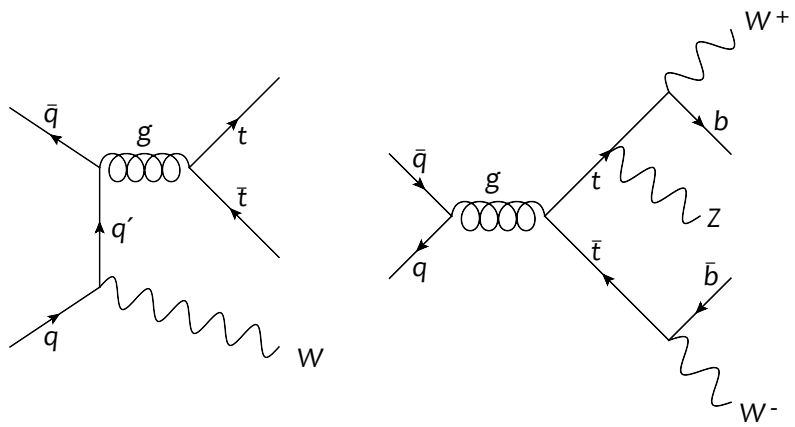

Figure 2.8: Tree-level diagrams for $t\bar{t}W$ (left) and $t\bar{t}Z$ (right).

The production of $t\bar{t}Z$ allows to constrain the coupling of the top-quark to the Z boson (tZ coupling). This is of interest because constraining the tZ coupling allows to probe several BSM models which modify the coupling. The $t\bar{t}W$ process is a rare source of two same-sign leptons in the Standard Model.

Both $t\bar{t}W$ and $t\bar{t}Z$ are important backgrounds to SUSY searches, where a SUSY candidate decays to the heaviest quark in the Standard Model, or to the $t\bar{t}H$ process, which has a smaller cross section than the $t\bar{t}V$ processes and has recently been observed [49, 50]. The main focus of this thesis is the $t\bar{t}Z$ process decaying into 4 leptons.

2.3.1 The tZ coupling in the Standard Model

The Z boson is able to couple to the Higgs boson, the electroweak bosons and all fermionic particles, including the top-quark. The tZ coupling is described via the vector and axial vector couplings within the framework of the electroweak interaction. Equations 2.17 and 2.18 show the definition of these Standard Model couplings along with their predicted numerical value [51].

$$C_{\mathrm{V}}^{\mathrm{Z,SM}} = \frac{T_t^3 - 2Q_t \sin^2\theta_{\mathrm{W}}}{2\sin\theta_{\mathrm{W}}\cos\theta_{\mathrm{W}}} \simeq 0.244, \tag{2.17}$$

$$C_{\mathrm{A}}^{\mathrm{Z,SM}} = \frac{-T_t^3}{2\sin\theta_{\mathrm{W}}\cos\theta_{\mathrm{W}}} \simeq -0.601, \tag{2.18}$$

where $Q_t = 2/3$ is the electric charge of the top-quark, $T_t^3 = 1/2$ is the third component of the weak isospin for the top-quark and $\theta_{\mathrm{W}} \approx 30°$ is the weak mixing angle.

The tZ coupling affects processes where either a top-quark radiates a Z boson or the Z boson enters a loop of a $t\bar{t}$ pair. The corresponding diagrams can be seen in Figure 2.9. The first case corresponds to a decay of $t \to WZb$ and has a branching fraction of $\sim 2 \cdot 10^{-4}$ [52].

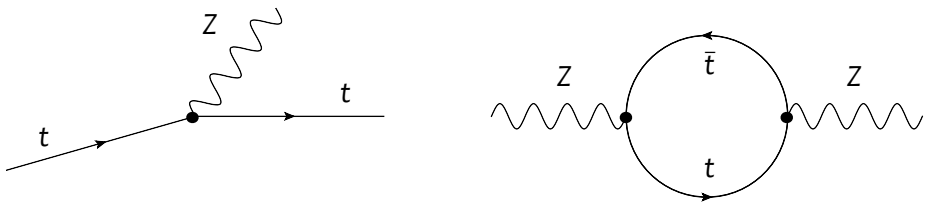

Figure 2.9: Diagrams showing the tZ couplings in the Standard Model.

2.3.2 The $t\bar{t}Z$ process

The $t\bar{t}Z$ process allows direct access to the tZ coupling and allows a precise determination, due to the top-quark being produced most commonly in a $t\bar{t}$-pair. It can be expressed in an interaction Lagrangian [51], as shown in Equation 2.19.

$$\mathcal{L}^{\mathrm{SM}}_{t\bar{t}Z} = e\,\bar{u}\,(p_t)\Big[\,\gamma^{\mu}\,\Big(C^{\mathrm{Z,SM}}_{\mathrm{V}} + \gamma_5\,C^{\mathrm{Z,SM}}_{\mathrm{A}}\Big)\Big]\,v\,(p_{\bar{t}})\,Z_{\mu}, \tag{2.19}$$

where e is the electromagnetic coupling constant, $\bar{u}\,(p_t)$ and $v\,(p_{\bar{t}})$ are the Dirac spinors of the top- and antitop-quark, Z_{μ} refers to the gauge field of the Z boson and $C^{\mathrm{Z,SM}}_{\mathrm{V}}$ and $C^{\mathrm{Z,SM}}_{\mathrm{A}}$ are the tZ vector and axial vector couplings, as shown in Equations 2.17 and 2.18.

In this thesis the $t\bar{t}Z$ cross section is measured. The predicted cross section depends on the centre-of-mass energy ($\sqrt{s}$) the accelerator is operated and increases with $\sqrt{s}$. Figure 2.10 shows the dependence of the cross section as a function of $\sqrt{s}$ for $t\bar{t}Z$, $t\bar{t}W$ and $t\bar{t}H$. The $t\bar{t}W$ cross section is split into $t\bar{t}W^{+}$ and $t\bar{t}W^{-}$ due to the larger abundance of valence up-type quarks in pp-collisions. It can be seen that the absolute cross section of all processes shown, is predicted to increase with higher energies, but both $t\bar{t}Z$ and $t\bar{t}H$ have a larger slope.

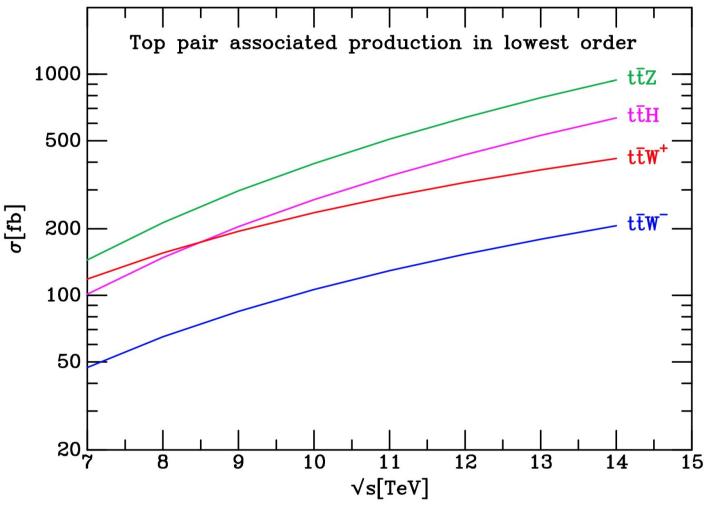

Figure 2.10: Predicted leading order cross sections for $pp \rightarrow t\bar{t}Z$, $t\bar{t}W$ and $t\bar{t}H$ as a function of $\sqrt{s}$ [53].

The predicted cross sections in NLO QCD and EW of $t\bar{t}Z$ and $t\bar{t}W$ at the LHC with a centre-of-mass energy of 13 TeV are [54]:

$$\begin{aligned}\sigma_{t\bar{t}Z} &= 0.88^{+0.08}_{-0.10}\,(\text{scale}) \pm 0.02\,(\text{PDF}) \pm 0.02\,(\alpha_S)\ \text{pb}\,,\\ \sigma_{t\bar{t}W} &= 0.60^{+0.08}_{-0.07}\,(\text{scale}) \pm 0.01\,(\text{PDF}) \pm 0.02\,(\alpha_S)\ \text{pb}\,.\end{aligned} \tag{2.20}$$

2.3.3 The $t\bar{t}Z \to 4\ell$ channel

The tetralepton channel of the $t\bar{t}Z$ process provides the cleanest signature, since it features the most leptons among all possible $t\bar{t}Z$ decay channels and a small amount of jets. However, due to the branching ratios of the electroweak gauge bosons, this channel has the smallest branching fraction. To calculate it, the branching fractions of the two electroweak bosons need to be known. Additionally the branching fraction of τ leptons to electrons or muons is necessary. These are shown in Table 2.3.

Z decay	BR
l^+l^-	$(10.099 \pm 0.0191)\%$
$q\bar{q}$	$(69.911 \pm 0.056)\%$
$\nu_l\nu_{\bar{l}}$	$(20.000 \pm 0.055)\%$

W decay	BR
$l\nu_l$	$(32.72 \pm 0.40)\%$
$q\bar{q}'$	$(67.41 \pm 0.27)\%$

τ decay	BR
$e\bar{\nu}_e\nu_\tau$	$(17.82 \pm 0.04)\%$
$\mu\bar{\nu}_\mu\nu_\tau$	$(17.39 \pm 0.04)\%$

Table 2.3: Branching fractions of the electroweak bosons and the τ lepton [10]. Here, l stands for e, μ, τ.

Since it is common to only refer light leptons (electrons and muons) as leptons in the analysis (due to the short lifetime of the τ lepton), it can be concluded that at most 35.2% of all τ leptons are recognized as leptons by the detector. With this information all possible decay channels of the $t\bar{t}V$ processes can be calculated. This is shown in Table 2.4.

Figure 2.11 shows a leading order Feynman diagram for the $t\bar{t}Z$ tetralepton channel at tree level.

Possible background processes with four leptons are few in the Standard Model. The process with the highest cross section among these is the ZZ process. Other important backgrounds with four leptons are tWZ, $t\bar{t}H$. Any other process with four leptons in the final state has a cross section which is too small to matter, for example 4 top quarks, $t\bar{t}WW$ or triboson processes with four leptons (WWZ and WZZ). In addition, it is possible for processes with three leptons to appear as backgrounds, if fake leptons are present. This is discussed in more detail in Sections 3 and 5.

2.3.4 Measurements of the $pp \to t\bar{t}Z$ cross section at the LHC

So far the $t\bar{t}Z$ cross section has been always measured together with the $t\bar{t}W$ cross section at the LHC, due to the similarities of the two processes in terms of final state objects and background compositions. It is common to perform a two-dimensional fit to extract the two cross sections simultaneously. The analysis channels, their motivations and background compositions are only introduced here, while they are discussed in detail for the analysis of this thesis in Section 5. A comparison of the result from the three measurements discussed in this section can be seen in Table 2.5.

Z decay	BR
0ℓ	90.71%
1ℓ	1.54%
2ℓ	7.75%

W decay	BR
0ℓ	74.65%
1ℓ	25.35%

$t\bar{t}Z$ decay	BR
0ℓ	50.55%
1ℓ	35.19%
2ℓ	10.73%
3ℓ	3.03%
4ℓ	0.50%

$t\bar{t}W$ decay	BR
0ℓ	41.60%
1ℓ	42.38%
2ℓ	14.39%
3ℓ	1.63%

Table 2.4: Branching fractions of the electroweak bosons and the $t\bar{t}V$ processes to light leptons. Here, ℓ stands for e or μ.

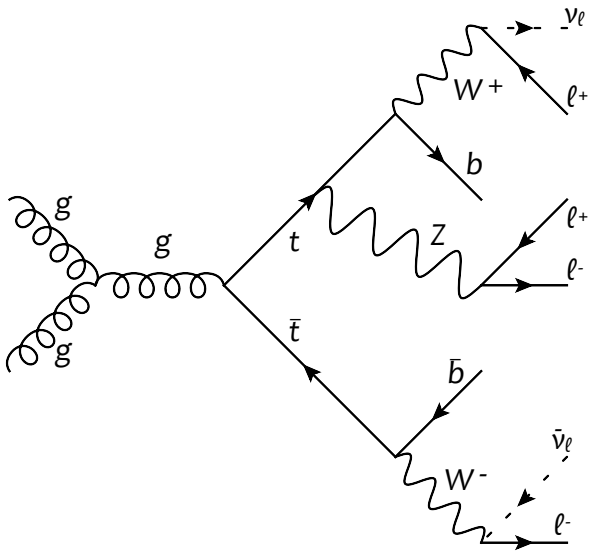

Figure 2.11: $t\bar{t}Z$ leading order production diagram with subsequent decay into 4 leptons.

ATLAS measurement with $\sqrt{s} = 8$ TeV and $\mathcal{L} = 20.3$ fb^{-1}

This $t\bar{t}V$ search by the ATLAS collaboration uses the full 8 TeV dataset of 20.3 fb^{-1} collected in 2012 [55]. Some of the analysis regions presented in this thesis are based on the regions for this early search. The following analysis channels were part of this search: 2ℓOS, 2ℓSS, 3ℓ and 4ℓ. The 2ℓOS (opposite-sign) channel includes three signal regions, which all use a neural network discriminant [60, 61] to extract the $t\bar{t}Z$ or $t\bar{t}W$ signal. It provides the lowest sensitivity to both $t\bar{t}W$ and $t\bar{t}Z$, at the level of 0.1 and 1.1σ, due to large background contributions of $t\bar{t}$. The 2ℓSS (same-sign) channel targets only the $t\bar{t}W$ process in three signal regions, depending on the lepton flavour (ee, $e\mu$ and $\mu\mu$). It provides a large sensitivity of 5.0σ. The trilepton channel is able to target both signal processes and has four analysis regions. It has the sensitivity to $t\bar{t}Z$ with an observed significance of 3.3σ and 1.0σ for $t\bar{t}W$. Finally, the 4ℓ channel is

Search	$\sqrt{s}$	Data collected	$\sigma_{t\bar{t}W}$	$\sigma_{t\bar{t}Z}$
ATLAS [55]	8 TeV	20.3 fb^{-1}	369^{+86}_{-79}(stat.) ± 44 (syst.) fb	176^{+52}_{-48}(stat.) ± 24 (syst.) fb
CMS [56]	8 TeV	19.5 fb^{-1}	170^{+90}_{-80}(stat.) ± 70 (syst.) fb	$200^{+80}_{-70}(\text{stat.})^{+40}_{-30}$ (syst.) fb
NLO QCD [57]	8 TeV	-	203.1 ± 0.3 fb	205.7 ± 0.2 fb
ATLAS [58]	13 TeV	3.2 fb^{-1}	0.92 ± 0.29 (stat.) ± 0.10 (syst.) pb	1.50 ± 0.72 (stat.) ± 0.33 (syst.) pb
CMS [59]	13 TeV	35.9 fb^{-1}	$0.77^{+0.12}_{-0.11}(\text{stat.})^{+0.13}_{-0.12}$(syst.) pb	$0.99^{+0.09}_{-0.08}(\text{stat.})^{+0.12}_{-0.10}$(syst.) pb
NLO QCD+EW [54]	13 TeV	-	0.60 ± 0.08 pb	0.84 ± 0.10 pb

Table 2.5: Results of previous measurements for $t\bar{t}V$, including comparisons to the relative predictions.

sensitive to only $t\bar{t}Z$ and comes with 5 signal regions which depend on the flavour of the leptons and the number of b-tagged jets and a control region for the ZZ background [62]. It is worthwhile to note that four of these regions are still used in the analysis presented in this thesis. Since this channel is statistically limited, further optimization in this channel proved to be very difficult. The observed significance in this channel was 2.4σ.

In conclusion the combined observed significances for $t\bar{t}W$ and $t\bar{t}Z$ at 8 TeV in ATLAS are 5.0σ and 4.2σ, respectively. The extracted cross sections agree with the Standard Model within the uncertainties and can be seen in Figure 2.12.

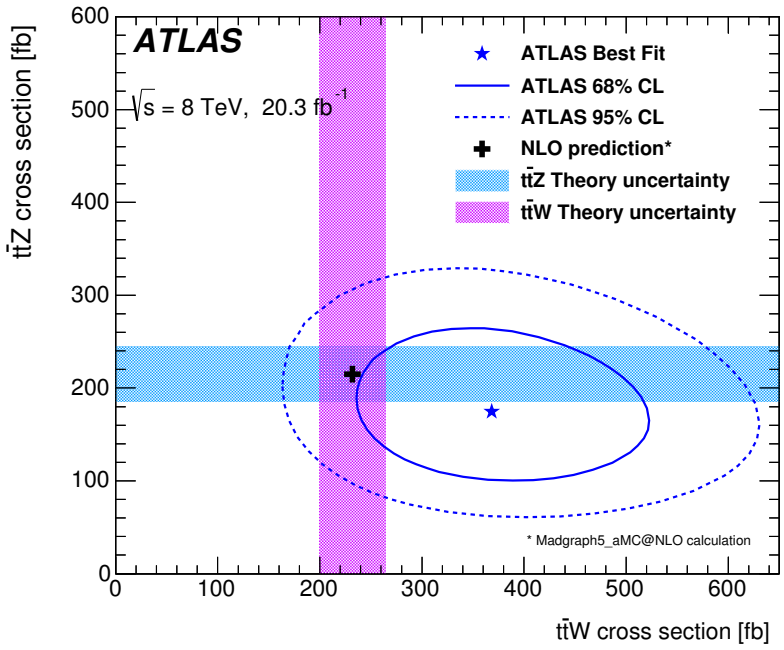

Figure 2.12: ATLAS result of the two-dimensional fit to extract the $t\bar{t}W$ and $t\bar{t}Z$ cross sections at 8 TeV. The SM prediction along with the corresponding uncertainty is included [55].

ATLAS measurement with $\sqrt{s}$ = 13 TeV and $\mathcal{L}$ = 3.2 fb^{-1}

The first published $t\bar{t}V$ search from Run 2 used a small dataset of 3.2 fb^{-1} [58]. However, the increase in the centre-of-mass energy $\sqrt{s}$ to 13 TeV also increases the $t\bar{t}V$ production cross sections significantly, as shown in Figure 2.10. This compensates for the smaller dataset compared to the search at 8 TeV. This search was largely based on the previous ATLAS search at 8 TeV, but a few changes were made. The included analysis channels are: 2ℓSS, 3ℓ and 4ℓ. The 2ℓSS channel only includes a region with two same-sign muons, since electrons are more prone to be fake leptons and a more comprehensive study on the fake lepton background was avoided. In the trilepton channel a control region for the WZ background was added. In the tetralepton channel the signal region with 0 b-tagged jets was dropped. In total the observed significances are 2.2σ and 3.9σ for $t\bar{t}W$ and $t\bar{t}Z$, respectively. The dominating systematic uncertainty for $t\bar{t}W$ are related to fake lepton and charge-flip background, while $t\bar{t}Z$ is limited by the available data. Both extracted cross sections agree within their uncertainties with the Standard Model and can be seen in Figure 2.13.

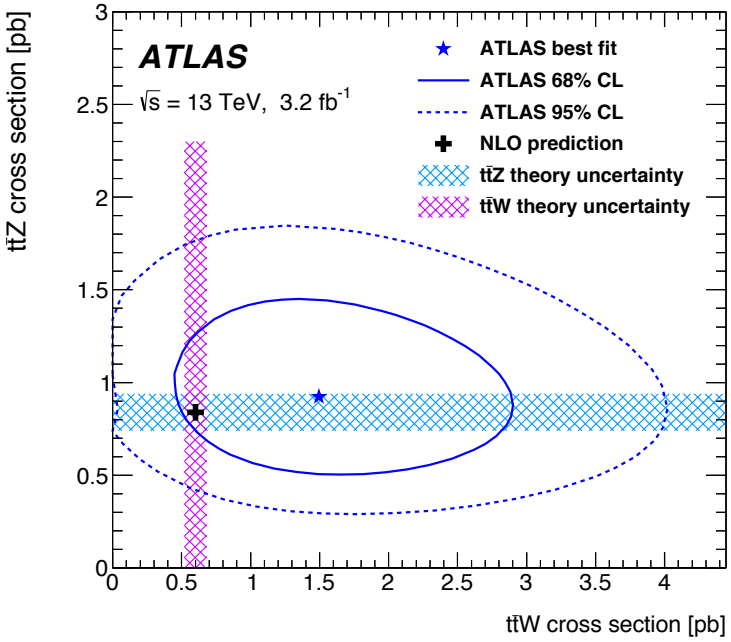

Figure 2.13: ATLAS result of the two-dimensional fit to extract the $t\bar{t}W$ and $t\bar{t}Z$ cross sections at 13 TeV. The SM calculations along with the corresponding uncertainties are included [55].

CMS measurement with $\sqrt{s}$ = 13 TeV and $\mathcal{L}$ = 35.9 fb^{-1}

The CMS collaboration carried out two searches in Run 1 at 7 and 8 TeV [56, 63]. The latest search at 13 TeV is the most interesting since it uses a larger dataset of 35.9 fb^{-1} [59], similar to the results presented in this thesis. The included analysis channels are: 2ℓSS, 3ℓ and 4ℓ. The 2ℓSS channel uses a boosted decision tree (BDT) to separate the $t\bar{t}W$ signal from the backgrounds. The channel is further separated depending on the absolute charge of the lepton pair (+2 or -2). The observed significance in this channel is 5.3σ. The trilepton channel only provides sensitivity to $t\bar{t}Z$ and includes 9 signal regions depending on the multiplicity of jets and b-tagged jets. The tetralepton analysis uses two signal regions:

four lepton events with 0 or ≥ 1 b-tagged jet. The tri- and tetralepton channels are combined to extract the $t\bar{t}Z$ cross section and provide an observed significance > 5.0σ. The extracted cross sections from a two-dimensional fit are shown in Figure 2.14.

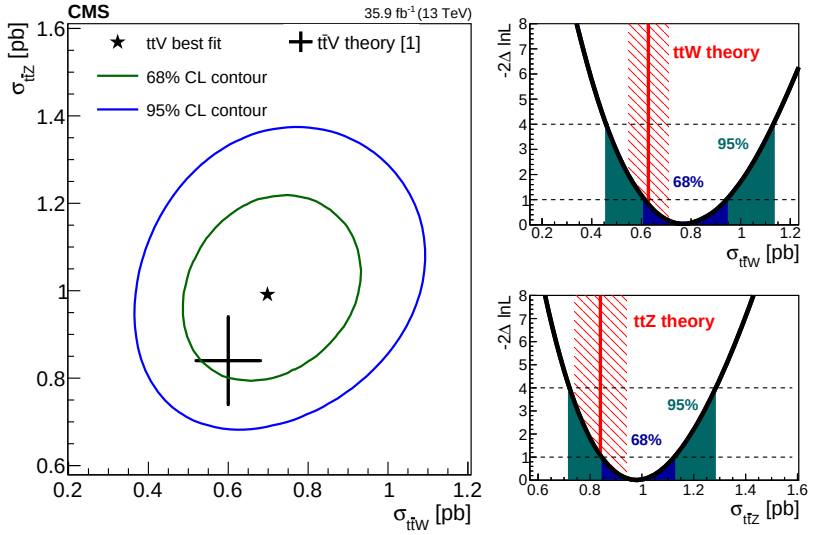

Figure 2.14: CMS result of the two-dimensional fit compared to the calculations (left) and individual measured cross sections with 68% and 95% CL intervals (right) [59].

In addition, this search is the first $t\bar{t}V$ search, that includes an interpretation of the results in terms of effective field theory (EFT). Figure 2.15 shows the fit 2D fit result in addition to the best-fit value with a single free floating Wilson coefficient. More details on the Wilson coefficients and the framework behind EFT is discussed in the following section.

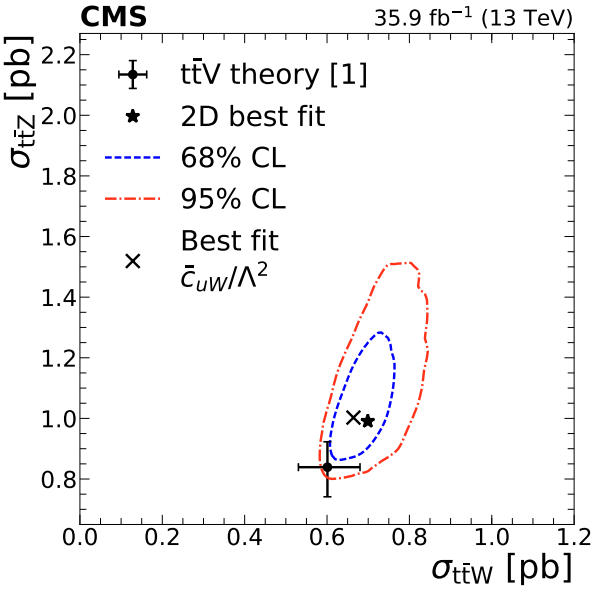

Figure 2.15: The $t\bar{t}V$ cross sections corresponding to the best-fit value of the shown Wilson coefficient. The two-dimensional best fit and the theory prediction are shown for comparison [59].

2.4 EFT interpretation

With the discovery of the Higgs boson, the final piece of the Standard Model has been found. One of the tasks in high-energy physics today is to search for physics beyond the Standard Model.

One promising approach is introducing and parameterising anomalous couplings via effective field theory (EFT) in a model independent way [6–8]. The basic idea is to introduce low-energy physics effects at high-energy scales, since new physics is believed to manifest at higher energies but it also affects processes at lower energies. Here, the energy scale Λ at which SM particles can be produced (O(MeV- TeV)) is still considered as low-energy scale. At this scale, the new effects are suppressed by multiple magnitudes of inverse power of Λ. Thus, introducing EFT modifies the Lagrangian density as follows:

$$\mathcal{L}_{\text{EFT}} = \mathcal{L}_{\text{SM (dim.4)}} + \frac{C_{i,5}}{\Lambda} O_{i\,\text{(dim.5)}} + \frac{C_{i,6}}{\Lambda^2} O_{i\,\text{(dim.6)}} + \frac{C_{i,7}}{\Lambda^3} O_{i\,\text{(dim.7)}} + ... \tag{2.21}$$

In this equation C_i are the Wilson coefficients to the operators O_i. Those operators appear together with their hermitian conjugate. In each term the Wilson operators have a different dimension and the dimension of the energy-scale Λ increases accordingly, such that the mass always has dimension 4. Only the term introducing dimension 6 operators $\propto \Lambda^{-2}$ is studied, because the other terms are negligible: There is only one possible dimension 5 operator, the Weinberg operator, that generates Majorana masses for neutrinos and violates the lepton family number, which is forbidden in the Standard Model [64]. Terms of higher dimensional operators can be neglected because the power of Λ suppresses their contribution. So the EFT Lagrangian can be rewritten as:

$$\mathcal{L}_{\text{EFT}} = \mathcal{L}_{\text{SM (dim.4)}} + \frac{C_i}{\Lambda^2} \left(O_{i\,\text{(dim.6)}} + O^{\dagger}_{i\,\text{(dim.6)}} \right) \tag{2.22}$$

The Wilson operators of dimension-six, contributing to $O(\Lambda^{-2})$, to top-quark physics are shown in Equation 2.23. In other words, the equation shows a parametrisation of the top-quark couplings to the SM gauge bosons (gluon and electroweak). Any other possible operators parameterising the top-quark interacting with other particles, for example with fermions, are not considered. A study, showing which operators are the most relevant in collider physics in given is Reference [65]. They are:

$$\begin{aligned}
O^{(3)}_{\varphi Q} &= \frac{i}{2} y_t^2 \left(\varphi^{\dagger} \overleftrightarrow{D}^I_{\mu} \varphi \right) \left(\bar{Q} \gamma^{\mu} \tau^I Q \right) \\
O^{(1)}_{\varphi Q} &= \frac{i}{2} y_t^2 \left(\varphi^{\dagger} \overleftrightarrow{D}_{\mu} \varphi \right) \left(\bar{Q} \gamma^{\mu} Q \right) \\
O_{\varphi t} &= \frac{i}{2} y_t^2 \left(\varphi^{\dagger} \overleftrightarrow{D}_{\mu} \varphi \right) \left(\bar{t} \gamma^{\mu} t \right) \\
O_{tW} &= y_t g_W \left(\bar{Q} \sigma^{\mu\nu} \tau^I t \right) \tilde{\varphi} W^I_{\mu\nu} \\
O_{tB} &= y_t g_Y \left(\bar{Q} \sigma^{\mu\nu} t \right) \tilde{\varphi} B_{\mu\nu} \\
O_{tG} &= y_t g_s \left(\bar{Q} \sigma^{\mu\nu} T^A t \right) \tilde{\varphi} G^A_{\mu\nu},
\end{aligned} \tag{2.23}$$

where $y_t = \sqrt{2}\, m_t / v$ is the Yukawa coupling for the top quark, which depends on the Higgs field vacuum expectation value v, Q is the left-handed doublet of the third quark generation, while t is the right-handed singlet for the top quark. The operators $\overleftrightarrow{D}^I_{\mu}$ and $\overleftrightarrow{D}_{\mu}$ are covariant derivatives that act left

and right on the Higgs field $\varphi^\dagger$ and φ, following the conventions of Reference [66]. Finally g_W, g_Y and g_s are the SM gauge coupling constants (sometimes called g_1, g_2 and g_3 instead). The definition of the covariant derivative can be seen in Equation 2.24.

$$D_\mu = \partial_\mu - g_Y Y B_\mu - \frac{i}{2} g_W \tau^I W_\mu^I - g_s T^A G_\mu^A, \text{ following the conventions of Reference [66]} \tag{2.24}$$

Five of the six operators shown in Equation 2.23 enter the $t\bar{t}Z$ process: In all operators, except for O_{tG}, the Z boson appears either in the form of the field strengths $W^I_{\mu\nu}$ and $B_{\mu\nu}$, or in the covariant derivatives. The operator O_{tG} is the chromomagnetic dipole operator parameterising the top-quark interaction with gluons and modifies the $t\bar{t}b$ vertex (and can therefore also affect the $t\bar{t}Z$ process). The operators O_{tW} and O_{tB} represent the top-quark interacting with the weak hypercharge and isospin gauge bosons: both modify the $t\bar{t}Z$ and $t\bar{t}\gamma$ vertex. Finally the first three operators are modifying the vector and axial-vector couplings of the top-quark to the electroweak gauge bosons. An overview at the operators modifying the $t\bar{t}+X$ vertex is given in Table 2.6, illustrating how a combination of different EFT studies with different processes in top-quark physics can be beneficial.

	$t\bar{t}Z$	$t\bar{t}W$	$t\bar{t}\gamma$
$O^{(3)}_{\varphi Q}$	✓	✓	
$O^{(1)}_{\varphi Q}$	✓	✓	
$O_{\varphi t}$	✓	✓	
O_{tW}	✓	✓	✓
O_{tB}	✓	✓	✓
O_{tG}			✓

Table 2.6: Overview of dimension-6 operators modifying different $t\bar{t}+X$ processes.

Figure 2.16 illustrates how the $t\bar{t}Z$ vertex can be modified by the dimension-6 operators.

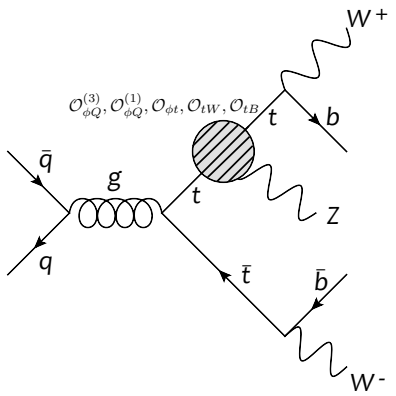

Figure 2.16: $t\bar{t}Z$ diagram affected by the dimension-6 operators. The shaded area indicates how any of the operators enter the vertex.

The dimension-6 operators introduced in the modified Lagrangian in Equation 2.21 alter the cross section as follows:

$$\sigma_{\text{EFT}} = \sigma_{\text{SM (dim.1)}} + \sum_i \frac{C_i}{\Lambda^2}\,\sigma_{i\,\text{(dim.1)}} + \sum_{i\leq j} \frac{C_i C_j}{\Lambda^4}\,\sigma_{ij\,\text{(dim.2)}} \tag{2.25}$$

The additional terms in Equation 2.25 are:

- $\propto \sigma_{i\,\text{(dim.1)}}$: cross section of interference between diagrams with Wilson operators O_i and and SM diagrams.
- $\propto \sigma_{ij\,\text{(dim.2)}}$: cross section of interference between two diagrams with one EFT vertex each. This quadratic term becomes relevant when $i = j$, in which case the term becomes $O(\Lambda^{-2})$.

Starting from Equation 2.19 the $t\bar{t}Z$ Lagrangian is modified by the Wilson operators by translating the SM vector and axial vector couplings (see Equations 2.17-2.18) into four dimension-six operators. These anomalous couplings follow the conventions introduced in Reference [66] and are calculated in Reference [67]. Those couplings are:

$$\begin{aligned}
C^Z_{1,V} &= \frac{1}{2}\left(C^{(3)}_{\varphi Q} - C^{(1)}_{\varphi Q} - C_{\varphi t}\right)\frac{m_t^2}{\Lambda^2 \sin\theta_{\text{W}}\cos\theta_{\text{W}}},\\
C^Z_{1,A} &= \frac{1}{2}\left(-C^{(3)}_{\varphi Q} + C^{(1)}_{\varphi Q} - C_{\varphi t}\right)\frac{m_t^2}{\Lambda^2 \sin\theta_{\text{W}}\cos\theta_{\text{W}}},\\
C^Z_{2,V} &= \frac{1}{2}\left(C_{t\text{W}}\cos^2\theta_{\text{W}} + C_{t\text{B}}\sin^2\theta_{\text{W}}\right)\frac{2\,m_t\,m_z}{\Lambda^2 \sin\theta_{\text{W}}\cos\theta_{\text{W}}},\\
C^Z_{2,A} &\approx 0.
\end{aligned} \tag{2.26}$$

It can be seen that the five Wilson coefficients C_i only enter as combinations of differences in the anomalous couplings. Therefore, any $t\bar{t}Z$ related measurement will only allow to constrain the difference of any two or three given Wilson coefficients. As mentioned before it is essential to do similar measurement aiming towards EFT sensitivity for other $t\bar{t}+X$ processes. A study of the sensitivity of kinematic properties in the $t\bar{t}Z$ process on the anomalous couplings introduced in Equation 2.26 can be seen in Figure 2.17. The corresponding variables are studied in Section 6.

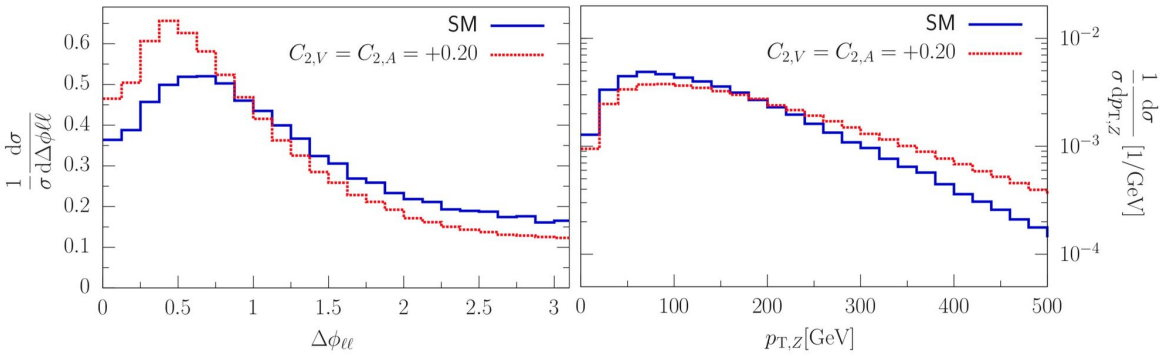

Figure 2.17: NLO distributions of $\Delta\phi(\ell\ell)$ and $p_{\mathrm{T},Z}$ for SM $t\bar{t}Z$ couplings and anomalous dipole couplings $C_{2,V}^{Z} = C_{2,A}^{Z} = 0.2$ [68]. The distributions are normalized to the overall cross section.

CHAPTER 3

The ATLAS experiment

The ATLAS experiment is located at "The European Organization for Nuclear Research" (CERN), which is a research centre built to study the constituents of matter and answer fundamental questions in physics. The abbreviation CERN originates from the french name: 'Conseil européen pour la recherche nucléaire'. The CERN laboratory complex is located at the border of France and Switzerland, close to the city of Geneva. It was founded in 1954 as the first joint European scientific research centre after the World War II. Today, CERN hosts 22 member states beyond the borders of Europe, making it the largest research centre of its kind. CERN is most commonly known for its particle accelerators and detectors and also for the development of the world-wide web (www) in the 90's. Several elementary particles of the Standard Model were discovered by experiments located at CERN, most recently the Higgs boson by the ATLAS and CMS experiments [1, 2].

In this chapter, the Large Hadron Collider (LHC) [69] and the ATLAS experiment will be introduced and an overview of the detector components of the ATLAS detector is given. Most of the information in this chapter is based on the technical design reports for the LHC [70] and the ATLAS experiment [71, 72].

3.1 The Large Hadron Collider

The Large Hadron Collider, located at CERN, is a circular particle accelerator with a circumference of 26.7 km that collides protons and ions. It is the biggest machine of its kind with the aim to study elementary particles and to possibly discover new physics beyond the Standard Model. The protons are accelerated in bunches of $\sim 10^{11}$ protons each in sets of up to 2808 bunches. These sets are called "*bunch trains*" and are injected in intervals of 25 or 50 ns, until 72 bunches are allocated in a train, after which injection is paused for a period corresponding to 12 bunches until the next train is injected. At the point of injection, two beams of protons, kept at a transverse size of $\sim 17\,\mu$m are led through a single beam pipe for ~ 140 m in opposite directions. In order to avoid collisions during the acceleration period, the beams are led through separate, parallel pipes after the initial single beam pipe. The two beams are accelerated in opposite directions along the ring with the help of 1232 dipole (to keep the beams in the ring) and 392 quadrupole (to focus the beams) magnets and finally collide at the collision points of one of the experiments.

The magnetic field strength to bend and focus the proton beams is 8.33 T and the magnets in the LHC are cooled to 2 K with super-fluid helium, in order to have superconductivity. To reach this level of precision in temperature, despite the large magnetic field, that need to act on two oppositely oriented beams, a cyrostat is used that houses both beam pipes that are surrounded by superconducting coils

shielded by a vacuum vessel. Both a schematic view and a photo of the cross section of a dipole magnet at the LHC are shown in Figure 3.1.

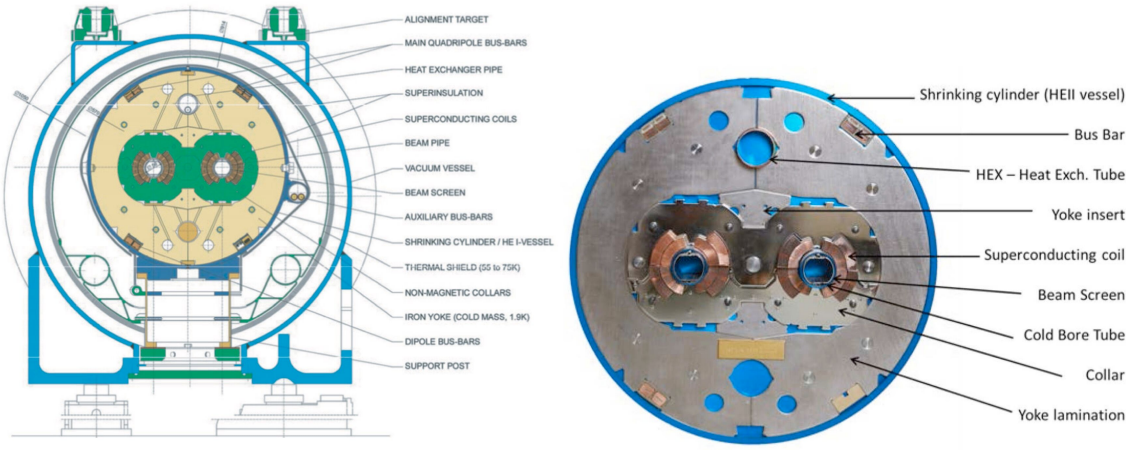

(a) schematic [69]

(b) real [73]

Figure 3.1: Cross section of a dipole magnet at the LHC. Both a schematic view and a real photo are shown.

The acceleration of protons does not start in the LHC but undergoes different steps. The protons originate from a hydrogen source and are accelerated in a linear accelerator (LINAC 2) to 50 MeV. After that the protons enter the Synchotron Booster, where they are accelerated to 1.4 GeV. Then they are injected to the Proton Synchotron (PS) to gain an energy of 25 GeV and are then taken to the Super Proton Synchotron (SPS) until they reach an energy of 450 GeV. Finally the protons enter the LHC, where they are accelerated to the final centre-of-mass energy and are brought to collision. The collisions occur at a rate of 40 MHz for every colliding pair of bunches from the two proton beams. In addition to colliding protons, the machine is also able to accelerate and collide heavy ions. Those undergo the same procedure as described above to enter the LHC, only using a different LINAC for the first acceleration step. A schematic overview of the different accelerators and their purpose at CERN can be seen in Figure 3.2.

The relation of the collision rate (of 40 MHz for the proton beams) to the total cross section σ of the collision is shown in Equation 3.1

$$\frac{\mathrm{d}N}{\mathrm{d}t} = \mathcal{L} \cdot \sigma \tag{3.1}$$

The coefficient of the collision rate and cross section is the instantaneous luminosity $\mathcal{L}$. It's definition can be seen in Equation 3.2

$$\mathcal{L} = \frac{N_b^2 n_b f_{\mathrm{rev}} \gamma F}{4\pi\beta^* \epsilon} \tag{3.2}$$

Here, N_b is the number of particles per bunch, while n_b is the number of bunches per beam. ϵ is the emittance of the beam and β^* is the beta function, which describes the narrowness of the beam at the collision point. The remaining factors in Equation 3.2 are the revolution frequency f_{rev}, the Lorentz gamma and the function F that accounts for the angle of the colliding beams. Maximizing the instantaneous luminosity increases the collision rate and thus the data available. This is the main challenge when designing a particle accelerator. The design luminosity for the LHC is $10^{34}\,\mathrm{cm}^{-2}\mathrm{s}^{-1}$.

The delivered data is measured in terms of the integrated luminosity (luminosity in the following) and is proportional to the number of events for the cross section σ of a given process:

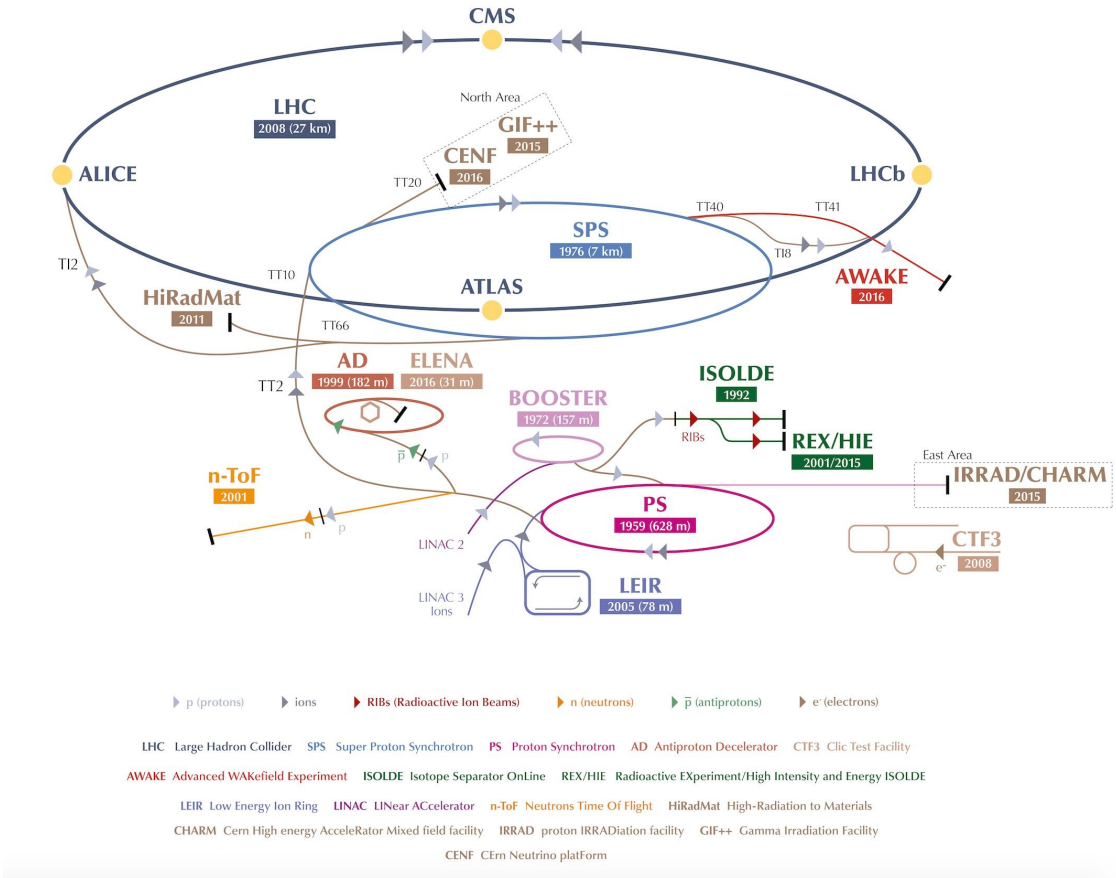

Figure 3.2: Overview of the accelerator complex at CERN [74].

$$L = \int \mathcal{L}\,\mathrm{dt} = \frac{N}{\sigma} \tag{3.3}$$

3.1.1 Periods of operation

The LHC was designed for a centre-of-mass energy ($\sqrt{s}$) of 14 TeV. This design energy has not been reached so far. The operation of the LHC is divided into different runs. In between those runs the accelerator and its experiments receive upgrades.

Run 1 took place in the years of 2009 - 2013 with a centre-of-mass energy of up to 8 TeV. During the first period the LHC was operated at 7 TeV and delivered a total of 47 pb^{-1} and 5.5 fb^{-1} in 2010 and 2011, respectively [75]. In the following year, the LHC was operated at 8 TeV and delivered 22.7 fb^{-1} [76]. In 2013 Run 1 was finished and the LHC was shut-down and upgraded until 2015.

Run 2 started in 2015 with a centre-of-mass energy of 13 TeV. A total of 158 fb^{-1} of data were collected until the end of 2018, initiating the second long shutdown.

Table 3.1 shows the parameters used in the years of operation. Figure 3.3 shows the delivered data to the ATLAS experiment as a function of time.

Parameters	2010	2011	2012	2015	2016	2017	2018	design
$\sqrt{s}$ [TeV]	7	7	8	13	13	13	14	
$\int \mathcal{L}\,dt$ [fb^{-1}]	0.048	5.5	22.8	4.2	38.5	50.2	65.0	3000
peak $\mathcal{L}$ [10^{33} cm^{-2}s^{-1}]	0.2	3.7	7.7	5.0	13.8	20.6	21.4	10
pileup $\langle\mu\rangle$	9.0	11.6	20.7	13.7	24.9	37.8	37.0	-
bunch spacing [ns]	50	50	25	25	25	25	25	25

Table 3.1: Parameters of operating the LHC during different years compared to the designed values [77, 78].

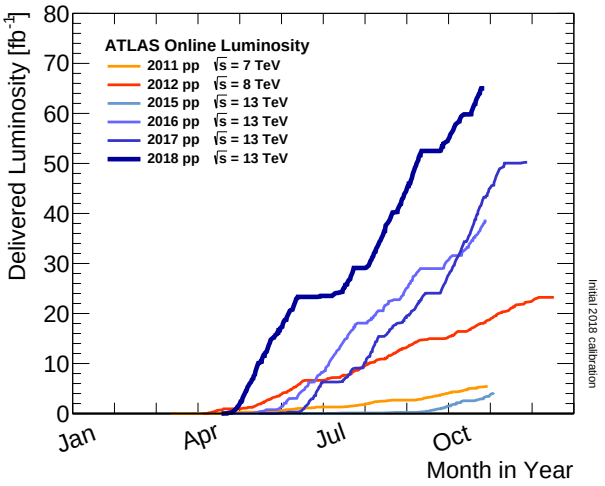

Figure 3.3: Delivered Luminosity to the ATLAS experiment as a function of months in different years [78].

.

3.1.2 The experiments at the LHC

The LHC houses four main experiments: ATLAS (A Toroidal LHC Apparatus) [79], CMS (Compact Muon Solenoid) [80], ALICE (A Large Ion Collider Experiment) [81] and LHCb (Large Hadron Collider beauty) [82]. ATLAS and CMS are general-purpose detectors, searching for unknown particles and performing precision measurements for known particles. The ALICE experiment studies the quark-gluon plasma created by colliding heavy ions, while the LHCb experiment studies b-physics and is able to probe CP violation, among other things. Additionally, the LHC also hosts smaller experiments that study specific topics, like magnetic monopoles or the proton-proton cross section. These smaller experiments are described in more detail in Reference [69].

3.2 The ATLAS detector

As one of the two general purpose detectors for particle physics, the ATLAS detector was built with the aim to discover the Higgs boson, search for physics beyond the Standard Model and provide precision measurements for Standard Model processes.

Similarly to experiments at other circular colliders, the ATLAS detector has subdetector systems

structured in layers. It is built in a cylindrical shape with a barrel and two end caps. It consists of an inner detector very closely located to the interaction point, which is covered by the calorimeter system and the muon spectrometer as the outermost detector. Both the inner detector and the muon spectrometer have separate magnetic fields, a solenoidal field of 2 T for the inner detector and a toroidal field of up to 4 T for the outer detector. The large coils of the toroidal field of the outer magnet system give the ATLAS detector a characteristic appearance. A sketch of the ATLAS detector is shown in Figure 3.4.

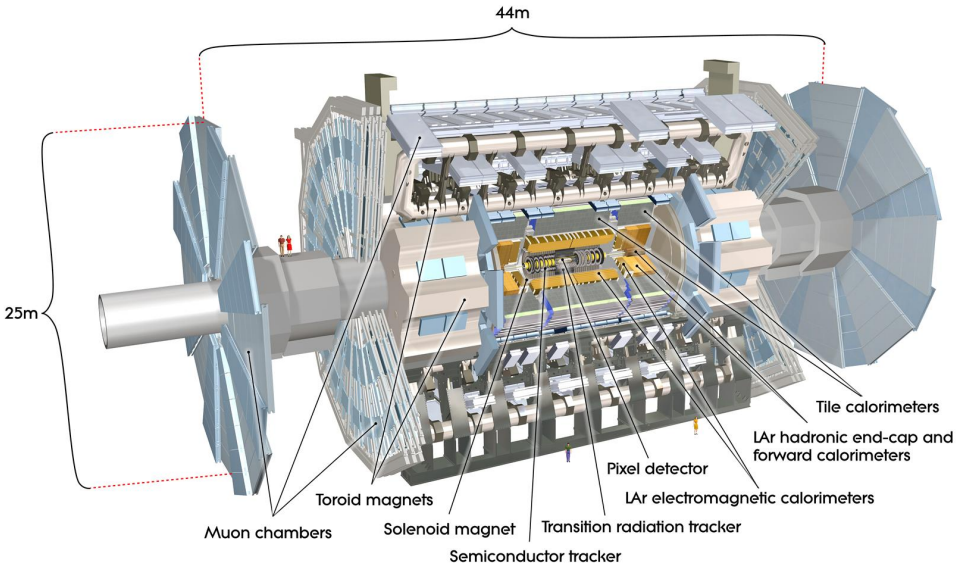

Figure 3.4: Overview of the ATLAS detector with its detector components [79].

Due to its structure and detector components, the ATLAS detector covers the full azimuthal angle and is able to precisely determine the depleted energy and reconstruct tracks of charged particles. In addition, different kinds of charged and neutral particles can be differentiated and their position in the detector determined, as illustrated in Figure 3.5.

In order to meet the conditions of the LHC design, the detector has to cope with multiple interactions per bunch crossing, called "*pile-up*" and to maintain functionality during long time of exposure in a high radiation environment. To identify the tracks from the hard collision of interest, several primary vertex candidates are built. The candidate with the highest transverse momentum, summed over all tracks associated to the primary vertex candidate, is reconstructed as the primary vertex. The number of interactions per bunch crossing was 30-40 on average during Run 2, as illustrated in Figure 3.6.

3.2.1 Coordinate system

Owing to the shape of the ATLAS detector a cylindrical coordinate system is used. The point of origin lies at the interaction point of the colliding beams, with the colliding beams traveling along the z-axis. The x-axis points to the centre of the LHC ring, while the y-axis points upwards. The Cartesian coordinates xyz are transformed to cylindrical coordinates $\phi\theta z$ as follows: The azimuth angle ϕ is the angle inside the xy-plane, also called transverse plane and the polar angle θ is the angle with respect to the z-axis. A transformation of the angle Θ, the pseudorapidity η, is commonly used in ATLAS, because the difference in the pseudorapidity of two particles is Lorentz invariant for boosts along the z-axis:

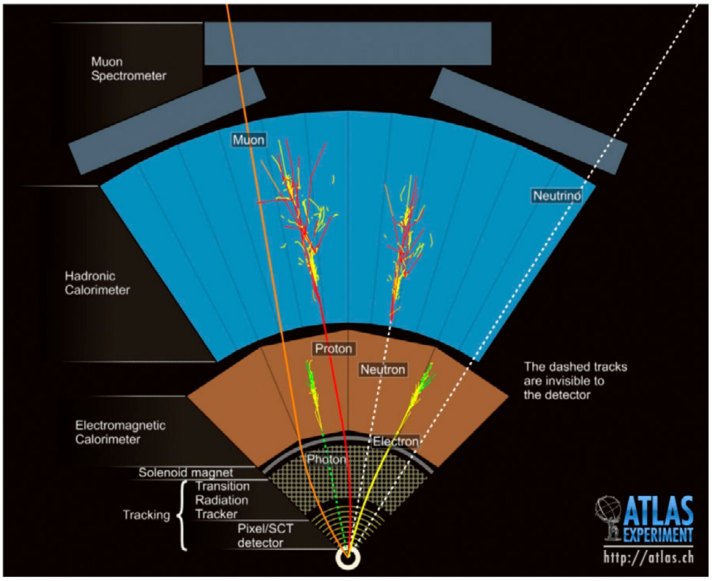

Figure 3.5: Schematic overview of particle identification with the ATLAS detector [79].

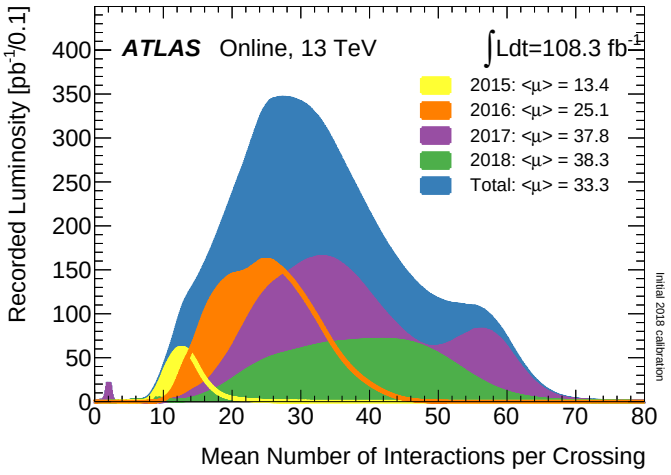

Figure 3.6: Pileup during data-taking in 2015-2018 [78].

$$\eta = -\ln\left(\frac{\theta}{2}\right). \tag{3.4}$$

It is defined such that, $\eta = 0$ in the transverse plane, $\eta \to \infty$ along the z-axis and $\eta = 1$ for 45° between the z-axis and the transverse plane.

The angular distance between two particles in the ATLAS coordinate systems is then:

$$\Delta R = \sqrt{|\eta_2 - \eta_1|^2 + |\phi_2 - \phi_1|^2}. \tag{3.5}$$

If a given particle is massless, the pseudorapidity is equal to the rapidity y:

$$y = \frac{1}{2} \ln \frac{E + p_z}{E - p_z}. \tag{3.6}$$

Finally, energy and momentum of particles are projected to the transverse plane, since the z-component of the momentum is not known:

$$\begin{aligned} p_{\mathrm{T}} &= \sqrt{p_x^2 + p_y^2}, \\ E_{\mathrm{T}} &= E \cdot \sin\phi \end{aligned} \tag{3.7}$$

3.2.2 Magnetic field

Two magnetic fields are used to bend the paths of charged particles inside the ATLAS detector. Both magnet systems are cooled with liquid helium to 4.7 K to make use of superconductivity. Covering the inner detector, a solenoid magnetic field of 2 T is applied in z-direction. The materials used for the inner magnet system are aluminum, copper and cables alloyed with niobium-titanium. The overall thickness of the inner magnet system is $\sim$ 10 cm only. The other magnet system has a toroidal structure (name giving for ATLAS) that bends charged particles in ϕ-direction. It is built as part of the Muon spectrometer and consists of a barrel toroid and two end-cap toroids. Each of the toroid parts uses eight superconducting coils, made of the same material composition as the inner magnetic system. The toroid system provides a magnetic field of up to 4 T. The toroid magnet coils in the barrel are distributed as pipes, allowing the detector parts of the muon spectrometer to be placed above, between and beneath the coils. The coils for the barrel and end-cap toroids are shown in Figure 3.7.

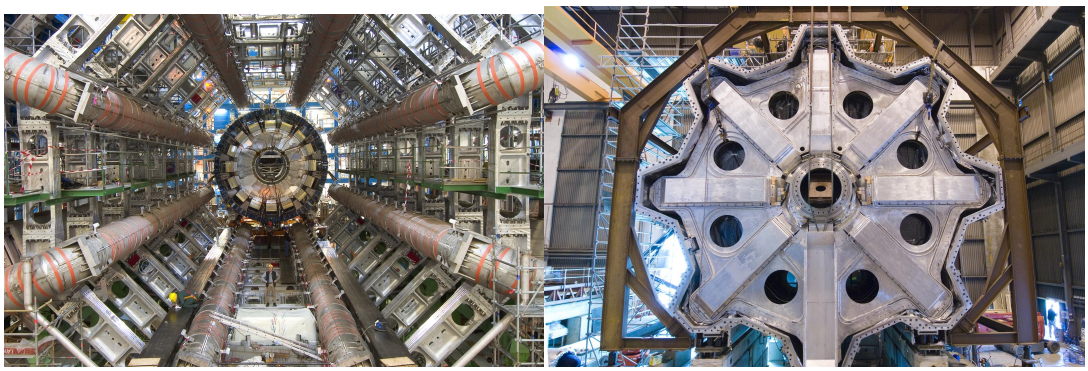

(a) barrel toroid coils (b) end cap toroid coils

Figure 3.7: Pictures of the toroid magnet coils, barrel toroid (left) and end cap toroid (right) [79].

3.2.3 Detector structure

Inner detector

In the inner detector, charged particles are reconstructed as tracks, with the help of the solenoid field of 2 T. The reconstruction is done by combining several position measurements, called hits. In addition, multiple tracks can be combined to reconstruct primary and secondary vertices coming from the initial pp

collision or from decays of long-lived secondary particles. The hits are determined by using information from three sub-detectors:

- The pixel detector:
  The innermost detector consists of n-in-n silicon pixels modules. The pixels are arranged in three cylindrical layers plus two end caps with three disks each, that are all centered around the beam pipe. The innermost layer, located at a radius of 50.5 mm around the beam pipe used to be the B-layer and helps detecting secondary vertices coming from b-jets. It received a high dose of radiation and was expected to be exchanged during the long shutdown in 2014. However, the radiation damage was modereate. Instead of exchanging the three layers of pixel modules, an additional layer, the Insertable B-layer (IBL), was installed at a radius of 33 mm in 2014 [83]. In order to fit, the radius of the beam pipe inside the ATLAS detector was decreased. With four layers of pixel modules, the pixel detector is often able to provide four hits per charged particle that has $|\eta| < 2.5$, unless the radiation damage the pixel modules. Each pixel on the IBL has a size of 50 x 250 μm, while the pixels on the three outer layers have a size of 50 x 400 μm. This results in a resolution of $\sigma_\phi = 10\,\mu$m and $\sigma_{z,r} = 115\,\mu$m in the ϕ, z and r coordinates of ATLAS. A schematic view of the pixel detector from two different angles is shown in Figure 3.8.

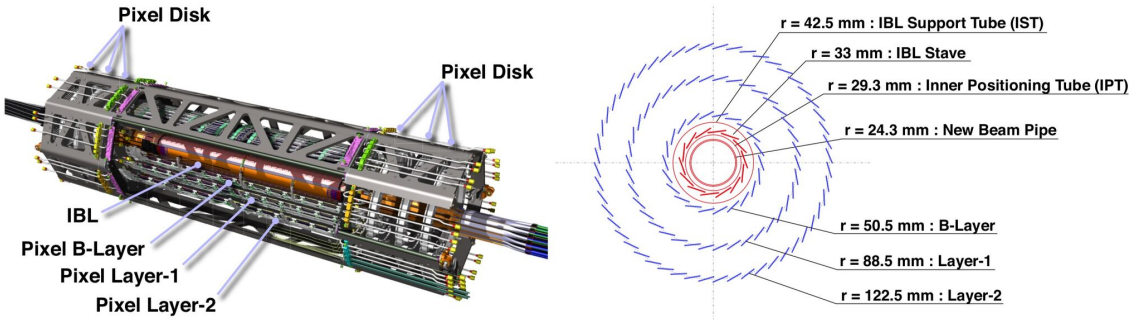

Figure 3.8: Schematic view of the pixel detector from two different angles [84].

- The semiconductor tracker (SCT):
  An additional four layers and two end caps, with nine disks each, of silicon detectors are added to the pixel detector. Each layer contains 2112 modules, while each end cap contains 988 modules. The modules on the end caps are arranged such, that four hits will be registered for any particle passing through, as for the four pixel barrel layers. Instead of pixel modules, the SCT modules consist of 768 strips and has a size of 6.36 x 6.40 cm^2 with a pitch of 80 μm. The larger surface helps to associate the hits to a given track. In each module there are two layers of silicon microstrips, that have a resolution of $\sigma_\phi = 17\,\mu$m and $\sigma_{z,r} = 580\,\mu$m.

- The transition radiation tracker (TRT):
  The outermost detector consists of tubes with a diameter of 4 mm, filled with a gas composition of Xe (70%), CO_2 (27%) and O_2 (3%) and a wire in the centre. Thus, the tubes act as a straw tube detector, providing information about the charge in addition to the position measurement. The TRT has several modules, with each module containing hundreds of tubes. In the barrel modules, the tubes are aligned parallel to the beam pipe, while they have a radial arrangement in the end-caps. The TRT provides a resolution $\sigma_\phi = 130\,\mu$m but lacks information in other coordinates. Since it is

the outermost detector system of the inner detector, it's main purpose is to help extend the tracks that could be formed with the pixel detector and the SCT.

The inner detector as a whole has a cylindrical form with a length of 7 m and a radius of 1.1 m, centred around the interaction point. A schematic view of the inner detector with its sub-systems can be seen in Figure 3.9.

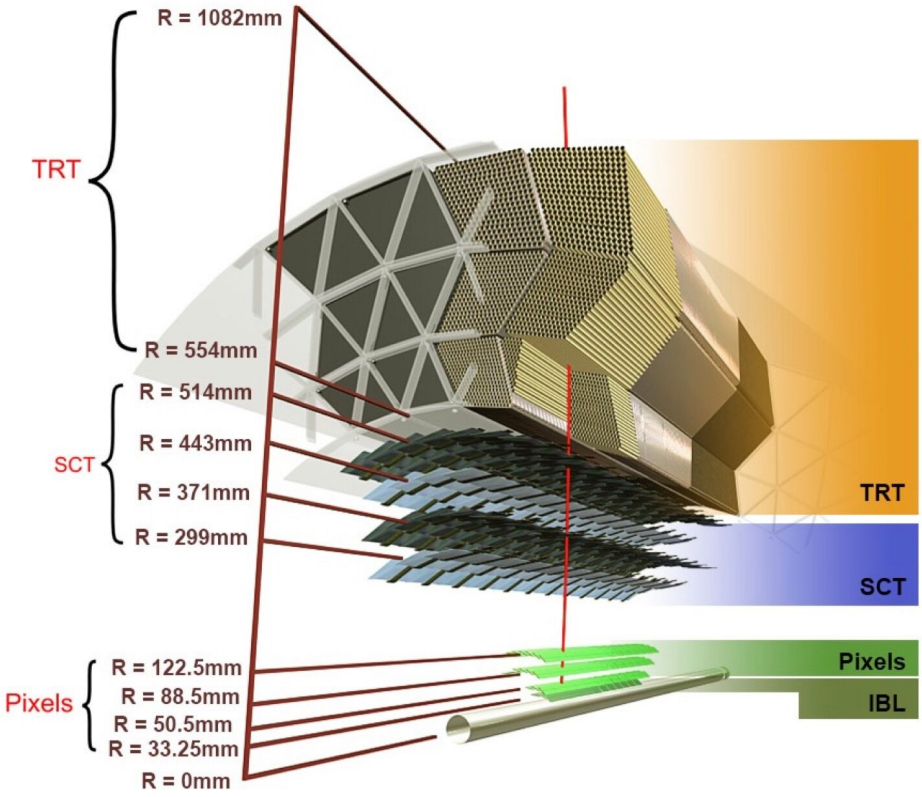

Figure 3.9: Schematic view of the inner detector sub-systems [85].

Calorimeter system

The ATLAS detector has two main calorimeters: the Electromagnetic Calorimeter (ECAL) and the Hadronic Calorimeter (HCAL). They are located outside of the inner detector, measuring both the position and the deposited energy of particles. Particles that undergo the electromagnetic or strong interactions, create a "*particle shower*", producing many secondary particles. The energy of the shower is measured in the calorimeters. Particles with $|\eta| < 4.9$ are detectable by the calorimeters.

The calorimeters are composed of layers of different materials, in order to initiate particle showers, measure the shower components and allow the complete absorption of the shower, such that the calorimeters are compact. Each layer has different segments in order to obtain the position in both, ϕ and z coordinates. The choice of absorbing materials depend on the interaction that initiated the shower. In an electromagnetic shower, only photons, electrons and positrons are created. These are usually completely contained in the calorimeter. In hadronic showers (initiated by the strong interaction) heavier

particles need to be considered, including neutral particles, muons and hadrons. Most of the hadronically interacting particles are able to escape the ECAL, since hadronic showers involve more energies and are usually longer than EM showers. Thus, both ECAL and HCAL are needed to distinguish electromagnetic from hadronic showers, i.e. electrons and photons from jets. Particles able to escape both calorimeter layers are neutrinos and muons. The deposited energy of the particles in hadronic showers is calibrated to account for hadronic showers escaping the outermost calorimeter layer. A precise reconstruction of the energy balance is important, in order to be able to reconstruct the missing energy and thus measure invisible particles indirectly.

Figure 3.10 shows the inside of one of the barrel parts of the calorimeter system, showing both the components of the ECAL and HCAL.

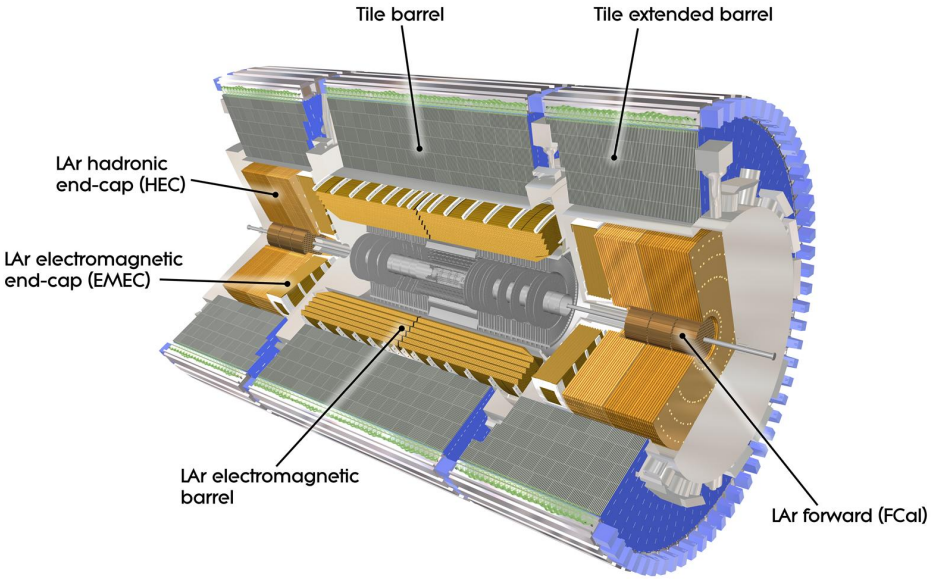

Figure 3.10: Inside-the-barrel view of the ATLAS calorimeter system [79].

ECAL

The ECAL consists of two barrel parts and two wheels on each end of the barrels. The barrels are structured such, that the full ϕ coordinates are covered. In addition, the barrels and the wheels cover $|\eta| < 1.475$ and $1.375 < |\eta| < 3.2$, respectively. However, in the region $1.37 < |\eta| < 1.52$ between the barrels and the wheels there is free space for cables and the inner detector structure. In this transition region, also called the "*crack region*", particles are not detected by the EM calorimeter.

The ECAL uses lead to absorb EM showers. The segmentation of the layers is finer than in the HCAL, which allows for a precise measurement of the EM showers that are usually entirely absorbed here. The showers are initiated using liquid argon as active material. The liquid argon is located in gaps between the lead material and ionizes when charged particles traverse the material and creates an electric field with the help of electrodes, to allow particle detection. Figure 3.11 shows the inside of one of the barrel of the ECAL showing the lead and liquid argon material.

Figure 3.11: Picture of the inside of the ECAL [79].

HCAL

The HCAL consists of a tile calorimeter and an end cap calorimeter, covering $|\eta| < 1.7$ and $1.5 < |\eta| < 3.25$, respectively. The tile calorimeter is segmented with plastic scintillators and has two parts, the barrel and two extended barrels, visible in Figure 3.10. The scintillators are distributed perpendicular to the beam direction and act as active material to initiate hadron shower. Steel absorbers are located in the gaps between the scintillators. The scintillators are connected to photomultipliers tubes to allow reading the position of particle showers.

The end-cap calorimeter has two wheels on each end cap, segmented and filled with liquid argon and is located directly behind the end caps of the ECAL. It covers a large η-range and overlaps with other calorimeter parts to avoid gaps in the transition regions. A view of the end-cap calorimeter can be seen in Figure 3.12.

FCAL

In addition to the two main calorimeters a forward calorimeter (FCAL) is used to cover the forward region in the range of $3.1 < |\eta| < 4.9$. It is designed to be very dense, since particle showers in the forward region are energetic and numerous. The FCAL consists of three parts: the inner one uses liquid argon and copper to measure EM showers, and the outer two use tungsten to absorb as much as possible from hadron showers, to avoid them from spreading to the central region. A picture of the assembly of the FCAL, where the three parts can be seen is shown in Figure 3.13.

3.2.4 Muon Spectrometer

The Muon Spectrometer [87] is the outermost detector system of ATLAS and covers the calorimeter system completely. It consists of four parts, that each have three layers: the Resistive Plate Chambers

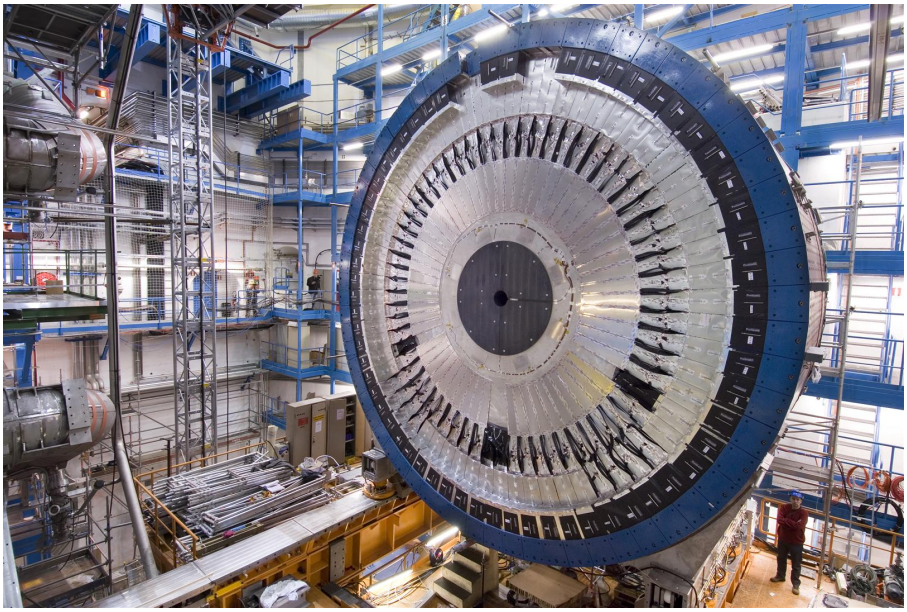

Figure 3.12: Picture of the end cap calorimeter [79].

Figure 3.13: Picture of the assembly of the FCAL [86].

(RPC) are located in the barrel region and provide trigger signals together with the Thin Gap Chambers (TGC) in the end caps. Both are tracking detectors and their time resolution lies below the designed bunch spacing of 25 ns. The Monitored Drift Tubes (MDT) are the largest detector parts and are located at the end caps together with the TGCs with the purpose of providing precise position and timing measurements, when muons pass through the gas in the drift tubes. The Cathode Strip Chambers (CSC) complement the Muon Spectrometer and are located in the forward region, where the flux of particles is highest. Therefore the granularity of the cathode strips is very high.

It is able to detect muons with energies between GeV-TeV that are in the range of $|\eta| < 2.7$ with an

efficiency of ~ 98%. Since muons are able to pass through the calorimeter system and the bending of the toroid magnets can lead to large trajectories of the muon tracks, a large η coverage is necessary. The Muon Spectrometer with its subsystems can be seen in Figure 3.14. A front view on one of the end caps of the Muon Spectrometer is shown in Figure 3.15.

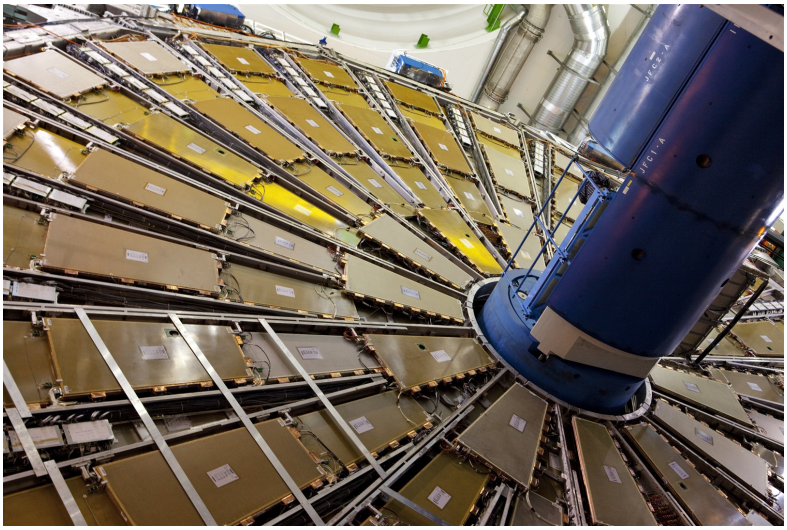

Figure 3.14: Front view of the end cap of the Muon Spectrometer [79].

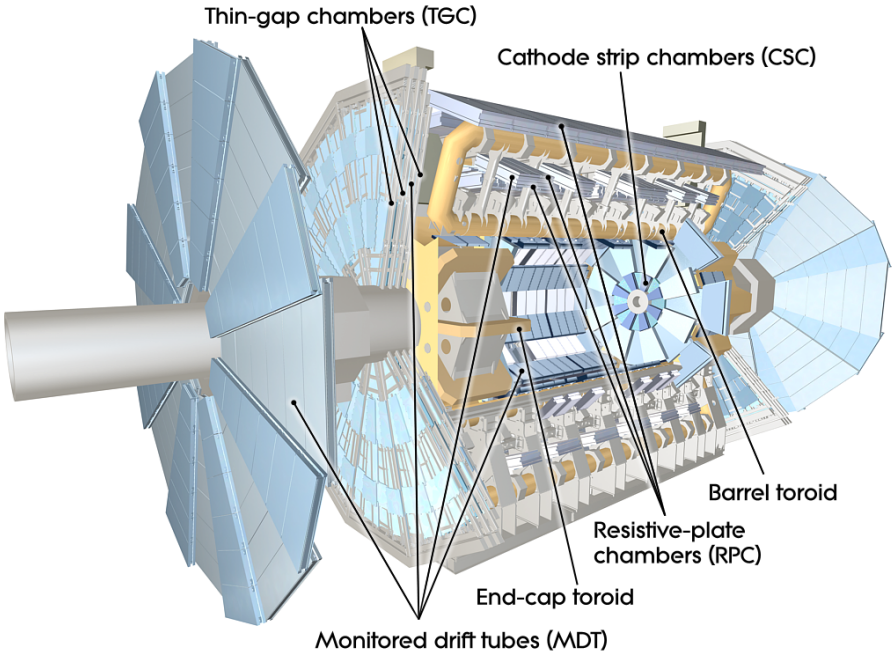

Figure 3.15: Layout of the Muon Spectrometer with the four sub-detectors [79].

3.2.5 Trigger system and data acquisition

Due to the high rate of collisions in the ATLAS detector of 40 MHz, which translates into millions of collisions per second, a trigger system is necessary to filter events of interest. The system is split into three levels of triggers:

- Level 1 (L1):
  The L1 trigger reduces the initial rate of collisions from 40 MHz to 100 kHz, by selecting events with high E_{T} and $E_{\mathrm{T}}^{\mathrm{miss}}$. In addition it selects electrons, muons, tau leptons, jets or photons with high p_{T}. Since the L1 has only $\sim \mu$s to decide which events to keep, it can only access limited information from the calorimeters and muon spectrometer. Information from reconstructed tracks or vertices are not available at this stage. The readout for the L1 trigger is using electronics only.

- Level 2 (L2):
  The L2 trigger further reduces the input rate to 3 kHz and has a time-window of $\sim$ *m*s to take decisions. As such, it can make use of network and computer software already. It analyses regions of interest selected by the L1 trigger and further filters by taking into account the position of candidate objects in the detector.

- Event filter (EF):
  At the last trigger level the input rate is reduced to 400 Hz (design value, which was upgraded to 1 kHz for Run 2), with a time-window of seconds to take decisions. The EF has access to the full detector information and analyses the event thoroughly. This last level is fully software-based.

Together, the L2 trigger and the EF are part of what is called the high-level trigger (HLT), a two-level trigger system. It is able to analyze events in parallel. Output from the L2 trigger is already passed to build an event, regardless of the decision of the EF. If the event passes both triggers, the information from the two is merged together and saved on storage disks. Starting from a bunch spacing of 25 ns, the amount of data stored without a trigger system would be 6 TB/s. The trigger system is able to reduce this information to 600 MB/s. The data is then stored on a computing grid system, granting access to ATLAS members world-wide.

A list of the upgrades that were undertook to improve the ATLAS trigger system for Run 2 are listed in Reference [88].

3.3 Simulation

In order to be able to analyze data provided by the ATLAS experiment, simulations of physics processes are necessary. These simulations usually rely on the Standard Model predictions, but also BSM models can be simulated. In a cross section measurement the prediction by the simulation of both signal and background processes is compared to the data and a ratio between the two, called "*signal strength*" is computed to extract the measured cross section. Similar to data, the simulation includes events, generated by Monte Carlo (MC) event generators. In order to precisely predict the physics processes, a MC generator simulates interaction of particles, their decay with accurate branching ratios and the interaction with the detector material. In order to have a precise prediction, the MC is generated in different steps. This is illustrated in Figure 3.16.

As the first step of simulating the physics process resulting from a pp collision, the hard process, i.e. the interaction on parton level, is generated. Partons carrying a fraction of the momentum of the colliding protons at a certain energy scale is described by the Parton Distribution Function (PDF), that is an

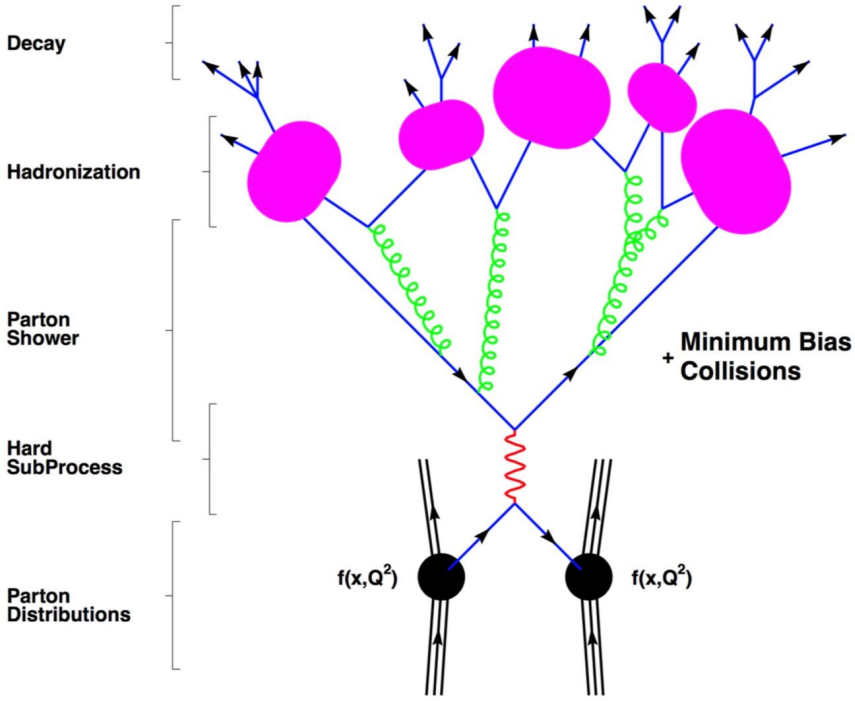

Figure 3.16: Steps of MC generation of pp collisions [89].

exchangeable part of every MC simulation. The simulation on parton level is performed by parton-level generators that generate the matrix elements of the given process. Commonly used parton-level generators for the ATLAS experiment are: MadGraph [90], MadGraph5_aMC@NLO [54], Powheg-Box [91–93] and Sherpa [94]. This set of generators turned out to provide the best balance of accuracy and computing time. The parton interactions are computed with a fixed number of partons in the final state, specific to the simulation sample. In the next simulation step, extra radiations from the initial, intermediate or final state are computed. These radiations can be photons, gluons or even electroweak bosons and are summarized as Parton Shower (PS). The particles radiated can initiate a cascade, for example a gluon can become two gluons, via gluon splitting or decay to a quark-antiquark pair. This often leads to extra photons or jets in the event. If the energy scale becomes lower than $\sim$ 1 GeV the hadronization begins, which means that partons hadronize to colour-neutral particles. Their decay is also simulated. Furthermore, remnant partons of the proton also undergo interactions, called underlying event. The steps of PS, hadronization and decay are handled by either the parton-level generators themselves, like Sherpa, while others use external generators for these steps. A commonly used external generator is Pythia [95, 96], most often seen combined with Powheg-Box. The interaction of final state particles with the detector material is modelled by a detector simulation, a common example is Geant [97]. Finally, a parameter for every MC generator is the tune, which are non-physical parameter that are calibrated by data. The generators for the simulated samples used in the analysis are described in Section 4.2.2.

CHAPTER 4

Objects, datasets and simulation

This chapter describes the object reconstruction, analysed dataset and simulated samples of the $t\bar{t}V$ multilepton analysis, while the event selection and results are presented in Chapter 5.

4.1 Object reconstruction

The objects of interest in this thesis, that can be reconstructed with the ATLAS detector are leptons, jets and missing transverse momentum ($E_{\mathrm{T}}^{\mathrm{miss}}$). Their definitions are described below. Tau leptons are classified via their decay products, which are reconstructed as leptons, jets and $E_{\mathrm{T}}^{\mathrm{miss}}$ themselves (depending on the decay mode of the tau lepton).

4.1.1 Leptons

Leptons that can be reconstructed via their tracks with the ATLAS detector are electrons and muons only. As discussed in Section 2, ℓ=e,μ.

A likelihood-based quality criterion is imposed on the leptons, which is called the identification. Several working points for the ID are defined in ATLAS. The lepton efficiency and background rejection (shown as efficiency to identify hadrons as electrons) can be seen in Figure 4.1 and Table 4.1 for electrons and muons respectively. Both, for reconstructed electrons and muons the medium identification (ID) is used for the analysis described in Section 5.

	$4 < p_{\mathrm{T}} < 20$ GeV		$20 < p_{\mathrm{T}} < 100$ GeV	
Selection	$\epsilon_{\mu}^{\mathrm{MC}}$ [%]	$\epsilon_{\mathrm{Hadrons}}^{\mathrm{MC}}$ [%]	$\epsilon_{\mu}^{\mathrm{MC}}$ [%]	$\epsilon_{\mathrm{Hadrons}}^{\mathrm{MC}}$ [%]
Loose	96.7	0.53	08.1	0.76
Medium	95.5	0.38	96.1	0.17
Tight	89.9	0.19	91.8	0.11

Table 4.1: Muon efficiency and background rejection for two different ranges of the transverse momentum [99].

The choice of working points and isolation is a compromise between signal efficiency and fake lepton reduction. For the purpose of this analysis, fake leptons are objects reconstructed as leptons, that do not arise from the decay of the Z boson, W boson or the τ lepton. Fake leptons include leptons from the

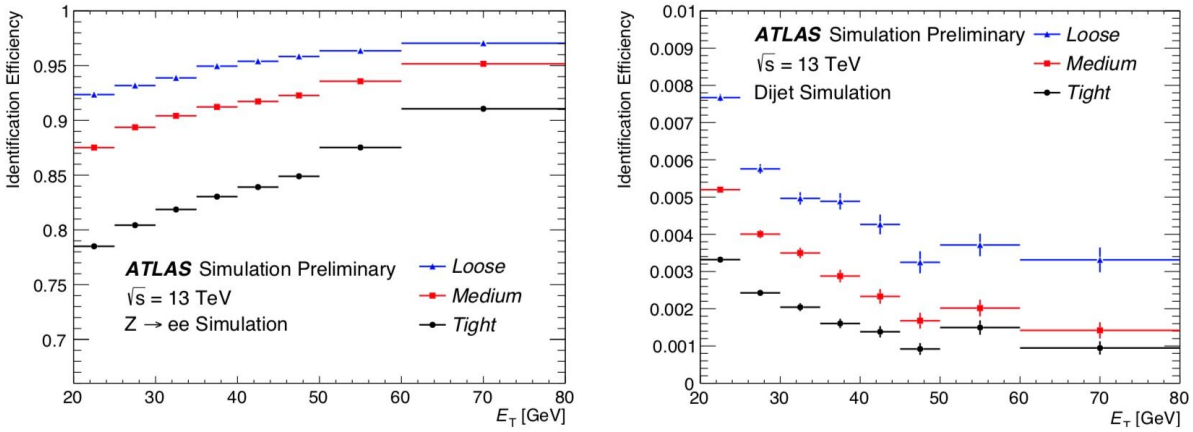

Figure 4.1: Electron efficiency (left) and efficiency to identify hadrons as electrons (right) as a function of the transverse energy for the three different working points [98].

decay of a bottom or charm meson in b-jets, electrons from photon conversions, muons from a pion or kaon decay, or jets misreconstructed as electrons. For the $t\bar{t}Z$ analysis, as opposed to the $t\bar{t}W$ analysis, the fake lepton background is not dominant, so the medium ID was chosen for the leptons. It was found that the tight lepton definition led to a signal loss of $\sim 15\%$.

In addition to the identification, a working point is chosen for the isolation of leptons. This is necessary on top of the ID to precisely define a lepton object and to reject candidates which are close to other objects, that likely originated from those objects, for example electrons in or close to jets.

For both electrons and muons, scale factors and uncertainties are derived to correct modelling inconsistencies between data and simulation, as described in Section 5.4.1. The scale factors are applied to each simulated process as an event weight.

Electrons

For the identification, electrons use the information from the ECAL, as described in Reference [98] and are required to satisfy the `MediumLH` criteria [100]. Furthermore, electrons are required to have at least 7 GeV of transverse momentum (p_{T}) and at most an absolute pseudorapidity of the calorimeter energy cluster corresponding to the electron of 2.47 ($|\eta_{\mathrm{Cluster}}|$). In addition, any electron candidate within the region of $1.37 < |\eta_{\mathrm{Cluster}}| < 1.52$, which corresponds to the transition of the EM calorimeter barrel to the end-cap, as described in Section 3, is discarded.

For the isolation a working point for electrons is chosen such that the sum of the calorimeter cluster transverse energies and the sum of track transverse momenta in a cone of $\Delta R = 0.2$ around the electron is less than 6% of the electron p_{T}. This choice of calorimetric and track isolation helps to reduce fake leptons [98]. The electron candidates have a 97% signal efficiency in terms of assigning the correct charge of the candidate (avoiding "*charge-flips*").

Muons

Muons are reconstructed combining the information of the layers in the muon spectrometer and associated tracks in the inner detector. For the identification, medium muons are required, satisfying certain track quality requirements (Medium Track [99]). Furthermore, muons are required to have at least 7

GeV transverse momentum and at most an absolute pseudorapidity of 2.5 and the following requirements on the impact parameters: $\left|d_0/\sigma(d_0)\right| < 3$ and $z_0\sin(\theta) < 0.5$ mm,

where d_0 and z_0 are the transverse and longitudinal impact parameters. The impact parameter is defined as the closest distance of the reconstructed trajectory to a point of interest. An illustration where d_0 is shown can be seen in Figure 4.2, where the point of interest is the primary vertex.

For the track isolation, a p_{T}-dependent cone size of $\Delta R = 0.3/p_{\mathrm{T}}^{\mu}$ [GeV] is used. The p_{T} dependence helps to improve the correct identification of muons produced with large momentum [99]. A fixed cone of $\Delta R = 0.2$ around the calorimeter cluster of muon candidates is used to better isolate the muon candidate and avoid overlap with other objects, similar to the electrons.

4.1.2 Jets

Jets are reconstructed using the anti-k_t algorithm [101], with $R = 0.4$ as distance parameter. The reconstruction uses topological calorimeter clusters [102] following the `EMTopo` scheme. Furthermore, jets are required to have $p_{\mathrm{T}} > 25$ GeV and $|\eta| < 2.5$. Additionally, multivariate techniques are used to reject jet candidates likely to be associated to pile-up events. The tool used to achieve this is called "*Jet Vertex Tagger*" (JVT) in ATLAS [103].

Jets are distinguished and categorized according to their origin. Jets originated from b-quarks are of particular interest. Other origins, such as c-quarks, gluons or hadronically decaying tau leptons are far more difficult to identify. Therefore, for the purpose of this analysis, as described in Section 5, jets are separated into flavour-tagged (jets originated from b-quarks) and light-flavour jets (gluon and light quark initiated).

Flavour-tagged jets

Jets that originate from b-quarks are called b-jets. Identifying and differentiating them from other jets, called "*Flavour tagging*", is crucial to top-quark physics. During the hadronization a B hadron is formed inside a b-jet. Thus, the tracks inside a b-jet are from the decay of the B hadron and it's decay products and from the b quark parton shower. Due to the lifetime of a B hadron (~ps), the hadron travels a measurable distance inside the ATLAS detector (~mm, depending on the transverse momentum), before a secondary decay vertex associated to the hadron is created[1]. This applies also to c-jets, however the lifetime of a D hadron is and therefore the distance of the displaced vertex is shorter (by a factor of ~2). In addition, the B hadron decays predominantly to a charm quark, which then hadronizes to a D hadron that forms another displaced vertex inside the b-jet. This is illustrated in Figure Figure 4.2. Therefore a b-jet provides a clear signature, that can be flavour tagged.

Flavour-tagged jets (b-jets) are tagged using the MV2c10 algorithm [104]. This algorithm uses multivariate techniques combining three low level jet-tagging algorithms: JetFitter, IP3D and SV1 [105], which use information from the jets, track impact parameter and the secondary vertex, respectively. The secondary vertex algorithm used as an input for the training MV2c10 discriminator is introduced and studied in Appendix A. Multiple working points of the MV2c10 algorithm have been calibrated by the flavour tagging group [106], using $t\bar{t}$ simulation. The analysis described in Section 5 uses the 77% b-tag efficiency working point. It is a compromise between efficiently identifying b-jets and rejecting light-flavour jets. The corresponding light-flavour rejection is 6.2 for c-jets and 134 for light-jets (on average 1 out of 6.2 c- or 134 light-jets are mistakenly flavour-tagged by the algorithm). Using a calibrated working point has the advantage to have dedicated scale-factors and predetermined systematic uncertainties. An overview of the calibrated working points for the dataset of 36.1 fb^{-1} is shown in Table 4.2.

[1] The distance traveled by the B-Hadron is calculated via d = $\beta\gamma c\tau$.

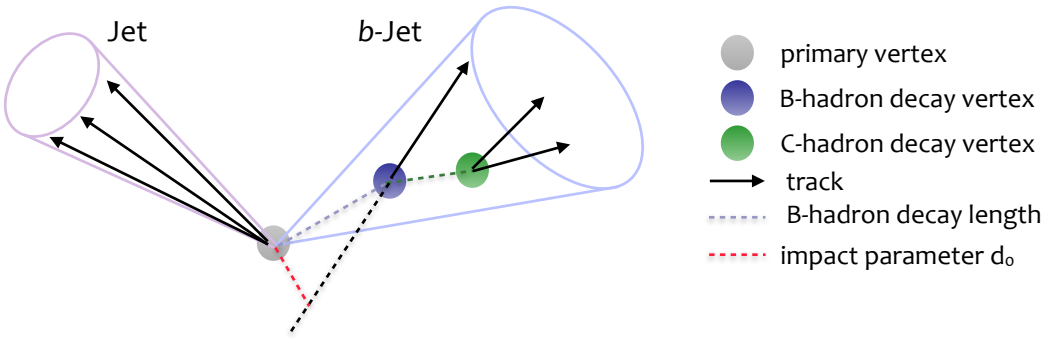

Figure 4.2: Illustration of displaced vertices in a b-jet.

b-jet efficiency	c-jet rejection	τ-jet rejection	light jet rejection
60	34	184	1539
70	12	55	381
77	6	22	134
85	3	8	34

Table 4.2: Calibrated working points of the MV2c10 algorithm along with benchmark numbers for efficiency and rejection [104]. Uncertainties are not quoted since the values were rounded to integers.

4.1.3 Missing transverse energy

Various signal and control regions in the $t\bar{t}V$ analysis depend on the $E_{\mathrm{T}}^{\mathrm{miss}}$ in the event. The missing transverse energy is calculated by summing the x- and y-components of the negative transverse energy of all leptons (including τ leptons), photons, jets and an additional soft term [107]:

$$E_{\mathrm{T}}^{\mathrm{miss}} = \sqrt{\left(E_{\mathrm{x}}^{\mathrm{miss}}\right)^2 + \left(E_{\mathrm{y}}^{\mathrm{miss}}\right)^2},$$

$$E_{\mathrm{x(y)}}^{\mathrm{miss}} = E_{\mathrm{x(y)}}^{\mathrm{miss},e} + E_{\mathrm{x(y)}}^{\mathrm{miss},\gamma} + E_{\mathrm{x(y)}}^{\mathrm{miss,\,jets}} + E_{\mathrm{x(y)}}^{\mathrm{miss},\,\mu} + E_{\mathrm{x(y)}}^{\mathrm{miss,\,soft}}.$$

The soft term is obtained by using information from all tracks that are not associated to any physical objects in the reconstruction. Contamination from pile-up interactions is avoided by associating these tracks to the primary vertex [108]. This method of calculating the $E_{\mathrm{T}}^{\mathrm{miss}}$ is called *track-based soft term* (TST) $E_{\mathrm{T}}^{\mathrm{miss}}$ [109]. Alternatively, the $E_{\mathrm{T}}^{\mathrm{miss}}$ can be calculated by using calorimeter deposits instead of track association with the primary vertex. Thus, the *calorimeter-based soft term* (CST) $E_{\mathrm{T}}^{\mathrm{miss}}$ is more sensitive to pile-up interactions than the TST $E_{\mathrm{T}}^{\mathrm{miss}}$ and not used in the analysis presented in Section 5.

4.1.4 Overlap removal

Jet activities close to reconstructed leptons are prone to double-counting of jets and leptons. Therefore an overlap removal is applied, which differs for electrons and muons

- **Electrons:** If there are any jets within a cone of $\Delta R = 0.2$, the closest one is removed. However if the closest jet is in a cone between $\Delta R = 0.2$ and 0.4 instead, the electron candidate is removed. In addition, any electron candidates that share a track with muon candidates are removed.

- **Muons:** Muons are likely to originate from heavy-meson decays inside heavy-flavour jets. Therefore any muon candidates are removed if the closes jet is within a cone of $\Delta R = 0.4$, unless the jet has less than 3 associated tracks, in which case the jet is removed instead.

4.2 Data and simulation samples

The analysis presented in this thesis analyses data taken with the ATLAS detector at a centre-of-mass energy of 13 TeV. The dataset corresponds to the data taken during the years 2015 and 2016 with an integrated luminosity of 36.1 fb^{-1} for the analysis presented in Sections 5-6. An overview of the data taken in Run 2 is given in Figure 3.3 and the corresponding integrated luminosity is discussed in more detail in the following section. A description of how the samples are processed within the ATLAS experiment, to be used for the analysis, is given in Appendix B.

4.2.1 Data

Each year of data-taking in the ATLAS experiment is separated into run periods by the ATLAS data acquisition system. A period corresponds to several runs of the LHC machine under the same conditions. Between two data-taking periods parameters like the number of bunches or the bunch spacing can change. The periods are split further into runs, which include multiple"*luminosity blocks*" (LBs). A run includes one fill of protons into the machine, while each LB corresponds to minutes of data-taking. Typically a run takes about twelve hours and is split into hundreds of LBs. The response of all sub-detector systems is checked for each LB and the LBs are added to a "*good-run list*" (GRL), depending on which sub-detector systems were fully operational. Typically, the first LBs of each run are being rejected, due to the time until the protons are injected in the LHC and brought to collision. Since the analysis in this thesis includes many different final states, only data from the GRL with all detectors operational was considered. In addition, only data from proton–proton collisions with a bunch spacing of 25 ns was analysed. A summary of the analysed data is given in Table 4.3.

year	date	periods	runs	pileup	integrated luminosity [fb^{-1}]
2015	03-Jun until 03-Nov	D-J	132	13.4	3.2
2016	22-Apr until 26-Oct	A-L	187	25.1	32.9
2017	23-May until 26-Nov	B-K	226	37.8	43.6
2018	17-Apr until 26-Oct	B-Q	243	38.0	59.9

Table 4.3: Overview of the data included in the GRL considered for the analysis [110]. Only proton–proton collisions are taken into account. In addition the data-taking during 2018 is shown but not analysed in this thesis. The column denoted as pileup refers to the mean number of interaction per bunch crossing for the given year of data taking [78].

4.2.2 Simulation

The general principles of the simulation samples used with the ATLAS experiment have been discussed in Section 3.3. This section provides a description of the simulated samples that were considered for the analysis. In general all samples have the masses of the top quark and the Higgs boson set to 172.5 GeV and 125 GeV, respectively. The modelling of heavy-flavour jets, initiated b- and c-quarks from hadron decays, is done using EvtGen [111], with the exception of samples simulated by Sherpa [94]. Photon emissions and τ lepton decays are simulated using Photos [112] and TAUOLA [113] for all samples not simulated by Sherpa. The pileup is modeled with a data-driven technique, reweighting the simulated distribution according to data, and validated through a comparison with Pythia8 [96], where additional pp-collisions in the same and nearby bunches are considered. Finally, the ATLAS detector response for stable particles (with $c\tau \geq 1cm$) is modeled fully by Geant [97, 114] for all simulated samples relevant for the analysis. Some samples used for systematic uncertainties, are modeled by the ATLAS fast simulation [115] instead, which uses a parametrised calorimeter response instead of relying on Geant for the calorimeter detector system. All simulated events are corrected in terms of object identification, reconstruction and trigger efficiencies, energy scales and energy resolutions by relying on scale factors obtained from comparisons to data.

Signal - $t\bar{t}Z$ and $t\bar{t}W$

For the $t\bar{t}Z$ process, only simulated samples with a decay of the Z-boson to two leptons (including two τ leptons) are considered. In addition, off-shell Z bosons, virtual photons with a minimum mass of the dilepton system at 1 GeV and their interference are included. However, no restrictions are imposed on the decay of the top quarks. All possible decay modes are included for the $t\bar{t}W$ process. The samples are generated at NLO by MG5_aMC, interfaced to Pythia8 with the A14 tune [116] and the NNPDF3.0NLOPDF PDF set [117], used for both signal processes. The samples are normalised to the NLO predictions in QCD and EW of $\sigma_{t\bar{t}Z} = 0.88$ pb and $\sigma_{t\bar{t}W} = 0.60$ pb [54, 118], which includes final states with an off-shell Z^* or γ^*.

Diboson background- WZ and ZZ

The diboson processes is generated using the Sherpa 2.1 generator at leading-order (LO), considering the following decay modes: 4ℓ, $\ell\ell\ell\nu$ and $\ell\ell\nu\nu$. The matrix element calculations include up to three partons, using the CT10 PDF set [119]. Unlike Pythia the Sherpa generator is not interfaced to an external parton shower generator, but generates it internally. All opposite-sign same-flavour (OSSF) lepton pairs have an invariant mass of at least 5 GeV in the simulation. The samples are normalised to the NLO in QCD, as shown in Table 4.4.

Final state	NLO QCD prediction [pb]
$\ell\ell\nu\nu$	12.74
$\ell\ell\ell\nu$	11.88
$\ell\ell\ell\ell$	11.69

Table 4.4: Cross sections at NLO in QCD for the considered final states of the simulated diboson processes [120].

Single top background - tZ and tWZ

The single top quark production in the t-channel in association with a Z boson is generated at leading-order (LO) with MadGraph [90] and interfaced to Pythia6 [95] with the four-flavour scheme. The scheme describes how many quark flavours inside the colliding protons are considered in the matrix element calculation [121, 122]. The CTEQ6L1 PDF PDF set [123] and Perugia2012 tune set [124] are used. The events are normalised to the NLO cross section [125].

The production of a single top quark in the Wt-channel in association with a Z boson is generated at NLO in QCD with MadGraph and showered by Pythia8 with the NNPDF3.0NLOPDF PDF set and the `A14` tune. Any overlap with the simulated samples of $t\bar{t}Z$ is avoided by removing diagrams containing a top-quark pair. The events are normalised to the NLO (in QCD) cross section of $\sigma_{tWZ} = 0.015$ pb, which is obtained from the generator [126].

Top pair Backgrounds - $t\bar{t}$ and $t\bar{t}H$

Events of the $t\bar{t}$ process are generated by Powheg-Box [91–93] with the NNPDF3.0NLOPDF PDF set and interfaced to Pythia8 with the NNPDF2.3LOPDF PDF set [117] for the parton shower and underlying event. The h_{damp} parameter, which regulates the recoil of additional gluon emissions against the $t\bar{t}$ system, is set to 1.5 times the top quark mass. The simulated sample is normalised to the NNLO cross section [32], including the NNLL soft-gluon resummation [33].

The simulated samples of $t\bar{t}$ events in association with a Higgs boson are generated at NLO in QCD with MadGraph and showered by Pythia8 with the NNPDF3.0NLOPDF PDF set and the `A14` tune. The samples are normalised to the NLO prediction shown in Reference [118].

Single boson background - W+jets and Z+jets

The production of single bosons with associated jets is generated at NLO in QCD by the Sherpa 2.2.1 generator. The NNPDF3.0NLOPDF PDF set is used with an internal tuning developed by the authors of Sherpa. Up to two partons at NLO or four partons at LO are considered for the matrix element calculation, which is performed by COMIX [127] and OpenLoops [128] and merged with the internal Sherpa parton shower. The samples are normalised to the NNLO cross section in QCD, using the "fully exclusive W and Z production" code (FEWZ) [129].

Other backgrounds

The following processes have minor contributions to the analysis:

- The Triboson background, which includes the final states: $2\ell 4\nu$, $3\ell 3\nu$, $4\ell 2\nu$ and 6ℓ (ℓ includes τ leptons), is generated and showered by the Sherpa 2.1 generator at leading-order (LO) with the CT10 PDF set.
- The background processes $t\bar{t}WW$ and three or four top quarks are generated with MadGraph interfaced to Pythia8 for the parton shower, using the NNPDF2.3LOPDF PDF set [117].
- The production of single top quarks in s-channel, t-channel and Wt-channel is generated by Powheg-Box and interfaced to Pythia6 for the parton shower. The CT10 PDF set was used, fixing it to the four-flavour scheme for the t-channel. Potential overlap with the simulated $t\bar{t}$ samples is avoided by using diagram removal in the simulated samples in the Wt-channel. The simulated samples are normalised to the NLO cross section [125]. In addition, a NNLL soft-gluon resummation is performed in the Wt-channel, similar to the $t\bar{t}$ samples.

- For Higgs boson decays, the production via gluon-gluon fusion and subsequent decay to four charged leptons is generated by POWHEG-BOX with the NNPDF3.0NLOPDF PDF set, interfaced to PYTHIA8, using the CT10 PDF set. The production of a Higgs boson in association with a W or Z boson is generated and showered by PYTHIA8, using the NNPDF2.3LOPDF PDF set.
- Processes involving vector-boson scattering (VBS), with at most one additional parton and electroweak vertex in each event, are generated and showered by the SHERPA 2.1 generator at leading-order (LO), using the CT10 PDF set.

CHAPTER 5

The $t\bar{t}V$ multilepton analysis with 36.1 fb^{-1}

This analysis aims to extract the cross sections of the $t\bar{t}W$ and $t\bar{t}Z$ processes, analyzing the dataset of 36.1 fb^{-1} taken by the ATLAS detector in the years 2015 and 2016. The measurement uses a two-dimensional profile likelihood fit and extracts both cross sections simultaneously. Multiple analysis channels are included that are either sensitive to the $t\bar{t}W$ or $t\bar{t}Z$ signal. A fit is also performed in each of the individual channels. This section aims to give an overview of all analysis channels and results, but provides greater detail for the 4ℓ channel targeting the $t\bar{t}Z$ process.

5.1 Analysis overview

Decay channels with multiple leptons are considered in the analysis. An overview of the considered analysis channels is given in Table 5.1. The table lists the final state particles in each channel, where quarks in final states are reconstructed as jets and neutrinos induce missing transverse momentum in the ATLAS detector. The background processes with a large cross section and identical final states are estimated by a fit in dedicated control regions. This is the case for the Z+jets, WZ and ZZ processes in the 2ℓOS, 3ℓ and 4ℓ channel respectively.

Targeted process	Analysis Channel	Final state particles
$t\bar{t}Z$	2ℓOS	$\ell^+\ell^- q\bar{q}bq\bar{q}\bar{b}$
	3ℓ	$\ell^+\ell^-\ell^{\pm(-)}\nu bq\bar{q}\bar{b}$
	4ℓ	$\ell^+\ell^-\ell^+\ell^-\bar{\nu}b\nu\bar{b}$
$t\bar{t}W$	2ℓSS	$\ell^\pm\ell^{\pm(-)}\nu bq\bar{q}\bar{b}$
	3ℓ	$\ell^+\ell^-\ell^\pm\bar{\nu}b\nu\bar{b}$

Table 5.1: Overview of all analysis channels contribution to the measurement of the $t\bar{t}Z$ and $t\bar{t}W$ cross sections.

Every region in the analysis requires the first lepton, which is the one with the highest transverse momentum, to have a transverse momentum of at least 27 GeV. This requirement is motivated by the lepton triggers. The analysis uses single lepton triggers, which means that each event needs to have at least one electron or muon to be triggered. Dilepton triggers are not used since they impose looser requirements on the lepton candidates and thus would increase the contribution of the fake lepton background to the analysis. In general, the leptons from the $t\bar{t}Z$ and $t\bar{t}W$ processes' final states are expected to be boosted and to pass the tight lepton object requirements. Therefore the usage of dilepton triggers would

not improve the overall results of the analysis. A dedicated menu of triggers is available for both data taking periods of 2015 and 2016 [88, 130]. For the simulated samples, events and corresponding pile-up reweighting profiles are randomly associated to the different periods in approximately the ratio that corresponds to the integrated luminosity of the two data taking periods. This ratio is:

$$\frac{\mathcal{L}_{2015}}{\mathcal{L}_{2016}} = \frac{3.2\text{fb}^{-1}}{32.9\text{fb}^{-1}} = 9.7\%. \tag{5.1}$$

A list of the single lepton triggers used in the analysis is given in Table 5.2. It can be seen that each period has a trigger menu of three and two single lepton triggers for electrons and muons, respectively. Each of the triggers is associated to either electrons or muons, a minimum threshold in transverse momentum and an identification. For electrons, the reconstructed candidates from calorimeter information are matched to tracks from the inner detector, by exploiting a likelihood discriminant that is obtained with multivariate techniques. The likelihood discriminants are related to the electron candidate identification. Thus all single electron triggers require an electron candidate with a certain identification. In addition, the HLT_e26_lhtight_nod0_ivarloose trigger requires the electron candidate to be isolated. For muons, coinciding hits in the three RPC layers of the muon spectrometer exceeding the p_{T} threshold of the given muon trigger are imposed on the muon candidates. The candidates need to pass the identification requirements as well. In addition, the candidates are required to be isolated, according to the relative transverse momentum of the track or the relative isolation track parameter in a ΔR cone of 0.2 around the candidate compared to the candidate transverse momentum for the HLT_mu20_iloose_L1MU15 and HLT_e140_lhloose_nod0 triggers, respectively.

Data taking period	Trigger	p_{T} threshold [GeV]
2015	HLT_e24_lhmedium_L1EM20VH	24
	HLT_e60_lhmedium	60
	HLT_e120_lhloose_L1EM20VH	120
	HLT_mu20_iloose_L1MU15	20
	HLT_mu50	50
2016	HLT_e26_lhtight_nod0_ivarloose	26
	HLT_e60_lhmedium_nod0	60
	HLT_e140_lhloose_nod0	140
	HLT_mu26_ivarmedium	26
	HLT_mu50	50

Table 5.2: Overview of the single lepton triggers for the data taking periods of 2015 and 2016 [88, 130] used in the analysis. As mentioned in Section 3.2.5, the High-level trigger (HLT) is a system that is composed of the L2 and EF triggers.

The lepton with the highest transverse momentum is required to exceed the minimum threshold of any of the single lepton triggers, such that a trigger is fired in each event. To ensure this, a requirement of 27 GeV, i.e. 1 GeV higher than this threshold, is imposed. This requirement applies to all regions in the analysis. Possible overlap between the simulated events of Z+jets and $Z+\gamma$ are removed, by rejecting all

events with a photon in the simulated sample of the Z+jets process.

5.2 The 4ℓ channel

This channel targets the $t\bar{t}Z$ process where both W bosons resulting from the top quark decays and the Z boson decay leptonically, which happens in ~0.5% of all $t\bar{t}Z$ decays, as computed in Section 2.3.3.

5.2.1 Signal regions

Four signal regions are defined which all rely on an event counting approach. Events with two pairs of opposite-sign leptons, among which at least one pair has same flavour leptons, are considered. The OSSF lepton pair with a reconstructed mass closest to m_Z of 91.2 GeV is attributed to the decay of the Z boson and denoted as Z_1. The remaining lepton pair is attributed to the decay of the W bosons from the top quark decays and denoted as Z_2. The signal regions are defined according to the number of b-jets and the flavour composition of the Z_2 pair. Even though two b-jets are in the final state of the $t\bar{t}Z$ process, events with one b-jet are considered due to the efficiency of tagging b-jets, as discussed in Section 4.1.2. Since the contribution of the dominant background, the ZZ process, significantly decreases with each b-jet in the event, the signal regions are split into requiring exactly one b-jet and more than one b-jet. A similar argument can be made for the Z_2 lepton pair. If both leptons have the same flavour, the ZZ background can contribute, while it can only contribute via τ lepton decays in case of a eμ Z_2 pair ($ZZ \to \tau\tau \to e\mu$). Thus, a total of four signal regions are defined combining the two categories and are denoted as 4ℓ-SF-1b, 4ℓ-SF-2b, 4ℓ-DF-1b and 4Lℓ-DF-2b in the following. The expected and observed events are shown in Table 5.3.

	4ℓ-SF-1b	4ℓ-SF-2b	4ℓ-DF-1b	4Lℓ-DF-2b	4ℓ-ZZ-CR
$t\bar{t}Z$	6.56 ± 0.39	6.14 ± 0.56	7.38 ± 0.42	5.99 ± 0.74	0.13 ± 0.04
ZZ	2.27 ± 0.75	1.06 ± 0.52	0.19 ± 0.06	0.00 ± 0.01	145.93 ± 20.84
tWZ	1.60 ± 0.46	0.55 ± 0.26	1.57 ± 0.30	0.51 ± 0.26	0.06 ± 0.07
$t\bar{t}H$	0.58 ± 0.07	0.62 ± 0.09	0.68 ± 0.08	0.57 ± 0.08	0.01 ± 0.01
Other	0.12 ± 0.03	0.09 ± 0.03	0.20 ± 0.05	0.10 ± 0.02	0.51 ± 0.36
Fake leptons	1.84 ± 0.82	1.23 ± 0.62	0.93 ± 0.16	0.39 ± 0.11	7.35 ± 9.14
Total	12.97 ± 1.33	9.69 ± 1.17	10.95 ± 0.65	7.57 ± 0.88	153.92 ± 24.71
Observed	18	14	11	5	144
Data/Simulation	1.39 ± 0.16	1.44 ± 0.17	1.00 ± 0.06	0.66 ± 0.08	0.94 ± 0.15

Table 5.3: The expected and observed events (pre-fit) in the 4ℓ signal regions and control region for an integrated luminosity of 36.1fb^{-1}. Both, statistical and systematic uncertainties are included. Processes included in "Other" are triboson, $t\bar{t}WW$, and 4 tops. All predictions are split into events with real and fake leptons. Events with fake leptons are scaled by the fake factors, as described in Section 5.2.3. Processes are included in "Fake lepons", if they have at least one lepton candidate identified as fake.

The region 4ℓ-ZZ-CR, included in Table 5.3 is described in Section 5.2.2. It can be seen that the amount of expected signal events among the four signal regions is roughly the same, while the background composition is different, which will be discussed for each region individually in the following sections. A total of 48 events are observed among all signal regions. Scaling the five events observed in the 4ℓ

channel in the previous measurement with an integrated luminosity of 3.2 fb^{-1} [58] to 36.1 fb^{-1}, a total of 56 observed events are expected. However, the previous analysis had large statistical uncertainties, used a smaller dataset and the reconstruction of several objects, e.g. the tagging of b-jets have been changed since. In general, there is good agreement between data and simulation when, taking the statistical uncertainties into account. Figures 5.1 - 5.3 show distributions of various kinematic variables in all signal regions combined. Most distributions show a good agreement between data and simulation. The distributions of the invariant mass of the Z_1 and Z_2 pairs show that the leptons from the Z boson and the $t\bar{t}$ system can be identified very well in this channel. Distributions in the individual signal regions are shown in the following sections.

An alternative set of signal regions for this channel, exploiting multivariate techniques is discussed in Appendix C. However, no significant improvements in the sensitivity of the fit in the 4ℓ channel, discussed in Section 5.6.1, were seen, which can be explained by the small amount of events observed in this channel.

The 4ℓ-SF-1b region

The event selection in this region consists of the following requirements:

- Four reconstructed leptons.
- The lepton flavour of the leptons associated to the Z_2 pair are required to be $e^{\pm}e^{\mp}$ or $\mu^{\pm}\mu^{\mp}$.
- The number of b-tagged jets is required to be exactly one.
- The missing transverse momentum must be larger than 80 GeV if the invariant mass of the Z_2 pair is within 10 GeV of 91.2 GeV. It must be larger than 40 GeV, otherwise.
- The sum of the transverse momentum of the third and fourth lepton, p_{T34} must be larger than 25 GeV.

Even though the ZZ background does not have b-jets in the final state at tree-level, it can contribute to this region via gluon splitting, where the gluon decays to b-jets. This is relatively rare and will be discussed in Section 5.2.2. To suppress this contribution, a requirement on the missing transverse momentum is imposed if the Z_2 lepton pair has an invariant mass close to m_Z. Since the resolution of this invariant mass is smeared out by definition (the Z_1 pair is required to have an invariant mass close to m_Z), a looser requirement is imposed if the invariant mass is outside a window of 10 GeV. The requirement of the transverse momentum of third and fourth lepton was found to reduce the contribution of fake leptons [62], since those tend to be the leptons with the lowest transverse momentum. Figure 5.4 shows distributions of variables related to the events selection. It can be seen how the ZZ background is concentrated in the central bin of Figure 5.4(b), while the fake lepton background is accumulated in the first bin of Figure 5.4(d).

The 4ℓ-SF-2b region

The event selection in this signal region is:

- Four reconstructed leptons.
- The lepton flavour of the leptons associated to the Z_2 pair are required to be $e^{\pm}e^{\mp}$ or $\mu^{\pm}\mu^{\mp}$.

- At least two b-tagged jets are required.
- The transverse momentum of every lepton must be larger than 10 GeV.
- The missing transverse momentum must be larger than 40 GeV if the invariant mass of the Z_2 pair is within 10 GeV of 91.2 GeV.

Since this region requires at least two b-jets, the ZZ background contribution decreases and the requirement on the transverse momentum is loosened compared to the 4ℓ-SF-1b region and only applied within the Z mass window. As a result, the fake lepton background becomes more important and a more strict requirement is imposed, requiring every lepton to have at least 10 GeV transverse momentum. A set of four distributions related to the requirements in this region is shown in Figure 5.5. The ZZ background is again concentrated in the central bin of Figure 5.5(b), but also in the first bin of Figure 5.5(c). The distribution of the 4th lepton's p_{T} shows in Figure 5.5(d) that almost all events accumulate in the first bin. However the second and third bin are almost entirely dominated of the signal process.

The 4ℓ-DF-1b region

The event selection in this region includes the following requirements:

- Four reconstructed leptons.
- The lepton flavour of the leptons associated to the Z_2 pair are required to be $e^{\pm}\mu^{\mp}$.
- The number of b-tagged jets is required to be exactly one.
- The sum of the transverse momentum of third and fourth lepton, $p_{\mathrm{T}34}$ must be larger than 45 GeV.

If the Z_2 pair is composed of an electron and a muon, the region is more pure since the ZZ background does not contribute, except if τ lepton decays are considered. In this region, the tWZ process is the dominant background, which is irreducible since it has the same final state particles as the $t\bar{t}Z$ process, if only one b-jet is successfully tagged. Since the only other important background is fake leptons, the event selection only requires a minimum amount of the transverse momentum of third and fourth lepton additionally. Figure 5.6 shows four distributions related to the event selection in this region. The individual figures show that the tWZ background has a very similar shape as the signal. These figures also show that the $t\bar{t}H$ processes enters this region as a background, since it can have the same final state as the signal process.

The 4ℓ-DF-2b region

Finally, the event selection in the last signal region is:

- Four reconstructed leptons.
- The lepton flavour of the leptons associated to the Z_2 pair are required to be $e^{\pm}\mu^{\mp}$.
- At least two b-tagged jets are required.
- The transverse momentum of every lepton must be larger than 10 GeV.

This region has the highest signal-to-background ratio (79%) among all signal regions in the whole analysis. Apart from the fake lepton background, no background processes with 4 reconstructed leptons contribute significantly to this region. Therefore, only the requirement on the transverse momentum of all leptons is imposed in addition. The individual distributions of Figure 5.7 do not show a good agreement of the data with the simulation, because only 5 events are observed in this region, which can be an unfortunate fluctuation of the data. Due to the high signal-to-background ratio in this region more observed events would have improved the results from the 4ℓ channel.

5.2.2 ZZ control region

The dominant background in the 4ℓ channel comes from the ZZ process, since it has the highest cross section among all processes with four real leptons in the Standard Model. The definition of the ZZ control region, denoted as 4ℓ-ZZ-CR, is:

- Exactly four reconstructed leptons.
- Two lepton pairs with opposite charge and same flavour are required, that are associated as the Z_1 and Z_2 lepton pairs.
- The invariant mass of both, the Z_1 and Z_2 pairs must be within 10 GeV of m_Z.
- The missing transverse momentum must be between 20 and 40 GeV.

The first three requirements ensure having two reconstructed Z bosons in each event. The requirement on the missing transverse momentum, however, has two thresholds that need to be motivated. The maximum allowed $E_{\mathrm{T}}^{\mathrm{miss}}$ of 40 GeV ensures orthogonality to the 4ℓ-SF-1b and 4ℓ-SF-2b signal regions. The minimum $E_{\mathrm{T}}^{\mathrm{miss}}$ of 20 GeV is imposed because the ZZ background enters the signal regions only accompanied with missing transverse momentum. No requirements on the number of jets or b-jets are imposed for the control region. Even though the signal regions have at least one b-jet required, the ZZ process roughly loses events in one order of magnitude per b-jet, as shown in Figure 5.9(b). The available events observed with a requirement of at least one jet would be too small to estimate the normalization of the ZZ background without a significant statistical uncertainty. A study of how well the simulated sample of the ZZ process is able to model the correct amount of b-jets is shown in Section 5.4.2 and propagated as a systematic uncertainty in the fit. Figures 5.8 - 5.10 show various kinematic distributions in the 4ℓ-ZZ-CR region. The expected and observed yields can be seen in Table 5.3. The distributions and event yields show that the 4ℓ-ZZ-CR is very pure and has almost no signal contamination.

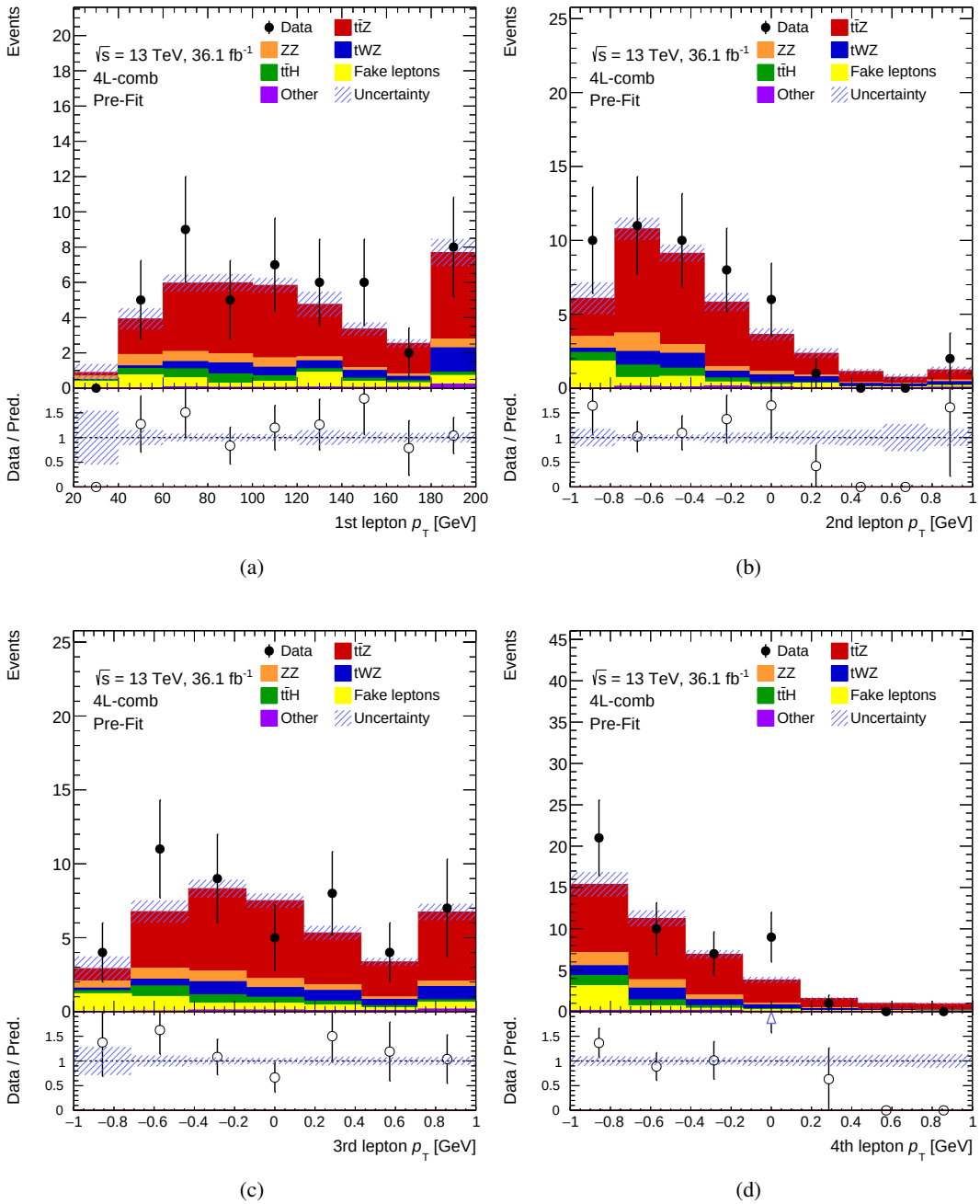

Figure 5.1: Distribution of the transverse momentum for each of the four leptons in all 4ℓ signal regions combined before the fit is performed. Both, statistical and systematic uncertainties are included. Each of the distributions includes the under and overflow in the first and last bin, respectively.

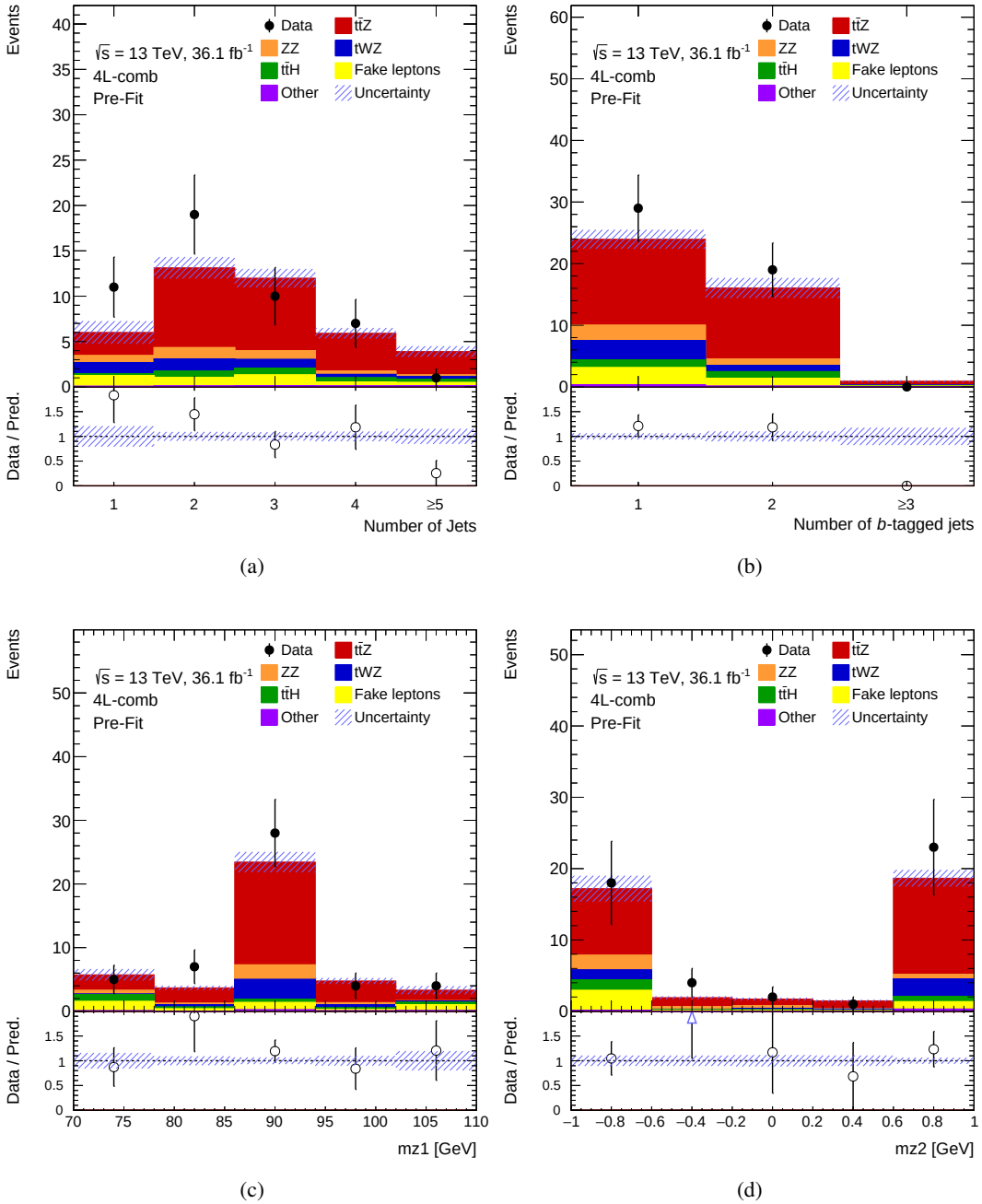

Figure 5.2: Distribution of the number of jets, number of b-jets and the invariant mass of the Z_1 and Z_2 lepton pairs in all 4ℓ signal regions combined before the fit is performed. Both, statistical and systematic uncertainties are included. Each of the distributions includes the under and overflow in the first and last bin, respectively.

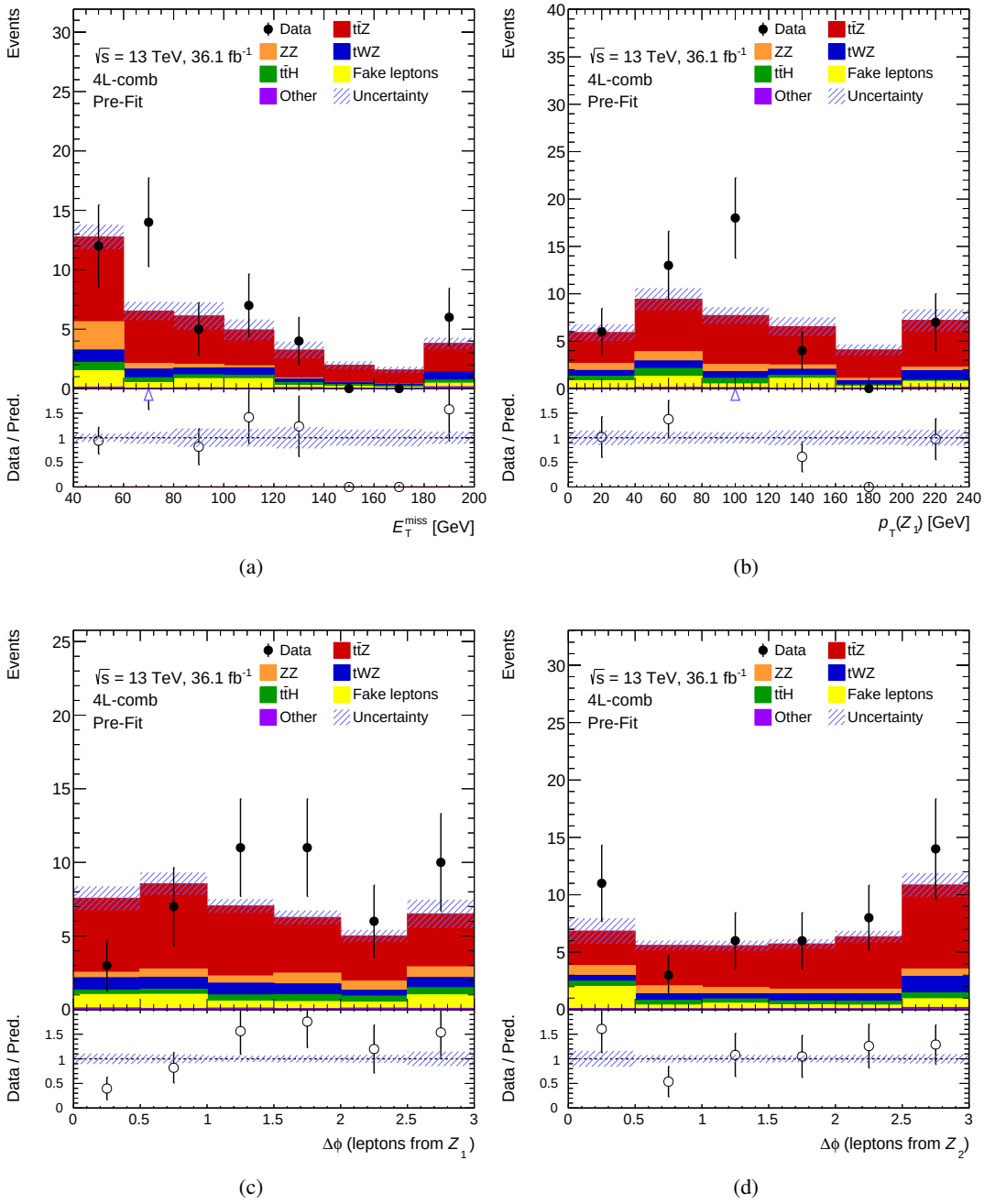

Figure 5.3: Distribution of the missing transverse momentum, the transverse momentum and $\Delta\phi$ of the Z_1 lepton pair and the $\Delta\phi$ of the Z_2 lepton pair in all 4ℓ signal regions combined before the fit is performed. Both, statistical and systematic uncertainties are included. Each of the distributions includes the under and overflow in the first and last bin, respectively.

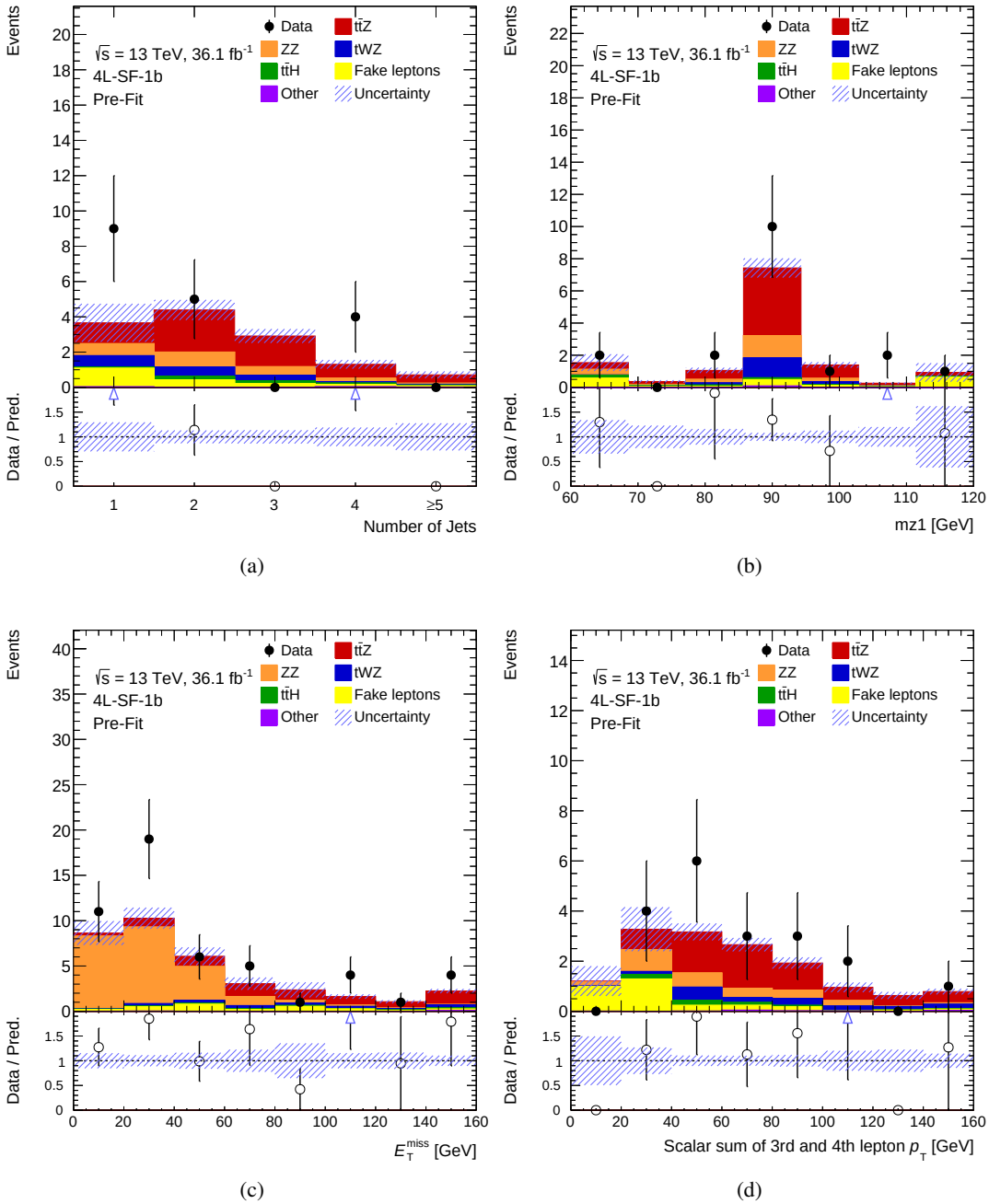

Figure 5.4: Distribution in the 4ℓ-SF-1b signal region before the fit is performed. The distributions of $E_{\mathrm{T}}^{\mathrm{miss}}$ and p_{T34} are shown before imposing a requirement on them. Both, statistical and systematic uncertainties are included. Each of the distributions includes the under and overflow in the first and last bin, respectively.

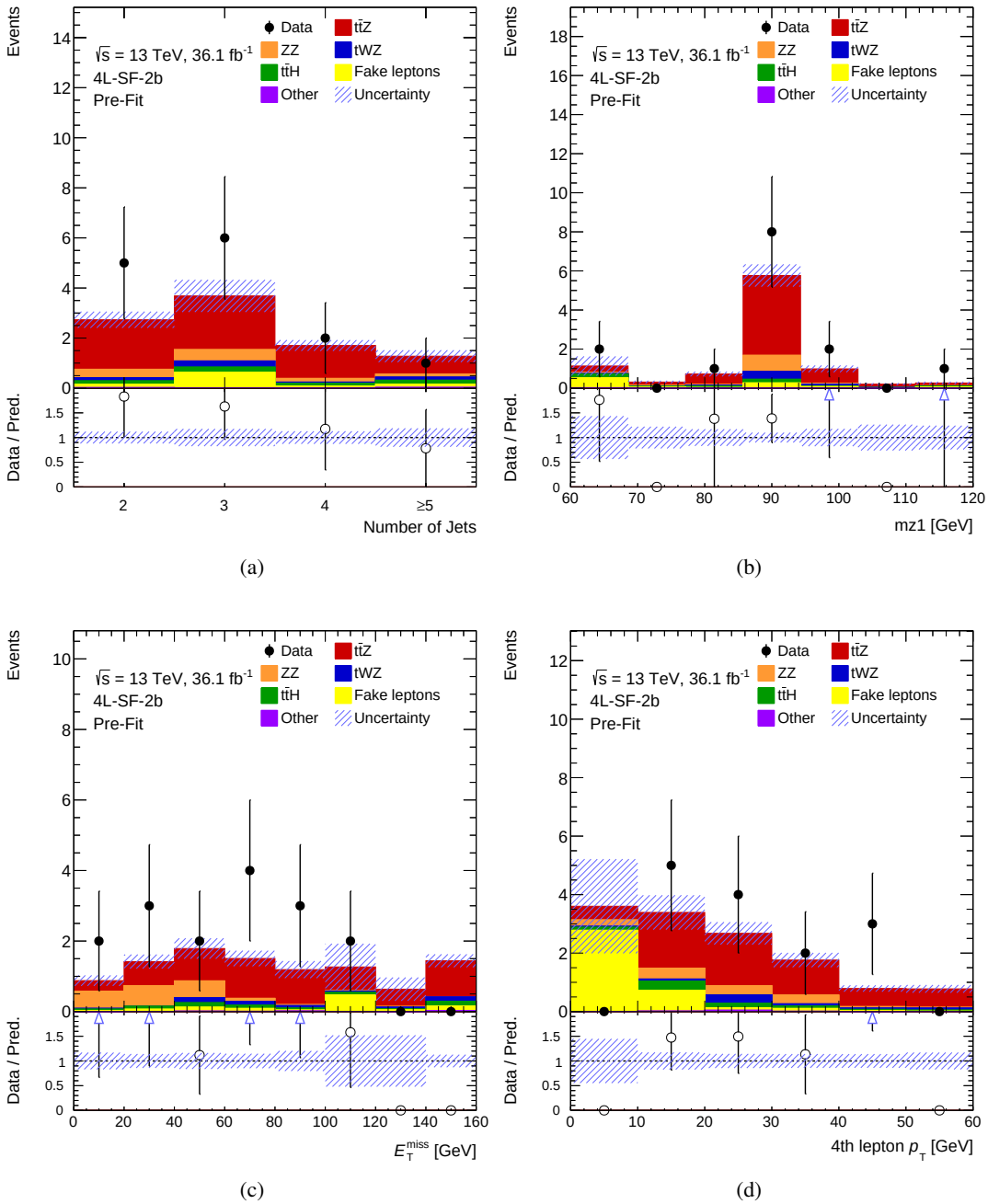

Figure 5.5: Distribution in the 4ℓ-SF-2b signal region before the fit is performed. Both, statistical and systematic uncertainties are included. The distributions of $E_{\mathrm{T}}^{\mathrm{miss}}$ and the fourth lepton p_{T} are shown before imposing a requirement on them. Each of the distributions includes the under and overflow in the first and last bin, respectively.

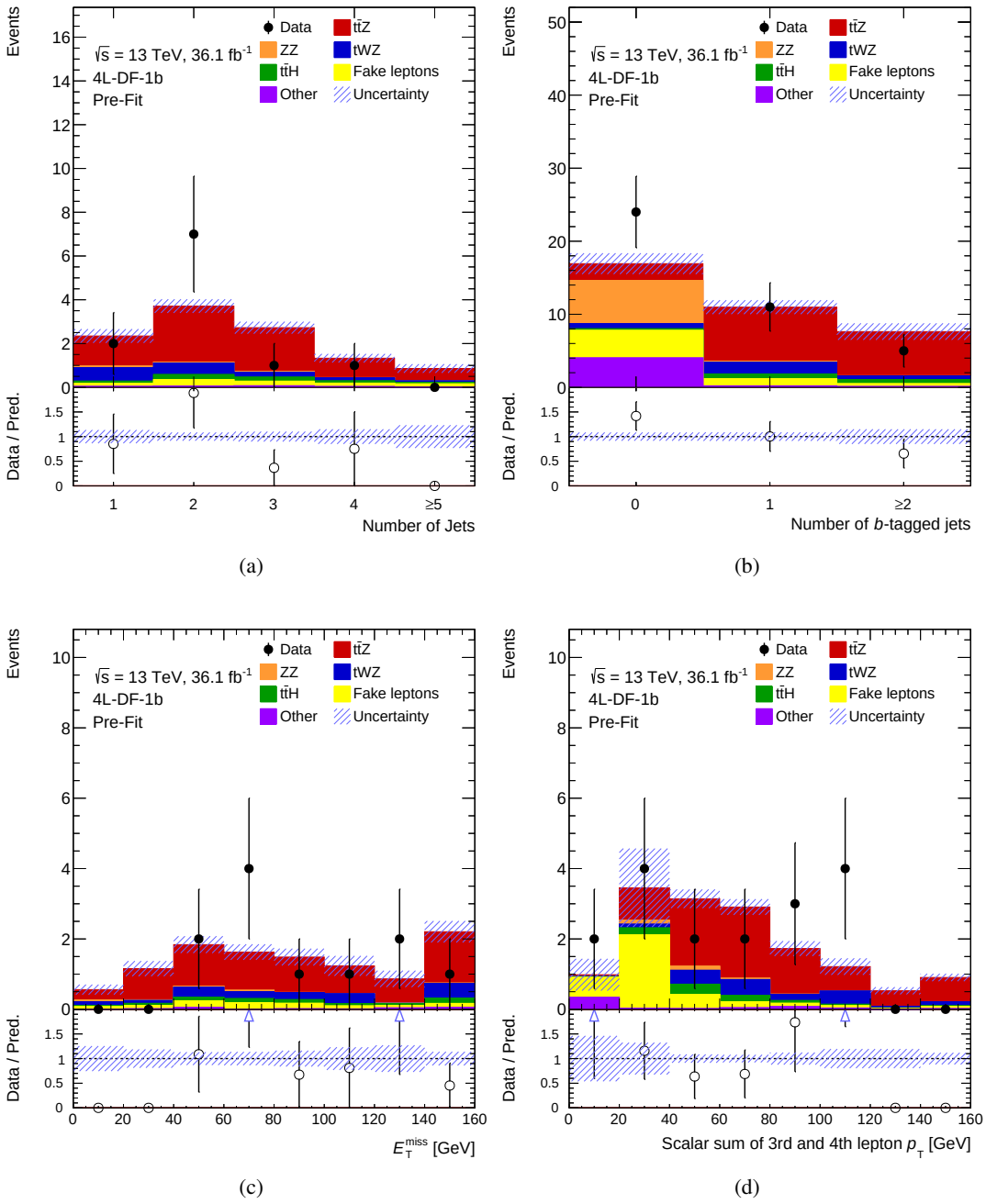

Figure 5.6: Distribution in the 4ℓ-DF-1b signal region before the fit is performed. Both, statistical and systematic uncertainties are included. The distributions of the number of b-tagged jets, $E_{\mathrm{T}}^{\mathrm{miss}}$ and p_{T34} are shown before imposing a requirement on them. Each of the distributions includes the under and overflow in the first and last bin, respectively.

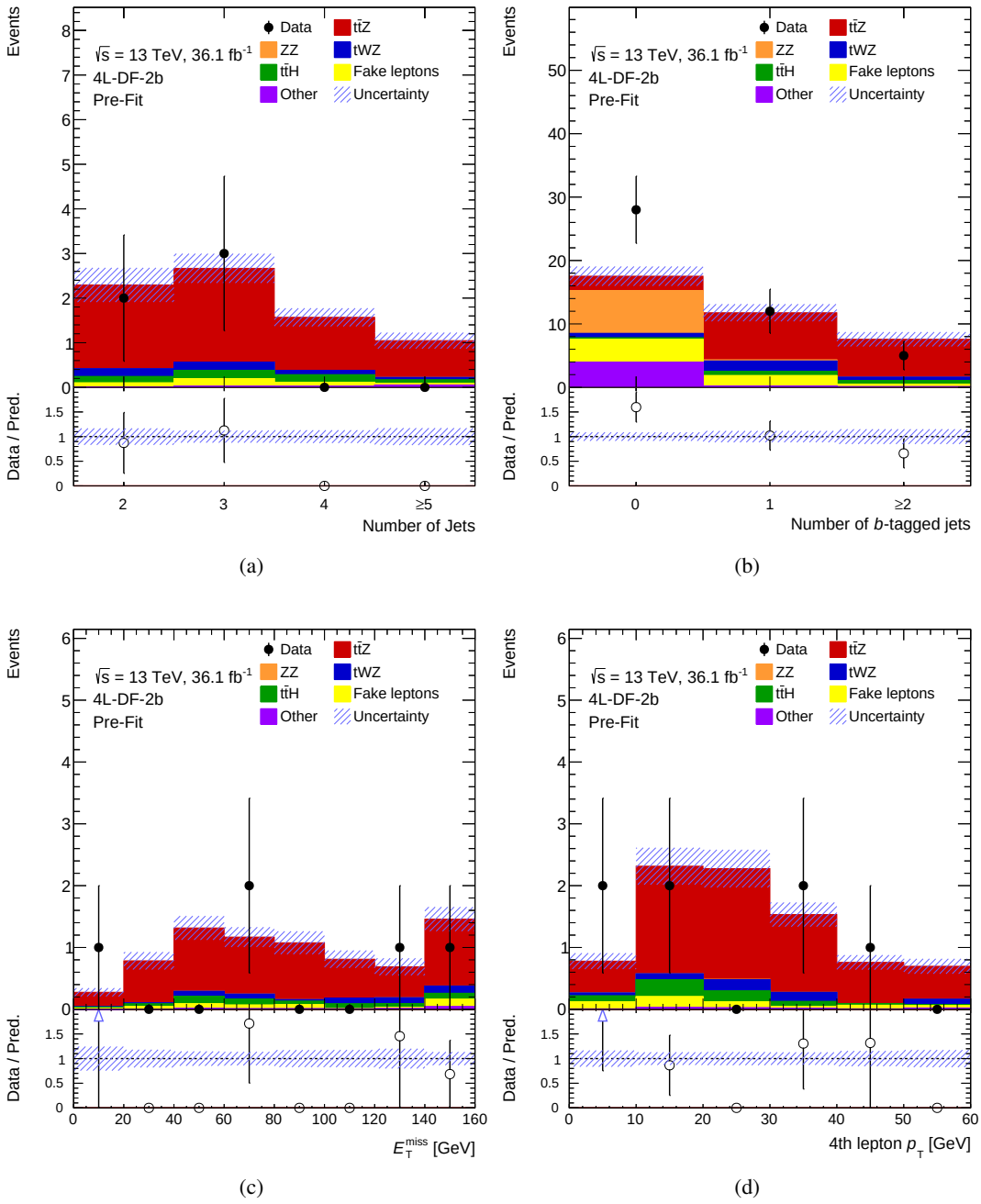

Figure 5.7: Distribution in the 4ℓ-SF-2b signal region before the fit is performed. Both, statistical and systematic uncertainties are included. The distributions of the number of b-tagged jets, $E_{\mathrm{T}}^{\mathrm{miss}}$ and the fourth lepton p_{T} are shown before imposing a requirement on them. Each of the distributions includes the under and overflow in the first and last bin, respectively.

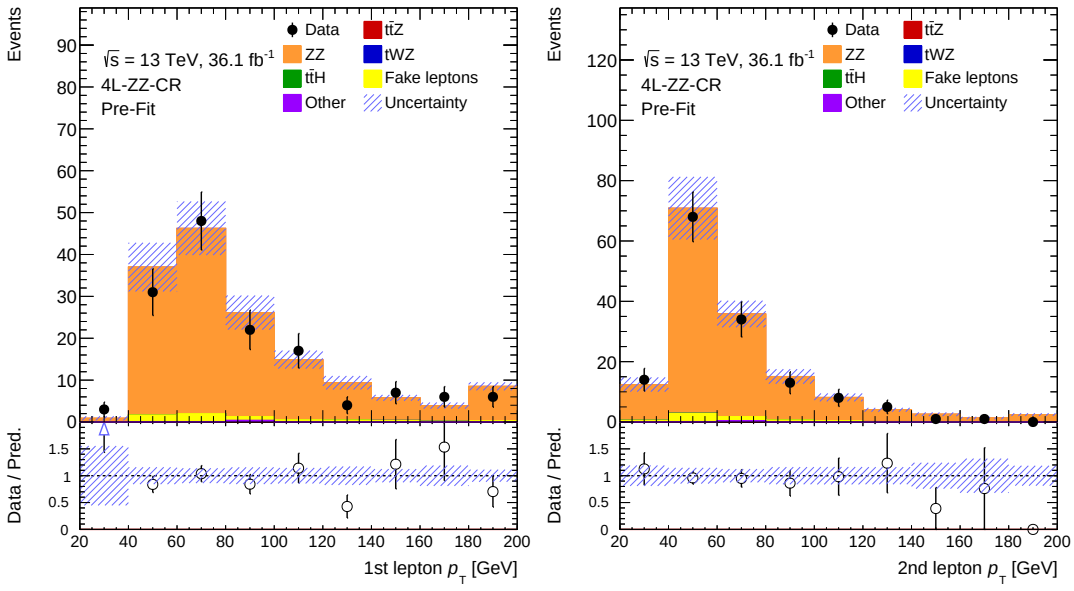

(a) (b)

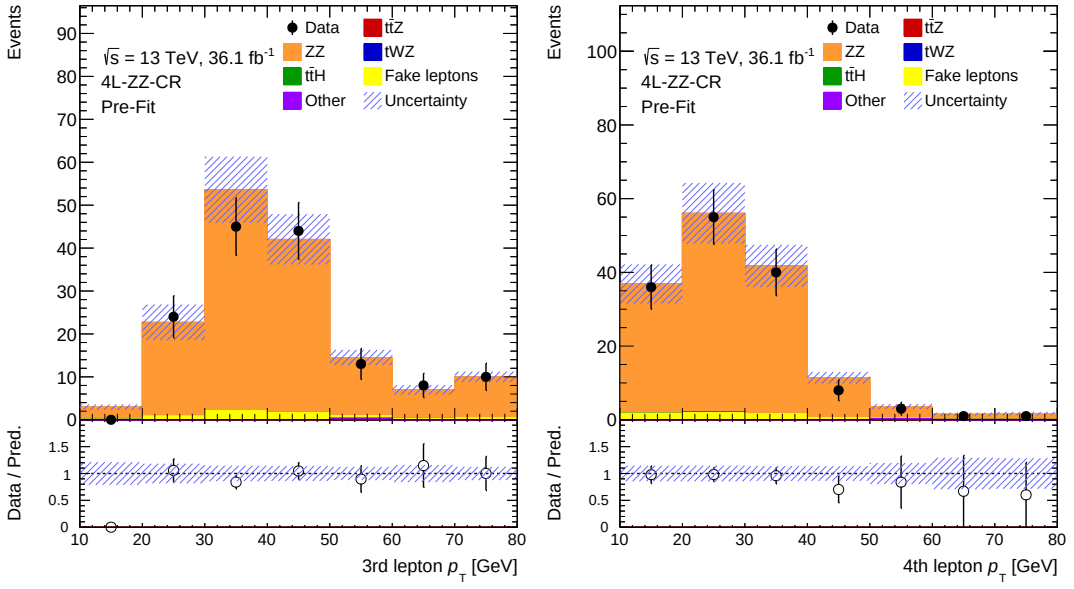

(c) (d)

Figure 5.8: Distribution of the transverse momentum for each of the four leptons in the 4ℓ-ZZ-CR before the fit is performed. Both, statistical and systematic uncertainties are included. Each of the distributions includes the under and overflow in the first and last bin, respectively.

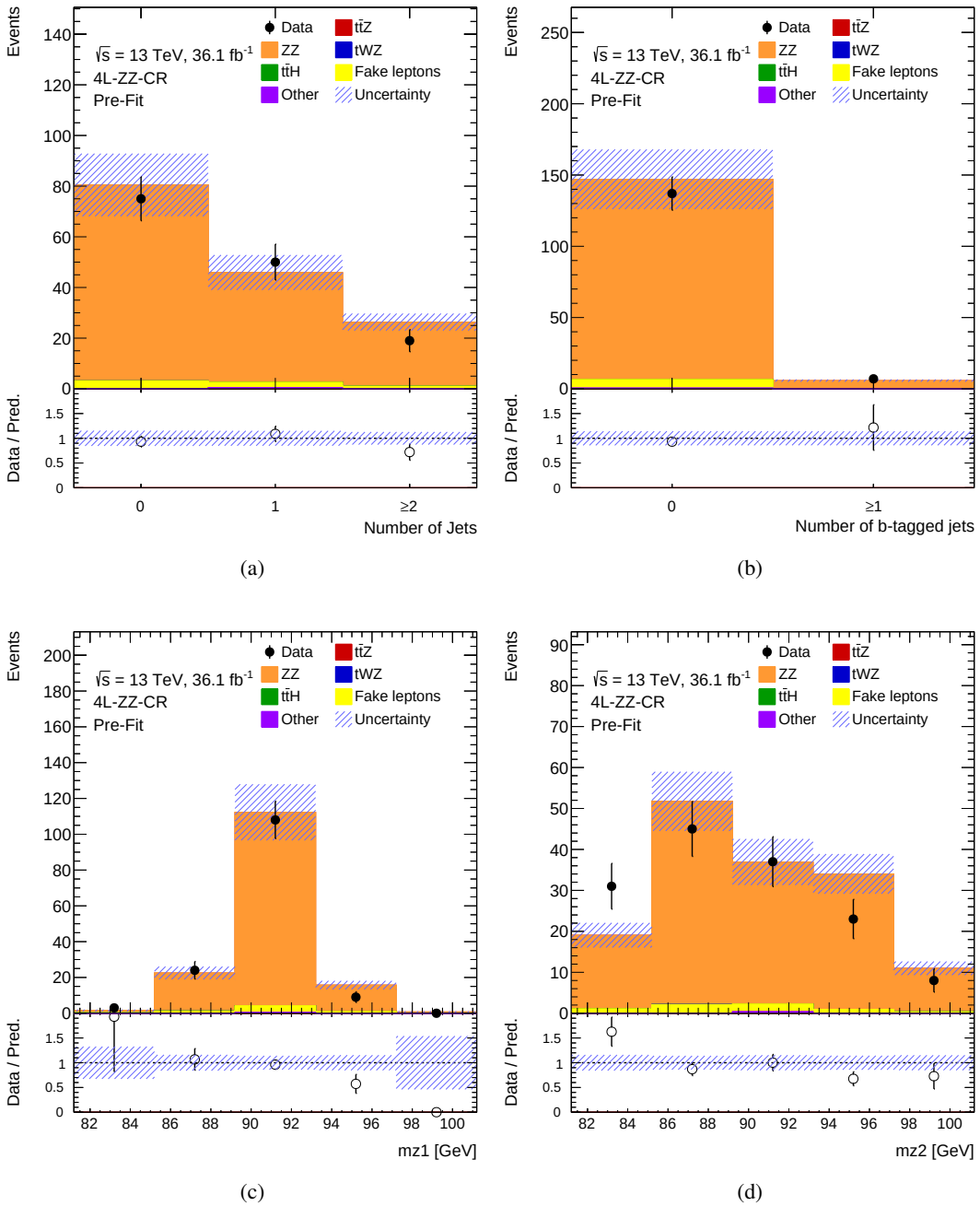

Figure 5.9: Distribution of the number of jets, number of b-jets and the invariant mass of the Z_1 and Z_2 lepton pairs in the 4ℓ-ZZ-CR before the fit is performed. Both, statistical and systematic uncertainties are included. Each of the distributions includes the under and overflow in the first and last bin, respectively.

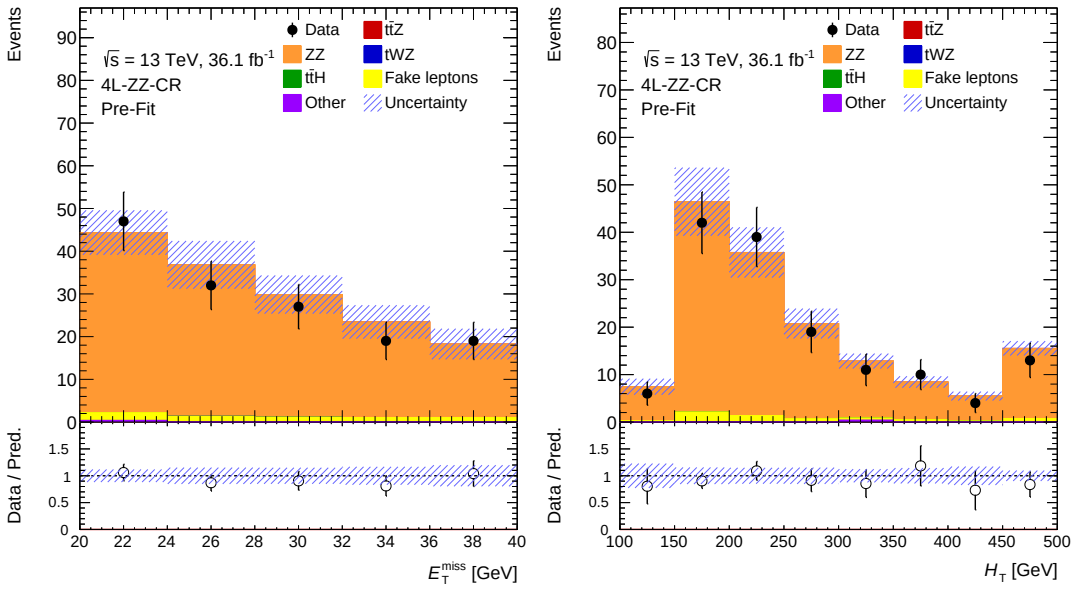

(a) (b)

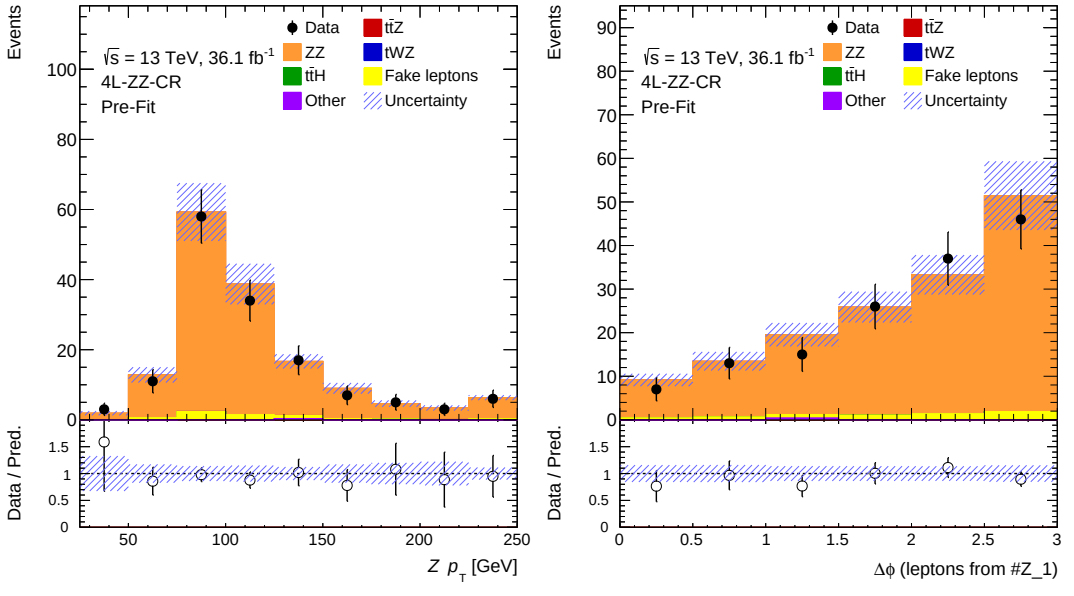

(c) (d)

Figure 5.10: Distribution of the missing transverse momentum, H_{T} (defined as the scalar sum of the transverse momentum of all leptons and jets) and both the transverse momentum and $\Delta\phi$ of the Z_1 lepton pair in the 4ℓ-ZZ-CR before the fit is performed. Both, statistical and systematic uncertainties are included. Each of the distributions includes the under and overflow in the first and last bin, respectively.

5.2.3 Estimation of fake leptons

The estimation of fake leptons in the 4ℓ channel relies on information from the simulated samples and is called "*fake factor method*". For this method, two control regions with a three lepton selection are defined, where the fake lepton candidate can be identified clearly. These regions are enriched with events of the $t\bar{t}$ and Z+jets process, respectively. The event selection for the the $t\bar{t}$ control region is:

- Exactly three lepton candidates are required.
- One lepton pair with opposite charge is required.
- No lepton pair with opposite charge and same flavour is allowed.
- At least one jet is required.
- The jet with the highest transverse momentum is required to have $p_{\mathrm{T}} > 30$ GeV.

In the $t\bar{t}$ control region the fake lepton is identified as the lepton with the lowest transverse momentum among the two lepton candidates with the same charge. The event selection for the Z+jets control region is:

- Exactly three lepton candidates are required.
- One lepton pair with opposite charge and same flavour is required.
- The missing transverse momentum is required to be less than 50 GeV.
- The transverse mass m_{T}[1] is required to be less than 50 GeV.
- At least one jet is required.

In the Z+jets control region the fake lepton is identified as the lepton that doesn't belong to the lepton pair with an invariant mass closest to m_Z.

The fake leptons are split into two categories according to their origin, obtained by accessing information from the simulation, which are refered to as "*light* and "*heavy* fake lepton origins in the following. The heavy fake leptons are originating from baryons or flavoured mesons, while the light fake leptons are mainly photon-electron conversions and are negligible for fake muon candidates.

To estimate how well the fake leptons are estimated by simulation, two fits are performed in the two control regions, separately for fake electron and fake muon candidates. The statistical background of the profile likelihood fit is explained in Section 5.5. The two fits include both control regions, since they are expected to have different contribution of light and heavy fake leptons. Thus a total of four fake lepton background normalizations, the "*fake factors*" are considered: μ^{e}_{heavy}, $\mu^{\mu}_{\mathrm{heavy}}$, μ^{e}_{light}, and $\mu^{\mu}_{\mathrm{light}}$.

As discussed previously, the contribution of light muon fake lepton candidates is expected to be negligible. Therefore $\mu^{\mu}_{\mathrm{light}}$ is fixed to 1 with an uncertainty of 50%. The other three fake factors are extracted from the two fits in both control regions. The yields expected and observed in the two control regions, split into whether the fake lepton candidate is identified as an electron or muon, are shown in Table 5.4. It can be seen how the composition of light and heavy fake lepton candidates differs among the regions and lepton flavours. Overall, more events are available in the Z+jets region, which dominates the fits performed to extract the fake factors. However, relatively, the amount of heavy fake lepton candidates is higher in the $t\bar{t}$ region.

The fake factors extracted from the two fits are:

[1] The transverse mass is defined as: $m_{\mathrm{T}} = \sqrt{2p^{\ell}_{\mathrm{T}}E^{\mathrm{miss}}_{\mathrm{T}} - 2\mathbf{p}^{\ell}_{\mathrm{T}} \cdot \mathbf{p}^{\mathrm{miss}}_{\mathrm{T}}}$

	Z+jets	$t\bar{t}$
Fake electron candidate		
$t\bar{t}Z$	23.3 ± 0.8	5.6 ± 0.2
heavy fake leptons	1260 ± 151	262 ± 27
light fake leptons	1714 ± 163	49.0 ± 5.0
WZ	510 ± 116	24.0 ± 3.0
ZZ	360 ± 80	4.0 ± 1.0
Other	37.6 ± 0.8	13.2 ± 0.2
Total	3904 ± 263	358 ± 34
Observed	5416	384
Fake muon candidate		
$t\bar{t}Z$	27.5 ± 1.1	6.4 ± 0.2
heavy fake leptons	2265 ± 145	291 ± 22
light fake leptons	496 ± 131	36.0 ± 2.0
WZ	676 ± 173	16.0 ± 4.0
ZZ	315 ± 9	3.0 ± 0.8
Other	37.2 ± 0.9	18.1 ± 0.4
Total	3816 ± 261	370 ± 22
Observed	4363	385

Table 5.4: Expected and observed events in the Z+jets and $t\bar{t}$ control regions, separately counted if the event has a fake electron or muon candidate [131]. Only statistical uncertainties are shown.

- $\mu^{e}_{\text{heavy}} = 0.90 \pm 0.14$
- $\mu^{\mu}_{\text{heavy}} = 1.07 \pm 0.09$
- $\mu^{e}_{\text{light}} = 1.84 \pm 0.27$
- $\mu^{\mu}_{\text{light}} = 1.00 \pm 0.50$

The result shows that most of the fake factors are compatible with the modelling provided by the simulation, except the fake electron candidates from photon conversions. It was checked, that all four kinds of fake leptons contribute to the 4ℓ signal regions. In addition, multiple checks to validate the fake factor method, like dependency on the number of b-jets and exchanging the generator for the simulated samples of Z-jets and $t\bar{t}$, have been performed.

5.3 Other analysis channels targeting $t\bar{t}Z$ or $t\bar{t}W$

The work presented in this thesis was dedicated towards the 4ℓ channel targeting the $t\bar{t}Z$ process. However, the 4ℓ channel is part of a measurement of both the $t\bar{t}Z$ and $t\bar{t}W$ cross sections, performed in multiple analysis channels. The choice of measuring both cross sections simultaneously is motivated by the similarity of the two processes. The cross section of the two processes is predicted to be similar and they have similar decay channels and final state particles. In addition, the simulated samples for the two

signal processes use the same generators and thus many systematic uncertainties are the same and can be compared, as described in the next section.

For the $t\bar{t}Z$ process, apart from the 4ℓ channel, two more channels have been considered: the 2ℓOS and the 3ℓ channel, while for the $t\bar{t}W$ process two analysis channels were considered: the 2ℓSS and the 3ℓ channel.

5.3.1 The 2ℓOS channel

This analysis channel was not part of the previous measurement of the $t\bar{t}Z$ cross section with the ATLAS experiment [58], but included in the analysis at 8 TeV, instead [55]. In this channel, each event is required to have exactly two reconstructed leptons with opposite charge and same flavour. The pair must have an invariant mass close to m_Z. Since this channel is dominated by the Z+jets and $t\bar{t}$ backgrounds, it makes use of multivariate techniques. A total of three Boosted Decision Trees (BDTs) are trained, split according to the number of jets and b-jets, denoted as 2ℓ-Z-6j1b, 2ℓ-Z-5j2b, 2ℓ-Z-6j2b and used as signal regions. The corresponding expected and observed events are shown in Table 5.5. It can be seen that the Z+jets background is split into different components, according to the number of b-jets found in the event. This is done since this channel is very sensitive to the number of jets and b-jets. The normalization for the backgrounds denoted as "Z + 1 HF" and "Z + 2 HF" are free parameters in the fit, similar to the normalization of the ZZ background in the 4ℓ channel. In addition, the $t\bar{t}$ background is estimated with a data-driven technique: The total background, excluding the $t\bar{t}$ contribution, is subtracted from data and scaled with a correction factor to account for detector effects, to estimate the $t\bar{t}$ background in this channel. On the other hand, the simulated $t\bar{t}$ process is used for the training of the BDTs to benefit from the larger set of events compared to data.

The most important variables contributing to the training of the BDT discriminants are the pseudorapidity of the dilepton system, the sum of transverse momenta of all jets divided by the sum of their energies and the first Fox-Wolfram moment, which is built from jets and leptons in each event [132]. The three BDT discriminants, before the fit (described in Section 5.6.3) is performed are shown in Figure 5.11. Looking at the curve for the signal normalized to the total background, it can be seen how the BDT is able to separate the signal from the background.

Overall this channel has the smallest sensitivity among the three channels targeting $t\bar{t}Z$, due to the large irreducible backgrounds.

	2ℓ-Z-6j1b	2ℓ-Z-5j2b	2ℓ-Z-6j2b
$t\bar{t}Z$	35.04 ± 6.40	36.78 ± 2.74	100.23 ± 13.14
$t\bar{t}$	35.76 ± 5.99	126.61 ± 11.77	188.19 ± 14.70
Z + 2 HF	111.42 ± 25.47	205.66 ± 30.70	297.43 ± 64.71
Z + 1 HF	135.43 ± 31.04	31.63 ± 8.79	42.75 ± 13.54
Z + 0 HF	72.26 ± 33.42	11.64 ± 10.08	15.18 ± 8.80
Other	43.89 ± 16.17	34.93 ± 9.33	62.15 ± 16.42
Total	433.79 ± 86.02	447.25 ± 42.63	705.92 ± 91.51
Observed	338	433	613
Data/Simulation	0.78 ± 0.16	0.97 ± 0.10	0.87 ± 0.12

Table 5.5: The expected and observed events (pre-fit) in the 2ℓOS signal regions for an integrated luminosity of 36.1fb^{-1} [131]. Both, statistical and systematic uncertainties are included.

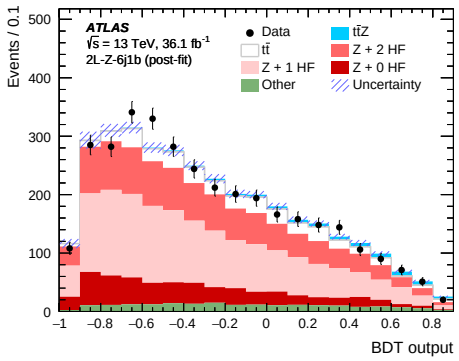

(a) 2ℓ-Z-6j1b

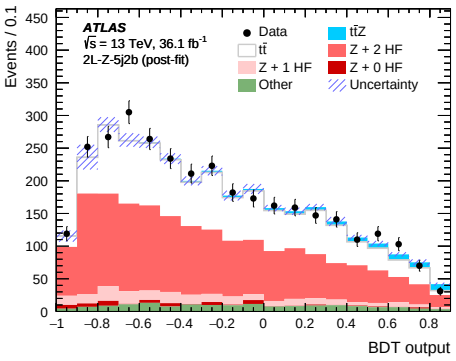

(b) 2ℓ-Z-5j2b

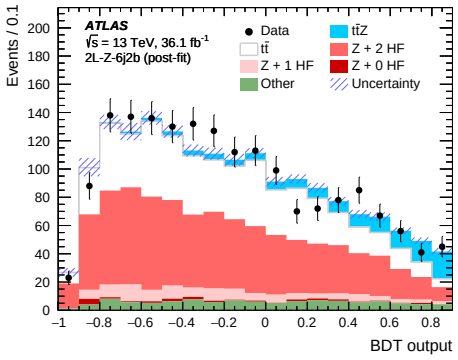

(c) 2ℓ-Z-6j2b

Figure 5.11: Distribution of the three BDT discriminants from the 2ℓOS channel before the fit has been performed [9]. The dashed line in light blue indicates the signal process normalized to the total background. Both, statistical and systematic uncertainties are included. Each of the distributions includes the under and overflow in the first and last bin, respectively.

5.3.2 The 3ℓ channel

This analysis channel provides the highest sensitivity among all channels targeting $t\bar{t}Z$ and the best compromise in terms of cross section and background composition for the available dataset. Four signal regions are defined that each require exactly three reconstructed leptons + one lepton pair with opposite charge and same flavour and are denoted as: 3ℓ-Z-1b4j, 3ℓ-Z-2b3j, 3ℓ-Z-2b4j and 3ℓ-noZ-2b4j. The regions are split according to the number of jets and b-jets. In addition, the region 3ℓ-noZ-2b4j, requires the lepton pair with opposite charge and same flavour to have an invariant mass different from m_Z. This regions targets the final state with an off-shell Z^* or γ^* (both are possible final states in the simulated sample of the signal process, as mentioned in Section 4.2.2), while the other regions target $t\bar{t}Z$. The dominant background in this channel is the WZ process, whose background normalization is a free parameter in the fit and which has a dedicated control region, similar to the ZZ background in the 4ℓ channel. Other important backgrounds are related to single top production or fake leptons. Unlike the 4ℓ channel, this channel relies on a fully data-driven fake estimation, called the "*matrix method*". Since this method is crucial to the $t\bar{t}W$ analysis, it is described in the next section. However, the background labeled as $\gamma + X$, is scaled by the fake factors that were derived for the 4ℓ channel. This background describes processes with photons in the final state, like $t\bar{t}\gamma$ and Z+γ. The expected and observed events for all regions are shown in Table 5.6. Kinematic distributions in the 3ℓ-Z-2b4j signal region and the WZ control region are shown in Figure 5.12.

	3ℓ-Z-1b4j	3ℓ-Z-2b3j	3ℓ-Z-2b4j	3ℓ-noZ-2b4j	3ℓ-WZ-CR
$t\bar{t}Z$	44.50 ± 5.32	57.00 ± 10.01	16.63 ± 3.30	12.71 ± 2.30	5.10 ± 1.20
$t\bar{t}W$	0.49 ± 0.29	0.52 ± 0.34	0.83 ± 0.42	3.67 ± 1.91	0.18 ± 0.10
WZ	36.72 ± 11.97	7.05 ± 3.82	3.32 ± 1.62	1.05 ± 0.59	210.77 ± 22.38
ZZ	3.00 ± 0.62	0.53 ± 0.10	0.68 ± 0.26	0.33 ± 0.19	11.49 ± 1.99
tZ	2.89 ± 0.96	3.41 ± 1.13	3.66 ± 1.19	0.32 ± 0.14	1.42 ± 0.52
tWZ	6.74 ± 1.90	5.77 ± 1.99	2.07 ± 0.44	0.67 ± 0.30	2.17 ± 0.66
$t\bar{t}H$	1.25 ± 0.19	1.42 ± 0.22	0.51 ± 0.09	4.87 ± 0.66	0.11 ± 0.03
Other	0.30 ± 0.16	0.37 ± 0.37	0.87 ± 1.04	2.13 ± 1.09	1.53 ± 1.17
Fake leptons	6.53 ± 2.85	4.01 ± 2.18	1.17 ± 1.15	3.16 ± 1.99	5.03 ± 2.78
$\gamma + X$	1.35 ± 1.15	0.49 ± 0.59	0.62 ± 0.65	4.88 ± 2.49	0 ± 0
Total	103.76 ± 14.23	80.57 ± 10.22	30.36 ± 4.47	33.78 ± 4.70	237.80 ± 22.97
Observed	86	78	45	37	211
Data/Simulation	0.83	0.96	1.48	1.09	1.13

Table 5.6: The expected and observed events (pre-fit) in the 3ℓ signal regions targeting $t\bar{t}Z$ for an integrated luminosity of 36.1fb^{-1} [131]. Both, statistical and systematic uncertainties are included.

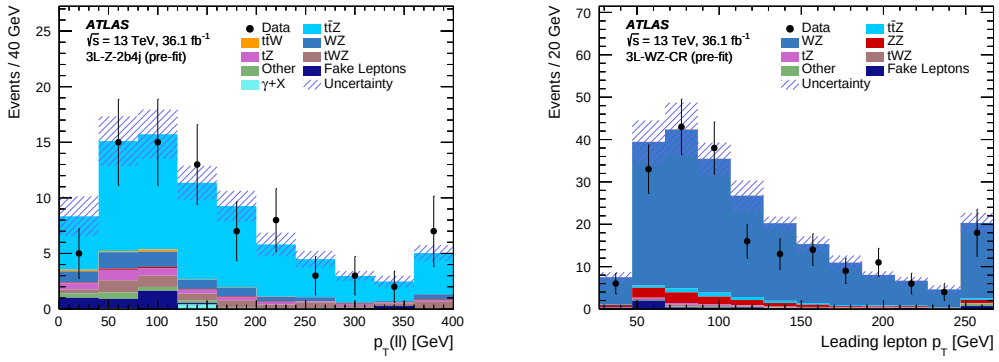

(a) 3ℓ-Z-2b4j (b) 3ℓ-WZ-CR

Figure 5.12: Distribution of the transverse momentum of the lepton pair coming from the Z boson in the 3ℓ-Z-2b4j signal region (left) and the transverse momentum of the leading lepton in the WZ control region (right), before the fit is performed [9]. Both, statistical and systematic uncertainties are included.

5.3.3 The $t\bar{t}W$ channels

The $t\bar{t}W$ cross section is measured together with the $t\bar{t}Z$ cross section in a two-dimensional fit. The $t\bar{t}W$ channels include the 2ℓSS and 3ℓ channels; the sensitivity is mostly driven by the 2ℓSS. The dominant background is the fake lepton background; other important backgrounds arise from electrons with misidentified charge and the WZ process. The matrix method, used to estimate the fake lepton background, was extensively used for top-quark publications of Run 1 already [133] and relies on fake lepton and real efficiencies that are estimated in dedicated control regions. In this analysis, the fake lepton efficiencies are extracted in 2ℓSS control regions, that are split according to the lepton flavour, the number of b-jets and also the total charge of the leptons, since the fake lepton background was found sensitive to these quantities, for a total of twelve 2ℓSS control regions. The real lepton efficiencies are estimated in four 2ℓOS regions instead. The efficiencies are extracted from a fit in the regions mentioned above, as a function of the sum of the transverse momentum of the two leptons and are shown in Figure 5.13. Since the 3ℓ regions targeting $t\bar{t}Z$ are also using the matrix method for their fake estimation, a different set of fake lepton efficiencies is used, matching the lepton definitions of the $t\bar{t}Z$ regions, which is different from the lepton definitions of the $t\bar{t}W$ regions, as mentioned in Section 4. The matrix method has been validated through multiple cross-checks, including a side-by-side comparison to the fake factor method, that is used in the 4ℓ regions in this analysis.

The signal regions in the 2ℓSS channel are defined accordingly to the twelve 2ℓSS control regions, in terms of lepton flavour, charge and number of b-jets. Orthogonality is ensured through requirements on the number of jets, the missing transverse energy or the H_{T}, depending on the given region. In addition, four signal regions with three leptons are defined, that are orthogonal to the four signal regions that target the $t\bar{t}Z$ process. These four regions, sensitive to $t\bar{t}W$, all require any possible lepton pair with same flavour and opposite charge to be outside the Z-mass window. Figure 5.14 shows the distributions of the missing transverse momentum in each of the 2ℓSSee, 2ℓSS$\mu\mu$, 2ℓSS$e\mu$ and 3ℓ regions, sensitive to $t\bar{t}W$:

The fit to extract the cross section of the $t\bar{t}W$ cross section includes the sixteen signal regions, as well as the twelve 2ℓSS control regions, where the fake lepton efficiencies are estimated. Since the signal contribution in the control regions was found not to be negligible, the fake lepton background and the signal processes are anti-correlated. Thus a total of 28 regions are part of the $t\bar{t}W$ fit. The results for the two-dimensional fit, that include the $t\bar{t}W$ regions, are presented in Section 5.6.3.

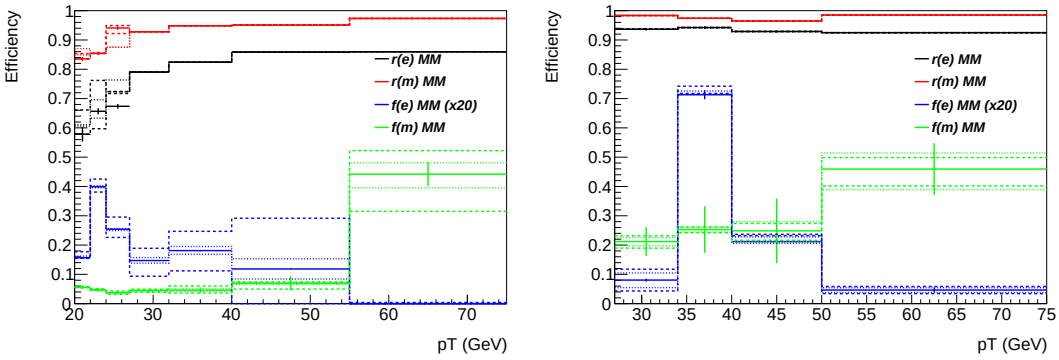

(a) $t\bar{t}W$ lepton definitions, events with one b-jet

(b) $t\bar{t}W$ lepton definitions, events with at least two b-jets

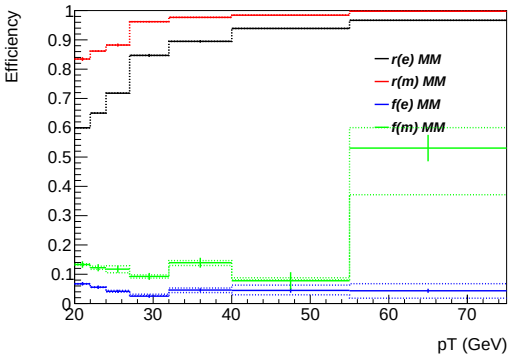

(c) $t\bar{t}Z$ lepton definitions, events with one b-jet

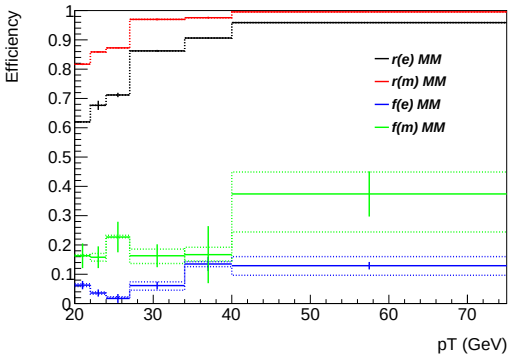

(d) $t\bar{t}Z$ lepton definitions, events with at least two b-jets

Figure 5.13: Fake and real lepton efficiencies as a function of the combined lepton's p_{T} [131]. The top and bottom rows show the efficiencies for the lepton definition of the $t\bar{t}W$ and $t\bar{t}Z$ regions, respectively. The left and right columns show the efficiencies for events with one or at least two b-jets. The entries include the statistical uncertainty only, while the dashed lines correspond to an up- and down-variation of the given signal process of 30%, as described in Section 5.4.1.

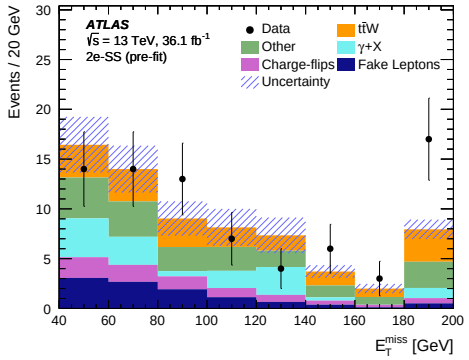

(a) All 2ℓSS ee regions combined

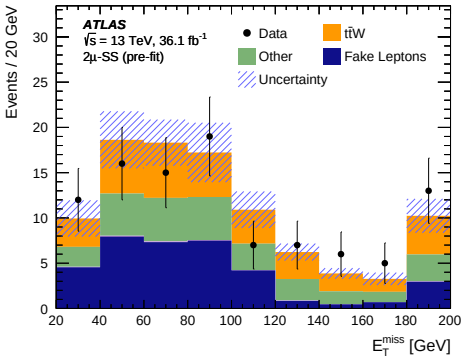

(b) All 2ℓSS $\mu\mu$ regions combined

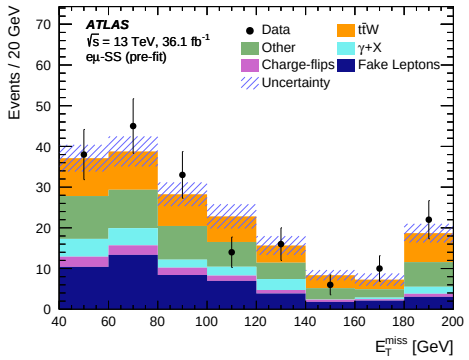

(c) All 2ℓSS $e\mu$ regions combined

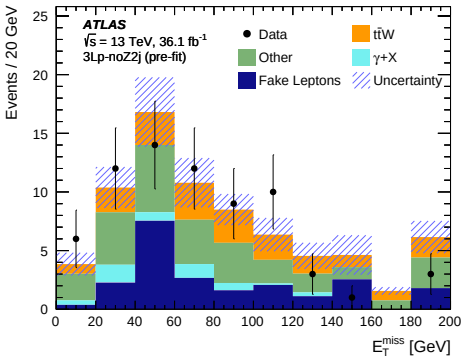

(d) All 3ℓ regions combined

Figure 5.14: Distributions of the missing transverse momentum in the $t\bar{t}W$ signal regions [9]. Each figure shows entries for multiple signal regions. Both, statistical and systematic uncertainties are included. Each of the distributions includes the under and overflow in the first and last bin, respectively.

5.4 Systematic uncertainties

The systematic uncertainties considered for analyses performed with the ATLAS experiment can roughly be split into two categories: The experimental uncertainties related to the ATLAS detector and common to all analyses and the theoretical uncertainties that rely on the set of processes relevant to the analysis. The second set of analysis includes uncertainties related to the simulation of physics processes as well as to any analysis techniques, like the fake lepton estimation.

5.4.1 Experimental uncertainties

Luminosity

The uncertainty on the integrated luminosity is derived from a calibration of the luminosity scale using $x-y$ beam-separation scans which were performed in 2015 and 2016 to determine the uncertainty when using the dataset of 36.1 fb^{-1}. A similar procedure that was used for the Run 1 dataset is shown in Reference [76]. The uncertainty was estimated to be 2.1% and is applied to all processes modeled by Monte Carlo simulation that enter the fit, except for processes whose normalizations are free parameters in the fit.

Pile-up reweighting

The correct pile-up profile of data is often difficult to model since it is not known when the Monte Carlo simulations are generated. Thus the pile-up distribution of the Monte Carlo generator is reweighted. An uncertainty for this pile-up reweighting is computed by performing a shape variation: The uncertainties on the number of reconstructed primary vertices, N_{PV}, and the dependence of the reconstructed jet kinematics on the number of inelastic pp interactions per bunch crossing, $<\mu>$, are considered in this variation. The shape variation is performed in two different ways. Either with "track-jets", where jets are reconstructed by using tracking information, or with "jet areas", where the area of the jet is defined and reconstructed with the transverse momentum density of the jet constituents [134, 135]. The pile-up reweighting uncertainty is assigned, using weights to each event and is applied to all processes modeled by Monte Carlo simulations.

Jet Vertex Tagger (JVT) Scale Factor

This uncertainty describes the efficiency to distinguish jets from pile-up and the hard scattering process. It is applied to the Monte Carlo scale factor of the jet vertex tagger algorithm (described in Section 4.1.2) and consists of three variations: The statistical uncertainty on the JVT scale factor is propagated, different generators are used to calibrate the algorithm using simulations of the Z+jets process, and the uncertainty on residual pile-up jets after applying the JVT algorithm is considered [103]. The JVT scale factor uncertainty is assigned using weights to all processes modeled by simulations.

Jet Energy Scale (JES) and Jet Energy Resolution (JER)

A total of twenty uncorrelated systematic variations are part of the JES uncertainties. The most important variations depend on the following parameters of jets: energy, flavour composition, pile-up, reconstruction at high momentum, pseudorapidity, and the imbalance of Z+jets and γ+jets events [136, 137].

The JER uncertainty is a single uncertainty estimated using events of Z+jets and γ+jets for low-p_{T} jets and dijet events for jets at high-p_{T} and η. The uncertainy derives from uncertainties in the calibration of

these events [138]. Both, the JES and JER uncertainties are derived using test-beam data, collision data and simulation and have a larger impact on jets with low p_T. The JES and JER uncertainties are applied to all processes modeled by Monte Carlo simulations and are assigned by varying the energy of all jets.

Flavour Tagging

The efficiency of tagging the flavour of each jet is measured separately for each flavour (b, c and light) using data and simulation. The uncertainties are considered uncorrelated between the jet flavours. Correction factors are determined to calibrate the tagging rates to match data using dedicated control samples. For b-jets, the uncertainties on the correction factors are estimated on observed and simulated b tagging rates in $t\bar{t}$ events in the dilepton channel [139]. For c-jets, a similar calibration is performed using W boson decays from $t\bar{t}$ events [140], while for light jets dijet events are used instead [105]. The uncertainties on the b- and c-tag efficiencies are estimated as a function of the jet p_T, employ seven variations for b- and four variations for c-jets and include bin-by-bin correlations. The uncertainties on the efficiency on tagging light jets are extracted as a function of the jet p_T and η and employ twelve variations. For b-jets with transverse momentum higher than the calibrated b-jets, an additional uncertainty is considered for the extrapolation to higher p_T. All uncertainties correspond to the working point 77% b-tagging efficiency [141] and are applied to each process modeled by simulation using event weights.

Electron selection

Electron selection uncertainties take the identification, isolation, reconstruction, trigger efficiency, and momentum scale and resolution into account. Scale factors and their uncertainties are derived to account for deviations of simulation and data. The scale factors are derived with a "*Tag and Probe method*", where the decay products of resonances are reconstructed as pairs of a tight (tag) and a loose (probe) object in events of $Z \to ee$ and $J/\psi \to ee$. Two cases are considered: the tag was reconstructed but the probe was not, or both were reconstructed. The data is fit to both shapes with the signal + background hypothesis and the ratio of the signal yield for both fits gives the efficiency of the object reconstruction. For the momentum scale and resolution the uncertainties are derived using the same events, examining the mass distribution of the resonances. The electron momentum is varied to compute the uncertainties. In addition, the ratio of deposited energy in the EM calorimeter and the momentum in the inner detector is determined in $W \to e\nu_e$ events and a scale factor with the corresponding uncertainty is computed. A description with more details can be found in References [98, 100, 142–144] for different periods of data taking at the LHC.

The uncertainties of all electron scale factors are applied to all processes modeled by simulation using event weights, while the uncertainties on the electron momentum scale and resolution are applied by varying the electron energy.

Muon selection

The uncertainties for the muon selection are uncorrelated to the electron uncertainties for all measurements within the ATLAS collaboration, but the same sources of uncertainties used for electrons are derived for muons as well. The scale factors and corresponding uncertainties for identification, isolation, reconstruction and trigger efficiency use the Tag and Probe method with the same events as the electrons, but requiring a muon pair in the decay of the resonances. However, the definitions of loose and tight muons differ from loose and tight electrons, since the reconstruction of muons happen in different detector systems, as described in Section 3.2.3. Therefore the uncertainty derived from $W \to \mu\nu_\mu$ events

is evaluated in the inner detector and the muon spectrometer. The muon scale and resolution uncertainties are derived from varying the muon energy and examining the mass peak of the resonances, as done for the electrons. The details on the Tag and Probe method and the scale and resolution uncertainties for muons is described in Reference [99]. The uncertainties on scale factors are applied as event weights, while scale and resolution uncertainties are estimated by varying the muon energy.

Fake Lepton Background

The estimation of the fake lepton background differs among the analysis channels. The fake factor method is used for the fake lepton background in the 4ℓ channel, as well as the $\gamma + X$ background (which includes $t\bar{t}\gamma$ and $Z + \gamma$ the processes) in the 3ℓ and 2ℓ-SS channels. The fake factor method derives four scale factors from a fit in $t\bar{t}$ and Z+jets control regions with a three lepton selection, depending on the source and flavour of the fake lepton. The uncertainties on the scale factors are estimated from the statistical uncertainties of the fit in the Z+jets and $t\bar{t}$ control regions, as described in Section 5.2.3. Only the uncertainty of the scale factor matching the type and source of the fake lepton is considered for that event.

The matrix method is used for the fake lepton background in the 3ℓ and 2ℓ-SS channels. Fake lepton efficiencies are measured in control regions with events with two real leptons or one real lepton and a photon conversion. A 30% uncertainty is assumed for this measurement of the efficiencies. In addition, the statistical uncertainty of the obtained fake lepton efficiencies is propagated. For the 3ℓ regions targeting $t\bar{t}Z$ a single nuisance per lepton flavour parameter is used, while for all regions targeting $t\bar{t}W$, this uncertainty uses multiple, parameterised in bins of the lepton p_{T}, per lepton flavour. Each nuisance parameter represents the maximum of the up and down shifts of the fake lepton efficiencies resulting from statistical uncertainties and the real-lepton background subtraction in the control regions used to measure the fake-lepton efficiency. Due to different lepton definitions in the regions targeting $t\bar{t}Z$ and $t\bar{t}W$, all uncertainties are assumed uncorrelated. The uncertainties resulting from the matrix method are applied as event weights on events with contributions of fake leptons.

Missing Transverse Momentum

Since a $E_{\mathrm{T}}^{\mathrm{miss}}$ requirement is imposed on several analysis regions, the uncertainties on $E_{\mathrm{T}}^{\mathrm{miss}}$ have to be considered. Systematic variations on the scale and resolution are considered. Both are estimated using $Z \to \mu\mu$ events in simulation and data, where no $E_{\mathrm{T}}^{\mathrm{miss}}$ contribution is expected. The imbalance of momentum of all reconstructed objects and the soft terms are calibrated as a function of the transverse momentum of the Z boson [107]. In total, there is one scale variation and two variations for the resolution considered. The uncertainties are applied to each process modeled by simulation, smearing the jet energy which is used to compute the soft term.

5.4.2 Modeling uncertainties

Signal

For the theoretical prediction of the signal processes, $t\bar{t}Z$ and $t\bar{t}W$, four sources of uncertainties have been considered: QCD scale, PDF, tune and choice of generator. The nominal generator MG5_aMC+Pythia8 is used with the `A14` tune and the NNPDF3.0NLOPDF for both signal processes.

The QCD renormalisation and factorisation scales, μ_R and μ_F are set to $\mu_R = \mu_F = m_{\mathrm{T}}/2$ [2]. This is

[2] Here, m_{T} is defined as the transverse mass, summing over all reconstructed objects: $\sqrt{p_{\mathrm{T}}^2 + m^2}$.

necessary to avoid divergences, since the strong coupling α_s is scale dependant. A variation of μ_R and μ_F by the factors 0.5 and 2 is performed. Since the two scales can both introduce divergencies, the variations are performed for both μ_R and μ_F independantly, as well as simultaneously. The resulting set of uncertainties is applied as an event weight.

The PDF uncertainty includes a variation of the eigenvector sets of the nominal PDF as well as a comparison to other PDF sets, following the description of Reference [145].

For the A14 tune variations of the parameters that affect colour reconnection, initial- and final-state radiations and parton interactions, are considered. The effect of multiple parton interactions dominates this uncertainty [146]. A description of the tunes available for Pythia 8 can be found in Reference [116]. This uncertainty is applied by using a separately generated sample and comparing it to the signal sample.

The nominal sample, generated with MG5_aMC+Pythia 8 is compared to a second sample, generated with Sherpa v2.2 at LO, including up to one (two) additional parton(s) in the matrix element for $t\bar{t}Z$ ($t\bar{t}W$). The sample is interfaced to the internal parton shower of Sherpa [147] and uses the same PDF as the nominal sample.

All signal modelling uncertainties for $t\bar{t}Z$ and $t\bar{t}W$ are treated as uncorrelated between $t\bar{t}Z$ and $t\bar{t}W$.

Diboson background

The diboson backgrounds are the dominant backgrounds in the $t\bar{t}Z$ 3ℓ and 4ℓ channels and a good modelling is crucial. Since all signal regions in those channels require at least one b-jet, which neither diboson process has at tree-level, a dedicated study is performed to estimate the diboson normalization and heavy flavour modelling uncertainties, called diboson theory uncertainty in the following. In addition, orthogonality from the ZZ control region to the signal regions in the 4ℓ channel is ensured by an $E_{\mathrm{T}}^{\mathrm{miss}}$ requirement, which is also covered by this uncertainty.

Several truth level samples with varying different generator parameters are generated with Sherpa:

- Renormalization scale: $\times 2$ and $\times 1/2$ (renorm4 and renorm025)
- Factorization scale: $\times 2$ and $\times 1/2$ (fac4 and fac025)
- Resummation scale (QSF parameter): $\times 2$ and $\times 1/2$ (qsf4 and qsf025)
- CKKW matching scale: nominal 20 GeV, variations setting it at 15 GeV and 30 GeV (ckkw15 and ckkw30)

To evaluate the diboson theory uncertainty, the yields in the signal and diboson control regions of the nominal and variation samples are estimated. The variation samples are normalised to the same cross section as the nominal diboson sample.

In order to have sufficient simulated events available, the selection of 4ℓ regions were modified as:

- Modified CR:
  exactly four leptons with at least one OSSF lepton pair, no b-jets and at most 40 GeVof $E_{\mathrm{T}}^{\mathrm{miss}}$. Each OSSF lepton pair is required to have an invariant mass of at least 15 GeV.
- Modified SR:
  The same selection as the modified CR but requiring exactly 1 b-jet.

Table 5.7 shows the yields obtained in the modified 4ℓ regions. With these yields, the ratio between the modified signal and control regions are computed, which are denoted as transfer factors. These transfer

factors are used to evaluate the uncertainty on the transition from 0 to multiple b-jets. The relative difference to the nominal sample is computed for each variation, using the largest relative difference among the up- and down-variations. The relative differences are shown in Table 5.8; the total uncertainty is calculated as the quadratic sum of the individual contributions. In conclusion, the theory uncertainty for the ZZ background is found to be 21% or 42% in the 4ℓ-1b or 4ℓ-2b regions, respectively.

Sample	Modified CR	Modified SR
Nominal	1721 ± 15	32.7 ± 1.4
fac4	1513 ± 24	26.1 ± 3.0
fac025	1884 ± 27	33.3 ± 3.5
renorm4	1716 ± 29	33.6 ± 3.2
renorm025	1674 ± 29	34.2 ± 3.6
qsf4	1749 ± 28	35.0 ± 3.9
qsf025	1688 ± 32	37.2 ± 3.4
ckkw15	1625 ± 30	34.5 ± 3.6
ckkw30	1827 ± 25	37.7 ± 4.8

Table 5.7: Yields from diboson nominal and variation samples of the ZZ background at truth level in the modified 4ℓ control and signal regions. The uncertainties only cover the limited sample size.

Table 5.8: Largest relative difference of the transfer factors to the nominal sample per systematic variation for the ZZ background in the 4ℓ regions.

Variation	max. relative difference
fac	10%
renorm	7.1%
qsf	13%
ckkw	10%
total	21%

A similar procedure is performed for the 3ℓ $t\bar{t}Z$ regions to evaluate the WZ theory uncertainty. Here, the available sample size allowed to compute the transfer factors for each signal region separately; the result can be seen in Table 5.9.

	3ℓ-Z-2b4j	3ℓ-Z-1b4j	3ℓ-Z-2b3j	3ℓ-noZ-2b
fac	5%	14$	5%	9%
renorm	25%	10$	18%	16%
qsf	40%	7$	29%	32%
ckkw	16%	24$	29%	21%
Total	50%	30$	45%	42%

Table 5.9: Largest relative difference of the transfer factors to the nominal sample per systematic variation for the WZ background in the 3ℓ regions [131].

For the $t\bar{t}W$ regions, a normalisation uncertainty of 30% on the diboson background is used.

$t\bar{t}H$ background

Two uncertainties are considered for the $t\bar{t}H$ background: a normalisation uncertainty of +5.8% and −9.2%, which corresponds to the scale and α_s uncertainties in the NLO cross section computation, and a PDF uncertainty of 3.6%. The $t\bar{t}H$ sample was generated with the same generator and settings as the signal sample and the scale and PDF uncertainties are evaluated accordingly [146].

tWZ background

A 10% normalization uncertainty is assigned to the tWZ background, where an interference effect between diagrams of tWZ at NLO and $t\bar{t}Z$ at LO, is taken into account [148].

In addition a comparison of two different parton showers, MG5_aMC+Pythia 8 (nominal) against MG5_aMC+Herwig++, is performed and quoted as tWZ shower uncertainty.

Other backgrounds

Other backgrounds, which include processes like $3t$, $4t$, triboson production or $t\bar{t}WW$, are assigned a flat uncertainty of 50%. Since these backgrounds are negligible, this uncertainty has a small impact on the measurement.

5.4.3 Sample size

The amount of events generated for any simulated sample is limited, typically ranging between $10^5 - 10^7$ events. The statistical uncertainty of the amount of events entering in a given region for each simulated processes is covered by this uncertainty and it is commonly referred to as "*gamma*". For this analysis, a single uncertainty is evaluated per bin in each region, summing the contribution from each simulated process, taking correlations accross the processes into account.

For data-driven backgrounds, used in the 2ℓOS and all $t\bar{t}W$ channels, separate uncertainties are considered for the limited amount of data in the control regions where these data-driven backgrounds are evaluated.

5.5 Fit

The analysis makes use of a profile likelihood fit, done with the TRexFitter package [149], which uses the HistFactory toolkit [150] to produce the workspace of the fit and calculate the likelihood function. The implementation is based on RooStats [151] and RooFit [152] and works in a similar manner as HistFitter [153].

The profile likelihood fit treats the signal strength μ, the normalisations of backgrounds and systematic uncertainties as free parameters. The signal strength for the $t\bar{t}Z$ process is defined as the ratio of the measured cross section to the SM expectation, as shown in Equation 5.2.

$$\mu_{t\bar{t}Z} = \frac{\sigma_{t\bar{t}Z}}{\sigma_{t\bar{t}Z}^{\mathrm{SM}}} \tag{5.2}$$

The systematic uncertainties, discussed in the previous section, enter the fit as "*nuisance parameters*" (NPs). They are included in the likelihood with a Gaussian probability density function, taking into

account correlations among the NPs. Most NPs are commonly estimated by the fit as a single parameter; the "gammas" are introduced per analysis region instead. The probability density function (or likelihood function), that is maximised during the fit can be seen in Equation 5.3.

$$L(\boldsymbol{n}, \boldsymbol{\theta}^0 \,|\, \mu, \boldsymbol{\theta}) = \prod_{i \in \text{Bins}} P(n_i \,|\, \lambda(\mu S(\boldsymbol{\theta}) + B(\boldsymbol{\theta}))) \times \prod_{j \in \text{NP}} G(\theta_j^0 \,|\, \theta_j) \tag{5.3}$$

In Equation 5.3, the likelihood function has a Poissonian and a Gaussian term, vectors are written in boldface. $P(n_i \,|\, \lambda(\mu S(\boldsymbol{\theta} + B(\boldsymbol{\theta})))$ represents the Poissonian distributions of the observed events n in bins of i. The fit usually includes multiple signal and control regions, each having their own set of bins, that are included in the product over all bins i. The Poissonian distributions depend on the signal strength μ and the background normalisations B, which each depend on the set of NPs $\boldsymbol{\theta}$. The profile likelihood ratio λ will be explained further below. $G(\theta_j^0 \,|\, \theta_j)$ is the Gaussian distribution for every NP j. θ^0 is the initial value of a given NP, while θ is the deviation from the initial value. A Gaussian distribution of $G(\theta^0 - \theta)$ is evaluated, such that a deviation of ± 1 corresponds to a shift of the systematic uncertainty of $\pm 1\sigma$. Most NPs have an initial value θ^0 of 0; exceptions are NPs that enter the fit as event weights, such as the "*gammas*" or scale factors. The TRexFitter package also allows the usage of Poissonians or gamma functions for the NPs; but this functionality is not used in the analysis.

Using this likelihood function allows to optimize the sensitivity by constraining systematic uncertainties. As a result it is possible to have systematic uncertainties "*pulled*" to higher or lower values as predicted by the simulation. In those instances the pulls need to be inspected and checked for motivation through the underlying physics. A more detailed explanation of how the likelihood function is constructed and how the significance is used is made in the following, closely following Reference [154]

The term significance and sensitivity are used equivalently, when quoting the results of the analysis in the following sections. The significance Z is calculated by assuming the null, or "*background-only*" hypothesis H_0. In the community of particle physics it was established that the rejection of the null hypothesis with a significance of 3 standard deviations, or 3σ, is regarded as evidence, while 5σ is regarded as a discovery. In addition to H_0, a signal-plus-background hypothesis H_1, also called "*alternative*" hypothesis, can be made. In order to exclude a given signal hypothesis, a significance under the H_1 assumption of $Z = 1.64$ is required, which corresponds to a 95% confidence level (C.L.). The signal strength μ that corresponds to the hypotheses H_0 and H_1 is 0 and 1, respectively.

In order to test the likelihood function shown in Equation 5.3, the profile likelihood ratio is considered:

$$\lambda(\mu) = \frac{L(\mu, \hat{\hat{\boldsymbol{\theta}}}(\mu))}{L(\hat{\mu}, \hat{\boldsymbol{\theta}})} \tag{5.4}$$

In this equation, $\hat{\hat{\boldsymbol{\theta}}}$ is the value of θ that maximises the likelihood function L for the given signal strength μ. This likelihood is called conditional maximum-likelihood (ML). The likelihood function is the unconditional maximum-likelihood instead, where $\hat{\boldsymbol{\theta}}$ is independent of μ. This ratio is different from 1, due to the effect of the systematic uncertainties on the measurement, where information of μ can be lost. Here, $\hat{\mu}$ is allowed to be negative, as long as $P(n_i \,|\, \mu S(\boldsymbol{\theta}) + B(\boldsymbol{\theta})) > 0$ and $0 < \lambda < 1$ remain true. Finally, the ratio is transformed to the test statistic $t_\mu = -2 \ln \lambda(\mu)$, which is a measure of the incompatibility between μ and data, where t_μ and said incompatibility have a linear relation. This transformation is made such that a decrease relative to the best estimate of t_μ by 0.5 defines the 68% C.L. error-band.

From t_μ, the p-value, a measure of discrepancy between data and a given hypothesis, can be computed:

$$p_\mu = \int_{t_\mu}^{\infty} f(t_\mu | \mu) \, \mathrm{d}t_\mu \tag{5.5}$$

Here, $f(t_\mu|\mu)$ is the probability density function, assuming the signal strength μ. Having defined the p-value, the significance is given as:

$$Z = \Phi^{-1}(1-p) \tag{5.6}$$

Both the relation of the p-value to the test statistic t_μ as well as to the significance Z is illustrated in Figure 5.15. Here, $\phi(x) = 1/\sqrt{2\pi}\exp(-x^2/2)$ is the standard Gaussian distribution.

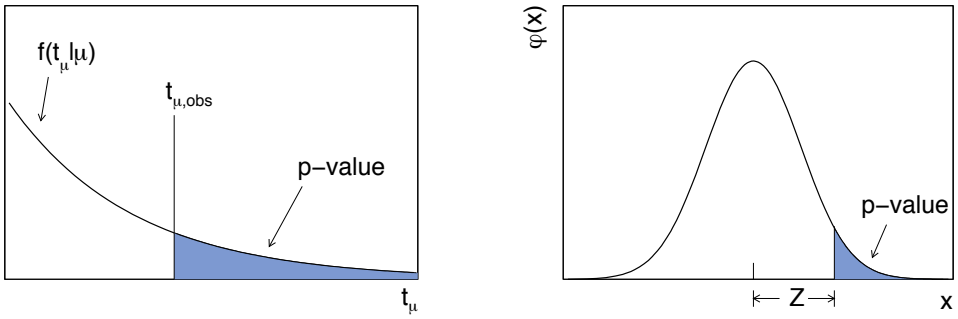

Figure 5.15: Relation of the p-value to the test statistic t_μ (left) and the significance Z (right) [154].

In the case of a discovery the aim is to reject the hypothesis H_0 with $\mu = 0$, by finding $\mu > 0$. In this scenario the test statistic is defined as:

$$t_\mu \equiv q_0 = \begin{cases} -2\ln\lambda(0) & \text{for } \hat{\mu} \geq 0, \\ 0 & \text{for } \hat{\mu} < 0. \end{cases} \tag{5.7}$$

Here, $\lambda(0)$ is the profile likelihood ratio with $\mu = 0$. If the signal strength $\hat{\mu}$ that maximises the likelihood is found to be negative, the data fluctuated such that the measurement showed less events than predicted by the background only, which could be described by systematic errors. The higher $\hat{\mu}$, the larger the test statistic q_0 becomes, which increases the incompatibility between the data and the H_0 hypothesis. Correspondingly, one can define the p-value and the significance for this scenario:

$$\begin{aligned} p_0 &= \int_{q_0}^{\infty} f(q_0|0)\,\mathrm{d}q_0, \\ Z_0 &= \Phi^{-1}(1-p_0) \end{aligned} \tag{5.8}$$

Similar considerations can be made in the case of setting an upper limit, instead of having a discovery, in which case the test statistic t_μ is required to fulfill $\hat{\mu} \leq \mu$.

Finally, in order to compute the p-value for any given hypothesis, a sampling of the test statistic is necessary. This is done by relying on several pseudo-experiments. A different probability density function $f(q_\mu|\mu')$ is defined, with $\mu' \neq \mu$, not relying on actual data. This distribution $f(q_\mu|\mu')$ can be found by using an approximation of A. Wald [155]:

$$t_\mu = -2\ln\lambda(\mu) = \frac{(\mu-\hat{\mu})^2}{\sigma_\mu^2} + O(1/\sqrt{N}). \tag{5.9}$$

In this approximation $\hat{\mu}$ follows a Gaussian distribution with mean μ' and standard deviation σ_μ. The

standard deviation is obtained from the covariance matrix of all nuisance parameters including μ itself. If the extra term $O(1/\sqrt{N})$ is neglected, Equation 5.9 resembles a χ^2 distribution with one degree of freedom, which is defined as:

$$f(t_\mu, \Lambda) = \frac{1}{2\sqrt{t_\mu}} \frac{1}{\sqrt{2}} \left[\exp\left(-\frac{1}{2} \left(\sqrt{t_\mu} + \sqrt{\Lambda} \right)^2 \right) + \exp\left(-\frac{1}{2} \left(\sqrt{t_\mu} - \sqrt{\Lambda} \right)^2 \right) \right], \quad \Lambda = \frac{(\mu - \mu')^2}{\sigma_\mu^2}. \tag{5.10}$$

Here, Λ is the non-centrality parameter of $f(t_\mu, \Lambda)$, which becomes zero in the case of $\mu = \mu'$. In this case, t_μ becomes a (regular) χ^2 test with one degree of freedom [156]. To ensure that the pseudo-experiments maximise the likelihood an "*Asimov*" dataset is used, where $\hat{\mu} = \mu'$ and $\hat{\boldsymbol{\theta}} = \boldsymbol{\theta}$ are assured, by using the approximation given in Equation 5.9. Thus a single Asimov dataset is able to replace multiple pseudo-experiments. This is used in the analysis to determine the expected significance and signal strength.

5.6 Results

This section shows the results of the cross section measurement of $t\bar{t}Z$ with the dataset of 36.1 fb^{-1}. It is divided into three parts. First, the results in the 4ℓ channel are presented, which is the channel this thesis contributed to the most. In Section 5.6.2 the combination of all channels sensitive to the $t\bar{t}Z$ process is shown. Finally, the two dimensional fit to extract both cross sections, of $t\bar{t}W$ and $t\bar{t}Z$, is discussed in Section 5.6.3.

For each channel two fits are performed: A fit using an Asimov dataset and the fit using data. The first fit is performed before the "*unblinding*" takes place, which means before data is used in any of the signal regions, to avoid any bias in the choice of event selection, fake lepton estimation or simulated samples towards the agreement of data and simulation. However, the agreement between data and simulation is checked in the control and validation regions, to verify a good understanding of the backgrounds and detector effects. The signal strength using an Asimov dataset is fixed to the SM prediction ($\mu = 1$). The nuisance parameters can be constrained by the fit but will not be pulled in any direction without including data. This procedure ensures to isolate any possible deviations from the Standard Model when including data in the signal regions. The fit results are summarized as expected and observed fit results for the fit with an Asimov dataset or actual data, respectively.

5.6.1 4ℓ only fit

This fit includes the 4 signal regions 4ℓ-SF-1b, 4ℓ-SF-2b, 4ℓ-DF-1b, 4ℓ-DF-2b and the ZZ control region. Each of those regions are treated as a single bin in the fit. Thus, a total of 5 "*Gammas*", the parameters to describe the limited sample size, are evaluated.

Expected fit results

For this fit all regions included in the fit, 4ℓ-SF-1b, 4ℓ-SF-2b, 4ℓ-DF-1b, 4ℓ-DF-2b and the ZZ control region, were "*blinded*", using an Asimov dataset. Prior to performing this fit a good agreement between data and simulation was found in the ZZ control region, as described in Section 5.2.

The fit results are:

$$\begin{aligned} \mu_{t\bar{t}Z} &= 1\ ^{+0.26}_{-0.23}\,(\text{stat.})\ ^{+0.10}_{-0.08}\,(\text{syst.}), \\ \text{norm}_{ZZ} &= 1 \pm 0.09\,(\text{stat.}) \pm 0.17\,(\text{syst.}), \end{aligned} \tag{5.11}$$

showing that the statistical uncertainty dominates the signal strength, while sufficient events are available to estimate the normalization for the ZZ background. This is discussed in more detail in the next section. An overview of how all nuisance parameters are constrained by the 4ℓ only fit is shown in Figure 5.16. The green and yellow band represent the 1 and 2σ deviation of the Gaussian distribution of a given NP. The black error bars correspond to the 1σ deviation of the post-fit Gaussian distribution. In most cases the green area overlaps with the black bars perfectly. For some nuisance parameters, like "*b-tag Eigenvar 1*", the post-fit Gaussian is slightly smaller, showing that the fit is able to constrain that nuisance parameter. For the "*Gammas*" shown in Figure 5.16, the width of the band corresponds to the statistical uncertainty arising from the limited sample size only. The correlations among the nuisance parameters with a threshold of at least 15% correlation, are shown in Figure 5.17(a). It can be seen that the largest correlations are found between nuisance parameters related to $E_{\text{T}}^{\text{miss}}$ (or JER) and the normalisation of the ZZ background, which is due to the $E_{\text{T}}^{\text{miss}}$ requirement in the selection of the ZZ control region or the SF signal regions, where the ZZ background contributes. The correlation between the "*JER*" nuisance parameter and the ZZ background normalization can be explained with the different jet composition in the control and signal regions. Finally, Figure 5.17(b) shows a ranking of the nuisance parameters that have the highest impact on the signal strength μ. This is evaluated using four different fit setups for each nuisance parameter: The initial value of each nuisance parameter is shifted up or down by 1σ in the simulated samples. This is done using the pre- and post-fit uncertainties, which are found in Figure 5.16 as the green band or the black error bar, respectively. Thus the impact $\Delta\mu$ is calculated for pre- and post-fit and sorted starting from the nuisance parameter with the largest $\Delta\mu$ in Figure 5.17(b). The three highest ranked nuisance parameters are related to flavour tagging, signal modelling and electron reconstruction. For the experimental part, flavour tagging is required in all signal regions and lepton reconstruction is exponentially more important, the more leptons are in a given event. The highly ranked $t\bar{t}Z$ generator uncertainty reflects the sub-optimal choice of comparing the NLO sample generated by MG5_aMC+Pythia 8 to a LO sample generated by Sherpa, as described in Section 5.4.2.

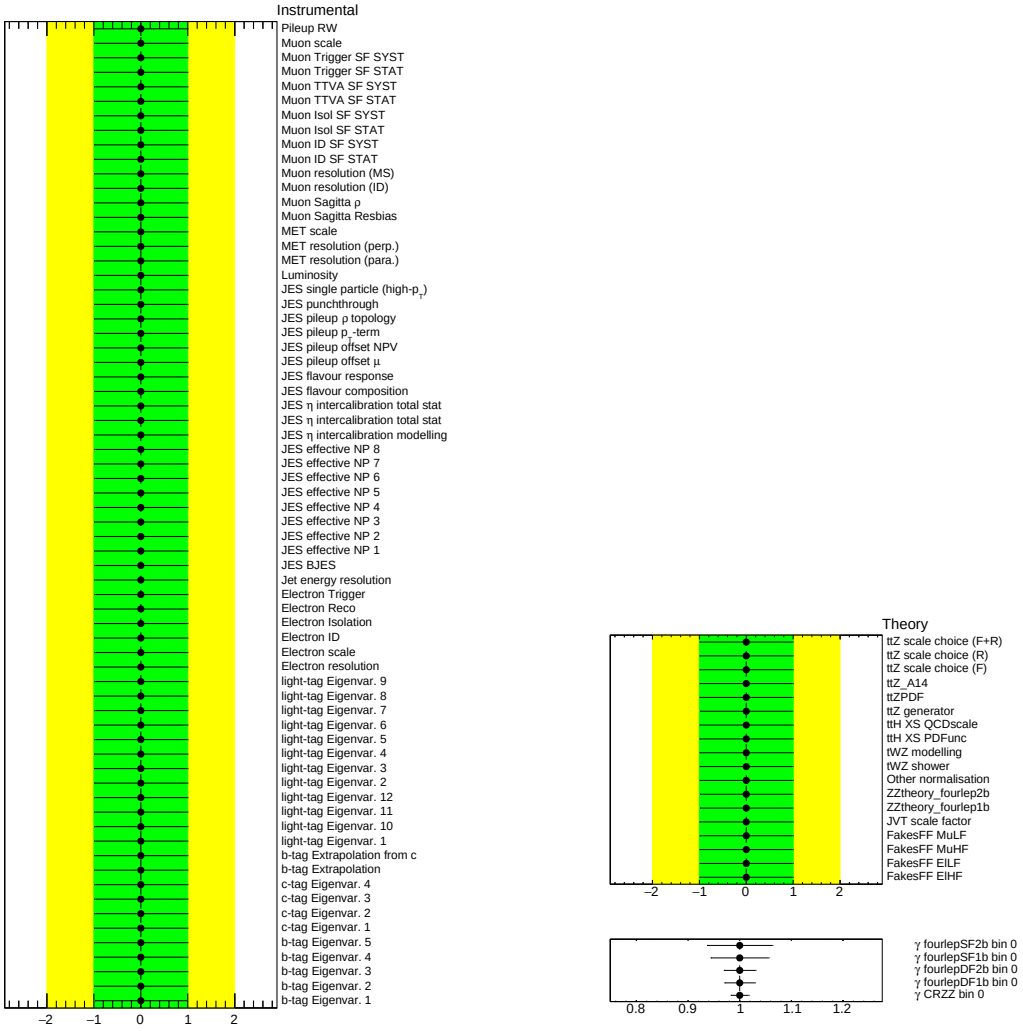

Figure 5.16: Nuisance parameters from the 4ℓ fit using an Asimov dataset. The left figure shows the detector related uncertainties, while the nuisance parameters on the top right figure are related to signal and background modelling. The bottom right figure shows the "*Gammas*" that are related to the limited amount of events used to simulate the signal and backgrounds, computed per region.

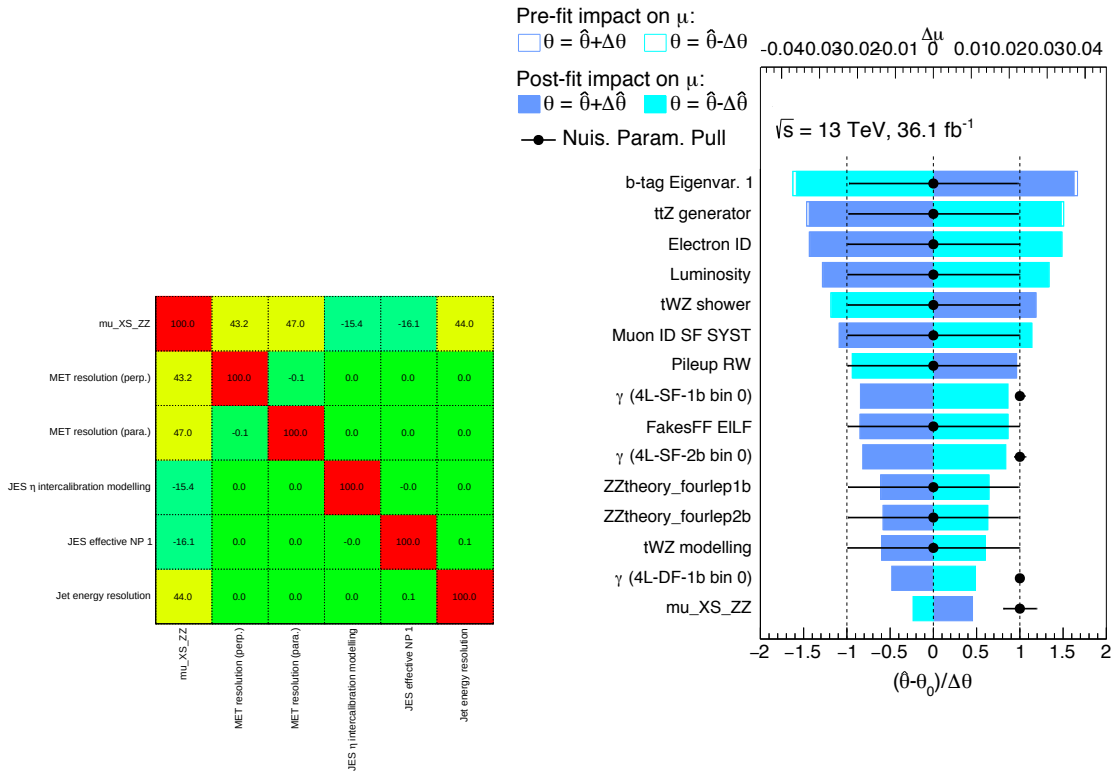

(a) Correlations

(b) Ranking of NPs

Figure 5.17: The correlations between nuisance parameters (left) and the ranking of NPs (right) in the 4ℓ fit using an Asimov dataset. Only correlations that exceed a threshold value of 15% and the 15 NPs with the highest impact on $\Delta\mu_{t\bar{t}Z}$ are shown.

Fit to data

The obtained signal strength extracted from the fit to data, performed in the 4ℓ channel is:

$$\mu_{t\bar{t}Z} = 1.21\ ^{+0.28}_{-0.25}\,(\text{stat.})\ ^{+0.11}_{-0.12}\,(\text{syst.}), \tag{5.12}$$

with an observed (expected) significance of 5.7σ (5.1σ). The normalization of the ZZ background was used as a free parameter in the fit and is found to be $\mu_{ZZ} = 0.94 \pm 0.18$. Thus the results are compatible with the prediction of the Standard Model. Since the total number of observed events in the four signal regions is 48, as shown previously in Table 5.3, the statistical uncertainty dominates the signal strength. The event yields, after the fit has been performed are shown in Table 5.10.

	4ℓ-SF-1b	4ℓ-SF-2b	4ℓ-DF-1b	4ℓ-DF-2b	4ℓ-ZZ-CR
$t\bar{t}Z$	8.00 ± 1.98	7.33 ± 1.73	8.89 ± 2.18	7.04 ± 1.71	0.15 ± 0.07
ZZ	2.21 ± 0.62	1.05 ± 0.53	0.18 ± 0.07	0.00 ± 0.01	137.43 ± 15.09
tWZ	1.61 ± 0.49	0.57 ± 0.29	1.57 ± 0.37	0.52 ± 0.28	0.06 ± 0.06
$t\bar{t}H$	0.58 ± 0.08	0.61 ± 0.10	0.67 ± 0.08	0.57 ± 0.09	0.01 ± 0.01
Other	0.12 ± 0.04	0.09 ± 0.04	0.20 ± 0.07	0.10 ± 0.03	0.51 ± 0.50
Fake leptons	1.90 ± 1.06	1.25 ± 0.83	0.93 ± 0.20	0.39 ± 0.14	6.82 ± 8.63
Total	14.41 ± 2.22	10.90 ± 1.94	12.46 ± 2.14	8.63 ± 1.69	144.91 ± 12.88
Observed	18	14	11	5	144
Data/MC	1.25 ± 0.18	1.28 ± 0.22	0.88 ± 0.15	0.58 ± 0.12	0.99 ± 0.09

Table 5.10: The expected and observed events after the fit has been performed, in the four 4ℓ signal regions and control region for an integrated luminosity of 36.1fb^{-1}. Both, statistical and systematic uncertainties are included. Processes included in "Other" are triboson, $t\bar{t}WW$, and 4 tops. All predictions are split into events with real and fake leptons. Events with fake leptons are scaled by the fake factors. Processes are included in "Fake leptons", if they have at least one lepton candidate identified as fake.

A summary of all regions included in the fit, before and after the fit has been performed, is shown in Figure 5.18. A breakdown of all uncertainties is given in Table 5.11, where the systematic uncertainties are summarized into categories and symmetrized. It is shown that the largest sources of systematic uncertainties arise from object reconstruction, signal modeling and background normalizations. The first category sums a large amount of contributions (electrons, muons, missing transverse momentum and jet related uncertainties). The importance of the signal modeling is reflected in Figure 5.20, discussed later, as well. The background normalization is related to the uncertainty of the ZZ normalizations, which is constrained due to the limited amount of events in a 4ℓ selection.

An overview of all nuisance parameters and how they were constrained by the 4ℓ fit is shown in Figure 5.19, along with possible pulls. It can be seen that pulls are visible for the "*ttZ Generator*", "*Jet energy resolution*", "*tWZ shower*", "*FakesFF ElLF*" and both the "*ZZtheory*" nuisance parameters. However, all of those are well within the 1σ band of the pre-fit Gaussian distribution; the strongest pull is seen by the "*ttZ Generator*" nuisance parameter.

To get a full picture, Figure 5.20 shows the nuisance parameters with the highest impact on $\Delta\mu_{t\bar{t}Z}$, where the pulls are also visible. Comparing it to the same figure obtained from the fit with an Asimov dataset, the order of the nuisance parameters slightly changed, which is expected with a signal strength of 1.21, where the fit does constrain nuisance parameters differently as with $\mu = 1$. In total, the "*ttZ*

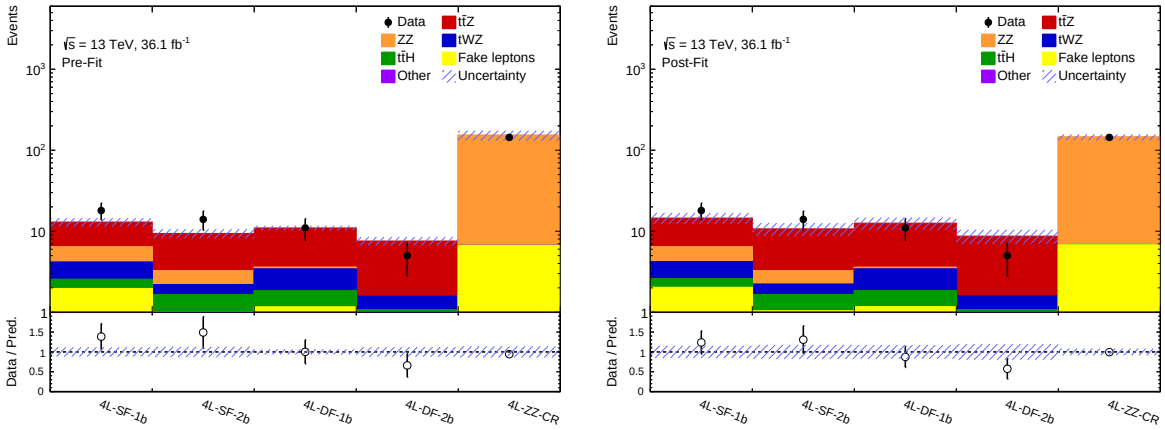

(a) Pre-fit

(b) Post-fit

Figure 5.18: Regions included in the 4ℓ fit before and after the fit has been performed. Both, statistical and systematic uncertainties are included.

Generator" nuisance parameter has the highest impact on $\Delta\mu_{t\bar{t}Z}$ and shows the largest pull (which is still reasonably small). The correlations among the NPs are similar to the correlations of the fit with an Asimov dataset, show in Figure 5.17(a) and have been discussed already.

Figure 5.21 shows the impact of this nuisance parameter per signal region for the signal process only for three different parameterisations: a single bin as it is used in the fit, as a function of the number of jets or as a function of the number of b-tagged jets in the event. The dashed cross shows the nominal $t\bar{t}Z$ prediction, which is modeled by MG5_aMC+Pythia 8, while the nominal value of the given nuisance parameter along with the $\pm 1\sigma$ shift is indicated by the straight lines in black and red/blue, respectively. The latter corresponds to the $t\bar{t}Z$ prediction modeled by Sherpa for this nuisance parameter. It can be seen that the alternative $t\bar{t}Z$ generator Sherpa predicts less events in the first bin of the number of jet distribution. Thus the impact on $\Delta\mu_{t\bar{t}Z}$ of this nuisance parameter can be traced to modelling issues of Sherpa for events with 1-2 jets and it has the highest impact in the 4ℓ-DF-2b signal region. Aside from that it should be noted that the largest impact on $\Delta\mu_{t\bar{t}Z}$ comes from the limited observed events in the 4ℓ channel.

The cross section extracted from the 4ℓ fit is:

$$\begin{aligned}\sigma^{4\ell}_{t\bar{t}Z} &= 1065^{+279}_{-249}\,(\text{stat.})^{+104}_{-87}\,(\text{syst.})\,\text{fb}, \\ &= 1065^{+298}_{-264}\,\text{fb}.\end{aligned} \tag{5.13}$$

This result uses the NLO prediction in QCD and EW of $\sigma_{t\bar{t}Z} = 880\,\text{fb}$, that includes all possible Z boson decays and contributions with an off-shell Z^* or γ^* [54].

$\mu_{t\bar{t}Z}$	1.21
Other object-related	4.6%
Signal modelling	3.8%
Background normalizations	3.8%
Flavour tagging	3.6%
Modelling of backgrounds from simulation	3.6%
Luminosity	2.8%
Fake lepton estimation	2.4%
Background cross section	1.7%
JES/JER	0.9%
Simulated sample statistics ("*Gammas*")	0.7%
Statistical uncertainty	23%
Total systematic uncertainty	9.7%
Total	25%

Table 5.11: Impact of the uncertainties on $\Delta\mu_{t\bar{t}Z}$ in the 4ℓ channel. The uncertainties are symmetrized and presented as relative uncertainties on the signal strength $\mu_{t\bar{t}Z}$.

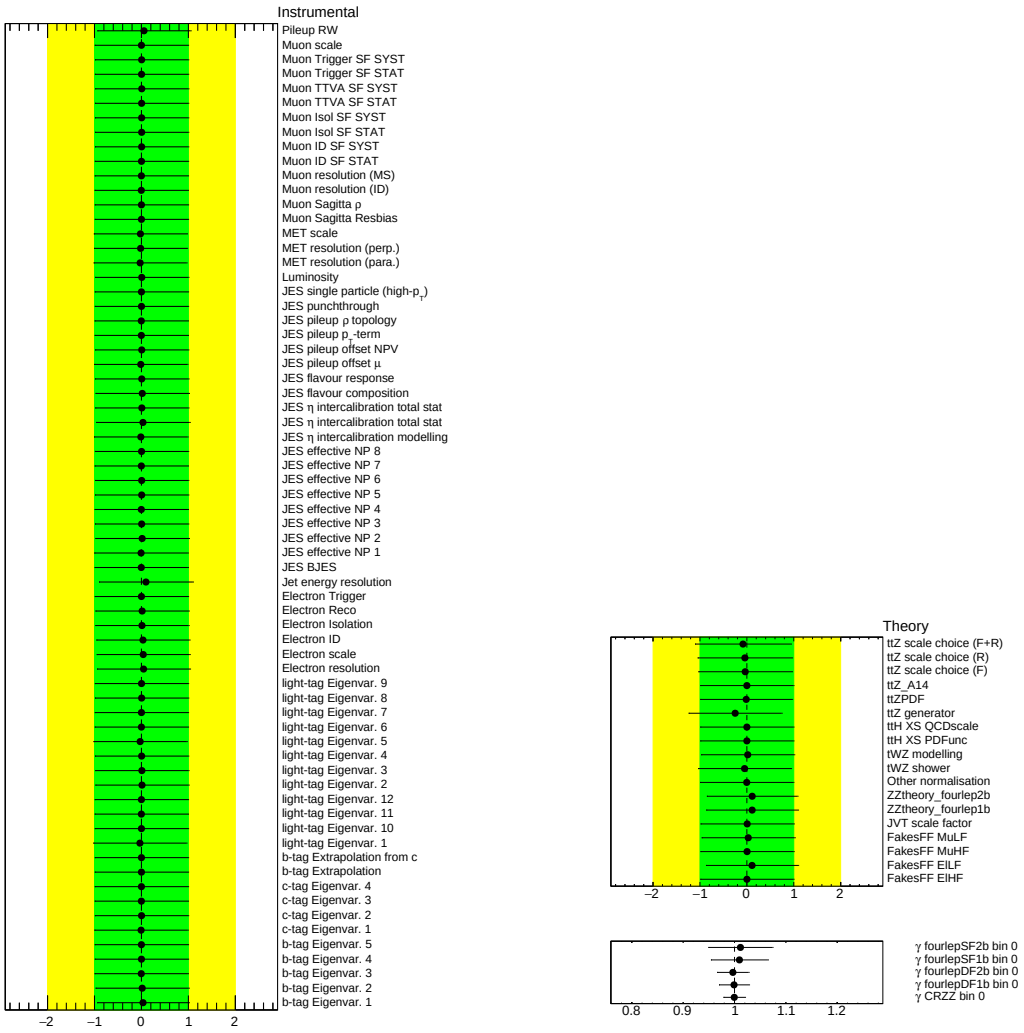

Figure 5.19: Obtained nuisance parameters from the 4ℓ fit under the signal-plus-background hypothesis. The left figure shows the detector related uncertainties, while the nuisance parameters on the top right figure are related to signal and background modelling. The bottom right figure shows the "*Gammas*" that are related to the limited number of events used to simulate the signal and backgrounds, computed per region.

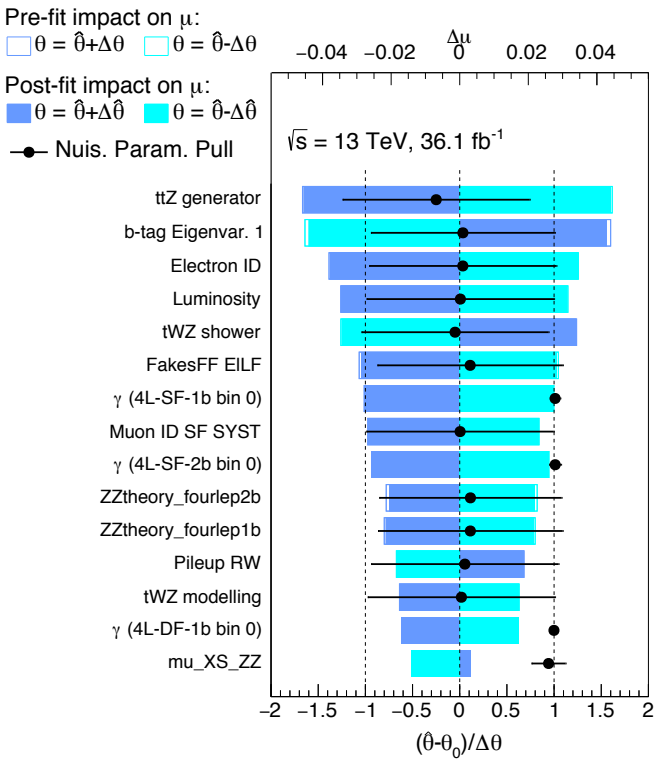

Figure 5.20: The ranking of the NPs in the 4ℓ fit. Only the 15 nuisance parameters with the highest impact on $\Delta\mu_{t\bar{t}Z}$ are shown.

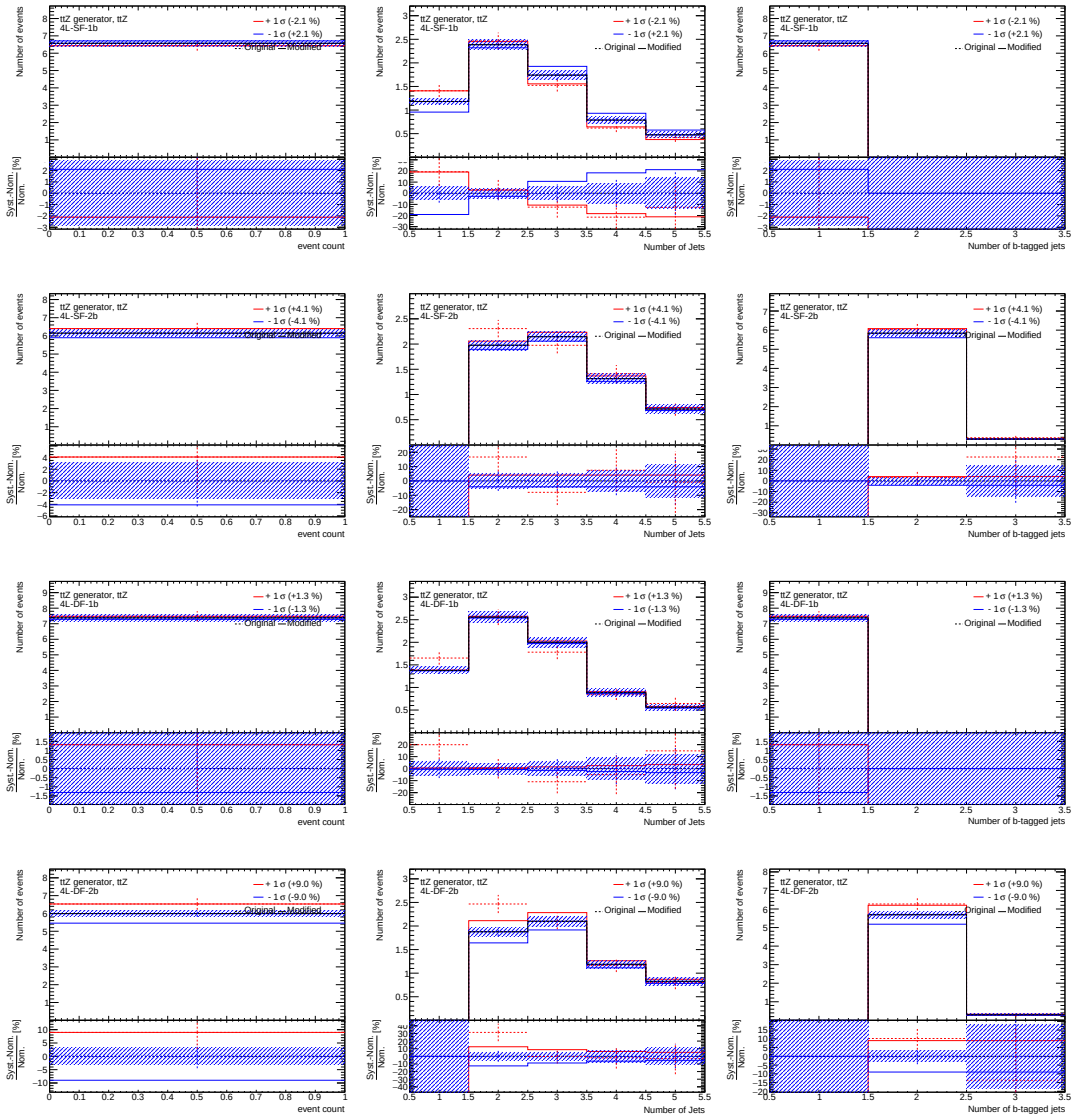

Figure 5.21: Effect of the $t\bar{t}Z$ generator nuisance parameter variation for different distributions (left: event yield, centre: number of jets, right: number of b-tagged jets) in the 4ℓ signal regions (from top to bottom: 4ℓ-SF-1b, 4ℓ-SF-2b, 4ℓ-DF-1b, 4ℓ-DF-2b), compared to data.

5.6.2 Combined $t\bar{t}Z$ fit results

In this section the combination of the 2ℓOS, 3ℓ and 4ℓ channels, that are all sensitive to the $t\bar{t}Z$ process is shown. The significance in each of those channels is shown in Table 5.12 and shows that the 3ℓ provides the highest significance. As mentioned before, the significance is calculated assuming the null hypothesis H_0. Both the 3ℓ and 4ℓ channels managed to exceed the threshold to claim a discovery.

Channel	Expected significance	Observed significance
2ℓOS	3.8σ	3.0σ
3ℓ	6.4σ	7.2σ
4ℓ	5.1σ	5.7σ
$t\bar{t}Z$ combination	8.4σ	8.9σ

Table 5.12: Expected and observed significance obtained from each channel and the $t\bar{t}Z$ combination [131].

Figure 5.22(a) shows the signal strength extracted from the fit in individual channels as well as the signal strength of the combined $t\bar{t}Z$ fit. While the 2ℓOS and 4ℓ channels have a signal strength below and above one, the combination yields a results very close to the Standard Model prediction. A comparison of the uncertainties show that the combination of the three channels is able to reduce the total uncertainty by ~20% compared to the 3ℓ only fit.

The ranking of the nuisance parameters with the highest impact on $\Delta\mu_{t\bar{t}Z}$ is shown in Figure 5.22 and shows that the previously discussed uncertainties related to flavour tagging and $t\bar{t}Z$ modelling have a large impact on the combined result as well. In addition, the uncertainty to describe the heavy flavour modelling in the WZ process (described in Section 5.4.2 for the ZZ process) plays an important role. The latter nuisance parameter does benefit from more data, since the estimation of the uncertainty will improve if more events of the diboson background are available with b-jets.

Compared to the 4ℓ channel, some nuisance parameters in Figure 5.22 are pulled significantly. This is expected, since the systematic uncertainty has a higher impact on the $t\bar{t}Z$ result in this combination. A lot of these pulled nuisance parameters are pulled in the 3ℓ fit as well, and have been studied there. Figure 5.23 shows the normalisation of the data driven backgrounds obtained from the individual fits and how they change in the combined $t\bar{t}Z$ fit. The normalisation of the ZZ background shows a large change from the 4ℓ channel compared to the combined $t\bar{t}Z$ fit. This is due to the "*Jet energy resolution*" nuisance parameter that has a high correlation with the normalization of the ZZ background and is pulled to a higher value in the fit. Investigations showed that this pull is coming from the fit in the 2ℓOS channel.

A breakdown of the uncertainties can be seen in Table 5.13, which shows that the systematic uncertainty is slightly higher than the statistical uncertainties. Therefore future measurements of the $t\bar{t}Z$ cross section will not be able to improve the result much further without improving the systematic error.

The fit results in terms of the cross section $\sigma_{t\bar{t}Z}$ in the combined $t\bar{t}Z$ fit is:

$$\begin{aligned}\sigma_{t\bar{t}Z} &= 927^{+105}_{-95}\,(\text{stat.})^{+115}_{-112}\,(\text{syst.})\,\text{fb},\\ &= 927^{+155}_{-147}\,\text{fb}.\end{aligned} \tag{5.14}$$

This result uses the NLO prediction in QCD and EW of $\sigma_{t\bar{t}Z} = 880\,\text{fb}$ [54], as discussed in the previous

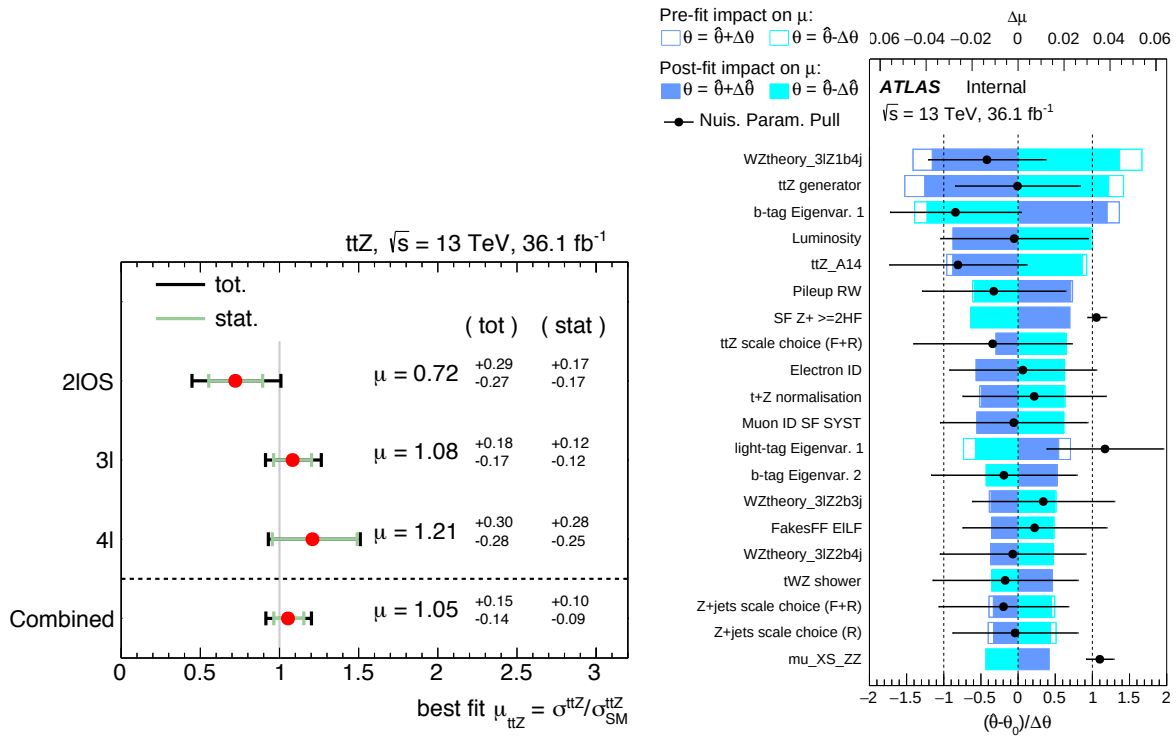

(a) $\mu_{t\bar{t}Z}$ individual and combined

(b) Ranking of NPs for the combined $\mu_{t\bar{t}Z}$ [131]

Figure 5.22: The left figure shows the signal strengths extracted from the fit in individual channels and the combined $t\bar{t}Z$ fit. The vertical line at $\mu = 1$ indicates the prediction from the Standard Model. The right figure shows the ranking of the nuisance parameters in the combined $t\bar{t}Z$ fit. The 20 nuisance parameters with the highest impact on $\Delta\mu_{t\bar{t}Z}$ are shown.

section.

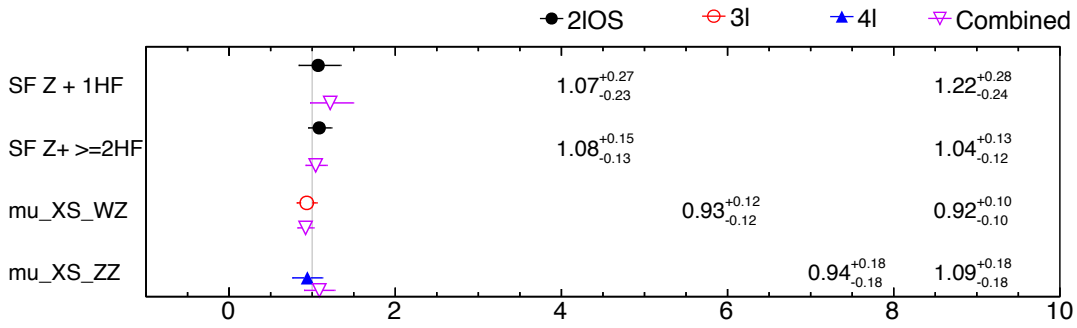

Figure 5.23: Background normalizations obtained from fits in the individual channels compared to the combined $t\bar{t}Z$ fit. The numbers are written in 4 columns which correspond to the fits performed in the 2ℓOS, 3ℓ, 4ℓ and all $t\bar{t}Z$ channels from left to right.

$\mu_{t\bar{t}Z}$	1.05
Signal modelling	5.2%
Flavour tagging	4.6%
Other object-related	3.7%
Background normalizations	3.2%
Luminosity	2.9%
Data-driven background statistics	2.6%
Background cross section	2.5%
Modelling of backgrounds from simulation	2.4%
Simulated sample statistics ("*Gammas*")	2.1%
JES/JER	1.8%
Fake lepton estimation	1.7%
Total systematic uncertainty	11%
Statistical uncertainty	9.5%
Total	14%

Table 5.13: Impact of the uncertainties on $\Delta\mu_{t\bar{t}Z}$ in all $t\bar{t}Z$ channels combined. The uncertainties are symmetrized and presented as relative uncertainties on the signal strength $\mu_{t\bar{t}Z}$.

5.6.3 Two dimensional fit results

In this section the combination of all channels sensitive to the $t\bar{t}Z$ and $t\bar{t}W$ processes is shown. The fit is performed extracting both signal strengths, $\mu_{t\bar{t}Z}$ and $\mu_{t\bar{t}W}$, simultaneously. In total, 27 regions are included in this fit. A comparison of the fit paramaters obtained from the three fit setups presented in this section is given in Table 5.14. The fit results of the two dimensional fit are very similar to the combined $t\bar{t}Z$ fit, e.g. the normalization of the ZZ background is higher than in the fit performed in the 4ℓ channel only. As discussed previously, this is due to the pulls observed in the 2ℓOS channel.

A comparison of the fit results to the prediction is shown in Figure 5.24 after converting the measured signal strengths to the measured cross sections. Since the prediction lies within the 1σ contour, which covers all considered uncertainties in the two-dimensional fit, a good agreement is with the Standard Model found. A breakdown of the uncertainties can be seen in Table 5.15 for both, $\mu_{t\bar{t}Z}$ and $\mu_{t\bar{t}W}$. The uncertainties for $\mu_{t\bar{t}W}$ are higher in general, since the amount of events observed is smaller and the fake lepton estimation introduces significant systematic uncertainties. Several crosschecks have been performed, including correlating the signal modelling uncertainties among the two signal processes, which led to a similar result. The numerical values of both cross sections extracted from the two-dimensional fit are:

Fit parameter	4ℓ $t\bar{t}Z$	$t\bar{t}Z$ 1D	$t\bar{t}Z$ + $t\bar{t}W$ 2D	included in
$\mu_{t\bar{t}Z}$	$1.21^{+0.30}_{-0.28}$	1.05 ± 0.15	1.08 ± 0.14	2ℓOS, 3ℓ, 4ℓ
$\mu_{t\bar{t}W}$	–	–	1.44 ± 0.32	2ℓSS, 3ℓ
norm$_{ZZ}$	0.94 ± 0.18	1.09 ± 0.18	1.11 ± 0.17	4ℓ
norm$_{WZ}$	–	0.92 ± 0.10	0.91 ± 0.10	3ℓ
norm$_{Z1HF}$	–	1.22 ± 0.27	1.19 ± 0.25	2ℓOS
norm$_{Z2HF}$	–	1.04 ± 0.13	1.09 ± 0.13	2ℓOS

Table 5.14: Extracted fit parameters from different fit setups [131]. "4ℓ $t\bar{t}Z$" corresponds to the fit presented in Section 5.6.1, "$t\bar{t}Z$ 1D" refers to the $t\bar{t}Z$ combination shown in Section 5.6.2 and "$t\bar{t}Z$ + $t\bar{t}W$ 2D" represents the two dimensional fit. The last column shows in which channels a given fit parameter is allowed to vary.

$$\begin{aligned} \sigma_{t\bar{t}Z} &= 952 \pm 79\,(\text{stat.}) \pm 98\ \ (\text{syst.})\,\text{fb}, \\ &= 952 \pm 126\,\text{fb}, \\ \sigma_{t\bar{t}W} &= 867 \pm 133\,(\text{stat.}) \pm 139\ \ (\text{syst.})\,\text{fb}, \\ &= 867 \pm 193\,\text{fb}. \end{aligned} \tag{5.15}$$

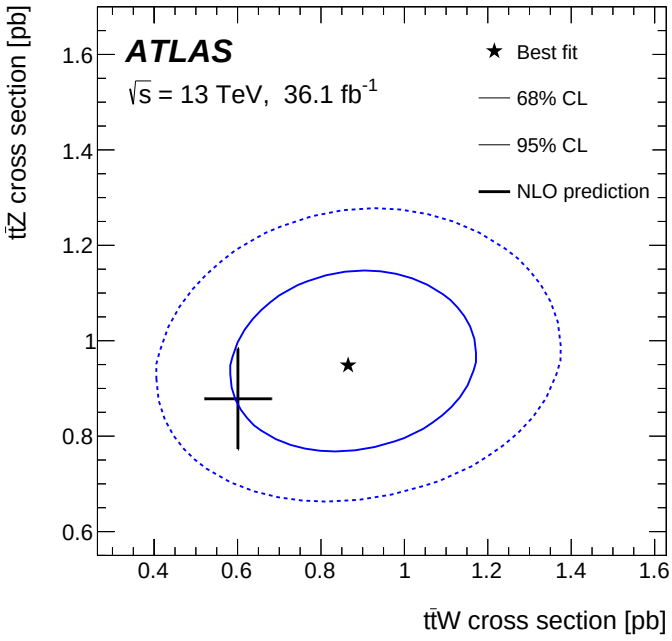

Figure 5.24: Results of the two-dimensional fit along with 1σ and 2σ contours that included all uncertainties. The black cross represents the prediction in QCD and EW NLO [9]. It includes renormalization and factorization scale uncertainties as well as PDF uncertainties including α_s variations. [54].

Category	$t\bar{t}Z$ POI	$t\bar{t}W$ POI
Signal strength	1.08	1.44
Modelling of backgrounds from simulation	5.3%	2.6%
Flavour tagging	4.2%	3.7%
Signal modelling	4.9%	8.5%
Other object-related	3.7%	2.5%
Background normalizations	3.2%	3.9%
Luminosity	2.9%	4.5%
Data-driven background statistics	2.5%	6.3%
Background cross section	2.3%	4.9%
Simulated sample statistics ("*Gammas*")	2.0%	5.3%
JES/JER	1.9%	4.1%
Fake lepton estimation	1.8%	5.7%
Total systematic uncertainty	10%	16%
Statistical uncertainty	8.4%	15%
Total	13%	22%

Table 5.15: Impact of the uncertainties on $\Delta\mu_{t\bar{t}Z}$ and $\Delta\mu_{t\bar{t}W}$ for the two dimensional fit. The uncertainties are symmetrized and presented as relative uncertainties on the signal strength $\mu_{t\bar{t}Z}$ and $\mu_{t\bar{t}W}$ [131].

5.6.4 Comparison to other $t\bar{t}V$ measurements

A comparison of the results from this analysis to previous $t\bar{t}V$ measurements and the Standard Model prediction at 13 TeV is given in Table 5.16. The improvement of this analysis compared to the previous ATLAS result is reflected by the increase of statistics. In addition the 2ℓOS region and the 2ℓSS regions with electrons were added to the analysis. Comparing the analysis from this thesis to the latest CMS result with a comparable amount of data shows similar significance between the two, despite the systematic uncertainties are evaluated differently for the ATLAS and CMS experiments[3] and the event and object selections are different. It can be seen that all measurements are compatible with the Standard Model prediction within their uncertainties. However, all measurements observe an excess in data, especially in the $t\bar{t}W$ regions. Some ideas in the community to explain this potential mismatch include missing contributions from the Standard Model prediction, e.g. tW scattering in $t\bar{t}W$ events with an extra jet [157].

5.6.5 EFT interpretation of the result

Following the notation introduced in Section 2.4, limits have been set on the Wilson coefficients C_i. Dedicated samples of the $t\bar{t}Z$ process, simulated by MadGraph5_aMC@NLO and interfaced to Pythia 8, have been generated where the numerical value of a single Wilson coefficient has been changed to an

[3] For instance, the flavour tagging of jets is based on a different algorithm in the CMS collaboration

Search	Data collected	$\sigma_{t\bar{t}Z}$	$\sigma_{t\bar{t}W}$
Results of this analysis			
ATLAS 4ℓ only fit	36.1 fb^{-1}	$1.07^{+0.28}_{-0.25}$ (stat.)$^{+0.10}_{-0.09}$ (syst.) pb	–
ATLAS two-dimensional fit	36.1 fb^{-1}	0.95 ± 0.08 (stat.) ± 0.10 (syst.) pb	0.87 ± 0.13 (stat.) ± 0.14 (syst.) pb
Previous results			
ATLAS [58]	3.2 fb^{-1}	1.50 ± 0.72 (stat.) ± 0.33 (syst.) pb	0.92 ± 0.29 (stat.) ± 0.10 (syst.) pb
CMS [59]	35.9 fb^{-1}	$0.99^{+0.09}_{-0.08}$(stat.)$^{+0.12}_{-0.10}$(syst.) pb	$0.77^{+0.12}_{-0.11}$(stat.)$^{+0.13}_{-0.12}$(syst.) pb
Standard Model prediction			
NLO QCD+EW [54]	-	0.84 ± 0.10 pb	0.60 ± 0.08 pb

Table 5.16: Fit results obtained from this analysis compared to other $t\bar{t}V$ measurements and the Standard Model prediction at 13 TeV.

arbitrary number. The other Wilson coefficients are set to 0. In total two simulated samples have been generated for each Wilson coefficient: an up- and a down-variation. An overview of the chosen values for the Wilson coefficients in the simulated samples is given in Table 5.17. The samples have been validated and show similar detector resolution efficiencies as the Standard Model signal sample of $t\bar{t}Z$ used in the analysis.

Wilson Coefficient	$C_i/(\Lambda/1\ \text{TeV})^2$
$C_{\phi Q}^{(3)}$	+6
$C_{\phi Q}^{(3)}$	-6
$C_{\phi t}$	+6
$C_{\phi t}$	-6
C_{tW}	+2
C_{tW}	-2
C_{tB}	+5
C_{tB}	-5

Table 5.17: The values for C_i/Λ^2 chosen for generating the $t\bar{t}Z$ EFT simulated samples. Each row refers to a different simulated sample with all Wilson coefficients not mentioned set to zero.

A fit is performed using all 4ℓ and 3ℓ signal regions targeting $t\bar{t}Z$. New nuisance parameters are the normalization uncertainty of the $t\bar{t}Z$ process of 12% and uncertainties resulting from the limited events available to simulate the EFT samples to estimate the Wilson coefficients. They are calculated with the test statistic $\lambda(C_i)$, following the notations introduced in Section 5.5. The minimum of the test statistic corresponds to the best-fit value of a given Wilson coefficient. Those likelihood curves are shown in Figure 5.25 for the Wilson coefficients $C_{\phi t}$ and C_{tW}. The left curve shows a second minimum at negative values which is excluded by constraints from other measurements. Further likelihood curves for other Wilson coefficients are shown in Reference [9].

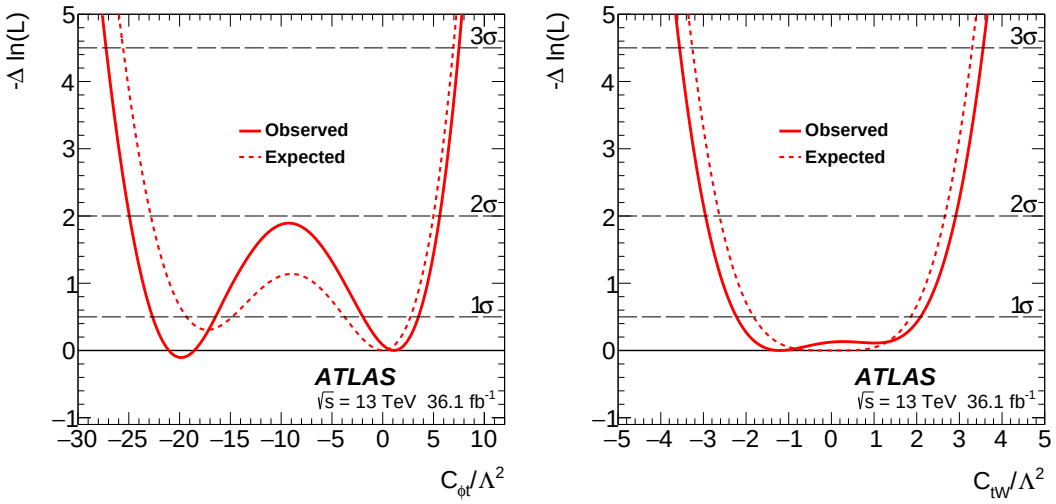

(a) (b)

Figure 5.25: The test statistic $\lambda(C_i)$ as a function of $C_{\phi t}$ and C_{tW} [9].

Using the likelihood curves of $\lambda(C_i)$, limits at 1σ and 2σ can be extracted. Those are shown in Table 5.18. A comparison to previous direct and indirect constraints are given in References [158–161]. This analysis was able to set competitive constraints on the Wilson coefficient $C_{\phi t}$.

Coefficient	Expected limits	Observed limits
$C_{\phi Q}^{(3)}/\Lambda^2$	[-2.1, 1.9], [-4.5, 3.6]	[-1.0, 2.7], [-3.3, 4.2]
$C_{\phi t}/\Lambda^2$	[-3.8, 2.7], [-23, 4.9]	[-2.0, 3.5], [-25, 5.5]
C_{tB}/Λ^2	[-2.9, 3.0], [-4.2, 4.3]	[-3.7, 3.5], [-5.0, 5.0]
C_{tW}/Λ^2	[-1.8, 1.9], [-2.6, 2.6]	[-2.2, 2.1], [-2.9, 2.9]

Table 5.18: Expected and observed intervals of the Wilson coefficients, corresponding to the 1σ and 2σ bands, shown in units of $1/\text{ TeV}^2$ [9]. The limits on the Wilson coefficients have been converted according to Reference [8], using the following conversion factors: $0.5 \cdot y_t^2$ for $C_{\phi Q}^{(3)}$ and $C_{\phi t}$, $y_t g_Y$ for C_{tB} and $y_t g_W$ for C_{tW}. The values for those coefficients are: $y_t = 0.994$, $g_W = 0.653$ and $g_Y = 0.349$ (see Equation 2.23).

CHAPTER 6

Unfolding of data in the $t\bar{t}Z$ 4ℓ channel

6.1 Principles

The unfolding procedure aims at obtaining a truth spectrum from a measured distribution [162]. This is beneficial, because limited detector resolution and acceptance smear out measured distributions. The unfolding enables a direct comparison of the measurement to the theoretical prediction. As such, the unfolding is usually performed on data, while a matrix, called "*migration matrix*", describing how the measured observable and the truth spectrum align, is determined in simulation.

In order to perform the unfolding, the migration matrix is inverted, for which multiple methods exist. The results in this section make use of the iterative Bayesian method (IBS) [163]. A cross-check to validate the unfolding is to compare it to two other methods, the singular value decomposition (SVD) [164] and the bin-by-bin correction [165]. After having unfolded the data, "*differential cross section*", can be measured.

After having obtained the migration matrix from simulation, the number of observed signal events is required, which is obtained by subtracting the expected background events from data and referred to as N_{reco} in the following. Since distribution of observables are unfolded, the number of events are counted per bin i of a given distribution:

$$N_{\text{reco},i} = N_{\text{data},i} - N_{\text{bkg},i}. \tag{6.1}$$

Due to detector and acceptance effects, the data needs to be corrected, according to the events that were not part of the truth spectrum, but were reconstructed:

$$\begin{aligned} N^{\text{corr}}_{\text{reco},i} &= \left(N_{\text{data},i} - N_{\text{bkg},i}\right) \times \left(1 - f_{\text{mig},i}\right), \\ f_{\text{mig},i} &= \frac{N^{\text{non-fid}}_{\text{reco},i}}{N_{\text{reco},i}}, \end{aligned} \tag{6.2}$$

where $f_{\text{mig},i}$ is the fraction of events reconstructed, that where not part of the truth spectrum (also referred to as fiducial volume). Therefore, N_{reco} gets corrected with a factor smaller than one. The unfolding, e.g. applying the inverse migration matrix to the corrected amount of events, results in the truth spectrum:

$$N^{\text{unf}}_{j} = N^{\text{corr}}_{\text{truth},j} = \sum_{i} M^{-1}_{ij} \times N^{\text{corr}}_{\text{reco},i}. \tag{6.3}$$

Here, the indices i and j correspond to the bins of the truth and reconstructed spectrum, respectively. With these quantities, a differential cross section can be computed:

$$\begin{aligned}\sigma_j^{\text{diff}} &= \frac{1}{L\epsilon_j} \times \sum_i M_{ji}^{-1} \times \left(N_{\text{data},i} - N_{\text{bkg},i}\right) \times \left(1 - f_{\text{mig},i}\right) \\ &= \frac{1}{L\epsilon_j} \times N_j^{\text{unf}}.\end{aligned} \tag{6.4}$$

The additional correction factor, ϵ_j, is an efficiency, that describes the amount of events that were reconstructed in bin j and also part of the truth spectrum:

$$\epsilon_j = \frac{N_{\text{reco},j}^{\text{fid}}}{N_{\text{truth},j}^{\text{fid}}}. \tag{6.5}$$

Following the IBS approach of unfolding, each element of the migration matrix, M_{ij} (and similarly the inverse matrix), can be expressed as a probability for observing bin i, given the truth spectrum in bin j:

$$\begin{aligned}M_{ji} &= P(E_i|C_j), \\ M_{ij}^{-1} &= P(C_j|E_i),\end{aligned} \tag{6.6}$$

where the effect E and cause C correspond to the measured and truth values. Following the Bayesian theorem, this probability is expandable into several iterations k:

$$P(C_j|E_i) = \frac{P(E_i|C_j) \times P_0(C_j)}{\sum_k P(E_i|C_k) \times P_0(C_k)}, \tag{6.7}$$

with $P_0(C_j)$ being the prior truth value in bin j, obtained from simulation, and $P_0(C_k)$ being the result from the previous iteration $k-1$. The iterative procedure is repeated until the value of $P_0(C_k)$ converges in all bins. In other words, the unfolded distribution, obtained from the inverted migration matrix M_{ij}^{-1} is updated with each iteration k. With each iteration, the unfolded distribution becomes closer to the truth distribution. The number of iterations chosen in the unfolding is discussed in Section 6.2.

6.2 Results

6.2.1 Region and observables

The number of events observed after subtracting the expected background events are necessary to determine a reasonable number of bins for the distribution of observables of interest. A glance at Table 5.3, which shows the yields in all signal regions in the 4ℓ channel, reveals that roughly 33 events are available after subtracting the expected background, summed over the four regions. Therefore the unfolding is performed in all signal regions combined.

As discussed in Section 2.4, distributions, sensitive to anomalous couplings and therefore of interest to unfold for the $t\bar{t}Z$ process, are the $\Delta\phi$ from the leptons and the transverse momentum of the reconstructed Z boson [68]. The binning for these distributions is chosen such that a sufficient amount of events per bin is available, while the shape can still be seen. The distributions of these variables with an appropriate binning are shown in Figure 6.1.

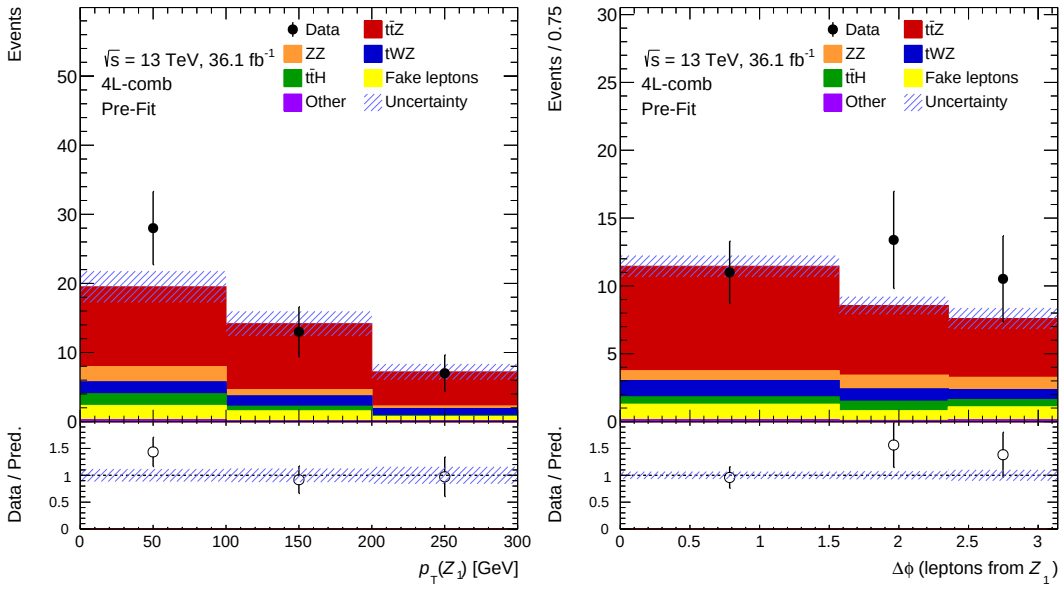

(a) (b)

Figure 6.1: Distribution of the transverse momentum (left) and $\Delta\phi$ (right) of the Z_1 lepton pair in all 4ℓ signal regions combined. Both, statistical and systematic uncertainties are included. The binning of the $\Delta\phi$ distribution is chosen in units of π ($\frac{\pi}{2}$, $\frac{3\pi}{4}$, π). The p_{T} distribution includes the overflow in the last bin.

All tools necessary to perform the unfolding are included in the RooUnfold package [166], which is compatible with ROOT [167].

6.2.2 Preparation with simulation

With the region, observables and binning discussed in the previous section, the migration matrix M_{ij} and the coefficients of Equation 6.4 can be determined for each observable, using the simulated samples for the $t\bar{t}Z$ process. Figure 6.2 shows the migration matrices, while Figure 6.3 shows the coefficients of the differential cross section: the inverse of the efficiency ϵ_j and $(1 - f_{\mathrm{mig}})$.

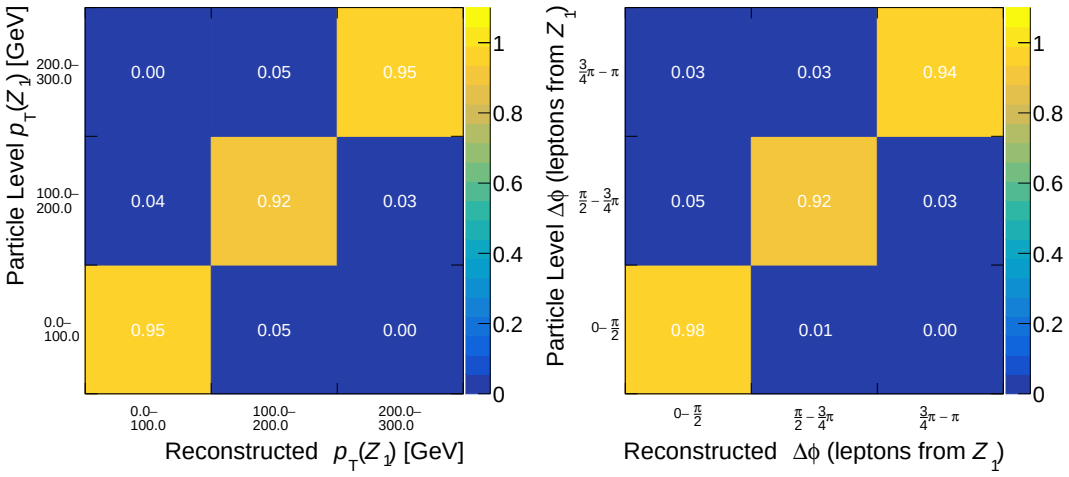

(a) (b)

Figure 6.2: Migration matrices for the transverse momentum (left) and $\Delta\phi$ (right) of the Z_1 lepton pair in all 4ℓ signal regions combined, using three bins per observable. The matrices are derived using simulated samples of $t\bar{t}Z$.

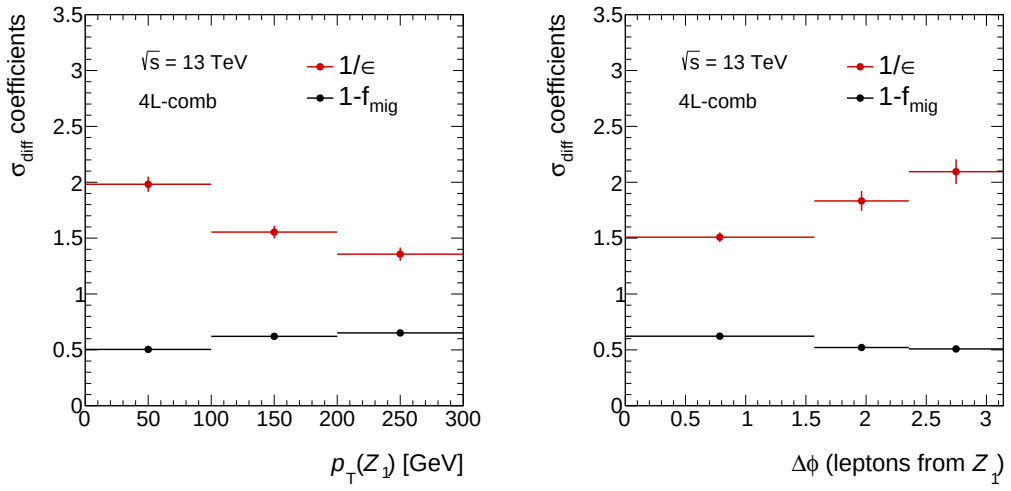

(a) (b)

Figure 6.3: Distributions of $1/\epsilon_j$ and $(1 - f_{\text{mig}})$ for the transverse momentum (left) and $\Delta\phi$ (right) of the Z_1 lepton pair in all 4ℓ signal regions combined, using three bins per observable. The coefficients are computed using simulated samples of $t\bar{t}Z$. Only statistical uncertainties are shown.

Cross checks

A number of cross checks are performed in order to validate the choice of binning and to derive the optimal number of iterations. To perform some of these checks, the simulated sample acts as *"pseudo-data"* and is unfolded. The pseudo-data is generated by dividing the simulated $t\bar{t}Z$ sample into a testing and training part. The training part is used to derive the migration matrix, while the testing part is unfolded.

In total, 100 separate pseudo-datasets are generated, where the testing and training part use 96% and 4% of the available events, respectively. However, the assignment of each event is done randomly, to create different pseudo-data sets.

Optimal number of iterations

The optimal number of iterations is determined by the convergence speed, the speed by which the IBS method transforms the unfolded distribution to the truth distribution. An infinite number of iterations is avoided, as a bias on statistical fluctuations could be otherwise introduced. For the convergence speed, the desired minimum change per iteration in each bin j is set to:

$$\frac{\left|N_{j+1}^{\text{unfolded}} - N_{j}^{\text{unfolded}}\right|}{N_{j+1}^{\text{unfolded}}} < 5\%. \tag{6.8}$$

The value of 5% is chosen based on the number of simulated events available in each bin of the distributions and roughly corresponds to the statistical uncertainty.

A pseudo-data distribution is built from the reconstructed distributions of the testing part of each of the 100 pseudo-datasets, distributed with the help of a Poissonian function. Then, the resulting distribution is unfolded using the migration matrix from the training part of the corresponding pseudo-datasets. Equation 6.8 is calculated for each iteration. The result is shown in Figure 6.4. It can be seen that the change per iteration is different for each bin. For both variables, the third bin shows the largest change. Equation 6.8 is fulfilled after 7 and 16 iterations in all bins for the transverse momentum and $\Delta\phi$ of the Z_1 lepton pair. The second bin in Figure 6.4(b) shows that the change actually slightly increases for a large number of iterations, indicating a behaviour of over-optimization.

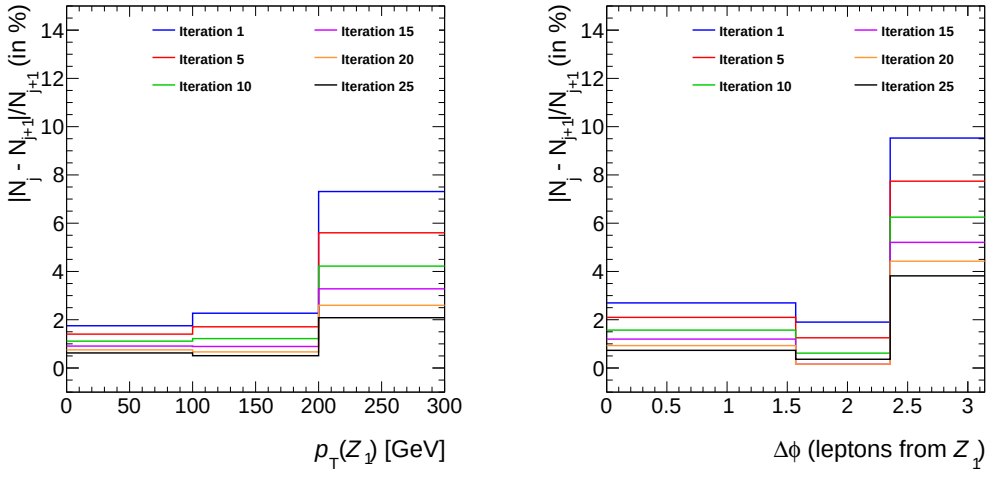

(a) (b)

Figure 6.4: . Relative change for each iteration with respect to the previous iteration for the transverse momentum (left) and $\Delta\phi$ (right) of the Z_1 lepton pair in all 4ℓ signal regions combined. The unfolded distribution was built from 100 pseudo-datasets with the help of a Poissonian function. The desired threshold of $< 5\%$ change per iteration is reached at 7 and 16 iterations for the transverse momentum and $\Delta\phi$ of the Z_1 lepton pair, respectively.

Closure test

The closure test checks if the unfolded distribution resembles the truth distribution. The same 100 pseudo-datasets are used for the unfolding with the number iterations determined in the previous test. The unfolded events (originating from the test part of the pseudo-data) are compared to the truth distribution of the training part of the pseudo-data to avoid bias. Figure 6.5 shows the result of the closure test, by comparing the number of events of the truth and the unfolded pseudo-data distributions, using the number of iterations determined in the previous test.

The unfolded distribution shows a satisfactory agreement with the truth distribution. The third bin in Figure 6.5(b) shows the largest disagreement, but is not worrying due to the number of observed events when unfolding data.

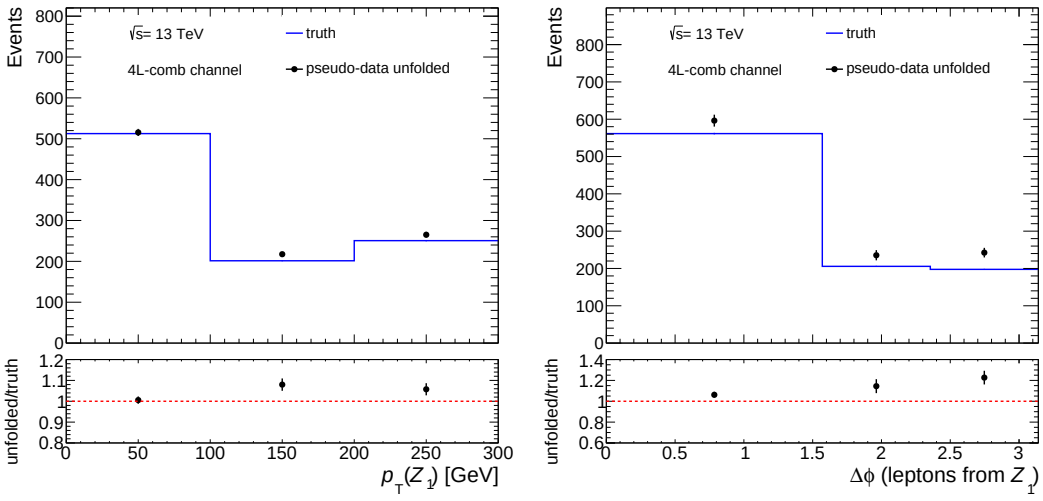

(a) (b)

Figure 6.5: Comparison of the truth and the unfolded pseudo-data distributions for the transverse momentum (left) and $\Delta\phi$ (right) of the Z_1 lepton pair in all 4ℓ signal regions combined. The unfolded pseudo-data uses the number of iterations determined in the previous test. Only statistical uncertainties are shown.

6.2.3 Unfolding of data

As mentioned, the background expectation is subtracted from the data before the unfolding. However, both the truth distribution of the signal process and the background expectation are scaled by the post-fit result of the combined $t\bar{t}Z$ measurement, reported in Section 5.6.2. The unfolding is performed with the number of iterations determined in the previous section.

The uncertainties per bin are defined as follows: The statistical uncertainty corresponds to the uncertainty before the background expectation was subtracted. The statistical uncertainty of the background expectation is expected to be small and therefore neglected here. Since the statistical uncertainty dominates in the 4ℓ channel, the systematic uncertainty per bin is approximated as the systematic uncertainty of the post-fit background expectation in that bin.

Using Equation 6.4, the differential cross section is computed by scaling the unfolded events with the inverse of the efficiency and luminosity. Figure 6.6 shows the differential cross sections compared to the truth distribution of the signal process from simulation, scaled to the same cross section. The

unfolded data and the truth distribution reasonably agree, given the large statistical uncertainty. Table 6.1 summarises the results of the unfolding. The differential cross sections are quoted as the total $t\bar{t}Z$ cross section, multiplying the results (of Figure 6.6) by the branching ratio of $t\bar{t}Z \to 4\ell$ (0.5%). A direct comparison to the predicted $t\bar{t}Z$ cross section of 840 fb [54] is not sensible here, since the differential cross sections was obtained using the 4ℓ selection and is therefore expected to be smaller. However, the order of magnitude of the differential cross sections fit to the prediction.

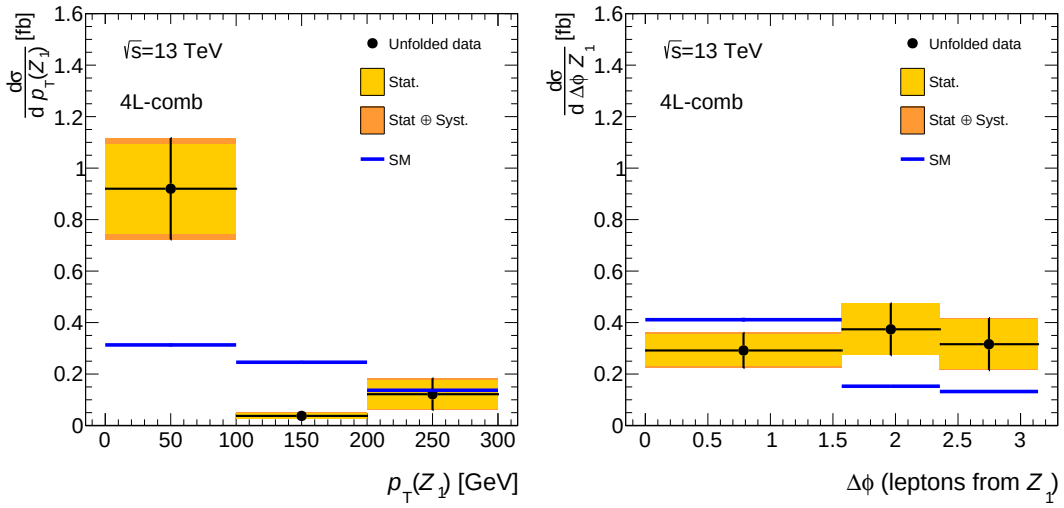

(a) (b)

Figure 6.6: Differential cross section as a function of the transverse momentum (left) and $\Delta\phi$ (right) of the Z_1 lepton pair in all 4ℓ signal regions combined, compared to the truth distribution (blue line). The systematic uncertainty per bin is approximated as the systematic uncertainty of the post-fit background expectation in that bin.

p_T (Z_1) [GeV]	0 – −100 GeV	100 – −200 GeV	> 200 GeV
ϵ_j	0.50 ± 0.02	0.64 ± 0.02	0.74 ± 0.03
$N_{\text{data},i} - N_{\text{bkg},i}$	19.9 ± 5.3 (stat.) ±2.8 (syst.)	8.1 ± 3.6 (stat.) ±2.3 (syst.)	4.7 ± 2.6 (stat.) ±1.3 (syst.)
N_j^{unf}	33.2 ± 6.3 (stat.) ±3.3 (syst.)	1.4 ± 0.4 (stat.) ±0.2 (syst.)	5.9 ± 2.2 (stat.) ±1.1 (syst.)
$\sigma_j^{t\bar{t}Z}$ [fb]	184.0 ± 34.8 (stat.) ±18.5 (syst.)	7.5 ± 2.1 (stat.) ±1.3(syst.)	24.3 ± 11.0 (stat.) ±5.6 (syst.)
$\Delta\phi$ (leptons from Z_1)	0 – $-\frac{\pi}{2}$	$\frac{\pi}{2}$ – $-\frac{3\pi}{4}$	> $\frac{3\pi}{4}$
ϵ_j	0.66 ± 0.02	0.55 ± 0.03	0.48 ± 0.03
$N_{\text{data},i} - N_{\text{bkg},i}$	15.3 ± 4.8 (stat.) ±1.4 (syst.)	10.5 ± 3.7 (stat.) ±0.5 (syst.)	7.7 ± 3.3 (stat.) ±1.1 (syst.)
N_j^{unf}	11.3 ± 2.4 (stat.) ±1.2 (syst.)	14.0 ± 3.7 (stat.) ±0.5 (syst.)	10.7 ± 3.2 (stat.) ±1.1 (syst.)
$\sigma_j^{t\bar{t}Z}$ [fb]	58.3 ± 12.2 (stat.) ±6.0 (syst.)	74.8 ± 20.0 (stat.) ±2.7 (syst.)	63.2 ± 19.1 (stat.) ±6.5 (syst.)

Table 6.1: Results of the unfolding in the 4ℓ channel for the transverse momentum and $\Delta\phi$ of the Z_1 lepton pair in all 4ℓ signal regions combined. The statistical uncertainty corresponds to the uncertainty before subtracting the background expectation, while the systematic uncertainty per bin is approximated as the systematic uncertainty of the post-fit background expectation in that bin.

Following the ideas of Reference [68], the unfolded distributions are expected to be sensitive to EFT effects. Therefore, a shape comparison of the nominal $t\bar{t}Z$ sample is made with dedicated $t\bar{t}Z$ samples, where the Wilson coefficients C_i are set to values beyond the Standard Model prediction, called $t\bar{t}Z$ EFT samples in the following. For each operator considered, a sample with a down- and and up-variation of the Wilson coefficients C_i is generated (as previously discussed in Section subs:eftint). Table 6.2 shows the Wilson coefficients C_i chosen for the generation of the simulated $t\bar{t}Z$ EFT samples. The values of the coefficients C_i roughly correspond to the best limits available at the time of the generation of these samples [67].

Operator	C_i [$(\Lambda/\ \mathrm{TeV})^2$]
$O_{\varphi Q}^{(3)}$	$\pm$ 6
$O_{\varphi t}$	$\pm$ 6
O_{tW}	$\pm$ 2
O_{tB}	$\pm$ 5
O_{tG}	$\pm$ 0.3

Table 6.2: Wilson Coefficients C_i chosen for the simulated samples of $t\bar{t}Z$ with EFT effects. The values roughly correspond to the best limits available at the time of the generation of these samples [67].

The comparison is made with truth level distributions using the same bins as before, normalized to the differential cross section for all samples and can be seen in Figure 6.7. It can be seen, that most of the $t\bar{t}Z$ EFT samples have a very similar shape and can hardly be distinguished. It's mentioned in reference [68] that in order to reach sensitivity, a dataset of >300 fb^{-1} is required. The largest deviations are observed for the $O_{\varphi Q}^{(3)}$ and $O_{\varphi t}$ operators, considering the different values set for the Wilson coefficients C_i (see Table 6.2), e.g. it was shown in Reference [67], that O_{tG} has an effect on the shape of the p_{T} distribution with a value set to $C_{tG}/\Lambda = 1\ \mathrm{TeV}^{-2}$. Finally, Table 6.3 summarizes the ratio between the nominal $t\bar{t}Z$ sample and the $t\bar{t}Z$ EFT samples for each bin. Given the small number of events observed in the 4ℓ channel with the present dataset, there is not enough sensitivity to discover EFT effects for the $t\bar{t}Z$ process.

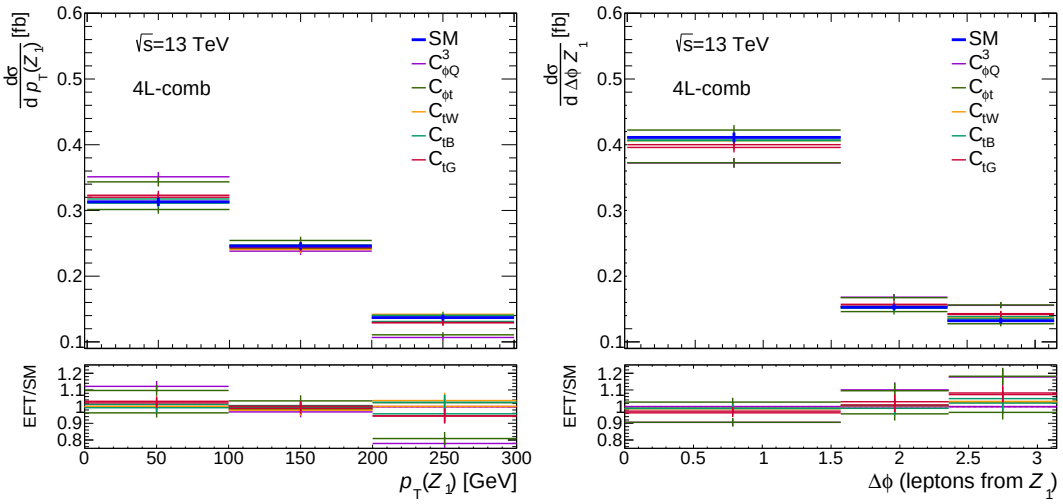

(a) (b)

Figure 6.7: Shape comparison of the truth distributions of the nominal $t\bar{t}Z$ (SM) and the $t\bar{t}Z$ EFT samples. Each $t\bar{t}Z$ EFT sample has two entries per bin, corresponding to the down- and up-variations. The uncertainties shown correspond to the available events in each of the simulated samples.

p_T (Z_1) [GeV]	0-100 GeV	100-200 GeV	> 200 GeV
$O^{(3)}_{\varphi Q}$	1.12 ± 0.02	1.03 ± 0.02	0.78 ± 0.02
$O_{\varphi t}$	1.10 ± 0.02	0.98 ± 0.02	0.81 ± 0.03
O_{tW}	1.00 ± 0.02	0.98 ± 0.02	0.96 ± 0.03
O_{tB}	1.01 ± 0.02	0.99 ± 0.02	0.96 ± 0.03
O_{tG}	1.03 ± 0.02	0.99 ± 0.02	0.94 ± 0.03

$\Delta\phi$ (leptons from Z_1)	0-$\frac{\pi}{2}$	$\frac{\pi}{2}-\frac{3\pi}{4}$	> π
$O^{(3)}_{\varphi Q}$	0.91 ± 0.02	1.10 ± 0.03	0.18 ± 0.04
$O_{\varphi t}$	0.91 ± 0.02	1.10 ± 0.03	1.18 ± 0.04
O_{tW}	0.99 ± 0.02	1.01 ± 0.03	1.03 ± 0.03
O_{tB}	0.99 ± 0.02	0.99 ± 0.03	1.05 ± 0.03
O_{tG}	0.96 ± 0.02	1.03 ± 0.03	1.08 ± 0.03

Table 6.3: Deviations of the $t\bar{t}Z$ EFT samples compared to the nominal $t\bar{t}Z$ sample. For each operator, the highest deviation between the down- and up-variation is quoted. The uncertainties correspond to the available events in each of the simulated samples.

CHAPTER 7

Summary and conclusions

This thesis described the measurement of the cross section of the top-quark pair production in association with a Z boson using 36.1 fb^{-1} of proton-proton collisions at $\sqrt{s}$ = 13 TeV, collected by the ATLAS detector. The analysis combined various multilepton final states and simultaneously extracted the $t\bar{t}Z$ and $t\bar{t}W$ cross sections in a two-dimensional fit. The result is:

$$\sigma_{t\bar{t}Z} = 0.95 \pm 0.08\,(\text{stat.}) \pm 0.10\ \ (\text{syst.})\,\text{pb},$$
$$\sigma_{t\bar{t}W} = 0.87 \pm 0.13\,(\text{stat.}) \pm 0.14\,(\text{syst.})\,\text{pb},$$

which both agree with the Standard Model prediction. Focusing on the $t\bar{t}Z$ analysis in the final state with four leptons, a total of 48 events were observed. In this channel the total number of events is small and the expected signal fraction of $> 60\%$ is high. Additionally, the differential cross-section for the transverse momentum boson and the $\Delta\phi$ of the corresponding lepton pair has been measured. In terms of EFT operators, it was shown that the Wilson operators $O_{\varphi Q}^{(3)}$ and $O_{\varphi t}$ are sensitive to the shape of the distributions of the two observables. Appendix C gives an example of possible improvements to the analysis, by showing how the 4ℓ channel can benefit from exploiting multivariate techniques to extract the signal process from the background in an optimal way. Other possible improvements include a better fake lepton background estimation and a better understanding of the modeling of b-jets.

With the recent conclusion of Run 2, the available dataset, recorded by the ATLAS detector at $\sqrt{s}$ = 13 TeV amounts to 140 fb^{-1}, allowing for measurements with improved precision. Concerning the future of the LHC, the machines and experiments are currently being upgraded for Run 3, which is planned to collect 300 fb^{-1} of data. The subsequent upgrade, planned during the 2020s and referred to as the High-Luminosity LHC (HL-LHC), will increase the centre-of-mass energy to 14 TeV and the luminosity by a factor of five, allowing data to be collected at a higher rate [168]. For the $t\bar{t}Z$ process, current limits set on EFT operators, as shown in Sections 5 and 6, can be improved significantly with more data and constraints for various BSM models can be made. Furthermore, the $t\bar{t}Z$ production cross section, already exceeding the 5σ threshold for discovery (in the 4ℓ channel alone), as shown in Section 5, can be measured at a high precision. Therefore efforts will be made to reduce systematic uncertainties of various kinds. A potential improvement for the $t\bar{t}Z$ multilepton analysis is reducing the signal modelling uncertainty, by simulating samples with large amount of events and proper event filters, done with multiple generators. Also, new final states can be accessible with more data, such as a single lepton channel or decays of $Z \rightarrow$ invisible.

Many open questions remain in high-energy particle physics today, such as the nature of dark matter or the exclusion of gravity from the Standard Model. On the other hand, various observables, like the masses of elementary particles can be measured with high precision. Therefore, high-energy particle

physics remains a very active field and is at crossroads between understanding fundamental interactions and deepening the knowledge established since the previous centuries. As such, potential new collider projects are discussed in the community to complement or excel the experiments at the LHC.

Bibliography

[1] ATLAS Collaboration, *Observation of a new particle in the search for the Standard Model Higgs boson with the ATLAS detector at the LHC*, Phys. Lett. **B716** (2012) 1, arXiv: 1207.7214 [hep-ex].

[2] CMS Collaboration, *Observation of a new boson at a mass of 125 GeV with the CMS experiment at the LHC*, Phys. Lett. **B716** (2012) 30, arXiv: 1207.7235 [hep-ex].

[3] ATLAS, CDF, CMS and DØ Collaborations, *First combination of Tevatron and LHC measurements of the top-quark mass*, arXiv: 1403.4427 [hep-ex].

[4] CDF Collaboration, *Observation of top quark production in $\bar{p}p$ collisions*, Phys. Rev. Lett. **74** (1995) 2626, arXiv: hep-ex/9503002.

[5] DØ Collaboration, *Observation of the top quark*, Phys. Rev. Lett. **74** (1995) 2632, arXiv: hep-ex/9503003.

[6] C. Degrande et al., *Effective Field Theory: A Modern Approach to Anomalous Couplings*, Annals Phys. **335** (2013) 21, arXiv: 1205.4231 [hep-ph].

[7] N. Greiner, S. Willenbrock and C. Zhang, *Effective Field Theory for Nonstandard Top Quark Couplings*, Phys. Lett. **B704** (2011) 218, arXiv: 1104.3122 [hep-ph].

[8] D. Barducci et al., *Interpreting top-quark LHC measurements in the standard-model effective field theory*, arXiv: 1802.07237 [hep-ph].

[9] ATLAS Collaboration, *Measurement of the $t\bar{t}Z$ and $t\bar{t}W$ cross sections in proton-proton collisions at $\sqrt{s}$ = 13 TeV with the ATLAS detector*, (2019), arXiv: 1901.03584 [hep-ex].

[10] M. Tanabashi et al., *Review of Particle Physics*, Phys. Rev. **D98** (2018) 030001.

[11] J. C. Maxwell, *A dynamical theory of the electromagnetic field*, Philosophical Transactions of the Royal Society of London **155** (1865) 459.

[12] S. L. Glashow, *Partial Symmetries of Weak Interactions*, Nucl. Phys. **22** (1961) 579.

[13] A. Salam and J. C. Ward, *On a gauge theory of elementary interaction*, Nuovo Cim. **19** (1961) 165.

[14] S. Weinberg, *A Model of Leptons*, Phys. Rev. Lett. **19** (1967) 1264.

[15] UA1 Collaboration, *Experimental observation of isolated large transverse energy electrons with associated missing energy at $\sqrt{s}$=540 GeV*, Phys. Lett. B **122** (1983) 103.

[16] UA2 Collaboration, *Observation of single isolated electrons of high transverse momentum in events with missing transverse energy at the CERN pp collider*, Phys. Lett. B **122** (1983) 476.

[17] UA1 Collaboration, *Experimental observation of lepton pairs of invariant mass around 95 GeV at the CERN SPS collider*, Phys. Lett. B **126** (1983) 398.

[18] UA2 Collaboration, *Evidence for $Z^0 \to e^+e^-$ at the CERN pp collider*, Phys. Lett. B **129** (1983) 130.

[19] J. Ellis, "Higgs Physics", *Proceedings, 2013 European School of High-Energy Physics (ESHEP 2013): Paradfurdo, Hungary, June 5-18, 2013*, 2015 117, arXiv: 1312.5672 [hep-ph].

[20] M. Kobayashi and T. Maskawa, *CP Violation in the Renormalizable Theory of Weak Interaction*, Prog. Theor. Phys. **49** (1973) 652.

[21] Z. Maki, M. Nakagawa and S. Sakata, *Remarks on the unified model of elementary particles*, Prog. Theor. Phys. **28** (1962) 870.

[22] B. Pontecorvo, *Inverse beta processes and nonconservation of lepton charge*, Sov. Phys. JETP **7** (1958) 172.

[23] MARK-J Collaboration, *Discovery of Three Jet Events and a Test of Quantum Chromodynamics at PETRA Energies*, Phys. Rev. Lett. **43** (1979) 830.

[24] TASSO Collaboration, *Evidence for Planar Events in e+ e- Annihilation at High-Energies*, Phys. Lett. B **86** (1979) 243.

[25] M. C. Gonzalez-Garcia and M. Maltoni, *Phenomenology with Massive Neutrinos*, Phys. Rept. **460** (2008) 1, arXiv: 0704.1800 [hep-ph].

[26] Planck Collaboration, *Planck 2013 results. XVI. Cosmological parameters*, Astron. Astrophys. **571** (2014) A16, arXiv: 1303.5076 [astro-ph.CO].

[27] S. P. Martin, *A Supersymmetry primer*, Adv.Ser.Direct.High Energy Phys. **18** (1998) 1, arXiv: hep-ph/9709356.

[28] M. Cristinziani and M. Mulders, *Top-quark physics at the Large Hadron Collider*, J. Phys. **G44** (2017) 063001, arXiv: 1606.00327 [hep-ex].

[29] U. Husemann, *Top-Quark Physics: Status and Prospects*, Prog. Part. Nucl. Phys. **95** (2017) 48, arXiv: 1704.01356 [hep-ex].

[30] LHCTopWG, *LHCTopWG Summary Plots*, 2018, URL: https://twiki.cern.ch/twiki/bin/view/LHCPhysics/LHCTopWGSummaryPlots.

[31] R. R. Wilson, *The Tevatron*, Physics Today **30** (1977) 23.

[32] M. Czakon, P. Fiedler and A. Mitov, *Total Top-Quark Pair-Production Cross Section at Hadron Colliders Through $O(\alpha_S^4)$*, Phys. Rev. Lett. **110** (2013) 252004, arXiv: 1303.6254 [hep-ph].

[33] M. Czakon and A. Mitov, *NNLO corrections to top pair production at hadron colliders: the quark-gluon reaction*, JHEP **01** (2013) 080, arXiv: 1210.6832 [hep-ph].

[34] A. Giammanco, *Single top quark production at the LHC*, Rev. Phys. **1** (2016) 1, arXiv: 1511.06748 [hep-ex].

[35] ATLAS Collaboration, *Top Quark Physics Public Results*, 2018, URL: https://twiki.cern.ch/twiki/bin/view/AtlasPublic/TopPublicResults.

[36] CMS Collaboration, *Top Physics Publications*, 2018, URL: http://cms-results.web.cern.ch/cms-results/public-results/publications/TOP/index.html.

[37] J. C. Hardy and I. S. Towner, *Superallowed $0^+ \to 0^+$ nuclear beta decays: A New survey with precision tests of the conserved vector current hypothesis and the standard model*, Phys. Rev. **C79** (2009) 055502, arXiv: 0812.1202 [nucl-ex].

[38] N. Cabibbo, E. C. Swallow and R. Winston, *Semileptonic hyperon decays*, Ann. Rev. Nucl. Part. Sci. **53** (2003) 39, arXiv: hep-ph/0307298.

[39] G. De Lellis, P. Migliozzi and P. Santorelli, *Charm physics with neutrinos*, Phys. Rept. **399** (2004) 227, [Erratum: Phys. Rept.411 (2005) 323].

[40] Belle Collaboration, *Measurements of branching fractions of leptonic and hadronic D_s^+ meson decays and extraction of the D_s^+ meson decay constant*, JHEP **09** (2013) 139, arXiv: 1307.6240 [hep-ex].

[41] BaBar Collaboration, *Measurement of the hadronic form-factor in $D^0 \to K^- e^+ \nu_e \ell$*, Phys. Rev. **D76** (2007) 052005, arXiv: 0704.0020 [hep-ex].

[42] Belle Collaboration, *Measurement of $|V(ub)|$ from Inclusive Charmless Semileptonic B Decays*, Phys. Rev. Lett. **104** (2010) 021801, arXiv: 0907.0379 [hep-ex].

[43] J. A. Bailey et al., *The $B \to \pi \ell \nu$ semileptonic form factor from three-flavor lattice QCD: A Model-independent determination of $|V_{ub}|$*, Phys. Rev. **D79** (2009) 054507, arXiv: 0811.3640 [hep-lat].

[44] LHCb Collaboration, *Precision measurement of the B_s^0-$\bar{B}_s^0$ oscillation frequency with the decay $B_s^0 \to D_s^- \pi^+$*, New J. Phys. **15** (2013) 053021, arXiv: 1304.4741 [hep-ex].

[45] DØ Collaboration, *Evidence for s-channel single top quark production in $p\bar{p}$ collisions at $\sqrt{s} = 1.96$ TeV*, Phys. Lett. **B726** (2013) 656, arXiv: 1307.0731 [hep-ex].

[46] CMS Collaboration, *Measurement of the single-top-quark t-channel cross section in pp collisions at $\sqrt{s} = 7$ TeV*, JHEP **12** (2012) 035, arXiv: 1209.4533 [hep-ex].

[47] ATLAS Collaboration, *Measurement of the t-channel single top-quark production cross section in pp collisions at $\sqrt{s} = 7$ TeV with the ATLAS detector*, Phys. Lett. **B717** (2012) 330, arXiv: 1205.3130 [hep-ex].

[48] ATLAS and CMS Collaborations, *Combination of single top-quark cross-sections measurements in the t-channel at $\sqrt{s}$=8 TeV with the ATLAS and CMS experiments*, CMS-PAS-TOP-12-002. ATLAS-CONF-2013-098, 2013, URL: https://cds.cern.ch/record/1601029.

[49] ATLAS Collaboration, *Observation of Higgs boson production in association with a top quark pair at the LHC with the ATLAS detector*, Phys. Lett. **B784** (2018) 173, arXiv: 1806.00425 [hep-ex].

[50] CMS Collaboration, *Observation of $t\bar{t}H$ production*, Phys. Rev. Lett. **120** (2018) 231801, arXiv: 1804.02610 [hep-ex].

[51] R. Röntsch and M. Schulze,
Constraining couplings of top quarks to the Z boson in $t\bar{t}$ + Z production at the LHC,
JHEP **07** (2014) 091, [Erratum: JHEP09 (2015) 132], arXiv: 1404.1005 [hep-ph].

[52] G. Altarelli, L. Conti and V. Lubicz,
The $t \to WZ\, b$ decay in the standard model: A Critical reanalysis, Phys. Lett. **B502** (2001) 125,
arXiv: hep-ph/0010090.

[53] J. M. Campbell and R. K. Ellis, *$t\bar{t}W^{\pm}$ production and decay at NLO*, JHEP **07** (2012) 052,
arXiv: 1204.5678 [hep-ph].

[54] J. Alwall et al., *The automated computation of tree-level and next-to-leading order differential cross sections, and their matching to parton shower simulations*, JHEP **07** (2014) 079,
arXiv: 1405.0301 [hep-ph].

[55] ATLAS Collaboration, *Measurement of the $t\bar{t}W$ and $t\bar{t}Z$ production cross sections in pp collisions at $\sqrt{s}$ = 8 TeV with the ATLAS detector*, JHEP **11** (2015) 172,
arXiv: 1509.05276 [hep-ex].

[56] CMS Collaboration, *Measurement of top quark-antiquark pair production in association with a W or Z boson in pp collisions at $\sqrt{s}$ = 8 TeV*, Eur. Phys. J. **C74** (2014) 3060,
arXiv: 1406.7830 [hep-ex].

[57] M. V. Garzelli et al., *$t\,\bar{t}\,W^{\pm}$ and $t\,\bar{t}\,Z$ Hadroproduction at NLO accuracy in QCD with Parton Shower and Hadronization effects*, JHEP **11** (2012) 056, arXiv: 1208.2665 [hep-ph].

[58] ATLAS Collaboration, *Measurement of the $t\bar{t}Z$ and $t\bar{t}W$ production cross sections in multilepton final states using 3.2 fb^{-1} of pp collisions at $\sqrt{s}$ = 13 TeV with the ATLAS detector*,
Eur. Phys. J. **C77** (2017) 40, arXiv: 1609.01599 [hep-ex].

[59] CMS Collaboration, *Measurement of the cross section for top quark pair production in association with a W or Z boson in proton-proton collisions at $\sqrt{s}$ = 13 TeV*,
JHEP **08** (2018) 011, arXiv: 1711.02547 [hep-ex].

[60] M. Feindt, *A Neural Bayesian Estimator for Conditional Probability Densities*, (2004),
arXiv: physics/0402093 [physics.data-an].

[61] M. Feindt and U. Kerzel, *The NeuroBayes neural network package*,
Nucl. Instrum. Meth. **A559** (2006) 190.

[62] K. H. Yau Wong,
Measurement of the top-quark mass and the $t\bar{t}Z$ cross section in ATLAS: the $t\bar{t}$ dilepton way,
CERN-THESIS-2015-089, PhD Thesis, University of Bonn, 2015,
URL: https://cds.cern.ch/record/2031141.

[63] CMS Collaboration, *Measurement of associated production of vector bosons and top quark-antiquark pairs at sqrt(s) = 7 TeV*, Phys. Rev. Lett. **110** (2013) 172002,
arXiv: 1303.3239 [hep-ex].

[64] S. Weinberg, *Baryon- and Lepton-Nonconserving Processes*, Phys. Rev. Lett. **43** (1979) 1566.

[65] A. Buckley et al., *Constraining top quark effective theory in the LHC Run II era*,
JHEP **04** (2016) 015, arXiv: 1512.03360 [hep-ph].

[66] J. A. Aguilar-Saavedra, *A Minimal set of top anomalous couplings*,
Nucl. Phys. **B812** (2009) 181, arXiv: 0811.3842 [hep-ph].

[67] O. Bessidskaia Bylund et al., *Probing top quark neutral couplings in the Standard Model Effective Field Theory at NLO in QCD*, JHEP **05** (2016) 052, arXiv: 1601.08193 [hep-ph].

[68] R. Röntsch and M. Schulze, *Probing top-Z dipole moments at the LHC and ILC*, JHEP **08** (2015) 044, arXiv: 1501.05939 [hep-ph].

[69] L. Evans and P. Bryant, *LHC Machine*, JINST **3** (2008) S08001.

[70] O. S. Brüning et al., *LHC Design Report*, CERN Yellow Reports: Monographs, CERN, 2004, URL: https://cds.cern.ch/record/782076.

[71] ATLAS Collaboration, *ATLAS detector and physics performance: Technical Design Report, 1*, Technical Design Report ATLAS, CERN, 1999, URL: https://cds.cern.ch/record/391176.

[72] ATLAS Collaboration, *ATLAS detector and physics performance: Technical Design Report, 2*, Technical Design Report ATLAS, CERN, 1999, URL: https://cds.cern.ch/record/391177.

[73] L. Rossi, "Manufacturing and Testing of Accelerator Superconducting Magnets", *Proceedings, CAS - CERN Accelerator School : Course on Superconductivity for Accelerators (CAS 2013): Erice, Italy, April 24-May 4, 2013*, 2014 517, arXiv: 1501.07164 [physics.acc-ph].

[74] E. Mobs, *The CERN accelerator complex. Complexe des accélérateurs du CERN*, (2016), General Photo, URL: https://cds.cern.ch/record/2197559.

[75] ATLAS Collaboration, *Improved luminosity determination in pp collisions at sqrt(s) = 7 TeV using the ATLAS detector at the LHC*, Eur. Phys. J. **C73** (2013) 2518, arXiv: 1302.4393 [hep-ex].

[76] ATLAS Collaboration, *Luminosity determination in pp collisions at $\sqrt{s} = 8$ TeV using the ATLAS detector at the LHC*, Eur. Phys. J. **C76** (2016) 653, arXiv: 1608.03953 [hep-ex].

[77] ATLAS Collaboration, *Luminosity Public Results for Run 1*, 2018, URL: https://twiki.cern.ch/twiki/bin/view/AtlasPublic/LuminosityPublicResults.

[78] ATLAS Collaboration, *Luminosity Public Results for Run 2*, 2018, URL: https://twiki.cern.ch/twiki/bin/view/AtlasPublic/LuminosityPublicResultsRun2.

[79] ATLAS Collaboration, *The ATLAS Experiment at the CERN Large Hadron Collider*, JINST **3** (2008) S08003.

[80] CMS Collaboration, *The CMS Experiment at the CERN LHC*, JINST **3** (2008) S08004.

[81] ALICE Collaboration, *The ALICE experiment at the CERN LHC*, JINST **3** (2008) S08002.

[82] LHCb Collaboration, *The LHCb Detector at the LHC*, JINST **3** (2008) S08005.

[83] F. Hügging, *The ATLAS Pixel Insertable B-Layer (IBL)*, Nucl. Instrum. Meth. **A650** (2011) 45, arXiv: 1012.2742 [physics.ins-det].

[84] H. Pernegger, *The Pixel Detector of the ATLAS experiment for LHC Run-2*, JINST **10** (2015) C06012.

[85] ATLAS Collaboration, *Track Reconstruction Performance of the ATLAS Inner Detector at $\sqrt{s} = 13$ TeV*, ATL-PHYS-PUB-2015-018, 2015, URL: https://cds.cern.ch/record/2037683.

[86] ATLAS Collaboration, *ATLAS-FCalTB*, 2018, URL: https://atlas-fcaltb.web.cern.ch/atlas-fcaltb/.

[87] ATLAS Collaboration, *ATLAS muon spectrometer: Technical Design Report*, CERN-LHCC-97-022, 1997, URL: https://cds.cern.ch/record/331068.

[88] ATLAS Collaboration, *Performance of the ATLAS Trigger System in 2015*, Eur. Phys. J. **C77** (2017) 317, arXiv: 1611.09661 [hep-ex].

[89] M. Dobbs and J. B. Hansen, *The HepMC C++ Monte Carlo event record for High Energy Physics*, Comput. Phys. Commun. **134** (2001) 41.

[90] J. Alwall et al., *MadGraph/MadEvent v4: The New Web Generation*, JHEP **09** (2007) 028, arXiv: 0706.2334 [hep-ph].

[91] P. Nason, *A New method for combining NLO QCD with shower Monte Carlo algorithms*, JHEP **11** (2004) 040, arXiv: hep-ph/0409146.

[92] S. Frixione, P. Nason and C. Oleari, *Matching NLO QCD computations with Parton Shower simulations: the POWHEG method*, JHEP **11** (2007) 070, arXiv: 0709.2092 [hep-ph].

[93] S. Alioli et al., *A general framework for implementing NLO calculations in shower Monte Carlo programs: the POWHEG BOX*, JHEP **06** (2010) 043, arXiv: 1002.2581 [hep-ph].

[94] T. Gleisberg et al., *Event generation with SHERPA 1.1*, JHEP **02** (2009) 007, arXiv: 0811.4622 [hep-ph].

[95] T. Sjöstrand, S. Mrenna and P. Z. Skands, *PYTHIA 6.4 Physics and Manual*, JHEP **05** (2006) 026, arXiv: hep-ph/0603175.

[96] T. Sjöstrand, S. Mrenna and P. Z. Skands, *A Brief Introduction to PYTHIA 8.1*, Comput. Phys. Commun. **178** (2008) 852, arXiv: 0710.3820 [hep-ph].

[97] S. Agostinelli et al., *GEANT4: A Simulation toolkit*, Nucl. Instrum. Meth. **A506** (2003) 250.

[98] ATLAS Collaboration, *Electron efficiency measurements with the ATLAS detector using the 2015 LHC proton-proton collision data*, ATLAS-CONF-2016-024, 2016, URL: https://cds.cern.ch/record/2157687.

[99] ATLAS Collaboration, *Muon reconstruction performance of the ATLAS detector in proton–proton collision data at* $\sqrt{s}$ *=13 TeV*, Eur. Phys. J. **C76** (2016) 292, arXiv: 1603.05598 [hep-ex].

[100] ATLAS Collaboration, *Expected electron performance in the ATLAS experiment*, ATL-PHYS-PUB-2011-006, 2011, URL: https://cds.cern.ch/record/1345327.

[101] M. Cacciari, G. P. Salam and G. Soyez, *The Anti-*k_t *jet clustering algorithm*, JHEP **04** (2008) 063, arXiv: 0802.1189 [hep-ex].

[102] ATLAS Collaboration, *Calorimeter Clustering Algorithms: Description and Performance*, ATL-LARG-PUB-2008-002, 2008, URL: https://cds.cern.ch/record/1099735.

[103] ATLAS Collaboration, *Tagging and suppression of pileup jets with the ATLAS detector*, ATLAS-CONF-2014-018, 2014, URL: https://cds.cern.ch/record/1700870.

[104] ATLAS Collaboration, *Expected performance of the ATLAS b-tagging algorithms in Run-2*, ATL-PHYS-PUB-2015-022, 2015, URL: http://cdsweb.cern.ch/record/2037697.

[105] ATLAS Collaboration, *Performance of b-Jet Identification in the ATLAS Experiment*, JINST **11** (2016) P04008, arXiv: 1512.01094 [hep-ex].

[106] ATLAS Collaboration, *Flavour Tagging Performance Public Results*, 2018, URL: https://twiki.cern.ch/twiki/bin/view/AtlasPublic/FlavourTaggingPublicResultsCollisionData.

[107] ATLAS Collaboration, *Performance of missing transverse momentum reconstruction for the ATLAS detector in the first proton-proton collisions at at* $\sqrt{s}$*= 13 TeV*, ATL-PHYS-PUB-2015-027, 2015, URL: https://cds.cern.ch/record/2037904.

[108] ATLAS Collaboration, *Pile-up Suppression in Missing Transverse Momentum Reconstruction in the ATLAS Experiment in Proton-Proton Collisions at* $\sqrt{s}$ *= 8 TeV*, ATLAS-CONF-2014-019, 2014, URL: https://cds.cern.ch/record/1702055.

[109] ATLAS Collaboration, *Expected performance of missing transverse momentum reconstruction for the ATLAS detector at* $\sqrt{s}$ = 13 *TeV*, ATL-PHYS-PUB-2015-023, 2015, URL: https://cds.cern.ch/record/2037700.

[110] ATLAS Collaboration, *Good Run Lists for Analyses with Run 2*, 2018, URL: https://twiki.cern.ch/twiki/bin/view/AtlasProtected/GoodRunListsForAnalysisRun2.

[111] D. J. Lange, *The EvtGen particle decay simulation package*, Nucl. Instrum. Meth. A **462** (2001) 152.

[112] P. Golonka and Z. Was, *PHOTOS Monte Carlo: A Precision tool for QED corrections in Z and W decays*, Eur. Phys. J. **C45** (2006) 97, arXiv: hep-ph/0506026.

[113] S. Jadach, J. H. Kuhn and Z. Was, *TAUOLA: A Library of Monte Carlo programs to simulate decays of polarized tau leptons*, Comput. Phys. Commun. **64** (1990) 275.

[114] ATLAS Collaboration, *The ATLAS Simulation Infrastructure*, Eur. Phys. J. **C70** (2010) 823, arXiv: 1005.4568 [physics.ins-det].

[115] C. ATLAS et al., *The simulation principle and performance of the ATLAS fast calorimeter simulation FastCaloSim*, ATL-PHYS-PUB-2010-013, 2010, URL: https://cds.cern.ch/record/1300517.

[116] ATLAS Collaboration, *ATLAS Run 1 Pythia8 tunes*, ATL-PHYS-PUB-2014-021, 2014, URL: http://cds.cern.ch/record/1966419.

[117] R. D. Ball et al., *Parton distributions with LHC data*, Nucl. Phys. **B867** (2013) 244, arXiv: 1207.1303 [hep-ph].

[118] D. de Florian et al., *Handbook of LHC Higgs Cross Sections: 4. Deciphering the Nature of the Higgs Sector*, (2016), arXiv: 1610.07922 [hep-ph].

[119] H.-L. Lai et al., *New parton distributions for collider physics*, Phys. Rev. **D82** (2010) 074024, arXiv: 1007.2241 [hep-ph].

[120] ATLAS Collaboration, *Multi-Boson Simulation for 13 TeV ATLAS Analyses*, ATL-PHYS-PUB-2016-002, 2016, URL: https://cds.cern.ch/record/2119986.

[121] J. M. Campbell et al., *NLO predictions for t-channel production of single top and fourth generation quarks at hadron colliders*, JHEP **10** (2009) 042, arXiv: 0907.3933 [hep-ph].

[122] R. Frederix, E. Re and P. Torrielli, *Single-top t-channel hadroproduction in the four-flavour scheme with POWHEG and aMC@NLO*, JHEP **09** (2012) 130, arXiv: 1207.5391 [hep-ph].

[123] J. Pumplin et al.,
New generation of parton distributions with uncertainties from global QCD analysis,
JHEP **07** (2002) 012, arXiv: hep-ph/0201195.

[124] P. Z. Skands, *Tuning Monte Carlo Generators: The Perugia Tunes*,
Phys. Rev. **D82** (2010) 074018, arXiv: 1005.3457 [hep-ph].

[125] M. Aliev et al., *HATHOR: HAdronic Top and Heavy quarks crOss section calculatoR*,
Comput. Phys. Commun. **182** (2011) 1034, arXiv: 1007.1327 [hep-ph].

[126] Ö. Ogul Öncel, *Search for Single Top Quark Production in Association with a W and a Z Boson in the 3 Lepton Final State with the ATLAS Experiment at 13 TeV*, CERN-THESIS-2018-076, Master Thesis, University of Bonn, 2018, URL: https://cds.cern.ch/record/2625170.

[127] T. Gleisberg and S. Hoeche, *Comix, a new matrix element generator*, JHEP **12** (2008) 039, arXiv: 0808.3674 [hep-ph].

[128] F. Cascioli, P. Maierhofer and S. Pozzorini, *Scattering Amplitudes with Open Loops*,
Phys. Rev. Lett. **108** (2012) 111601, arXiv: 1111.5206 [hep-ph].

[129] R. Gavin et al., *FEWZ 2.0: A code for hadronic Z production at next-to-next-to-leading order*,
Comput. Phys. Commun. **182** (2011) 2388, arXiv: 1011.3540 [hep-ph].

[130] ATLAS Collaboration, *Trigger Menu in 2016*, ATL-DAQ-PUB-2017-001, 2017,
URL: https://cds.cern.ch/record/2242069.

[131] ATLAS Collaboration, *Measurement of the $t\bar{t}Z$ and $t\bar{t}W$ production cross sections in multilepton final states using 36.1 fb^{-1} of pp collisions at 13 TeV at the LHC*, ATL-COM-PHYS-2016-1730, 2016, URL: https://cds.cern.ch/record/2235582.

[132] G. C. Fox and S. Wolfram,
Observables for the Analysis of Event Shapes in e^+e^- Annihilation and Other Processes,
Phys. Rev. Lett. **41** (1978) 1581.

[133] ATLAS Collaboration, *Measurement of the top quark-pair production cross section with ATLAS in pp collisions at $\sqrt{s}$ = 7 TeV*, Eur. Phys. J. **C71** (2011) 1577, arXiv: 1012.1792 [hep-ex].

[134] ATLAS Collaboration, *Pile-up subtraction and suppression for jets in ATLAS*,
ATLAS-CONF-2013-083, 2013, URL: http://cds.cern.ch/record/1570994.

[135] M. Cacciari, G. P. Salam and G. Soyez, *The Catchment Area of Jets*, JHEP **04** (2008) 005,
arXiv: 0802.1188 [hep-ph].

[136] ATLAS Collaboration, *Jet energy scale measurements and their systematic uncertainties in proton-proton collisions at $\sqrt{s}$ = 13 TeV with the ATLAS detector*,
Phys. Rev. **D96** (2017) 072002, arXiv: 1703.09665 [hep-ex].

[137] ATLAS Collaboration, *Jet Calibration and Systematic Uncertainties for Jets Reconstructed in the ATLAS Detector at $\sqrt{s}$ = 13 TeV*, ATL-PHYS-PUB-2015-015, 2015,
URL: http://cds.cern.ch/record/2037613.

[138] ATLAS Collaboration, *Monte Carlo Calibration and Combination of In-situ Measurements of Jet Energy Scale, Jet Energy Resolution and Jet Mass in ATLAS*, ATLAS-CONF-2015-037, 2015,
URL: https://cds.cern.ch/record/2044941.

[139] ATLAS Collaboration, *Calibration of b-tagging using dileptonic top pair events in a combinatorial likelihood approach with the ATLAS experiment*, ATLAS-CONF-2014-004, 2014, URL: https://cds.cern.ch/record/1664335.

[140] ATLAS Collaboration, *Measurement of b-tagging Efficiency of c-jets in $t\bar{t}$ Events Using a Likelihood Approach with the ATLAS Detector*, ATLAS-CONF-2018-001, 2018, URL: https://cds.cern.ch/record/2306649.

[141] ATLAS Collaboration, *Optimisation of the ATLAS b-tagging performance for the 2016 LHC Run*, ATL-PHYS-PUB-2016-012, 2016, URL: http://cds.cern.ch/record/2160731.

[142] ATLAS Collaboration, *Electron reconstruction and identification efficiency measurements with the ATLAS detector using the 2011 LHC proton-proton collision data*, Eur. Phys. J. **C74** (2014) 2941, arXiv: 1404.2240 [hep-ex].

[143] ATLAS Collaboration, *Electron efficiency measurements with the ATLAS detector using the 2012 LHC proton-proton collision data*, ATLAS-CONF-2014-032, 2014, URL: https://cds.cern.ch/record/1706245.

[144] ATLAS Collaboration, *Electron identification measurements in ATLAS using $\sqrt{s}$ = 13 TeV data with 50 ns bunch spacing*, ATL-PHYS-PUB-2015-041, 2015, URL: https://cds.cern.ch/record/2048202.

[145] M. R. Whalley, D. Bourilkov and R. C. Group, "The Les Houches accord PDFs (LHAPDF) and LHAGLUE", *HERA and the LHC: A Workshop on the implications of HERA for LHC physics. Proceedings, Part B*, 2005 575, arXiv: hep-ph/0508110 [hep-ph].

[146] ATLAS Collaboration, *Modelling of the $t\bar{t}H$ and $t\bar{t}V$ ($V = W, Z$) processes for $\sqrt{s}$ = 13 TeV ATLAS analyses*, ATL-PHYS-PUB-2016-005, 2016, URL: https://cds.cern.ch/record/2120826.

[147] S. Schumann and F. Krauss, *A Parton shower algorithm based on Catani-Seymour dipole factorisation*, JHEP **03** (2008) 038, arXiv: 0709.1027 [hep-ph].

[148] J. Campbell, R. K. Ellis and R. Röntsch, *Single top production in association with a Z boson at the LHC*, Phys. Rev. **D87** (2013) 114006, arXiv: 1302.3856 [hep-ph].

[149] ATLAS Collaboration, *TRExFitter*, 2018, URL: https://twiki.cern.ch/twiki/bin/viewauth/AtlasProtected/TtHFitter.

[150] M. Baak et al., *HistFitter software framework for statistical data analysis*, Eur. Phys. J. **C75** (2015) 153, arXiv: 1410.1280 [hep-ex].

[151] L. Moneta et al., *The RooStats Project*, PoS **ACAT2010** (2010) 057, arXiv: 1009.1003 [physics.data-an].

[152] D. Kirkby and W. Verkerke, *The RooFit Toolkit for Data Modeling*, 2018, URL: http://roofit.sourceforge.net/intro.html.

[153] K. Cranmer et al., *HistFactory: A tool for creating statistical models for use with RooFit and RooStats*, CERN-OPEN-2012-016, 2012, URL: https://cds.cern.ch/record/1456844.

[154] G. Cowan et al., *Asymptotic formulae for likelihood-based tests of new physics*, Eur. Phys. J. **C71** (2011) 1554, [Erratum: Eur. Phys. J.C73,2501(2013)], arXiv: 1007.1727 [physics.data-an].

[155] A. Wald, *Tests of Statistical Hypotheses Concerning Several Parameters When the Number of Observations is Large*, Transactions of the American Mathematical Society **54** (1943) 426.

[156] S. S. Wilks, *The Large-Sample Distribution of the Likelihood Ratio for Testing Composite Hypotheses*, Annals Math. Statist. **9** (1938) 60.

[157] J. A. Dror et al., *Strong tW Scattering at the LHC*, JHEP **01** (2016) 071, arXiv: 1511.03674 [hep-ph].

[158] C. Zhang, N. Greiner and S. Willenbrock, *Constraints on nonstandard top quark couplings*, Phys. Rev. D **86** (2012) 014024.

[159] A. Buckley et al., *Constraining top quark effective theory in the LHC Run II era*, JHEP **04** (2016) 015, arXiv: 1512.03360 [hep-ph].

[160] V. Khachatryan et al., *Measurement of the t-channel single-top-quark production cross section and of the $|V_{tb}|$ CKM matrix element in pp collisions at $\sqrt{s}$= 8 TeV*, JHEP **06** (2014) 090, arXiv: 1403.7366 [hep-ex].

[161] ATLAS Collaboration, *Measurement of the W boson polarisation in $t\bar{t}$ events from pp collisions at $\sqrt{s}$ = 8 TeV in the lepton + jets channel with ATLAS*, Eur. Phys. J. **C77** (2017) 264, arXiv: 1612.02577 [hep-ex].

[162] V. Blobel, *An Unfolding method for high-energy physics experiments*, (2002) 258, arXiv: hep-ex/0208022 [hep-ex].

[163] G. D'Agostini, *Improved iterative Bayesian unfolding*, (2010), arXiv: 1010.0632 [physics.data-an].

[164] A. Höcker and V. Kartvelishvili, *SVD approach to data unfolding*, Nucl. Instrum. Meth. **A372** (1996) 469, arXiv: hep-ph/9509307 [hep-ph].

[165] F. Spano, *Unfolding in particle physics: a window on solving inverse problems*, (2014), URL: http://inspirehep.net/record/1344095.

[166] T. Adye, *Unfolding algorithms and tests using RooUnfold*, (2011) 313, arXiv: 1105.1160 [physics.data-an].

[167] R. Brun and F. Rademakers, *ROOT: An object oriented data analysis framework*, Nucl. Instrum. Meth. **A389** (1997) 81.

[168] P. Azzi et al., *Standard Model Physics at the HL-LHC and HE-LHC*, (2019), arXiv: 1902.04070 [hep-ph].

[169] ATLAS Collaboration, *Secondary vertex finding for jet flavour identification with the ATLAS detector*, ATL-PHYS-PUB-2017-011, 2017, URL: https://cds.cern.ch/record/2270366.

[170] ATLAS Collaboration, *Simulation of top quark production for the ATLAS experiment at sqrt(s) = 13 TeV*, ATL-PHYS-PUB-2016-004, 2016, URL: https://cds.cern.ch/record/2120417.

[171] ATLAS Collaboration, *Performance of pile-up mitigation techniques for jets in pp collisions at $\sqrt{s}$ = 8 TeV using the ATLAS detector*, Eur. Phys. J. **C76** (2016) 581, arXiv: 1510.03823 [hep-ex].

[172] ATLAS Collaboration, *Performance of the ATLAS Secondary Vertex b-tagging Algorithm in 7 TeV Collision Data*, ATLAS-CONF-2010-042, 2010, URL: https://cds.cern.ch/record/1277682.

[173] ATLAS Collaboration, *Vertexing for b-Tagging*, ATL-PHYS-PUB-2009-019. ATL-COM-PHYS-2009-208, THis is one of the b-tagging CSC notes from the CDC book., 2009, URL: https://cds.cern.ch/record/1174260.

[174] ATLAS Collaboration, *Performance of b-Jet Identification in the ATLAS Experiment*, JINST **11** (2016) P04008, arXiv: 1512.01094 [hep-ex].

[175] J. Catmore et al., *A new petabyte-scale data derivation framework for ATLAS*, J. Phys. Conf. Ser. **664** (2015) 072007.

[176] A. Höcker et al., *TMVA: Toolkit for Multivariate Data Analysis*, PoS **ACAT** (2007) 040, arXiv: physics/0703039.

[177] H.-J. Yang, B. P. Roe and J. Zhu, *Studies of boosted decision trees for MiniBooNE particle identification*, Nucl. Instrum. Meth. **555** (2005) 370, eprint: physics/0508045.

[178] M. Karson, *Handbook of Methods of Applied Statistics. Volumes I & II*, Journal of the American Statistical Association **63** (1968) 1047.

[179] ATLAS Collaboration, *Measurement of the cross-section for producing a W boson in association with a single top quark in pp collisions at $\sqrt{s}$ = 13 TeV with ATLAS*, JHEP **01** (2018) 063, arXiv: 1612.07231 [hep-ex].

APPENDIX A

Secondary Vertex Finder

As introduced in Section 4.1.2, a multivariate algorithm is used for flavour tagging in the ATLAS experiment, called "MV2c10".

One of the inputs to the algorithm is the information about the displaced vertices inside a b-jet. Predominantly, a B-meson is formed inside a b-jet, which decays into a D-meson. Thus, the decay of the B-meson and the subsequent decay of the D meson provide displaced vertices inside a b-jet. A diagram of the decay of a B-meson is shown in Figure A.1.

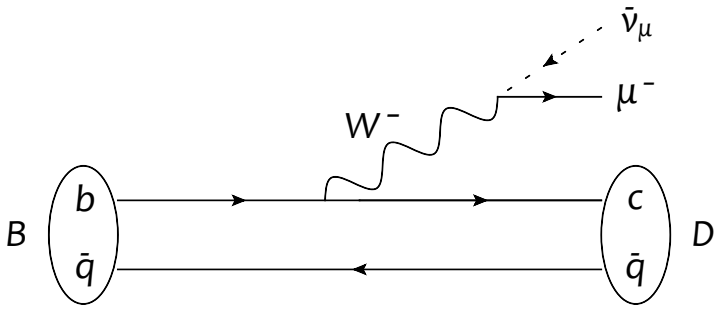

Figure A.1: Diagram for the decay of a B-meson.

The lifetimes of B- and D-mesons are in the order of 10×10^{-12} s (e.g. 1.5 ps and 0.4 ps for the B^0- and D^0-meson), which allows them to travel a few millimetres (taking relativistic effects into account) inside the detector before decaying. The Secondary Vertex Finder (SVF) algorithm aims to reconstruct the displaced vertices and its properties, in order to efficiently identify b-jets. The results presented in this appendix can be found in greater detail in Reference [169].

A.1 Simulated samples

The results of this appendix were obtained using simulated events of $pp \to t\bar{t}$ at a centre-of-mass energy of 13 TeV. Only events with at least one lepton are simulated, to reduces the amount of additional light jets when all W bosons decay hadronically, while having sufficient amount of events.

The simulated $t\bar{t}$ sample differs from the one described in Section 4.2.2, that was used for the $t\bar{t}V$ multilepton analysis. It is generated with Powheg-Box [91–93] and interfaced to Pythia6 [95] for the parton shower. The CT10 PDF set [119] was used. A detailed summary of how the $t\bar{t}$ process is simulated for the ATLAS experiment is given in Reference [170].

A.2 Jet selection

Jets are reconstructed with the anti-k_t algorithm, using a cone size of $R = 0.4$, in which tracks are associated to the jet. Each jet is required to have a transverse momentum of at least 20 GeV and a pseudorapidity of $|\eta| < 2.5$. In order to reduce the amount of pile-up, a requirement on the Jet Vertex Tagger (JVT) discriminator is imposed on jets (JVT < 0.59) that fulfill $p_{\mathrm{T}} < 60$ GeV and $|\eta| < 2.4$. The JVT is a multivariate algorithm to identify and reject jets from pile-up vertices [171].

The jet flavour is identified, by relying on information of the simulation using the following sequence: A b-jet is identified if a b-hadron is found within a distance of $\Delta R < 0.3$ of the jet axis. If there is no b-hadron present, but a c-hadron (a D-meson in most cases), then a c-jet is identified. If neither is found, but a τ lepton is present within the distance of $\Delta R < 0.3$ of the jet axis, a τ jet is identified. Finally, if no b-hadron, c-hadron or τ lepton are found, the jet is labeled as a light jet.

A.3 Description of the SVF algorithm

The SVF algorithm follows a sequence to reconstruct a single displaced vertex per jet. It considers all tracks within a jet p_{T}-dependent cone size, which is defined by a ΔR distance taken from the jet axis. The p_{T}-dependence of the cone size is motivated by an increasing number of tracks for jets with large transverse momentum and varies between $\Delta R = 0.45$ and 0.24, decreasing with the transverse momentum [105].

The algorithm is fed with the direction of the jet axis, the position of the primary jet vertex and the list of associated tracks. The associated tracks have to satisfy a set of quality requirements, which include a minimum transverse momentum and number of hits in the Pixel detector. From the remaining set of tracks, all possible vertices made from two tracks are evaluated. In order to reduce fake vertices, a cleaning procedure is performed. In this context, fake vertices refer to hadron interactions with the detector material, photon conversions or decays of kaons and Λ-baryons. The latter kind of vertices are real, but are labeled as fake vertices, since they are not vertices associated to B- or D-meson decays inside a b-jet. The cleaning procedure is described in Section A.3.1. Afterwards, one multi-track vertex is reconstructed. In the case of a b-jet, the decay vertices of the B- and D-meson are merged into one vertex, if they are close, or the vertex with most tracks is chosen. Due to its resolution, the ATLAS tracking detector often only reconstructs one track from the D-meson decay.

A.3.1 Cleaning procedure

Since the two-track vertices in the algorithm are reconstructed, based on the distance of the two tracks, a large fraction of fake vertices in jets with many tracks or in events with large pile-up, is observed. A good amount of fake vertices are reduced by requiring the hits of the tracks in the tracking detector to be consistent with the position of the reconstructed primary vertex. The contribution of photon conversions, as well as vertices from decays of kaons and Λ-baryons, denoted as V^0 decays in the following, are reduced by requiring the invariant mass of the decay products to be outside the resonance windows:

- K^0 resonance: $|m_{\pi^+\pi^-} - m_{K^0}| > 22$ MeV
- Λ^0 resonance: $|m_{p\pi^-} - m_{\Lambda^0}| > 8$ MeV
- Photon conversions: $m_{e^+e^-} > 40$ MeV.

Figure A.2 shows the invariant mass spectra of the resonance decays, which are obtained by using tracks from reconstructed two-track vertices in light jets. The mass peaks of each of the resonances or the photon conversion can clearly be identified. The window on the requirements were chosen such that they cover the width of the given mass peak. In addition, the mass peak of the $\rho(770)$ resonance can be seen in Figure A.2(a). No requirement is imposed to remove it, since it is already suppressed by the requirements made on the individual tracks.

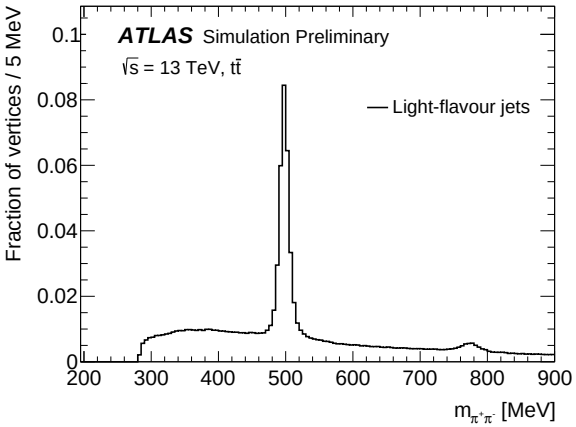

(a) $\pi^+\pi^-$ mass hypothesis

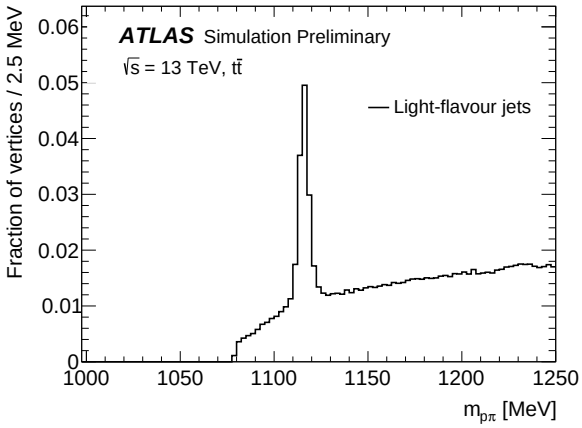

(b) $p\pi^-$ mass hypothesis

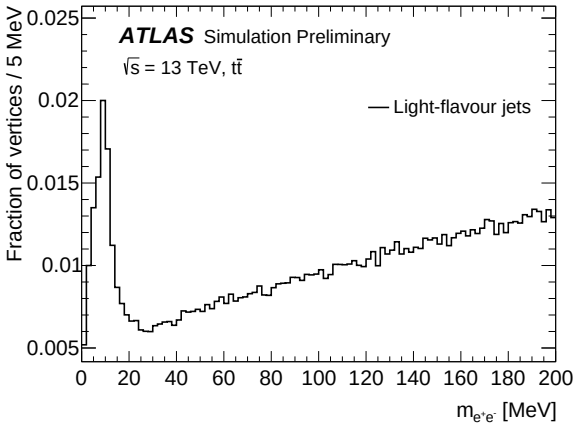

(c) e^+e^- mass hypothesis

Figure A.2: Invariant mass spectra of the resonance decays, obtained using track pairs from reconstructed vertices in light jets. The figures are normalised to one and include over- and underflow bins.

The contribution of vertices, caused by hadronic interactions with the detector material is reduced by removing vertices, whose transverse radii correspond to the beampipe (~25 mm) or the pixel detector layers (~34 mm, ~51 mm, ~89 mm, ~123 mm). In this case, also vertices from B- and D-meson decays are removed, since they cannot be distinguished from the vertices caused by the interactions. Figure A.3 shows the radial distance of secondary vertices in b- and light jets. It shows, that tracks from both b- and light jets interact with the detector material. The region < 20 mm is not shown, since it is too close to the primary vertex.

Figure A.4 shows the performance of the overall and individual cleaning procedures for b- and light

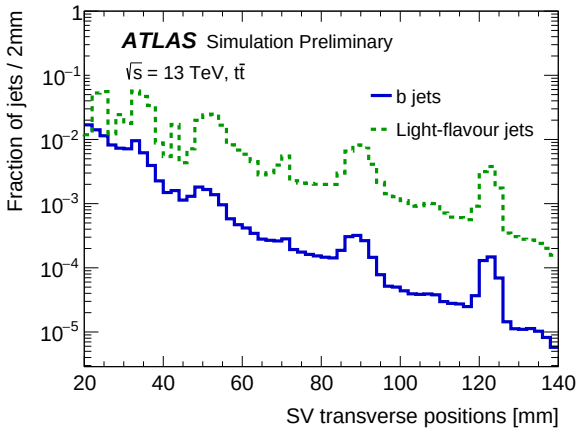

Figure A.3: Transverse positions of vertices in b- and light jets. The peaks, corresponding to the detector material can be seen clearly. The distributions are shown in logarithmic scale and are normalised to one.

jets. It shows the radial distance of the secondary vertex to the closest pixel detector layer or the beampipe. It can be seen, that vertices from b-jets are affected slightly by the material cleaning step, while vertices from light jets, which correspond to fake vertices, are heavily suppressed by both cleaning steps.

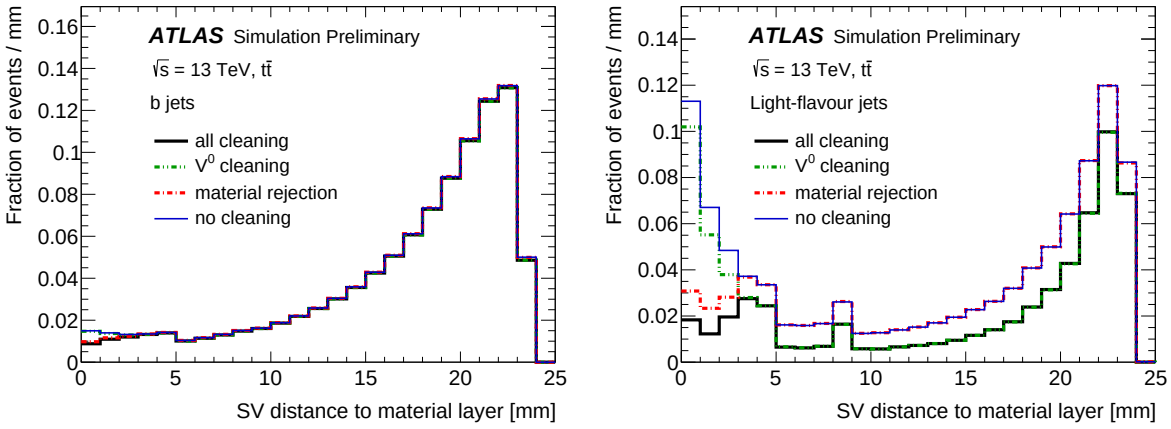

(a) b-jets (b) light jets

Figure A.4: Radial distance between the reconstructed secondary vertex and the nearest material layer for b- and light jets. The distributions are normalized to the black curve, which is normalized to one.

A.4 Results

After applying the SVF algorithm, a single secondary vertex per jet is reconstructed, along with several properties. Figure A.5 shows the mass of the reconstructed secondary vertex and the number of two-track vertices, after the cleaning procedure is applied, but before merging associated jets to a single multitrack vertex, for b-, c- and light jets. Since the number of tracks is higher in b-jets, the mass peak is smeared out and higher than in c- and light jets. In addition, more two-track vertices can be constructed with a higher

track multiplicity. Not all tracks associated to the two-track vertices in Figure A.5(b) are necessarily merged into one multi-track vertex. As described in Section A.3, if several multi-track vertices could be formed, the vertex with most associated tracks is chosen.

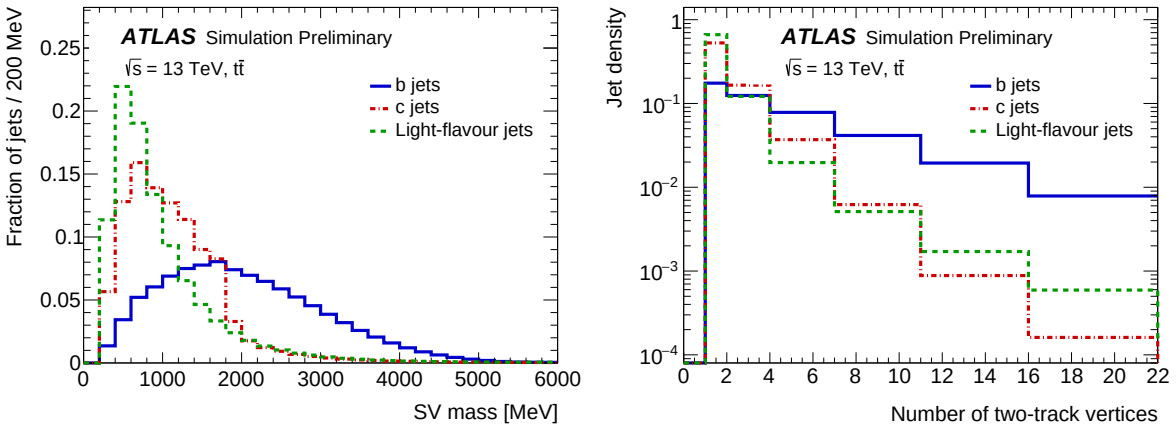

(a) (b)

Figure A.5: Mass of the secondary vertex (a) and the number of two-track vertices (b) for *b*-, *c*- and light jets. The distributions are normalised to one.

Figure A.6 shows the mean value of the mass of the reconstructed secondary vertex and the number of two-track vertices for *b*-, *c*- and light jets as a function of the transverse momentum of the jet. It shows, that these variables are mostly independent of the jet p_{T} for *b*-jets, while *c*- and light jets show a linear correlation. As a result, *b*-jets are harder to distinguish from *c*- and light jets at large transverse momenta.

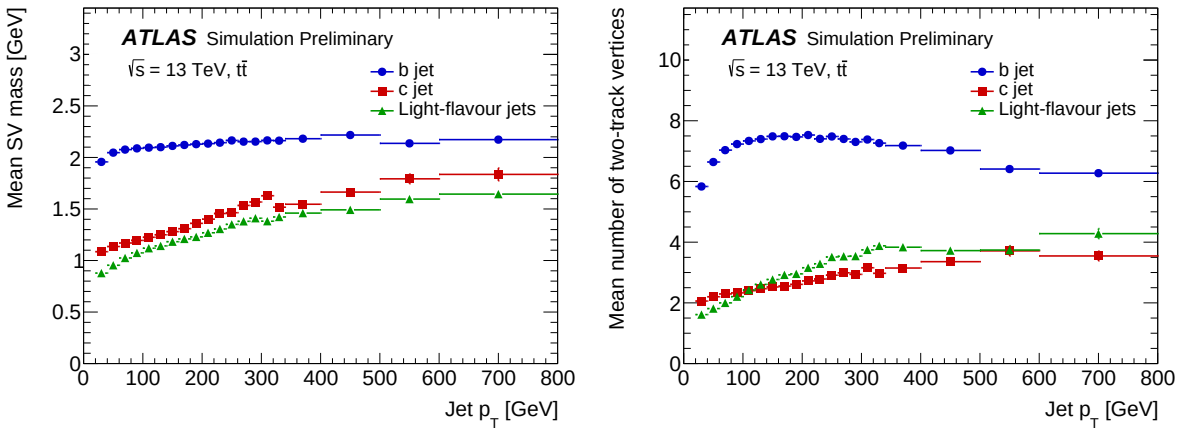

(a) (b)

Figure A.6: Mean mass of the secondary vertex (a) and mean number of two-track vertices (b) for *b*-, *c*- and light jets, as a function of the jet p_{T}.

A.4.1 Performance

The performance of the SVF algorithm is expressed in the efficiency to reconstruct a secondary vertex. This is shown in Figure A.7, as a function of the transverse momentum of the jet. On average, the algorithm is able to reconstruct a secondary vertex inside a b-jet in 80% of the cases, while the probability of reconstructing a fake vertex rises with the transverse momentum of the jet, due to the increase of the track multiplicity. The slight drop in reconstruction efficiency for b-jets with higher jet p_{T} can be explained by the collimation of tracks inside the b-jets, while the number of tracks associated to a b-jet remains constant.

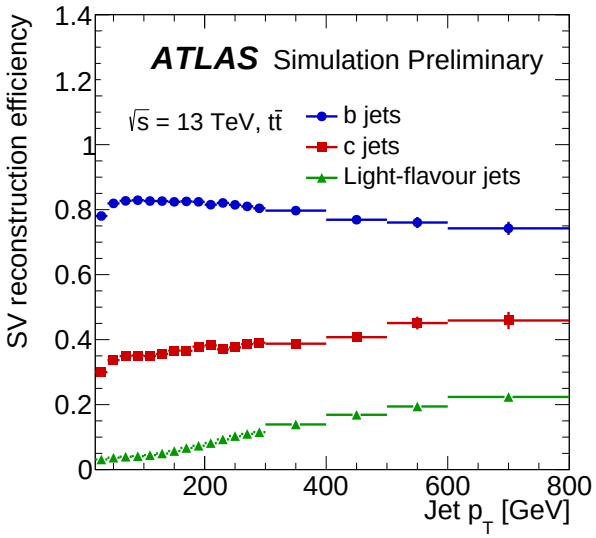

Figure A.7: Reconstruction efficiency of secondary vertices for b-, c- and light jets, as a function of the jet p_{T}.

A.4.2 Propagation to b-tagging algorithms in the ATLAS experiment

The b-tagging algorithms, which are based on the information of secondary vertices, that are provided by the SVF algorithm, are SV0, SV1 and SV2 [172, 173]. The SV0 algorithm uses the ratio of the three-dimensional distance L between the reconstructed secondary vertex and the primary vertex and its uncertainty, σ_L, to discriminate b-jets from other jets. The SV1 and SV2 algorithms use a likelihood ratio test, instead, and are more powerful. Variables, obtained directly from the SVF algorithm, such as the secondary vertex mass or the number of two-track vertices after the cleaning procedure was applied, are used as input for the PDF of the test statistic. More details on how a test statistic is constructed are given in Section 5.5 and Reference [154]. Figure A.8 shows the performance for the SV0, SV1 and the combined performance of the SV1 and IP3D algorithms, in terms of the b-jet efficiency, as a function of the light-jet rejection. The IP3D algorithm [174] relies on information of the impact parameter of the tracks associated to the jet. Figure A.8 shows that the combination of the information from the secondary vertex and the kinematics of the tracks results in a significantly better performance. Even when no secondary vertex can be reconstructed, as shown for b-jet efficiencies higher than 80%, the b-jet can still be identified, relying on tracking information only.

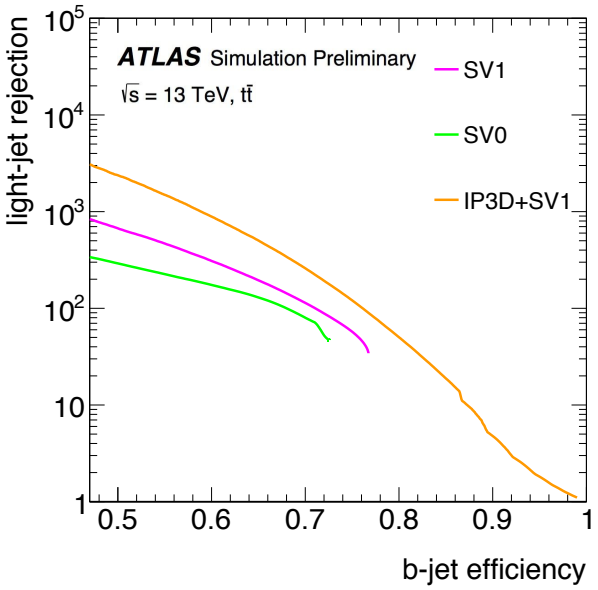

Figure A.8: The *b*-jet efficiency as a function of the light jet rejection for the SV0, SV1 and combined SV1+IP3D *b*-tagging algorithms.

APPENDIX B

ATLAS data formats

This appendix gives an overview of how recorded events by the LHC are pre-processed to be used in the physics analysis.

The pre-processing of ATLAS data is done within the Athena framework, up until the point where the analysis team uses an analysis framework to create ntuples, as described below.

B.1 ATLAS data formats

As introduced in Section 3.2.5, the LHC delivers a collision rate of 40 MHz, which is reduced to 1 kHz by the ATLAS trigger system. The output of the trigger system is in the RAW data format. As the name indicates, the RAW data still needs to be processed before it can be analysed. This is done in the bulk processing step. Here, the recorded events are monitored for whether the detectors function properly and whether all physics objects (muons, electrons and jets) can be reconstructed. This step is performed in sets of luminosity blocks, which each contain about 10^5 recorded events and correspond to roughly one minute of data taking, as explained in Section 4.2. The output of the bulk processing is (among other possible formats) the AOD (Analysis Data Object) format.

In addition to the recorded data, also simulated samples are stored in the AOD format, after all simulation steps (described in Section 3.3) have been performed.

In Run 2 an effort was made to have the AOD format readable by ROOT [167], which is the framework commonly used for data analysis in high energy experiments. Therefore all AODs are processed to the xAOD (extended AOD) format, which contains information about each event and reconstructed particles. In addition, each xAOD can be associated to the run, luminosity block and event within a given run.

B.1.1 Derivations

Usually, xAODs contain more information than needed for an analysis and than can be easily handled. Therefore, derivations (DxAODs) are introduced, which are a subset of xAODs. The derivations are obtained by removing information from xAODs in the following way:

- Events are removed (skimming).
- Object collections are removed (thinning).
- Object information is removed (slimming).

Events are removed, based on the selection used in the derivation. For the object collections, multiple collections are included per object in the xAODs. For example, multiple jet collections (based on different jet algorithms) are defined. Finally, variables not of interest for the analysis are removed in the slimming step. In total, the derivation should not exceed 4% of the size of the xAOD, after all three steps were performed.

The samples introduced in Section 4.2 use the "TOPQ1" derivation, which is the default derivation for an analysis involving top quarks with leptons in the final state and requires at least one lepton with a transverse momentum of at least 20 GeV. Other derivations for top-quark physics typically have a tighter event selection, requiring more leptons in the event.

B.1.2 Analysis framework

The derivations are further processed using a dedicated analysis framework. For an analysis with top quarks, the "AnalysisTop" framework is commonly used. The main task of this framework is to further reduce the size of the derivations, by imposing a tighter event selection and to apply object recommendations and calculate systematic uncertainties. Both object recommendations and systematic uncertainties are provided by combined performance (CP) groups within the ATLAS collaboration, as described below. As such, all object recommendations and systematic uncertainties are centralised among all physics analyses. Processing samples with the analysis framework is usually done for each analysis, since both the object and event selection and are customized for the purpose of the given analysis. The object selection, chosen for the $t\bar{t}V$ multilepton analysis is described in Section 4.

ATLAS CP groups

The ATLAS collaboration has six combined performance groups dedicated to reconstruct analysis objects and compute corresponding uncertainties to be used for physics analysis. The six CP groups are: Inner Tracking, E/gamma, Muon, Tau, Jet/Etmiss, Flavour Tagging. All instrumental uncertainties, described in Section 5.4.1, are provided by these groups and applied via the analysis framework. As an example, the Flavour Tagging group is responsible to train the multivariate b-tagging algorithm and calibrate working points for usage in the physics analysis.

B.1.3 Ntuple production

The output, obtained from the analysis framework is commonly referred to as "ntuples". Each ntuple contains a set of variables that is then used to impose an event selection or reconstruct objects in the analysis. In addition systematic uncertainties are embedded into the ntuples.

Figure B.1 shows how the xAOD format is reprocessed to the final ntuple format within the ATLAS experiment. The diagram indicates that the xAOD format can be read directly by the user. However, accessing the DxAOD via an analysis framework is the recommended route to produce the final ntuple format.

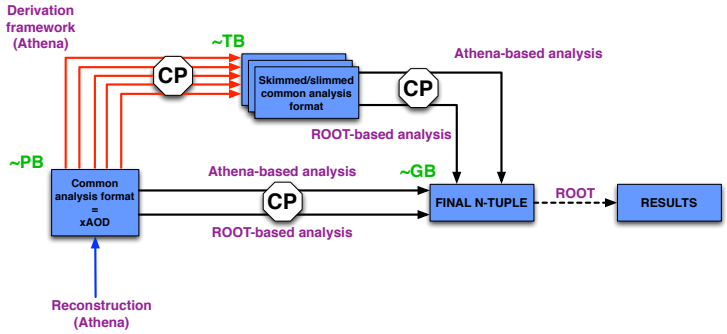

Figure B.1: Analysis model for the ATLAS experiment in Run 2 [175].

As described in Section 4.2, multiple samples for simulation and data are considered for the analysis. Therefore, running each sample necessary with the analysis framework takes a certain amount of diskspace and computing time. A typical ntuple production, that included all necessary samples and systematic uncertainties for the $t\bar{t}V$ multilepton analysis was using 900 GB of diskspace. Each sample was processed in parallel over the grid (a collection of computer centres, connected over the globe), in order to save computing time. As a final step, the cross section for each simulated sample had to be added as an event weight. In total, the full ntuple production took about a month to be completed.

APPENDIX C

Alternative signal regions using multivariate techniques with 36.1 fb^{-1}

Multivariate techniques are powerful tools to distinguish a given signal from the background, by extracting information from several input variables and combining them into a single output variable: the discriminator. This combination selects the signal events from different phase spaces depending on the input variable in a multi-dimensional way.

The multivariate approach is not limited to particle physics but finds applications in many fields of science. In particle physics, the most common ones are "*Boosted Decision Trees*" (BDT) and "*Neural Networks*" (NN) [60, 61]. The tool used for this analysis is the "*Toolkit for Multivariate Data Analysis*" (TMVA) [176], which provides a machine learning framework embedded into ROOT [167], the framework commonly used for data analysis in particle physics at CERN.

C.1 Introduction to Boosted Decision Trees

A "*Decision Tree*" is a binary classifier, which evaluates one input variable at a time. Multiple decisions, called "*nodes*" are sequenced to form a "*tree*" with the goal to separate signal from background events. The decision-making process of classifying events is called the training and simulated events of signal and background are provided by the user. The number of nodes per tree, labeled as tree depth, is defined by how many decisions it takes until the set percentage of events used for the training can be identified as signal or background. The events in the last node, also called "*leaf*", divide the phase space into signal- and background-like events. As such, multiple trees provide a multidimensional cut in the phase space to categorize the events used for the training. Both the number of trees and tree depth can be manually set by the user. Figure C.1 illustrates how events are classified for a single decision tree. It can be seen that a given input variable can be used in multiple nodes.

Given this setup a number of trees and nodes can be defined such that each leaf contains only one event, providing a perfect classifier. However such a training would be sensitive to statistical fluctuation in the pool of events used for the training. This concept is called "*overtraining*" and is avoided by limiting the number of trees and tree depth or by removing insignificant nodes. The latter procedure is referred to as "*pruning*", where nodes are removed in a way that does not influence the overall separation power of a given tree. Since multiple trees are combined in the training, the pruning can even remove whole trees, which happens if the separation power of a tree corresponds to random guessing. The algorithm behind combining pruned trees, avoiding overtraining, to get a powerful discriminator is called "*boosting*" [177]. In addition to the pruning, events classified from a given tree receive an event weight for the next decision

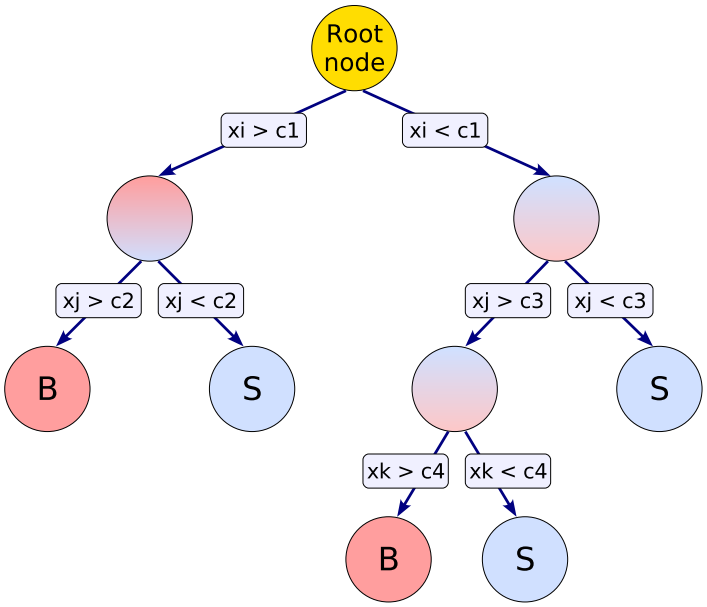

Figure C.1: Schematic view of a single decision tree. Multiple binary decisions (nodes) using input variables are made to categorize the events used for the training [176].

tree, to extract new information. TMVA provides several boosting algorithms:

- Adaptive Boost: A threshold for the classification for a given characteristic of the event pool is defined. For each of those characteristics a separate event weight is calculated and applied for the subsequent decision tree. By focusing on a large number of characteristics, the information from trees with a small separation power is used efficiently.

- Gradient Boost: A weighted sum of individual event weights, that focuses on single characteristics, is calculated and applied on the training events after each tree. Therefore, it is able to discard statistical fluctuations in the pool of training events in a more efficient way compared to the adaptive boosting.

- Bagging: During the training, the events get resampled in a way such that the output discriminant is the average of all individual outputs from every decision tree. Since this algorithm does not focus on combining the decision trees in an optimal way it is not considered as a boosting algorithm.

- Randomised Trees: Both, the set of input variables considered in each tree and the amount of training events is randomised.

After the training of the BDT has been performed, it is tested for overtraining. Even though the decision trees are combined in a BDT, a large number of trees or depth can still introduce statistical fluctuations in the training. Therefore the testing step is necessary. Using the TMVA framework, the pool of events is divided into a set of events used for the training and for testing, usually splitting the available events in half. In order to make use of the full amount of events available, a cross-training is performed: After the regular training and testing step, the training is repeated using the event pool used for the testing from the first training and vice versa. The cross-training requires to check the overtraining for both training steps, but ensures a stable performance of the BDT.

The TMVA framework performs a Kolmogorov-Smirnov test to measure the overtraining [178]. This test estimates the cumulative distance between the test and training samples by calculating the statistical significance. A null hypothesis is defined: in this case it corresponds to both test and training samples being equivalent. The probability $1 - \alpha$ is calculated, where α corresponds to the confidence level. If the test returns a probability larger than 0.05, then overtraining cannot be excluded with a 95% confidence level anymore. An example of the Kolmogorov-Smirnov test for the overtraining of a BDT as well as the output discriminator is shown in Figure C.2(a). The shape of the signal distriubtion of the test sample shows two peaks, indicating that some events are similar to the background and hard to distinguish.

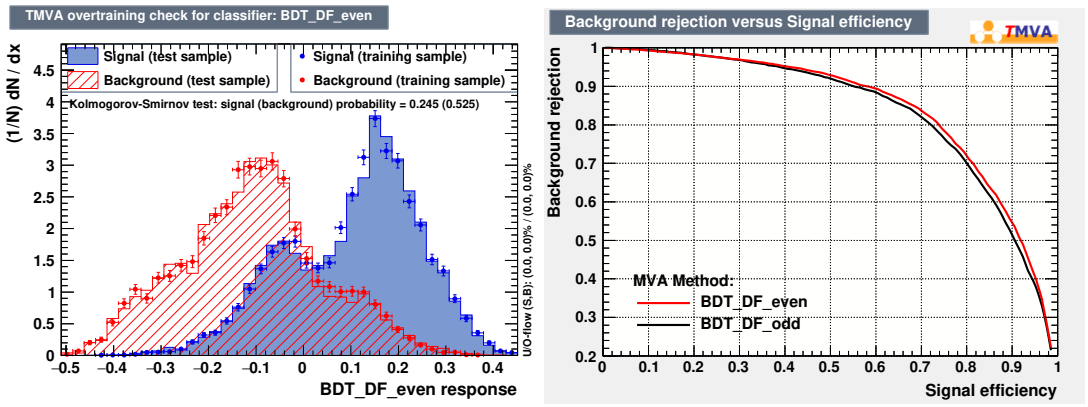

(a) Output discriminator (b) ROC curve

Figure C.2: Output discriminator (left) and ROC curve (right) provided by the TMVA framework. The dots in the left figure correspond to the events used for the training, while the histogram show the events used for the testing. The result of the Kolmogorov-Smirnov test shows no signs of overtraining. The example ROC curves in the right figure are obtained with a BDT using cross-training. The integral of the curves is 0.82 and 0.83 for the black and red curve, respectively, indicating a good performance. The BDT in this example used 500 decision trees with a depth of 2 and Adaptive boosting.

After the overtraining could be rejected, the performance of the BDT can be reviewed by checking the "*Receiver Operating Characteristic curve*" (ROC curve), which shows the signal purity as a function of the signal efficiency. The integral over this curve is a measure of the quality of the classifier, where an integral of 1 corresponds to a perfect classifier and an integral of 0.5 corresponds to random guessing. It is common to optimize the BDT according to the integral of the ROC curve. An example ROC curve is shown in Figure C.2(b).

C.2 Alternative signal regions

In the $t\bar{t}Z \rightarrow 4\ell$ analysis, described in Section 5.2, four signal regions are defined, split according to the number of b-jets and the flavour composition of the Z_2 lepton pair. In order to fully exploit the discrimination between signal and backgrounds and therefore improve the performance of the analysis, new signal regions are defined by training BDTs. Since a BDT is trained using information from input variables, the total amount of BDTs can be smaller than the amount of signal regions, as, the number of b-jets can be used as an input variable for the training. The Z_2 flavour composition on the other hand is a variable that only has two options, where the background composition varies significantly, while the number of b-jets is used as an input variable for the training. A total of two BDTs are trained, denoted as 4ℓ-SF and 4ℓ-DF, each having different backgrounds. For 4ℓ-SF the most dominating background is the ZZ process, while for 4ℓ-DF it is both the tWZ and the $t\bar{t}H$ process. Since these two BDTs are trained independently from each other, they each have their own set of input variables for the training. However, it was found that most of the variables have a good separation power and were included in the training of both BDTs. The parameters of the BDTs are given in Table C.1, while the list of input variables used is shown in Table C.2. Choosing the Adaptive boosting allowed to use a tree depth of two without having overtraining, which was not possible using the Gradient boosting. More input variables were used for 4ℓ-DF, because the backgrounds are harder to distinguish from the signal process in this region.

Decision trees	Tree depth	Boosting algorithm
500	2	Adaptive boosting

Table C.1: Parameters used for the training of the two BDTs. Since Adaptive bossting was used, overtraining is avoided by assigning small weights to statistical fluctuations and no pruning was applied during the training. The small tree depth helps further to avoid overtraining.

The number of b-jets, which was used before to differentiate the signal regions is now an input variable instead and used for both BDTs. A new variable is $p_{\mathrm{T}}^{\mathrm{sys}}$, which was shown to discriminate the $t\bar{t}$ background from the signal in a cross section measurement of the Wt process done by ATLAS [179]. In a similar manner this variable helps to discriminate the tWZ process from $t\bar{t}Z$. It exploits the kinematic information of the Z_2 lepton pair, which is different for the tWZ and $t\bar{t}Z$ process. The exact definition of $p_{\mathrm{T}}^{\mathrm{sys}}$ is:

$$p_{\mathrm{T}}^{\mathrm{sys}} = \sqrt{(p_x(\ell_{Z2\_1}) + p_x(\ell_{Z2\_2}) + p_x^{\mathrm{miss}})^2 + (p_y(\ell_{Z2\_1}) + p_y(\ell_{Z2\_2}) + p_y^{\mathrm{miss}})^2}. \tag{C.1}$$

Here ℓ_{Z2_1} and ℓ_{Z2_2} denote the two leptons from the Z_2 pair.

The highest ranked variables are $E_{\mathrm{T}}^{\mathrm{miss}}$ and m_{Z_2} for the 4ℓ-SF BDT and the number of b-jets and the scalar sum of the transverse momentum of all jets and leptons, H_{T}, for the 4ℓ-DF BDT. In addition to the input variables, a selection to train each BDT is defined. The selection is chosen such that the available amount of simulated events used for the training is sufficient to properly separate the background processes, while focusing on getting a good signal-to-background ratio. For the selection of the two BDTs, at least one b-tagged jet is required (in addition to the preselection as described in Section 5. Otherwise, the selection of two BDTs differ in terms of the flavour of the leptons associated to the Z_2 pair, only.

A signal region is defined for each BDT that was trained. In this setup, the shape of the BDT discriminator is used for the profile likelihood fit, instead of fitting a single bin, as it is done in the

Variable	4ℓ-SF	4ℓ-DF
Number of b-jets	✓	✓
$E_{\mathrm{T}}^{\mathrm{miss}}$	✓	✓
H_{T}	✓	✓
p_{T} (Z_1)	✓	✓
p_{T} (Z_2)	✓	
p_{T} (ℓ_3)		✓
p_{T} (ℓ_4)	✓	✓
$p_{\mathrm{T}}^{\mathrm{sys}}$	✓	✓
m_{Z_1}		✓
m_{Z_2}	✓	✓
$m_{4\ell}$	✓	✓
$\Delta\phi(Z_1)$	✓	✓
$\eta(b\text{-jet}_2)$		✓

Table C.2: Input variables used for the training of the BDTs.

analysis with four signal regions. The BDT discriminator distributions have three or four bins each in the fit, a compromise between amount of events available and the signal seperation in the last bin.

The distributions of the BDT discriminator is shown in Figure C.3 and compared to data. The agreement between data and simulation looks good. A set of four input variables for each BDT is shown in Figures C.4 and C.5.

The fit is performed, using the two signal regions and the ZZ control region, which is described in Section 5.2.2, additionally requiring 0 b-jets to avoid overlap with the two signal regions. In addition to the signal strength $\mu_{t\bar{t}Z}$, the normalization of the ZZ background is determined by the fit as well. The yields obtained from the three regions are shown in Table C.3.

The fit result is:

$$\begin{aligned} \mu_{t\bar{t}Z} &= 1.25^{+0.28}_{-0.25}(\text{stat.})^{+0.09}_{-0.10}(\text{syst.}), \\ \mu_{ZZ} &= 1.07 \pm 0.18, \end{aligned} \tag{C.2}$$

with an observed (expected) significance of 5.4σ (6.2σ). The event yields after the fit are shown in Table C.4, while the post-fit BDT discriminator distributions are shown in Figure C.6. A comparison of the fits with and without signal regions that rely on multivariate techniques is given in Table C.5.

The results are compatible within their uncertainties. While the normalisation of the $t\bar{t}Z$ process is very similar in both cases, further validating the result of the analysis, the normalisation of the ZZ background increased with the new set of regions. This can be explained by the additional contribution of ZZ background events in the 4ℓ-SF region. Those events are mostly in the first bin of the BDT discriminator distribution, as seen in Figure C.3(a). Since the signal region is missing any requirement on the missing transvere momentum, these events were absent in the setup without BDT signal regions.

Since the 4ℓ channel is dominated by the statistical uncertainty, the multivariate approach is able to

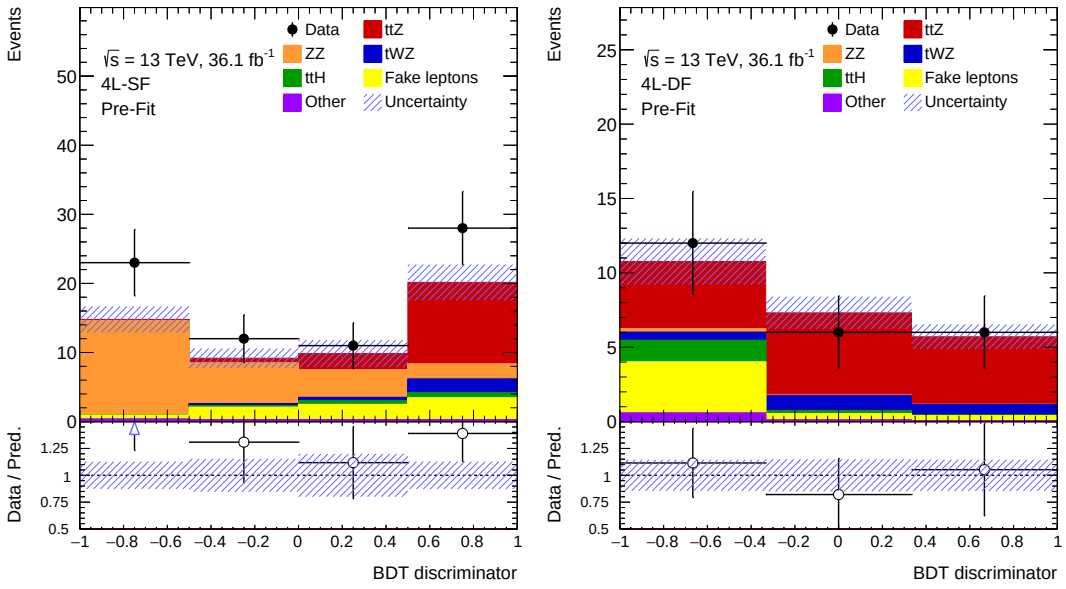

(a) 4ℓ-SF (b) 4ℓ-DF

Figure C.3: Comparison of data and simulation for the BDT discriminators, using the selection of the training. Both, statistical and systematic uncertainties are included.

	4ℓ-SF	4ℓ-DF	4ℓ-ZZ-CR
$t\bar{t}Z$	0.02 ± 0.01	15.03 ± 0.71	14.61 ± 0.71
ZZ	140.55 ± 20.43	25.71 ± 3.09	0.30 ± 0.08
tWZ	0.01 ± 0.01	2.74 ± 0.37	2.25 ± 0.33
$t\bar{t}H$	0.00 ± 0.00	1.59 ± 0.18	1.70 ± 0.18
Other	1.81 ± 0.85	1.14 ± 0.47	0.72 ± 0.28
Fake leptons	5.96 ± 1.36	7.73 ± 2.14	4.20 ± 1.26
Total	148.35 ± 21.22	53.95 ± 4.39	23.78 ± 1.71
Observed	137	74	24

Table C.3: Expected and observed events (pre-fit) in the 4ℓ channel using multivariate techniques. Both, statistical and systematic uncertainties are included. Processes included in "Other" are triboson, $t\bar{t}WW$, and 4 tops. All predictions are split into events with real and fake leptons. Events with fake leptons are scaled by the fake factors, as described in Section 5.2.3.

improve the result, since the BDT is efficient in isolating signal events, without loosing information by removing regions of phase space.

	4ℓ-SF	4ℓ-DF	4ℓ-ZZ-CR
$t\bar{t}Z$	0.02 ± 0.02	18.96 ± 4.12	18.34 ± 4.00
ZZ	138.47 ± 13.01	27.54 ± 3.24	0.31 ± 0.07
tWZ	0.01 ± 0.01	2.74 ± 0.37	2.25 ± 0.32
$t\bar{t}H$	0.00 ± 0.00	1.62 ± 0.18	1.73 ± 0.18
Other	1.85 ± 0.86	1.23 ± 0.51	0.76 ± 0.29
Fake leptons	5.45 ± 1.19	8.06 ± 2.18	4.44 ± 1.27
Total	145.80 ± 12.84	60.15 ± 5.25	27.85 ± 4.10
Observed	137	74	24

Table C.4: The expected and observed events after the fit has been performed (post-fit) in the 4ℓ channel using multivariate techniques. Both, statistical and systematic uncertainties are included. Processes included in "Other" are triboson, $t\bar{t}WW$, and 4 tops. All predictions are split into events with real and fake leptons. Events with fake leptons are scaled by the fake factors, as described in Section 5.2.3.

	4ℓ nominal	4ℓ BDT
$\mu_{t\bar{t}Z}$	$1.21^{+0.28}_{-0.25}(\text{stat.})^{+0.11}_{-0.12}(\text{syst.})$	$1.25^{+0.28}_{-0.25}(\text{stat.})^{+0.09}_{-0.10}(\text{syst.})$
μ_{ZZ}	0.94 ± 0.18	1.07 ± 0.18
Expected significance	5.1σ	5.4σ
Observed significance	5.7σ	6.2σ

Table C.5: Comparison of two fit setups in the 4ℓ channel. The fit denoted as 4ℓ nominal includes four signal regions and one control region and is described in Section 5.6.1, while the other fit denoted as 4ℓ BDT, contains two signal regions and one control region and is described in this section

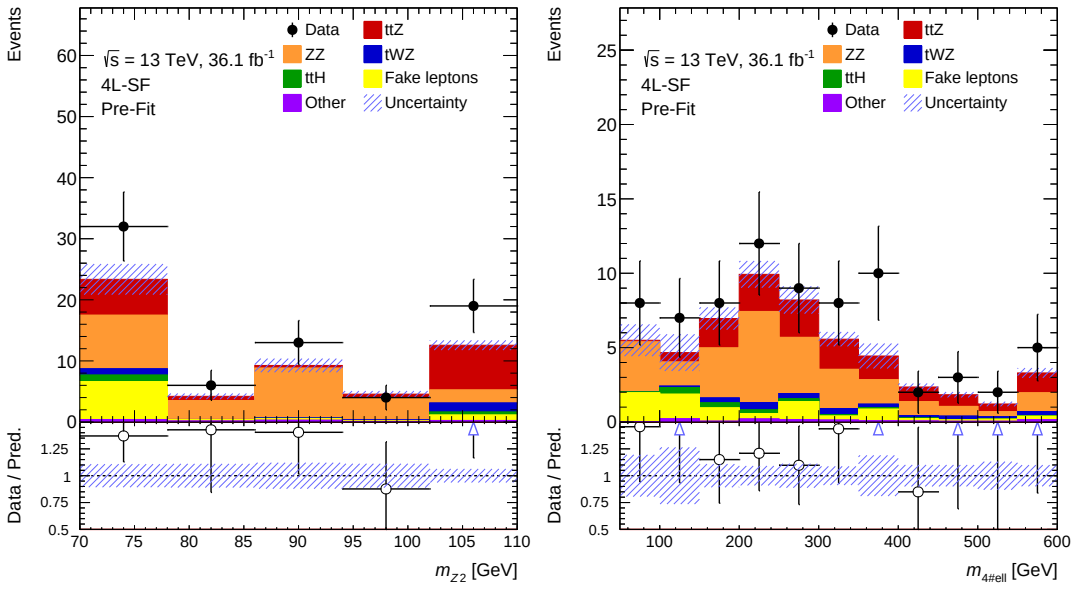

(a) (b)

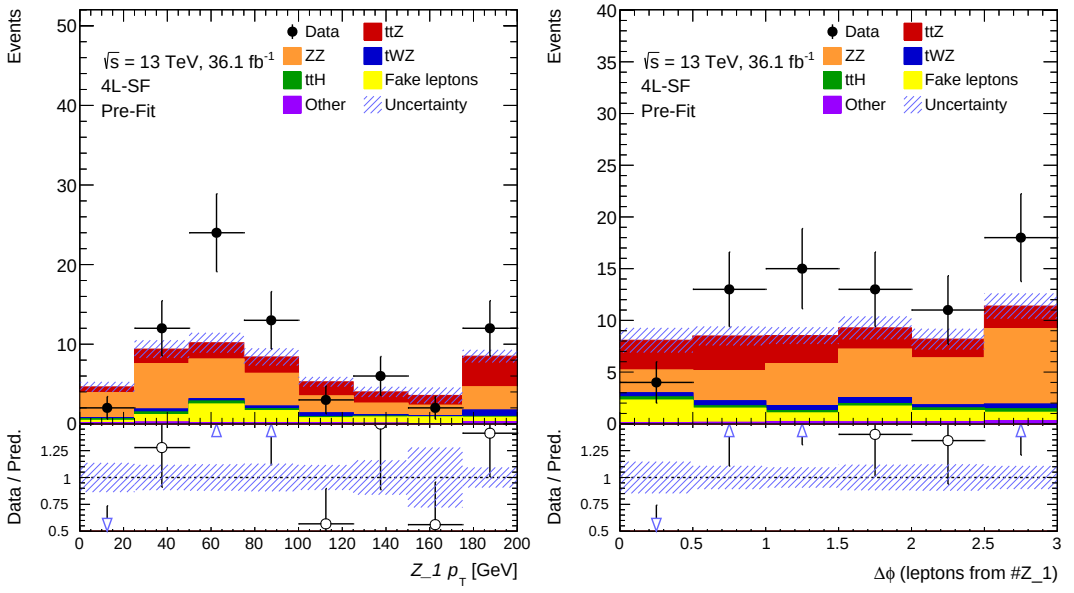

(c) (d)

Figure C.4: Comparison of data and simulation for input variables for 4ℓ-SF, using the selection of the training. Both, statistical and systematic uncertainties are included. Each of the distributions includes the under and overflow in the first and last bin, respectively.

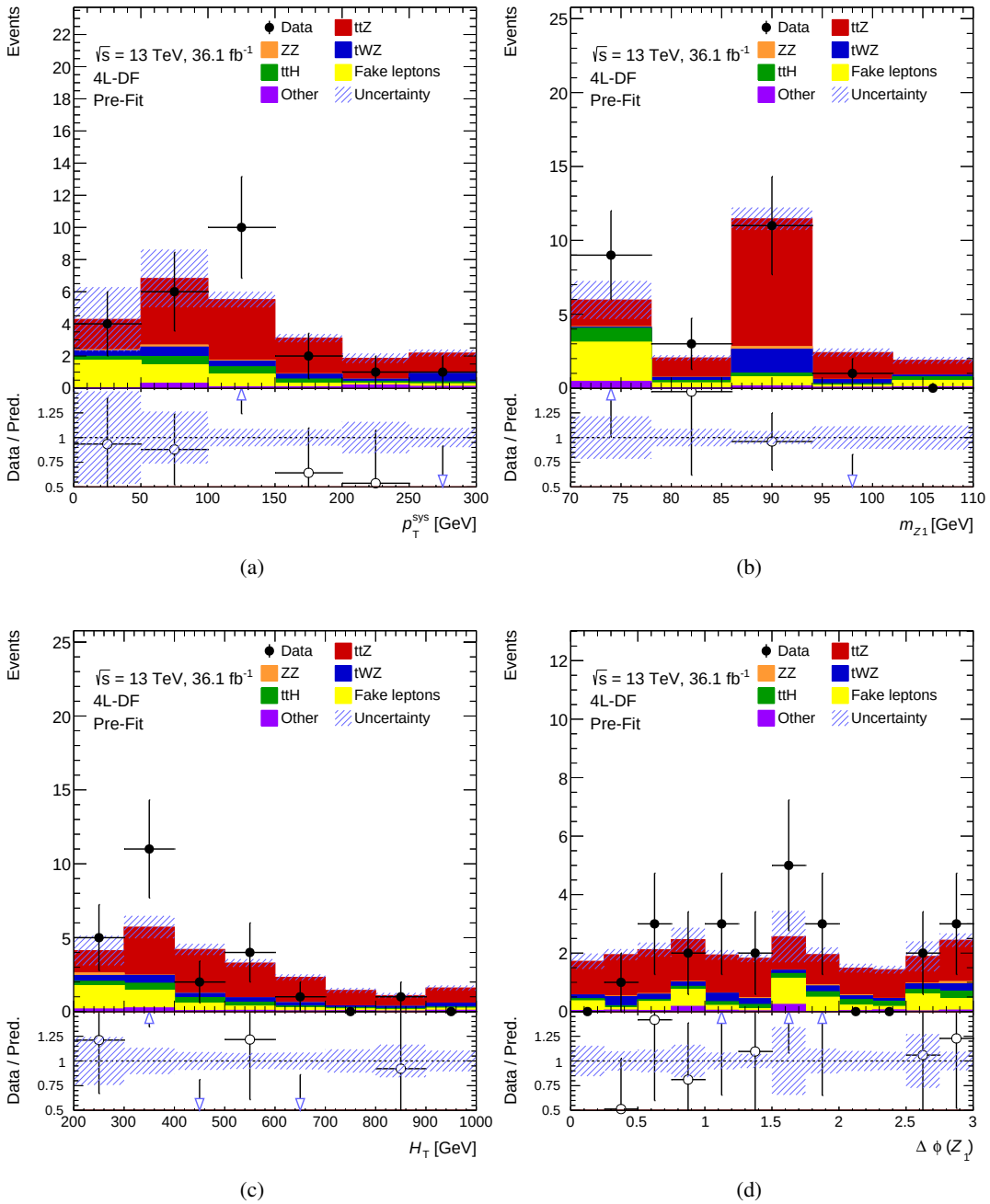

(a) (b) (c) (d)

Figure C.5: Comparison of data and simulation for input variables for 4ℓ-DF, using the selection of the training. Both, statistical and systematic uncertainties are included. Each of the distributions includes the under and overflow in the first and last bin, respectively.

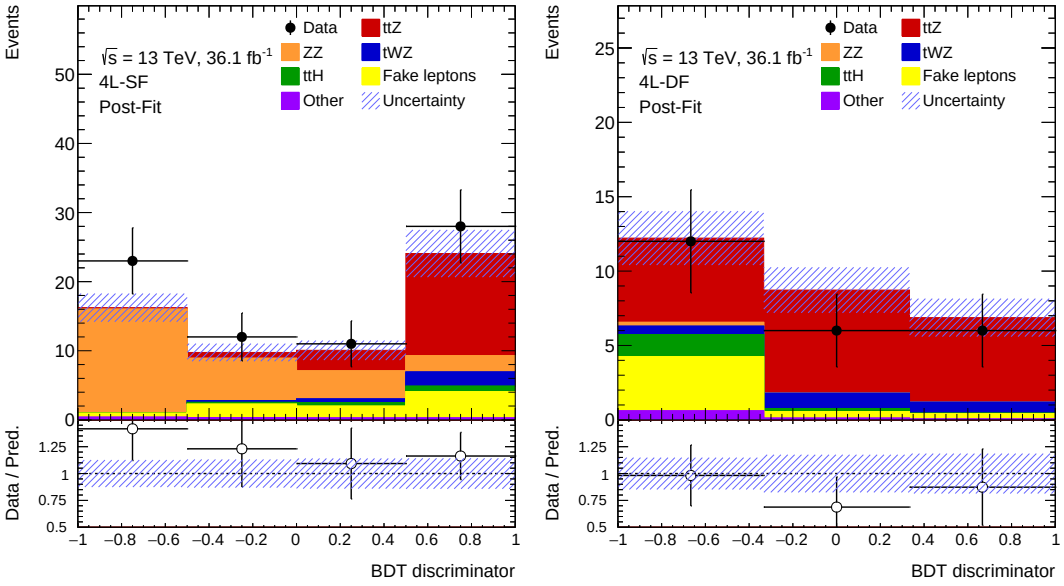

(a) 4ℓ-SF (b) 4ℓ-DF

Figure C.6: Comparison of data and simulation for the BDT discriminators after the fit has been performed, using the selection of the training. Both, statistical and systematic uncertainties are included.